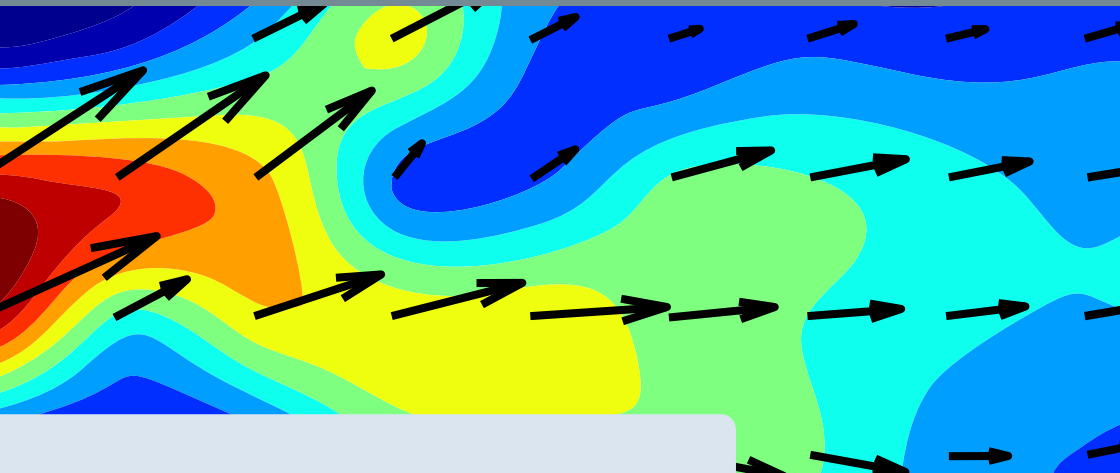# A design process for propellers for the agitation of high viscous fluids based on the design analysis of wind turbine blades

Lehrstuhl für Strömungsmechanik und Strömungsmaschinen
Prof. Dr.-Ing. M. Böhle

Thomas Reviol

TECHNISCHE UNIVERSITÄT KAISERSLAUTERN

A design process for propellers for the agitation of high viscous fluids based on the design analysis of wind turbine blades

Vom Fachbereich Maschinenbau und Verfahrenstechnik
der Technischen Universität Kaiserslautern
zur Erlangung der venia legendi für das Fach

Fluid mechanics and energy technology

genehmigte Habilitationsschrift

von
Herrn
Dr.-Ing. Thomas Reviol
aus Saarbrücken

D386

Dekan: Prof. Dr.-Ing. Tilmann Beck
Gutachter: Prof. Dr.-Ing. Martin Böhle
Prof. Dr.-Ing. habil. Uwe Janoske

Tag der Einreichung: 06.10.2020
Tag des Habilitationsvortrags: 29.06.2021

to my father

Acknowledgements

An undertaking such as this can never be accomplished without the help and support of others. In recent years, I have enjoyed the support of many friends and colleagues in the completion of this work. It is not possible to thank everyone who supported me here. I would like to thank everyone who has supported me and I would like to pay special tribute to a select few who played a significant or special part in the completion of this work:

First of all, I would like to thank Prof. Dr.-Ing. Martin Böhle for his many years of support and for our numerous professional and critical discussions. In addition to Prof. Dr.-Ing. Martin Böhle, I also want to thank Prof. Dr.-Ing. Uwe Janoske for preparing the expert reports. I would also like to express my thanks to the members of the Habilitation Commission: Prof. Dr.-Ing. Martin Böhle, Prof. Dr. Nicolas Gauger, Prof. Dr.-Ing. Erik von Harbou, Prof. Dr.-Ing. Alois Schlarb, Dr.-Ing. Kai Nikolaus and Janik Röckel.

I would also like to thank all my colleagues who I have worked with at the Institute over the years for their good cooperation and mutual support. In particular, Stefan Kluck and Peng Wang, with whom I had the opportunity to conduct some joint research.

Over the years, some colleagues became friends. To name a few of them: Rebecca Schäfer, Marco Schönwald and Anika Theis. They were always prepared to lend me a sympathetic ear. Especially the many supportive discussions with Anika Theis gave me further motivation, particularly towards the final stages of my thesis, which helped me to complete the thesis.

Most of all, I would like to thank my family: my wife Rebecca and my three children Lillie, Nora and Erik. Over the years, my family have experienced many highs and lows and has always accepted these in a wonderful way. They supported and motivated me every step of the way. Without them, this thesis would never have been possible. Thank you so much!

Obersülzen, July 2021, Thomas Reviol

Abstract

The subject of this thesis is the design of axial flow machines. The type of turbomachine under examination is used to supply energy for high viscous fluid flow, as used in mixing and stirring tasks. The high viscous media treated in these tasks usually have non-Newtonian fluid properties. This kind of fluid flow is frequently associated with the field of energy and process engineering. In order to narrow down the problem described, the field of turbomachinery is restricted to the consideration of propellers. Propellers are used in a wide range of fluid mechanics tasks. In the form of wind turbines, propellers extract kinetic energy from a control room and thereby slow down the flow. Propeller stirrers, on the other hand, increase the energy level of a flow and accelerate it. Both machines are based on the same principle – only the direction of the energy flow is to be considered as the opposite direction.

The design of new agitators is usually based on experience. Often, agitators are, therefore, not flow-optimised, and cannot be optimally operated. In this thesis, it is investigated whether the design processes of modern wind turbines, which are considered to be mature, can be adapted in order to generate a flow-optimised geometry for this type of turbomachine as well.

This thesis will first examine the basics of wind turbine design processes. Special attention will be paid to the differences caused by the viscous fluid properties under consideration. The highly viscous behaviour of the fluids under consideration means that the theoretical fundamentals have to be extended as a result. Such extensions are identified and supplement the theoretical basis. The thesis will then present and examine an analytically based design process for flow-optimised propeller mixers. The procedure is based on *blade element momentum theory*.

Application of *blade element momentum theory* requires detailed knowledge of the aerodynamic behaviour of the profiles used. This behaviour is usually only known for low viscosity and high-Re applications, as is usually the case for wind turbines or propeller engines. Comprehensive profile characteristics are not available for highly viscous and low-Re applications. In this thesis, these basics are generated using numerical methods.

In the next step, the newly introduced design method is combined with the results of the investigations of profile aerodynamics for high viscous low-Re fluid flow. This combination is done using a calculation process which produces the flow-optimised geometry of a propeller mixer. The theoretical principles of the methods are implemented in an algorithm in such a way that the resultant turbomachine can be designed for a previously selected operating point, the design point. In contrast to classical turbomachinery, the design point additionally requires the specification of viscous fluid properties.

However, in practical use, the final selected operating point of a turbomachine is often not the design point. The algorithm is examined for its suitability for inverse power calculation as well in order to compute the complete characteristic curve for a previously generated propeller mixer already in the design process.

Kurzfassung

Die vorliegende Arbeit stellt einen Beitrag zur Auslegung axial fördernder Strömungsmaschinen dar. Der untersuchte Typ einer Strömungsmaschine dient der Energiezufuhr in Strömungen hochviskoser Medien, wie diese z.B. für Misch- und Rühraufgaben eingesetzt werden. Die dort behandelten hochviskosen Medien verfügen meist über nichtnewtonsche Fluideigenschaften und treten häufig im Bereich der Energie- und Verfahrenstechnik auf.

Um das beschriebene Problem einzugrenzen, steht als Strömungsmaschine der Propeller im Fokus der Arbeit. Propeller werden in vielfältigen strömungsmechanischen Fragestellungen eingesetzt. In Form von Windenergieanalagen entziehen Propeller einem Kontrollraum kinetische Energie, und verzögern auf diese Art die Strömung. Propellerrührer hingegen erhöhen das Energieniveau einer Strömung und beschleunigen diese. Beide Maschinen basieren auf denselben Grundlagen – lediglich die Richtung des Energieflusses ist entgegengesetzt zu betrachten.

Der Entwurf neuer Rührorgane basiert in der Regel auf Erfahrung. Oft verfügen Rührorgane deswegen nicht über eine strömungsoptimierte Form und können nicht optimal betrieben werden. In dieser Arbeit wird untersucht, ob die als ausgereift geltende Auslegungsprozedur moderner Windenergieanalagen auf Propellerrührer adaptiert werden kann, um eine strömungsoptimierte Geometrie auch für diese Art Strömungsmaschine zu generieren.

Zunächst werden in dieser Arbeit die Grundlagen der Auslegungsprozeduren von Windenergieanalagen analysiert. Insbesondere die Unterschiede infolge des betrachten Fluides werden hierbei berücksichtigt. Durch das hochviskose Verhalten der betrachteten Fluide ergeben sich notwendige Erweiterungen der theoretischen Grundlagen. Diese werden identifiziert und die theoretische Basis wird um diese notwendigen Erweiterungen ergänzt. Daran anschließend wird eine analytisch basierte Auslegungsprozedur für strömungsoptimierte Propellermischer eingeführt und untersucht. Diese basiert auf der Verwendung der *Blattelement-Momenten-Methode*.

Die Verwendung der *Blattelement-Momenten-Methode* erfordert das detaillierte Wissen über das aerodynamische Verhalten der eingesetzten Profile.

Dieses Verhalten ist bislang meist nur für niedrigviskose high-Re Anwendungsfälle bekannt, wie dies üblicherweise bei Windenergieanalagen oder bei Propellertriebwerken der Fall ist. Für hochviskose low-Re Anwendungen sind umfassende Profilcharakteristika nicht vorhanden. Diese Grundlagen werden im Rahmen dieser Arbeit mit numerischen Methoden generiert.

Die neu eingeführte Auslegungsprozedur wird im letzten Schritt der Arbeit mit der Profilaerodynamik für hochviskose low-Re Strömungen kombiniert. Die Kombination erfolgt in einer numerischen Prozedur, deren Resultat die strömungsoptimierte Geometrie eines Propellerrührers ist. Die theoretischen Grundlagen der Methoden werden derart in einem Algorithmus umgesetzt, dass die resultierende Strömungsmaschine für einen zuvor gewählten Auslegungspunkt zur Verfügung gestellt werden kann. Im Gegensatz zum klassischen Strömungsmaschinenbau erfordert der Auslegungspunkt zusätzlich die Angabe der viskosen Fluideigenschaften.

Kenntnisse über den im Betrieb anfallenden Leistungsbedarf einer Strömungsmaschine sind wesentlich zur Einsparung von Ressourcen. Häufig ist der gewählte Betriebspunkt einer Strömungsmaschine allerdings nicht der Auslegungspunkt. Es wird daher weiterhin untersucht, inwiefern der verwendete Algorithmus invers ausgeführt werden kann, um das Leistungskennfeld a priori für zuvor generierte Propeller zu berechnen.

Contents

List of Figures

List of Tables

Nomenclature

Latin symbols

Symbol	Description	Unit
$\mathbf{1}$	Unit tensor	$-$
a	Factor of interference, approximation factor	$-$
A	Area	m^2
b	Width	m
c	Absolute velocity	m/s
c	Concentration	$wt.\%$
C	Coefficient	$-$
D	Diameter	m
$\mathbf{D}$	Rate of deformation tensor	s^{-1}
De	Deborah number	$-$
E	Energy	J
f	Function	$-$
F	Force	N
$\mathcal{F}$	Antiderivative of a function	$-$
g	Gravity constant	$m\,s^{-2}$
G	Shear modulus	MPa
H	Height	m
i	Control variable	$-$
I	Momentum	$N\,s$
j	Control variable	$-$
k	Control variable	$-$
k	Consistency	$Pa\,s^m$
l	Chord length	m
L	Length	m
$\mathbf{L}$	Velocity gradient tensor	s^{-1}
m	Mass	kg
m	Flow index	$-$

Symbol	Description	Unit
$\dot{m}$	Mass flow rate	$kg\,s^{-1}$
$\vec{n}$	Normal vector	m
n	Shaft speed	min^{-1}
n_{z}	Amount of an entity	$-$
Ne	Newton number	$-$
p	Pressure	Pa
P	Power	W
R	Radius	m
r	Coordinate, radial direction	m
Re	Reynolds number	$-$
$\mathbf{S}$	Cauchy stress tensor	Pa
t	Time	s
T	Torque	Nm
$\mathbf{T}$	Extra stress tensor	Pa
$\mathcal{T}$	Mixing time	s
u	Circumferential velocity	m/s
v	Velocity magnitude	m/s
v_{x}	Velocity component in x-direction	m/s
v_{y}	Velocity component in y-direction	m/s
v_{z}	Velocity component in z-direction	m/s
V	Volume	m^3
$\dot{V}$	Volume flow rate	$l\,s^{-1}$
w	Relative velocity	m/s
x	Coordinate, x-direction	m
$\mathfrak{x}$	Arbitrary entity	$[\ldots]$
$\underline{\mathfrak{x}}$	Matrix with arbitrary entities	$[\ldots]$
y	Coordinate, y-direction	m
z	Coordinate, z-direction	m

Greek symbols

Symbol	Description	Unit
α	Flow angle	$^\circ$
γ	Shear strain	$-$
$\dot{\gamma}$	Rate of shear strain	s^{-1}
Γ	Circulation	$m^2\,s^{-1}$
δ	Glide angle	$^\circ$
ε	Longitudinal strain	$-$
ϵ	Lift-to-drag ratio	$-$
$\dot{\varepsilon}$	Rate of longitudinal strain	s^{-1}
ζ	Angle of jet divergence	$^\circ$
η	Efficiency	$-$
θ	Temperature	K
ϑ	Coordinate, angular direction	$^\circ$
Θ	Relative angle	$^\circ$
λ	Relaxation time	s
Λ	Tip speed ratio	$-$
μ	Dynamic viscosity	$Pa\,s$
μ_0	Dynamic zero-shear-rate-viscosity	$Pa\,s$
μ_∞	Dynamic infinity-shear-rate-viscosity	$Pa\,s$
ν	Kinematic viscosity	$m^2\,s^{-1}$
π	Dimensionless entity, Archimedes' constant	$-$
ρ	Density	$kg\,m^{-3}$
σ	Normal stress	Pa
ς	Standard deviation	[...]
τ	Shear stress	Pa
τ_0	Yield stress	Pa
Υ	Auxiliary function	[. . .]
φ	Mounting angle	$^\circ$
χ	Scalar-valued function	[. . .]
ψ	Normal stress coefficient	$Pa\,s^2$
ω	Frequency	s^{-1}

Subscripts

Symbol	Description
0	Point upstream from propeller
1	Point in propeller plane
2	Point downstream from propeller
$-\infty$	Unaffected position, upstream from propeller
$+\infty$	Unaffected position, downstream from propeller
∞	Ambient condition
C	Circumferential
CA	Profile camber
Co	Entity of core or initial region of jets
D	Drag
Dev	Entity of fully developed flow of jets
Des	Design point
Eff	Effective value
En	Entrainment
L	Lift
Hub	Hub
Ind	Induced
Jet	Jet
LE	Leading edge
m	Meridional component
max	Maximum value
$mean$	Mean value
n	Normal component of an entity
OP	Operating point
P	Quantity related to propeller
PP	Quantity related to the propulsion
R	Resulting
t	Tangential component of an entity
T	Thrust
TE	Trailing edge

Symbol	Description
TH	Profile thickness
u	Swirl component

Superscripts

Symbol	Description
χ^*	Hypothetical value
$\vec{\chi}$	Vectorial formulation of an entity
$\overline{x}$	Mean value
$\hat{\chi}$	Arbitrary spatial position
$\check{\chi}$	Reaction force
$\widetilde{\chi}$	Simplified value
χ'	Space derivative
$\dot{\chi}$	Time derivative
χ^+	Dimensionless distance in space
$\chi_{\mathcal{P}-}$	Entity infinitesimal upstream from point $\mathcal{P}$
$\chi_{\mathcal{P}+}$	Entity infinitesimal downstream from point $\mathcal{P}$

Abbreviations

Symbol	Description
BEM	Blade element momentum theory
CAD	Computer aided design
CMC	Carboxymethyl cellulose
CFD	Computational fluid dynamics
GG	Guar gum
LBM	Lattice-Boltzmann method
LES	Large eddy simulation
LVE	Linear viscoelastic regime
$NLVE$	Non-linear viscoelastic regime
PAA	Polyacrylamide
$RANS$	Reynolds-averaged Navier-Stokes equations
UDA	Ultrasonic Doppler anemometry
XG	Xanthan gum

Part I.

Synopsis

1. Introduction

1.1. Subject of research

Mixing is widely-used in process engineering. For instance, mixing is used in the pharmaceutical [8], food, and chemical industries [38; 190], as well as in the energy sector [109] and even in waste water treatment [56]. Mixing is important in many areas of process engineering [38; 154].

The process of mixing is applied to various tasks. It is often a matter of homogenising a heterogeneous system. Thus, mixing is not applied only to liquid media, but also to gas or even solid materials mixed with a fluid. In addition, mixing can reduce the thickness of the boundary layer. Hence, mixing is very suitable in heat transfer tasks. Mixing is sometimes subdivided into five major tasks in accordance with its different applications, for example, homogenisation, heat transfer, suspension and emulsion creation and dispersing, as suggested by Zlokarnik [246] and Stieß [218].

Owing to the wide range of mixing applications and tasks, different criteria have been developed for mixing process analysis and mixer type selection: a very important, widely used and often enhanced criterion is the mixing time analysis [38; 119; 218; 246]. But when performing a mixing time analysis, a further criterion is necessary, one which describes the goal of the mixing process. In the case of the homogenisation of two liquids with differing refraction, for example, a streak method can be applied, and the mixing time $\mathcal{T}$ may be defined as that time which has to pass until no streaks remain [218]. Obviously, this criterion is not suitable for heat transfer processes. Hence, assessing such mixing processes by analysing the mixing time is not appropriate and the mixing time is mostly related to the task of homogenisation.

Another more general criterion for mixer selection involves the analysis of the mixer power consumption. In many subfields of process engineering, the mixing technology requires an enormous amount of energy. Sometimes, the mixer is the most expensive item in energy billing for the whole facility. In biogas power plants, mixing and pumping technology consumes around 10% of the entire energy [101]. From this point of view, it is very desirable to select

power-optimised mixers to reduce energy input. Hence, for these types of mixing tasks, power consumption should be prioritised over other criteria.

Unfortunately, in many cases, it is not possible to determine the true power of a mixer before it is utilised. For non-Newtonian fluid flow or complex mixing systems in particular, estimating the power consumption is still a challenge [43; 195].

In addition to the uncertainties in presuming power consumption, the shape of the mixer is often not clearly defined [195], and sometimes taken from other engineering subfields [134]. In this case, the previous power calculation cannot be used and the calculation is instead performed by correlation methods. To meet the power requirements, the mixers are often driven by over-dimensioned motors to provide a minimum of drive power.

Hence, it needs to be emphasised that there are still open questions on how to design and how to select a mixer for specific tasks [121; 195].

1.2. Objective

As stated above, mixers that are not well designed will cause inefficiencies in mixing and in power performance. Achieving maximum energy efficiency across entire facilities has always been an aim not just since the time of the energy revolution – and is particularly important in the field of renewable energy technology.

Although there have been many research projects on mixing in the past and despite the enormous amount of knowledge that has been gained in this field in the last 100 years, many important facts about the design process are still unknown, especially in the subfield of non-Newtonian fluid flow [120; 121]. Therefore, within the scope of this work, a sub-area of mixing will be considered in order to develop a flow-optimised mixer form. The goal is to enable efficient mixing as well as an increase in performance, especially for low-Re viscous fluid flow, which is typically related to non-Newtonian fluid patterns.

As will be described later, the field of mixing is very broad, with many different mixer types and different mixing tasks (see Chapter 2.1 and Figure 2.3).

Hence, it is not possible to optimise the whole field of mixers by developing a single machine. The scope of this work, therefore, has to be reduced to clear, defined tasks in a limited subfield:

The geometrical shape of mixers is often designed by experience or is taken from other engineering fields (see Chapter 2.1). In the case of the propeller mixer, it is often taken from marine applications. A propeller is an aerodynam- ically or hydrodynamically developed flow machine, e.g. those constructed for aircrafts, ships, or wind turbines. It is more reasonable to adjust the design techniques of the aforementioned propeller types for mixing instead of applying a propeller from another field of engineering. These methods, therefore, have to be adjusted. Finally, a propeller can be developed especially for the purpose of mixing. Following this idea, the aim of this work is as follows:

To develop a design process for propellers specifically for the purpose of mixing.

The design method must provide the **geometrical shape** of this propeller for a specific and predefined mixing problem.

The drive power is of fundamental importance and must form the basis of the design process.

1.3. Solution concept

To develop the required design process for propeller mixers for the agitation of low-Re viscous fluid flow, the procedure will be developed in line with the design principles of modern wind turbines. Furthermore, jet theory will be

adopted. This means that the research project will consist of three different scientific fields:

- **Fluid mechanics**:
    - Hydro- and aerodynamics
    - Free jet theory
    - Mixing
- **Renewable energy technology**: wind turbines
- **Rheology**: non-Newtonian fluid flow

These three categories will be combined in such a manner that the aim of the research project will be a logical result, even though these categories are not commonly combined. Hence, some aspects will be discussed in detail to help explain their application. Therefore, a short overview of the solution concept is provided at this point to support understanding.

1.3.1. Overview

As with many fluid machinery design processes, *blade element momentum theory* will be applied here to develop a flow-optimised propeller mixer. This means that the propeller will be designed by considering the momentum forces at several different sections.

This creates a need for suitable flow profiles for the desired purpose. In the past, an enormous number of airfoils were developed and investigated for a variety of different applications. Unfortunately, most of them were developed for low viscosity and high-Re flow respectively. Nevertheless, some special flow profiles for hydrofoils or other marine applications can be found in literature. However, no investigation has been carried out into the performance of any flow profile in non-Newtonian fluid flow, which means that all the investigations performed previously are worthless with regard to the subject of the present work.

Repeating the investigations for the airfoil studies with regard to non-Newtonian fluid flow is not beneficial, specifically because these profiles were

not designed for high viscous fluid flow. Hence, this study will investigate the lift and drag characteristics of preselected flow profiles in non-Newtonian fluid flow. Subsequently, *blade element momentum theory* can be adopted to non-Newtonian fluid flow, as mentioned earlier, and can be used to establish the shape of a flow-optimised propeller by integration via the radial coordinate. Furthermore – in addition to the as yet unknown profile polar characteristics – this procedure requires knowledge of the flow conditions of the specific problem for which the propeller has to be designed.

Typically, the inflow condition into the control volume around the desired flow machine is not known. In the case of marine applications, the velocity of the ship is known and may be applied as an inflow condition, but, in the present case, the propeller is place-bound. To solve this problem, a control volume with known outflow conditions can be derived from propeller jet theory. Using mass and momentum balances, the inflow condition can be derived from the outflow conditions.

Bringing together all of the above fields will cause several problems. These problems are, however, dealt with in this work, and are discussed below.

1.3.2. Problems to solve

As outlined, bringing the individual tasks together will cause problems. The use of the above methods in non-Newtonian fluid flow is especially uncommon – in particular, *blade element momentum theory* has never been applied to non-Newtonian fluid flow before. Non-Newtonian fluid flow poses a challenge with most of the methods and procedures, and it causes the following problems, which were discussed in brief earlier.

The control volume

The application of *blade element momentum theory* requires the knowledge of the effective velocity at the flow profile – but at the early stages of the mixer design process, the inflow conditions are not known and the effective velocity cannot be calculated.

However, if the control volume and its outflow are known, the inflow mass flow rate can be calculated, provided continuity is achieved over the control room. A comprehensive work by Oebius [146] revealed the sole erosion of ship propellers in harbour basins. To find the momentum forces of the jet, Oebius developed a special jet theory for propellers. An expected mass inflow can be derived from this theory. Assuming the validity of the control volume, all necessary velocity profiles can be derived.

In Chapter 6, jet theory and propeller jet theory in particular will be explained in detail. In Chapter 7.1.1, Oebius' theory will be adopted for viscous fluid flow.

Profile characteristics

Blade element momentum theory involves airfoil characteristics such as drag and lift. The most convenient way of determining these characteristics is to perform investigations in a wind tunnel. The airfoil under investigation is mounted on multi-component scales. By varying the angle of attack and the flow velocity, a profile polar diagram consisting of lift and drag coefficients can be derived. Both coefficients are plotted against each other and the wind speed variation data is collected to produce a profile polar diagram which, according to Lilienthal [125], provides an array of curves, with its array parameter being given by the Reynolds number.

In the past, this was performed for a huge number of profiles – mostly in air, sometimes in water, but never in fluids with varying viscous properties. Hence, to utilise *blade element momentum theory*, the procedure of investigating flow profiles has to be repeated for a broad variation of non-Newtonian media. Owing to the enormous amount of available profile data, which has been analysed since the early work by Lilienthal in the late 19th century, it is not convenient to analyse all the available profiles for non-Newtonian flow. One alternative is to develop new profiles, but this is not suitable, either, since the common method in designing airfoils is related to potential flow and, thus, to inviscid fluid flow.

It makes more sende to select suitable profiles that are already available

for investigation with non-Newtonian media. Unfortunately, the loads for a flow profile on a small-sized test bench would be very low, while the effort in operating such a test bench with several non-Newtonian fluids would be very high. In this work, therefore, all profile investigations will be performed by numerical methods (see Chapter 7.2). The fundamentals of aerodynamics are discussed in Chapter 3.

The Reynolds number

When performing investigations of flow profiles in non-Newtonian fluid flow, a serious problem arises: there is no unambiguous viscosity for non-Newtonian fluids and the Reynolds number cannot be calculated. This means that the results that are obtained cannot be compared with each other. In the end, all the results will be worthless. Hence, a method is defined to calculate a Reynolds number for non-Newtonian fluid flow.

In Chapter 5, non-Newtonian fluid flow, together with common and advanced methods to calculate a Reynolds number for non-Newtonian fluid flow, will be discussed in detail.

Derivation of a geometrical shape

The aim of this work is to develop the shape of a flow-optimised propeller mixer. A further goal is to estimate the drive torque within the design process in a highly accurate manner.

The aim is to establish an analytical design method to solve the issue. Owing to the similarities between wind turbines and propeller mixers, common wind turbine design methods will be applied.

Unfortunately, the procedure requires the Reynolds number, while the Reynolds number is a function of chord length and local apparent viscosity. Both are unknown at the beginning of the design process and the method has to be solved iteratively. Because of this issue, the design process must apply numerical methods. In addition, the algorithm must be combined with an optimisation procedure to guarantee the most suitable solution.

Part III covers the overall design process and will be presented in detail in Chapter 7 and validated in Chapter 8 and 9 respectively. The fundamentals of the method, taken from the technique of wind turbines, is outlined in Chapter 4.

2. Brief literature overview

Before the mandatory fundamentals, as derived from the solution concept, are discussed, a brief literature overview is given in this chapter to outline recent developments in the main research areas this work is related to.

In general, the main research areas under consideration here are mixer design and the design concept of modern wind turbines. Nevertheless, mixers and wind turbines are not the only focus of this work. All applied fundamentals and techniques are described later in more detail along with the fundamentals of wind turbines. These can be found in Part II.

2.1. Mixer design processes

The beginning of mixing

Humankind has been mixing fluids and solids for centuries. Nevertheless, the history of mixing is not well documented. One of the first references can be found in Agricola's *'De Re Metallica Libri XII'* of 1556. There, Agricola [3] describes the application of mixing in the metallurgical process of gold extraction, [3; 120; 121], as illustrated in Figure 2.1. It can be assumed, therefore, that mixing is a centuries-old technique.

However, the main efforts in research and development are quite recent and took place as recently as the middle of the last century. The first detailed and scientific description of the knowledge of mixing was written by Fischer [64] in 1911. He called for increased efforts in investigating mixing processes due to the fact that mixing was still not well-researched and was even not accepted as a technical discipline in its own right. In contrast to Fischer's statement, Zlokarnik [246] summarised in 1999, that mixing had been well investigated for a variety of mixers. Hence, within about 90 years, the field of mixing had been researched with an enormous degree of effort [120; 121]. Nowadays, mixing is understood as a discipline in its own right, as a technique that is highly relevant to process engineering in particular, and is used in a very

Figure 2.1. *Historical application of mixers for metallurgical processes in the Late Middle Ages, taken from Kraume [121] according to Agricola [3]*

broad field of engineering, such as e.g. in the food or pharmaceutical industries, and in wastewater treatment and energy technologies [38; 119; 154].

As summarised by Kraume [120, 121], the investigation of two theoretical fields were of major importance for the study mixing and led to greater understanding of it. These fields were dimension analysis and statistic turbulence theory.

The first field of dimensional analysis, also called π theorem, is frequently associated with Buckingham [29]. However, it was originally formulated by Riabouchinsky [185] and Federmann [63]. The earlier publication by Vaschy [230] is also related to the field of dimensional analysis but was not recognised by the scientific community. The π theorem is still the procedure used to derive relevant dimensionless numbers to fully describe a problem; it is also the topic of many different work, such as those by Pawlowski [155], Spurk [216] or Zlokarnik [247]. In the field of mixing, the very important Newton

number Ne and the Reynolds number Re are derived from the dimensional analysis; see Chapter 5.3 for a detailed explanation.

The second field, statistic turbulence theory, is especially important for turbulent mixing. This theory traces back to the research on the energy cascade by Richardson [186], and the work of Kolmogorov [117, 118]. The work of both researchers helps explain the transfer of turbulent energy from the mixer to the mixed fluid.

Power consumption agitating Newtonian fluid flow

Although both theories help to understand the principles of mixing, they cannot answer the more general question about a mixer's power consumption. The first investigations into power consumption were performed by Thomson [221] and Unwin [227] in the late 19th century and by Buckingham [30] and Wood et al. [241] at the beginning of the 20th century, but the broad research of this field was investigated with regard to both aforementioned theories in parallel in the middle of the last century. In 1933, Hixson and Wilkens [98] investigated the power consumption of a $45\,°$ pitched blade turbine with four blades. By analysing the power consumption for a broad parameter variation, they performed the first comprehensive and documented study of a mixing system. White and Brenner [237] were also pioneers in the investigation of power consumption, but Rushton et al. [196, 197] published the first broad study of mixers in their famous works *'Power Characteristics of Mixing Impellers – Part I'* and *'Power Characteristics of Mixing Impellers – Part II'*. The final diagram of their results – see Figure 2.2 – was often adopted to additional results and published in fundamental literature, for example in Todtenhaupt and Zeiler [222], Zlokarnik [246], and in Kraume [119].

Power consumption of agitating non-Newtonian fluid flow

However, these researchers did not investigate the power consumption of agitating non-Newtonian fluid flow – this subfield of mixing came to be of interest in the 1950s. Magnusson [128] performed fundamental work in this field. He formulated the concept of effective viscosity, often referred to as apparent vis-
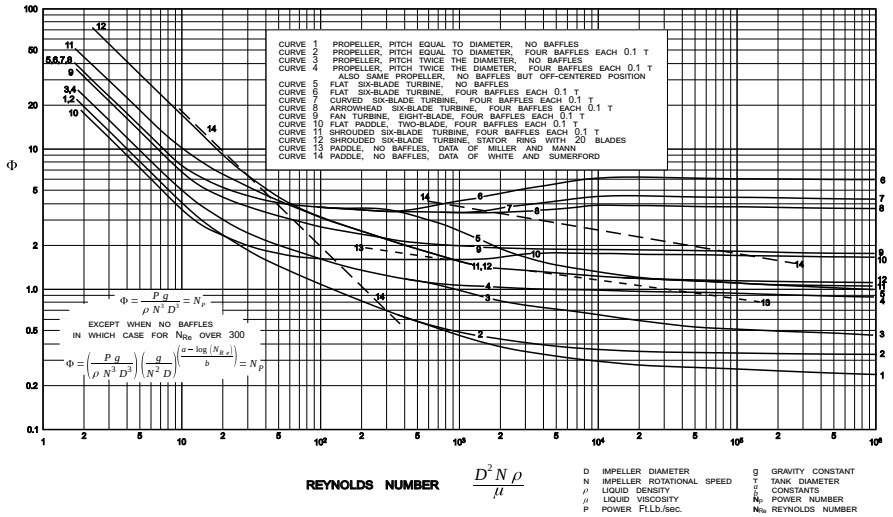
Figure 2.2. *Historical results of power characteristics according to Rushton et al. [196, 197]*

cosity: as a thought experiment, Magnusson considered two identical mixer systems. While the first system was filled with a Newtonian fluid, the second one was filled with a non-Newtonian fluid. Both mixers were driven with the same shaft speed while the torque was observed. By notionally changing the viscosity of the first system, the torque was adjusted to the torque of the second system until both mixing systems had the same torque values. Then, Magnusson assumed, the non-Newtonian fluid would have the same viscosity as the Newtonian fluid.

Based on this concept, a pseudo-correlation between Newtonian and non-Newtonian fluid patterns is suggested: it is possible to transform the investigations into the power consumption of Newtonian fluid flow to non-Newtonian fluid flow. One of the most important pieces of research in the design of mixers for non-Newtonian fluid flow was carried out by Metzner and Otto [131] in 1957. Metzner and Otto found that when the shear rate $(\partial v/\partial r)$ around a mixer is reduced to a mean value $\dot{\gamma}_{\mathrm{mean}}$, this value is proportional to the shaft speed of the mixer, provided the mixer is operating in the laminar regime[1]. Introducing a geometry-specific coefficient (often called Metzner and Otto's

constant) yields the shaft speed-based concept, which is the quasi-basis of the state-of-the-art design process for mixers agitating non-Newtonian fluid flow. In addition to the fundamental work of Metzner and Otto, Metzner and Taylor [133] and Metzner et al. [134] proved their origin concept and validated the concept for propeller mixers.

As well as the concept of Metzner and Otto, the research by Rieger and Novak [187, 188, 189] enables scale-up (or scale-down) of an existing mixer, as long as the power characteristics for agitating Newtonian fluid flow are known.

Both procedures are documented well in literature. For further details, refer to Nagata [139], Böhme [20], Todtenhaupt and Zeiler [222], Knoch [116], or Kraume [119].

Criticism and enhancements of Metzner and Otto's concept

Owing to the very simple relationship proposed by Metzner and Otto, and be- cause of its simplicity in practical use, the shaft speed-based concept is almost the standard procedure, and is common in the process industry. However, the concept has often been criticised, precisely because of its simplicity. The concept has been frequently commented on and examined for this reason, see Blasinski and Rzynski [25], Doraiswamy et al. [54], Shekar and Jayanti [211], and Henzler [93]. In other investigations, Metzner and Otto's concept has been analysed for special issues and, different researchers have often found contradictory results.

The concept of Metzner and Otto have mostly been criticized because of its fluid dependency. Kelkar et al. [111, 112] proved the concept and found that the concept is valid for creeping flow and also for viscoelastic fluids. However, Ulbrecht and Wichterle [226] and Pawlowski [156], emphasised the uncertainties of the concept. Godleski and Smith [79] discovered the validity of the concept for varying flow indices as well, while Tanguy et al. [220] and Reviol [178] found that the proportional coefficient of the concept has to depend on the fluid properties. Finally, as a first researcher, Höcker et al. [91] suggested that there must be a clear, pronounced dependency of the concept

on viscoelastic fluids, which was confirmed by Reviol et al. [180]. Hence, the concept apparently depends on the mixed fluid, while the dependencies are not fully understood. Pawlowski's critique in particular is theoretically based and targets the pseudo correlation of Newtonian and non-Newtonian fluid properties formulated by Magnusson.

The geometric dependency has also been frequently discussed. Even though Metzner and Otto claimed the proportional coefficient was depending on the geometry of the mixer, Calderbank and Moo-Young [31] assumed a constant coefficient, without any connection to the shape of the mixer. Schümmer [205], Bertrand and Couderc [14], Ducla et al. [58], and Shekar and Jayanti [211] investigated different mixers, with the conclusion that the proportional factor has to be constant but different for certain mixer types. This is in agreement with most of the research.

Alternatives to Metzner and Otto's concept

In the past, several more accurate procedures were presented, e.g. by Böhme [20] and Kluck [115], but they could not verify these themselves in practice because of their complexity. It seems to be more convenient to apply certain enhancements, such as those proposed by Henzler and Obernosterer [94], Wassmer and Hungenberg [236], or Reviol [178]; Reviol et al. [179]. As a consequence, the uncertainties of the concept seem to be accepted – and thus also the relevance of the concept for practical use because of its simplicity. For this reason, the concept of Metzner and Otto is accepted as sufficiently accurate [238] and is still the accepted method in designing mixers [181].

Design and operation purposes of different mixer types

While the history and design of mixers have been outlined, one major topic is missing: there is no method to derive the geometrical shape of a mixer, other than experience or by taking a mixer from another field [181]. In literature, however, design proposals such as DIN28131:09-1992 [53] can be found, though these proposals are approximate and do not answer the ques-
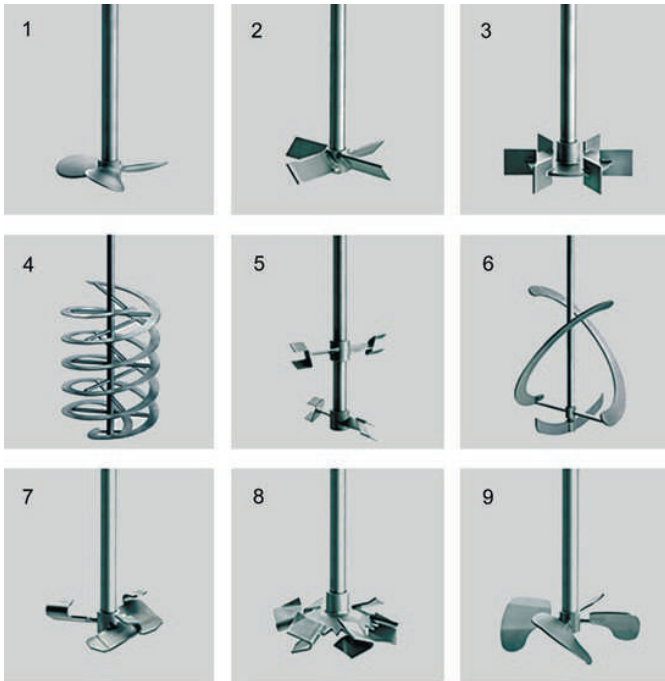
Figure 2.3. *Mixer types for different mixing tasks, Propeller (1), Pitched-blade turbine (2), Blade turbine (3), Helix (4), Intermig (5), Paravisc (6), Combijet (7), Phasejet (8), Isojet B (9), illustrations taken from Chmiel et al. [39]*

tions about flow optimisation. This is a crucial fact with respect to mixer efficiency. Therefore, contemporary applied mixers are highly specialised flow machines, optimised for one certain task, and often related to the operational experiences of single manufacturers, such as the INTERMIG impeller by EKATO, see Figure 2.3-5. Figure 2.3 illustrates other typical mixer types for different mixing applications.

The typical application of the mixer types shown is described for example in Chmiel et al. [39]. Since this work focuses on propeller mixers, only the common operational purpose of this type will be discussed: typically, propeller mixers are applied if high flow rates are the aim of the mixing task [246]. The arrangement is mostly centric to the symmetry axis of the vessel, but an

eccentric position is also possible. Propeller mixers are utilised to agitate turbulent and high viscous fluid flow – typical values for the viscosity are about $\mu = 500\,mPas$, but propeller mixers are also applied for agitating fluids with even higher viscosity of about $\mu = 8000\,mPas$ as well. The common circumferential velocity is $u = 2\text{--}15\,m/s$ [119; 246]. Owing to these facts, propeller mixers are widely used, such as e.g. in the field of wastewater treatment and biogas power plant technology.

2.2. Wind turbines

As noted above, the design process of wind turbines is adopted in this research work to design a fluid-optimised propeller mixer. The relevant fundamentals of wind turbines will, therefore, be discussed in the following.

Historical utilisation of wind energy

Mankind has been exploiting wind energy for many centuries. In the first millennium, wind was mainly used for sailing, with the first known utilisation of wind to drive a rotating machine at the end of the first millennium in around 950 AD, as reported by Baker [9]; Sørensen [215]; Wulff [243]. The principle of early windmills was drag-based. The east of Persia is believed to be the place where they were first used – which is why these early windmills are called *Persian windmills*. In Figure 2.4, the oldest known drawing of this concept [243] is shown along with a windmill in Nashtifan, Iran, which still works to this day.

However, the use of wind energy for industrial purposes is much younger and does not relate to the historical concept. As mentioned, the concept of the *Persian windmill* uses drag, while modern wind turbines use lift.

The theoretical fundamentals of the wind turbines used nowadays were first taken from marine-type propellers and from airscrews. Thus, wind turbines and propellers have the same theoretical background. Hence, only wind turbines will be discussed here, even though propellers are also a main part of this research project.
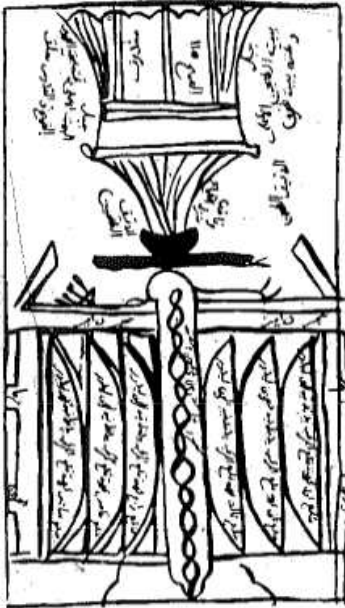
(a) Oldest known drawing of a Persian windmill, taken from Wulff [243], originally referenced to Al-Dimashqi [5]

(b) Original Persian windmill, Nashtifan, Iran, Copyright CC by 4.0 Tasnim News Agency (Attribution) and Mohammad Hossein Taghi (Photographer)

Figure 2.4. *The Persian windmill: the oldest means of converting wind energy: the illustration shows a historical drawing and a photograph of such a windmill in Iran*

Blade element momentum theory

Today, as summarised e.g. by Hansen et al. [89]; Jamieson [104]; Snel [212, 213], the common method used to design a wind turbine is *blade element momentum theory* – using computational enhancements based on CFD.

The first full formulation of the *blade element momentum theory* was documented by Glauert [77]. It is based on two important theoretical approaches, such as the pioneering work of Rankine [170] and R. E. Froude [67], known as *momentum theory*. However, this theory could not describe the geometrical shape of the machine, but only the energy transfer over a hypothetical rotating disc. In contrast to the considerations of *momentum theory*, *blade el-*

ement theory focuses the flow around a profile. This theory was developed by W. Froude [69], Drzewiecki [57], and Lanchester [122], and is the second part of Glauert's *blade element momentum theory*. While *blade element theory* is an alternative useful approach, this theory was associated with uncertainties because of the need to know the characteristics of the blades. For many years, even though all the relevant fundamentals were known, as detailed in the aforementioned publications, the two theoretical approaches could not be reconciled. However, Glauert is said to be the creator of the *blade element momentum theory*, thanks to his clear and methodological formulation of the fundamentals and connections of both theories.

Glauert and the other researchers formulated their theoretical considerations for airscrews and airplane propellers, but Glauert remarked that this theory is not only valid for airplane propellers, but also for other aerodynamic machines, such as windmills. Also by utilising *blade element momentum theory*, a propeller could be designed by (semi-)analytical methods.

The Betz-Joukowsky maximum

Along with *blade element momentum theory*, another important research topic should also be considered: the maximum Betz-Joukowsky limit. In the early 20th century, three famous European aerodynamics schools investigated the maximum theoretical efficiency of a wind energy machine. Their considerations were based on the *momentum theory*, devised by Rankine [170] and R. E. Froude [67], and led to three different publications with analogous content: by Lanchester [123] of the British scientific school, by Betz [17] of the German Institute for Technical Physics at the University of Göttingen, led by Ludwig Prandtl, and by Joukowsky [108] of the Russian Central Aerohydrodynamic Institute of Moscow. According to a review by Bergey [12], Lanchester and Betz found the value almost simultaneously. Hence – in their opinion – the limiting factor should be called the Lanchester-Betz maximum. Since Bergey did not know of the abovementioned publication of Joukowsky, van Kuik [229] suggested naming the limit after all three researchers, but Okulov and van Kuik [148] found that the work of Lanchester [123] is based

on a mistake, done by C. A. Parsons, as remarked in R. E. Froude [68], and suggested Betz-Joukowsky maximum as the name for the factor. Further, Munk [138] too, found the limiting value, but his publication was released after from the publications by Betz and Joukowsky. However, since 1920, the limiting factor has been known as the Betz-Joukowsky limit and amounts approximately to $59.3\,\%$, which means that only this amount of wind energy can be converted.

Chord line distribution of ideal wind turbines

Considerations regarding the maximum efficiency of a wind turbine are merely theoretical if no machine exists that can extract power from the wind. Unfortunately, the considerations above do not provide any guidance as to how to design the shape of a propeller for optimal conditions.

To obtain the shape, the *blade element momentum theory* is applied to calculate the power of an infinitesimal annulus, as described in Gasch and Twele [72] or Hansen [88]. This procedure can be traced back to Glauert [77] but had already been initially performed by Betz [19], though Betz considered infinitesimal axial forces instead of power. Subsequently, the infinitesimal power of the annulus is set equal to the infinitesimal power derived from ideal considerations. While Glauert applied an induction factor, Conrad [42] applied a graphical method based on the circulation. Schmitz [204] also enhanced the method of using the Betz-Joukowsky limit as the infinitesimal ideal power by considering the swirl in the wake of the flow.

Note that the German literature typically prefers the equality of the infinitesimal power to the Betz-Joukowsky limit at an annulus, while the Anglo-American literature mostly utilises the induction factors formulated by Glauert [72]. To fully design a wind turbine, further enhancements were necessary, such as e.g. the tip-loss correction by L. Prandtl in Betz [16], but these corrections are not within the scope of this work and, so, are not discussed here.

Figure 2.5.   *V164-9.5 MW turbines from MHI Vestas Offshore Wind [136]*

Additional concepts for the design of wind turbines

In addition to the *blade element momentum theory* and the Betz-Joukowsky limit, the wake was also a frequent point of interest in the work of several researchers. Although Betz [17] did take the wake into account, it was Goldstein [80] who first formulated the early *vortex theory*. Based on the consideration of a vortex, wind turbines can be designed by a *lifting line* or even a *lifting plane theory*, based on panel methods in accordance with Hess [97], as presented in Hansen [88]; Hansen et al. [89]. But as already mentioned, the *blade element momentum theory* is mostly used to design wind turbines, and only this theory was applied in this work.

Modern wind turbines

At the end of this brief overview, the recent state of the development of modern wind turbines is shown as a contrast to of the first wind turbines: nowadays, turbines are built with about 2 to $5\ MW$ onshore and 3 to $8\ MW$ for offshore. The largest projected wind turbine[2] in the world, the MHI V164-9.5,

was developed by MHI Vestas Offshore Wind. It is shown in Figure 2.5.

Notes

[1]The shaft speed-based concept of Metzner and Otto was often criticised because of its uncertainties, but these were often the result of the application of the concept outside of the laminar regime. However, not only may the flow regime change the proportional factor, but the geometrical shape and the stirred fluid may do so too, as stated by Metzner and Otto.

[2]The data for the largest planned wind turbine project was valid at the date of retrieval of the given information. This was in September 2018 and may no longer be current.

Part II.

Fundamentals

3. Fluid mechanics of flow profiles

This research aims to define a method to design a flow-optimised propeller mixer. As mentioned in Chapter 1, the method is based on the *blade element momentum theory* that is utilised in wind turbines. In this chapter, the aerodynamic fundamentals of the *blade element momentum theory* and the theory itself will be discussed. The design process of wind turbines has been described in Chapter 4.

The *blade element momentum theory* was created by Glauert [77] and is based on two previous approaches. The first fundamentals were discovered by Rankine [170] and R. E. Froude [67] and are known as the *axial momentum theory*. This theory is discussed in Chapter 3.2.1. The second theory is known as the *blade element theory* and was first established by W. Froude [69] and subsequently developed by Drzewiecki [57] and Lanchester [122]. The details of Froude's theory are discussed in Chapter 3.2.2.

Before *blade element momentum theory* is explained in Chapter 3.2, the role of the airfoil is discussed in Chapter 3.1, even though these considerations were published by Lilienthal [125] in 1889 and thus after the fundamentals of the *blade element momentum theory*. The aerodynamics of the profile will be discussed first for sake of understanding.

3.1. Profile aerodynamics

Considering the aerodynamics of an airfoil, the shape of this profile is very important for the aerodynamic load. While *blade element theory* has been known since its formulation by W. Froude [69] in 1878, the loads of a profile can be calculated in principle, but the significance of the profile's form for aerodynamic loads was discovered several years later by Lilienthal [125]. Due to his understanding of the physics, Lilienthal was able to reproduce the mechanics of flying for the first time [126; 210] and can be said to be the first flying man ever.

Lilienthal observed the flight of birds, especially their wings. Figure D.1 in Appendix D of this work shows the clear understanding that Lilienthal had from the form and the kinematics of a bird's wing. He carried out many experiments over a number of years to establish the influences of an arched profile on lift and drag. Finally, he published his famous book *'Der Vogelflug als Grundlage der Fliegekunst – Ein Beitrag zur Systematik der Flugtechnik'* *(Translation: Bird Flight as the Basis of Aviation: A Contribution to the System of Flying Technology)*. It contains the first polar diagrams, see e.g. Figure D.2 for a flat plate. These can be used to find the profile coefficients required by the *blade element theory*.

At almost the same time, Phillips [160] discovered arched profiles as well. In 1884, Phillips filed his results as a patent. Figure D.3 shows clear congruencies between Lilienthal's and Phillips' studies. They reached their results independently of each other [122; 210], but Lilienthal's investigations received more attention from the scientific community due to his methodology in research and, of course, because of the success of his spectacular practical experiments [126]. Hence, although Phillips published his findings some years before Lilienthal, Lilienthal is regarded as the man who first identified the influence of the profile form on aerodynamic loads. His proposal to plot the profile coefficients against the angle of attack and each other has been widely applied and remains the most-used method.

The form of an airfoil and its terminology will be considered first, then the resulting loads, and finally, the characteristics of a profile – as utilised in Part II of this work – will be derived.

3.1.1. General description

Many different profiles have been developed over time for different aerodynamic task. Most of them can be categorised by profile families, such as the well-known range of NACA profile series [1]. Each family, regardless of where it was created, is characterised by a methodological design process to create different profiles. The profile shape is commonly described by universal parameters. So, the shape of a profile and its universal parameters will
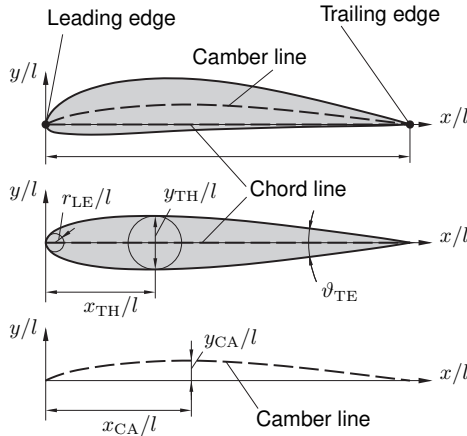
Figure 3.1. *Geometrical description of a profile: shape, thickness distribution, camber line, and relevant parameters for mathematical description, as shown for GOE-387*

be examined before the physics of the aerodynamical loads.

Shape

The shape of a profile typically consists of a thickness distribution and camber line. Figure 3.1 shows a GOE-387 profile (upper view), which is assembled by its thickness distribution (middle view) and camber line (lower view). This kind of profile is typical for subsonic flow only, while profiles for other flow tasks, such as supersonic flow, are quite different. However, only profiles for the subsonic flow are discussed, as these are more relevant for the project,.

Besides the mentioned parts, Figure 3.1 illustrates all typical parameters which characterise an airfoil. The length of the profile is given by the length of chord line l which reaches from the leading edge to the trailing edge of the profile. The maximum thickness is given by the relative thickness y_{TH}/l and is positioned at x_{TH}/l, while the relative maximum camber is y_{CA}/l at x_{CA}/l. The leading edge can be characterised by the relative leading edge radius r_{LE}/l and the trailing edge by the angle $2 \cdot \vartheta_{\mathrm{TE}}$. Lilienthal utilised most of these parameters to characterise the profiles of his investigations.
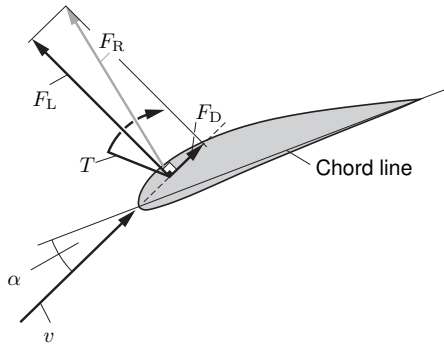
Figure 3.2. *Aerodynamic loads on a profile under flow conditions, as shown for GOE-387 – illustration schematically drawn and not to scale*

Kinematics and loads

A specific profile can be obtained on the basis of the parameters above. Depending on this profile and on a specific flow condition, different forces will result at the airfoil. Figure 3.2 gives an overview of the acting forces, with a profile under a flow with velocity v and angle of attack α.

While investigating flat plates and cambered profiles, Lilienthal recognised that, under the flow conditions described above, the lifting force F_L, which is perpendicular to the direction of the velocity v, will occur, while drag force F_D acting in the direction of the velocity. Both forces can be calculated by applying Equation 3.1 and Equation 3.2 [1], provided the coefficients C_L (lift) and C_D (drag) are known. The area A is mostly understood as a rectangle projected to the plane of the chord line and not as the surface of the profile.

$$F_L = C_L \cdot \frac{\rho}{2} \cdot v^2 \cdot A \tag{3.1}$$

$$F_D = C_D \cdot \frac{\rho}{2} \cdot v^2 \cdot A \tag{3.2}$$

The vector addition of F_L and F_D gives the resulting force F_R, which can be applied at the centre of pressure.

The centre of pressure results from the pressure distribution at the profile and
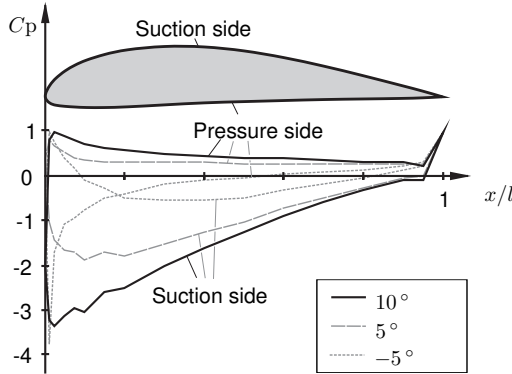
Figure 3.3. *Distribution of the pressure coefficient[4] C_p over a profile, illustration for three different angles of attack α for $Re = 1 \cdot 10^6$ exemplary for GOE-387, calculated with JavaFoil from Hepperle [95]*

is caused by the differences in the velocity field at the top and the bottom of the profile. Figure 3.3 shows the dimensionless pressure C_p, according to Equation 3.3, for the profile GOE-387 as a function of the dimensionless x-coordinate of the considered airfoil for different flow angles. In Figure 3.3, the Reynolds number was at a constant value of $Re = 1 \cdot 10^6$ while three different angles of attack were analysed. So, three different courses for C_p can be obtained[2]. For each course, the bottom (pressure side) and the top (suction side) are marked in the diagram. As can be seen, the course of the curves is varying with the angle of attack and thus the centre of pressure varies as well. [3]

$$C_\mathrm{p} = \frac{p - p_\infty}{\frac{1}{2}\, \rho\, v_\infty^2} \tag{3.3}$$

Under the assumption that the weight force always affects the centre of gravity, the pitching moment T has to be induced because of the variation of the centre of pressure.

In total, three mechanical moments are induced by the pressure distribution,

and all the three moments have to be considered with regard to the aerodynamical loads of a profile. These moments are the lifting force F_L, the drag force F_D, and the pitching moment T.

Aerodynamic characteristics of a profile

Consideration of the moments is not relevant for practical use and only the dimensionless coefficients of the loads will be considered, as proposed by Lilienthal.

Therefore, the coefficients lift C_L, drag C_D, and pitching moment C_T are taken into account when analysing the characteristics of a profile. Nevertheless, as described above, the centre of pressure moves with the flow conditions and hence is not suitable for describing the pitching moment. In the field of aerodynamics – especially in the subfield of flight stability – the pitching moment $C_{T,0.25}$ for $25\,\%$ chord length is analysed instead.

Figure 3.4 illustrates the three dimensionless coefficients using the example of the GOE-387 profile. Since the characteristics of subsonic airfoils are similar, these are illustrated by the chosen example:

Each subfigure of Figure 3.4 shows a coefficient as a function of the angle of attack α. To show the influence of the velocity, a family of curves is shown with the Reynolds number as the array parameter for each plot. Figure 3.4a also contains information about zero-lift and maximum-lift conditions – owing to reasons of simplicity, these are only given for a single Reynolds number as an example (here $Re = 1 \cdot 10^6$).

As can be seen in the lift plot shown in Figure 3.4a, the course of the curve is linearly rising for a huge interval of the angle of attack α, starting approximately with the zero-lift value and ending with the maximum-lift value: in the chosen example, zero-lift takes place at $\alpha = -5\,°$, while the maximum-lift of $C_L = 1.846$ is reached at $\alpha = 15\,°$. These parameters are very important for the design process and should be close to the given example for flow profiles with high aerodynamic loads.

For suitable flow profiles and for the mentioned region, the coefficient C_D reaches its lowest values, see Figure 3.4b. According to Gasch and Twele

(a) Lift curve   **(b)** Drag curve   **(c)** Pitching moment curve
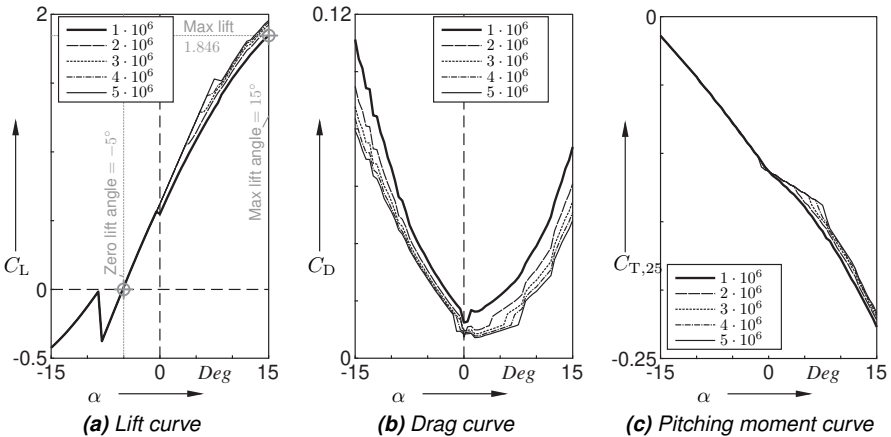
Figure 3.4. *Aerodynamic characteristics of a profile: lift coefficient C_L, drag coefficient C_D, and the pitching moment coefficient C_T over the angle of attack α for different Reynolds numbers, as shown for the airfoil GOE-387, calculated with JavaFoil from Hepperle [95] and taken from the AID Airfoil Investigation Database [4]*

[72], the lift coefficient is about 20–100 times higher than the drag coefficient for suitable profiled.

Figure 3.4c shows the course of the pitching moment coefficient $C_{T,25}$. All the curves of the array are negative and declining for rising flow angles. Although the pitching moment coefficient is very important for the flight stability of planes, the profiles are fixed at a hub in this work; thus, the pitching moment is not relevant for further considerations and will not be considered.

Typically, the coefficients of lift and drag are plotted against each other – Figure 3.5 shows this kind of plot for the chosen example of the GOE-387 profile. Since this type of a polar plot goes back to Lilienthal, these diagrams are given the name *Lilienthal polar*.

Figure 3.5 depicts the same *Lilienthal polar* twice, but only the view on the right is to scale. In this view, the plotted part of the curve can be understood as the laminar flow region of the profile which is well illustrated. Note that for stall, no results are drawn in Figure 3.5. However, the properly scaled view is not suitable for identifying further characteristics. So, in the left view, C_D is scaled to obtain a clear and comprehensive representation.
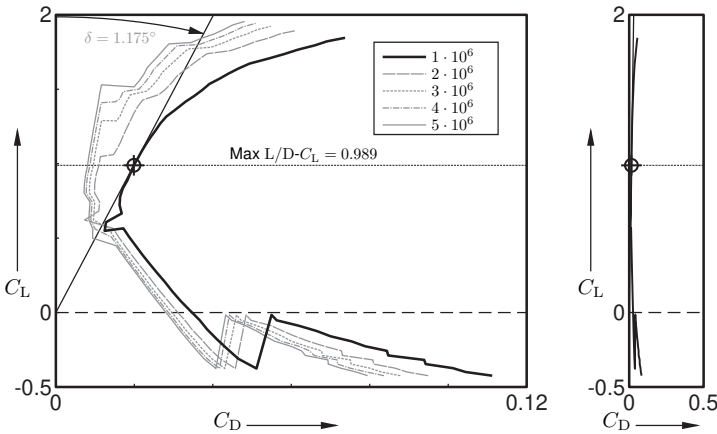
Figure 3.5. *Lilienthal polar of a profile for different Reynolds numbers, glide performance illustrated for $Re = 1 \cdot 10^6$, data aspect ratio not properly scaled (left) and properly scaled (right), as shown for GOE-387, calculated with JavaFoil from Hepperle [95] and taken from the AID Airfoil Investigation Database [4]*

The scaled *Lilienthal polar* shows the aerodynamic quality of a profile. When selecting a profile for an aerodynamic task, profiles with high lift values are generally desired, while the drag coefficient should be as low as possible. This optimum point can directly be found on the Lilienthal polar by creating a tangent curve through the origin of the diagram. While the slope of this tangent gives the optimum lift-to-drag ratio ϵ, the angle between the ordinate axis and the tangent curve leads to the glide angle $\delta = \tan^{-1} \epsilon^{-1}$. As will be seen in Chapter 7.3.1, the glide angle is an important criterion for a flow-optimised propeller shape.

Further details and explanations about the general description of airfoils and about deriving the shape by applying different mathematical methods can be found in Schlichting and Truckenbrodt [202].

3.2. Blade element momentum theory

The methods to design wind turbines are strongly associated with the *blade element momentum theory*, which is still the standard design process [89;

104; 212; 213]. Owing to the adaption of these methods to designing a flow-optimised propeller mixer, this theoretical approach is very important for the present work. The relevant points will be elucidated in detail below.

In the literature, Glauert is said to be the creator of the *blade element momentum theory*. However, in his underlying publication *'Airplane Propellers'*, he presents the fundamentals of this concept, which are *axial momentum theory* and *blade element theory*.

3.2.1. Axial momentum theory

The fundamentals of *axial momentum theory* were first formulated by Rankine [170, 171] to analyse ship propulsion. A few years later, R. E. Froude [67] analysed propulsion by considering the pressure differences. While both discussed the theory to establish the propulsion of a ship, Glauert [77] generalised the theory for every form of propeller-like fluid machinery.

In the following, the major steps of Rankine and Froude towards the modern form of the *axial momentum theory*, as formulated by Glauert, will be discussed. Note that only the parts relevant for the present work are discussed.

Underlying assumptions

The aim of the theory, as outlined by Rankine in 1865, was to determine the thrust F_T of a propeller to drive a ship under different ideal and non-ideal conditions. In his considerations, Rankine regarded an effective area in the propeller plane, as shown in Figure 3.6[5]. For the total thrust, he formulated Equation 3.4. Here, v_2 is the velocity downstream from the propeller, while v_0 is the velocity of the ship and thus the velocity of the propeller itself.

$$F_\mathrm{T} = \int\limits_{(A_2)} \rho\, v_2\, (v_2 - v_0)\; dA_2 \tag{3.4}$$

Glauert also applies this equation, but he assumed the principle of relative motion and thus assumed the propeller as rotating at a fixed point. For this,

v_0 is not related to the velocity of the ship, but to the inflow velocity into the control room.

Besides the thrust F_T, Rankine also discussed in detail how to estimate the work of the propeller. However, as already mentioned, these considerations are not relevant for the issue of the present work and are not considered here. For further details of Rankine's scientific work, refer to Rankine [170, 171]; Rankine et al. [172].

In 1889, Froude resumed Rankine's work and outlined the role of the pressure difference over a surface in the propeller plane [67]. He formulated the theory of the actuator disc by suggesting a *"...thin vertical plate, of finite area, immersed deeply in water and acted upon by a finite normal force."*[67, p. 391, §6]. Contrary the suggestion of Rankine, he proposed to consider the fluid flow as continuous without any sudden velocity changes, even though the pressure changes. And as an important result, he formulated Equation 3.5, which is generally known as Froude-Rankine's theorem.

$$v_1 = \frac{v_0 + v_2}{2} \tag{3.5}$$

The procedure, as outlined above, is deduced from sophisticated thought experiments. Though the origin publications come with several mathematical proofs, the modern form of the theory was formulated by Glauert. In this form, the theory was often adopted and can be found, for instance, in Gasch and Twele [72]; Hansen [88]; Hau [90]; Schlichting and Truckenbrodt [202]; Wilson and Lissaman [240]. Therefore, the modern form of the theory will be explained in detail below with all relevant mathematical derivations.

Control room

In line with the fundamentals outlined by Rankine and Froude, Glauert considered a vertical plate, but he followed Froude's assumptions in describing the stream tube in which the plate is positioned.

Figure 3.6 illustrates the hypothetical vertical plate together with its surround-
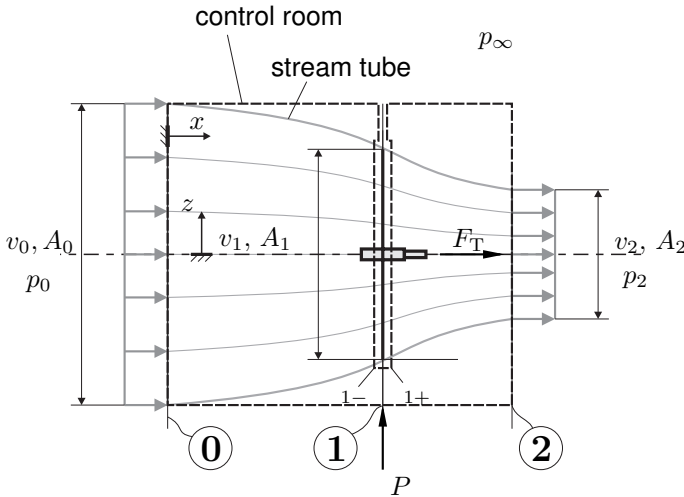
Figure 3.6. *Elementary stream tube to derive the general axial momentum theory, as considered by R. E. Froude [67] and Glauert [77]*

ing stream tube. To identify the relevant loads, a control room is also shown in the figure.

The fluid enters the control room through the stream tube with the conditions of the velocity v_0 and the pressure p_0 at Position $\textcircled{0}$. The entering distance of the stream tube is given by A_0. Owing to the supply of the flow with the power P at Position $\textcircled{1}$, the flow is accelerated and hence the stream tube will contract over the distance A_1 on the plane of the rotating plate to A_2 at the outflow Position $\textcircled{2}$. Just before the fluid flows through the rotating plane, the position in front of this plane is named with $_{1-}$, while the position just after the plane is named $_{1+}$.

The control room is subdivided into a free part and a bounded part. The free control room is chosen as a rectangular box that includes the stream tube and therefore the rotating plate, while the bounded control room contains only the surface of the vertical plate. Ambient pressure p_∞ affects around the free control room, except for the distances A_0 at the inflow and for A_2 at the outflow. In the bounded control room, all forces on the flow caused by the

plate have to be considered.

Two coordinates – x for the axial and z for the vertical direction – were introduced for the exact identification of the directions in the two-dimensional plane.

Continuity

First of all, the mass flow balance will be considered. Owing to continuity in the stream tube, the mass flow rate at the inlet has to be equal to the flow rate at the outlet, as given by Equation 3.6. From this, the meridional mass flow rate $\dot{m}_{\mathrm{m}}$ is known, which is also valid for Position $\textcircled{1}$, as well as for $_{1+}$ and $_{1-}$, see Equation 3.7. With the assumption of incompressible fluid flow, density is constant for the whole area. With Equation 3.8, it is clear that the velocity just in front of the rotating plane is equal to the velocity infinitesimally after the plane.

$$\dot{m} = \rho_0\, v_0\, A_0 = \rho_2\, v_2\, A_2 = \dot{m}_{\mathrm{m}} \tag{3.6}$$

$$\dot{m}_{\mathrm{m}} = \rho_{1-}\, v_{1-}\, A_{1-} = \rho_{1+}\, v_{1+}\, A_{1+} \tag{3.7}$$

$$v_{1-} = v_{1+} \tag{3.8}$$

Bernoulli's principle

Based on these assumptions, there is no flow through the surface shell of the stream tube. Hence, the fluid conditions of an arbitrary section plane perpendicular to the symmetry line can be reduced to the centre point of this section plane. This means that this single point is representative of the whole section plane. Thus, considering all possible sections between inflow and outflow, all the resulting points, taken together, will form a representative stream tube filament. Owing to the horizontally-aligned rotating axis, the resulting stream tube filament is also horizontal and identical to the symmetry line of the disc. The validity of a stream tube filament allows the application of Bernoulli's principle.

Nevertheless, due to the power supply of the flow at Position ①, the amount of the total pressure changes. Consequently, Bernoulli's principle is not valid when choosing a path that includes the disc. Therefore, two different stream tube filaments will be considered without including the disc. The first filament reaches from Position ⓪ to Position $_{1-}$, see Equation 3.9, while the second one describes the path from Position $_{1+}$ to Position ②, as described in Equation 3.10.

$$p_0 + \frac{\rho}{2} v_0^2 = p_{1-} + \frac{\rho}{2} v_{1-}^2 \tag{3.9}$$

$$p_2 + \frac{\rho}{2} v_2^2 = p_{1+} + \frac{\rho}{2} v_{1+}^2 \tag{3.10}$$

To find a relationship between inflow and outflow, Equation 3.10 is subtracted from Equation 3.9. This leads directly to the difference pressure Δp, as given in Equation 3.12.

$$\cancel{(p_0 - p_2)} + \frac{\rho}{2} \left(v_0^2 - v_2^2 \right) = (p_{1-} - p_{1+}) + \frac{\rho}{2} \left(\cancel{v_1^2 - v_{1+}^2} \right) \tag{3.11}$$

$$\Delta p = (p_{1-} - p_{1+}) = \frac{\rho}{2} \left(v_0^2 - v_2^2 \right) \tag{3.12}$$

Momentum balance

Subsequently, all loads that affect the boundaries of the control area will be balanced. Loads are either caused by pressure differences or as a reaction force induced by the geometrical shape of a body. Here, these forces are summarised by $\sum \vec{F}$. But loads are also caused by fluid momentums, as summarised by $\sum \vec{I}$. The equilibrium of loads is establishes when all fluid momentum forces are equal to the pressure and reaction forces, see Equation 3.13.
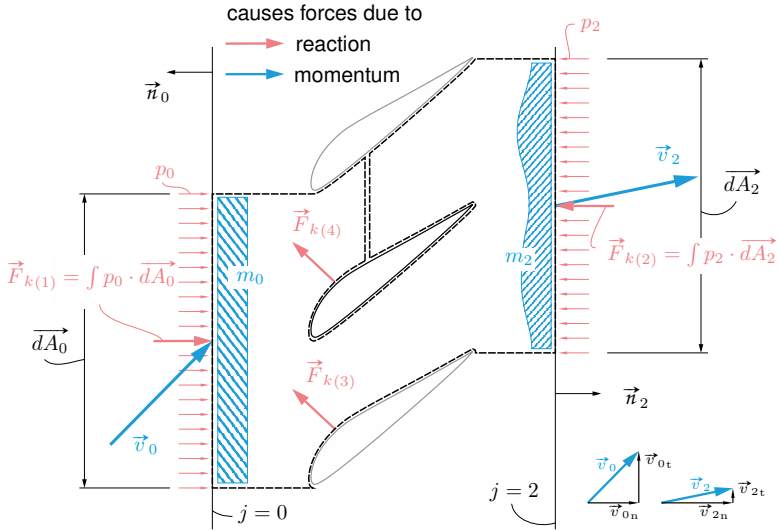
Figure 3.7. *Momentum balance for the example of an axial turbomachine, reaction forces are depicted in light red and momentum forces in light blue*

$$\sum_j \frac{\partial \vec{I_j}}{\partial t} = \sum_j \frac{\partial \left(m \cdot v_{\mathrm{n}} \, \iota \cdot \vec{n} \right)_j}{\partial t} \overset{!}{=} \sum_k \vec{F_k} \tag{3.13}$$

$$\sum_j \left[m_j \frac{\cancel{\left(\partial v_{j_{\mathrm{n}}} \iota_j \cdot \vec{n}_j \right)}}{\partial t} + \left(v_{j_{\mathrm{n}}} \iota_j \cdot \vec{n}_j \right) \frac{\partial m_j}{\partial t} \right] = \sum_j \dot{m}_j \cdot v_{j_{\mathrm{n}}} \iota_j \cdot \vec{n}_j \overset{!}{=} \sum_k \vec{F_k} \tag{3.14}$$

In this case, all momentum forces $\vec{\dot{I}}_j = \partial \left(m \cdot v_{\mathrm{n}} \, \iota \cdot \vec{n} \right)_j / \partial t$ can be reduced to $\vec{\dot{I}}_j = \dot{m}_j \cdot v_{j_{\mathrm{n}}} \iota_j \cdot \vec{n}_j$ because of the requirement for stationary conditions and Equation 3.14 results. In both equations ι is defined by $\iota = \frac{\vec{n} \cdot \vec{v}}{|\vec{n} \cdot \vec{v}|}$ and calculates the sign and thus the direction of $\vec{\dot{I}}$. Figure 3.7 shows the momentums discussed above for an example of an axial turbomachine.

$$\rho \, A_0 \, \left(v_{0\mathrm{n}} \, \iota_0 \cdot \vec{n}_0\right)^2 + \rho \, A_2 \, \left(v_{2\mathrm{n}} \, \iota_2 \cdot \vec{n}_2\right)^2 = p_0 \, A_0 + p_\infty \, (A_0 - A_2)$$
$$- p_2 \, A_2 + F_{\mathrm{T}} \qquad (3.15)$$
$$\rho \, A_0 \, \left(v_{0\mathrm{n}} \cdot (-1)\right)^2 + \rho \, A_2 \, \left(v_{2\mathrm{n}} \cdot (1)\right)^2 = p_0 \, A_0 + p_\infty \, (A_0 - A_2)$$
$$- p_2 \, A_2 + F_{\mathrm{T}} \qquad (3.16)$$
$$\check{F}_{\mathrm{T}} = \dot{m} \, (v_0 - v_2) \quad \text{if } v_{0\mathrm{n}} = v_0 \ \wedge \ v_{2\mathrm{n}} = v_2 \qquad (3.17)$$

Considering the fluid state at inflow and outflow as well as the reaction force at the disc (see Figure 3.6) enables the formulation of Equation 3.15 and hence Equation 3.16. Due to the relatively slow fluid velocity, the ambient pressure p_∞ and the inlet pressure p_0, as well as the outlet pressure p_2, are equal, and finally, Equation 3.17 can be found for the force affecting the disc. It must be noted that the force affecting the disc $\check{F}_{\mathrm{T}}$ is the reaction force of the force F_{T}, and thus, they differ by the factor (-1).

Froude-Rankine's theorem

Among the above-mentioned balances and principles, it is absolutely clear that the pressure change over the area A_1 of the rotating disc has to be equivalent to the force $\check{F}_{\mathrm{T}}$, see Equation 3.18.

$$\check{F}_{\mathrm{T}} = \Delta p \, A_1 \qquad (3.18)$$

Together with Equation 3.12, Froude-Rankine's theorem can be derived by Equations 3.17 and 3.18. Finally, Equation 3.20 results, which was also achieved by Froude (see Equation 3.5).

$$\dot{m}\left(v_0 - v_2\right) = \frac{\rho}{2}\left(v_0^2 - v_2^2\right) A_1 \tag{3.19}$$

$$\boxed{\Rightarrow v_1 = \frac{v_0 + v_2}{2}} \tag{3.20}$$

This is a very important intermediate result because Equation 3.20 applies a very simple relationship to calculate the velocity in the propeller plane for the given conditions at the inlet and outlet.

In addition to the explanations outlined above, Glauert formulated the interference factor a, which is commonly found in the Anglo-American literature, and Equation 3.21 results[6] for the velocity in the propeller plane. Within this thesis, the interference factor will not be considered.

$$v_1 = v_0\left(1 + a\right) \tag{3.21}$$

A further important fact, deduced by Glauert, is the validity of Froude-Rankine's theorem for individual annular elements – this is very important for the common design process of wind turbines, as described in Chapter 4.2.2, as well as for the derived design technique for propeller mixers, as described in Chapter 7.1.

However, the *axial momentum theory* is limited and comes with two enormous problems: the theory is totally decoupled from the geometrical form of the fluid machinery required to fulfil a propulsion task. This leads to the second problem – a rotatory fluid machine will cause swirl in the slipstream downstream from the machine, but the *axial momentum theory* was deduced from a two-dimensional problem.

The unsatisfactory decoupling from geometry in particular makes another concept indispensable in order to obtain the geometrical parameters of a fluid machine.
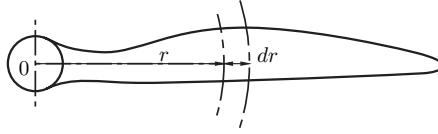
Figure 3.8. *Element of a blade with length dr at the distance r, Glauert [77]*

3.2.2. Blade element theory

The *blade element theory* can be adopted to design the geometrical shape of a fluid machine and was *"...initiated in a rather crude form by Froude in 1878."* [77, p. 178, Section 4]. Although Glauert credits Drzewiecki [57] as the real creator of the *blade element theory*, W. Froude [69] formulated the original basics of the theoretical approach, but he did not summarise the infinitesimal power over the propeller radius as other researchers did in later publications. Froude focused his considerations on the efficiency of the propeller rather than on thrust or power.

As mentioned, one of the most important research papers with respect to *blade element theory* was published by Drzewiecki. The fundamental idea of his *blade element theory* is to calculate the thrust and power of a fluid machine by taking single infinitesimal blade elements into account instead of considering the machine as a whole. Figure 3.8 shows such an element at an arbitrary position in the radial direction. Considering every possible blade element on the radial axis and bringing together all loads of each single element to an integral value, the amount of thrust and power can be calculated for the regarded blade. Figure 3.2 depicts an example element with acting loads.

To calculate thrust and power using *blade element theory*, it is mandatory to split these loads into their components. These are lift and drag. For an airfoil, the forces for lift and drag according to Equations 3.1 and 3.2, were found as a function of the related coefficients for lift C_L and drag C_D, respectively, see Chapter 3.1.1. However, applying the *blade element theory*, the forces for lift and drag have to be applied on a single blade element with infinitesimal thickness. This is only valid under the assumption that the physics of the

flow, as described in Chapter 3.1.1, at the airfoil are considered as equal to the flow at a single blade element with infinitesimal thickness – this means that the parameters for lift C_L and drag C_D, as calculated for a certain airfoil, must be valid for the blade element, and all blade elements are assumed to be independent of their neighbouring elements of the considered blade.

Under these assumptions, Equation 3.22 and Equation 3.23 follow, for the infinitesimal lift and drag force at a single blade element:

$$dF_\mathrm{L} = \frac{\rho}{2}\, w\left(r\right)^2 \cdot C_\mathrm{L}\left(\alpha\right) \cdot l\left(r\right)\, dr \qquad (3.22)$$

$$dF_\mathrm{D} = \frac{\rho}{2}\, w\left(r\right)^2 \cdot C_\mathrm{D}\left(\alpha\right) \cdot l\left(r\right)\, dr \qquad (3.23)$$

Note that in both equations, the effective velocity w, the chord length l, and even the coefficients C_L and C_D are functions of the radial position r due to their chained dependence on the angle α.

Since the aim of *blade element theory* is to calculate thrust and power – just like the *axial momentum theory* before – the forces dF_L and dF_D are not appropriate for this purpose and have to be converted with respect to the relevant directions of thrust and power. For this, an example section, as depicted in Figure 3.9, will be considered. In the figure, all acting loads caused by the attached velocity triangle are shown together with a breakdown of the forces dF_L, dF_T, and dF_R into their relevant components. The figure also contains the axis of rotation as well as the circumferential direction. The latter direction is a reference to the velocity triangle because of the perpendicular orientation of the wind speed to this direction.

Figure 3.9 clearly shows that for the calculation of the thrust, only the axial component dF_T of the resulting force dF_R is relevant, while only the circumferential component dF_C of the resulting force dF_R is mandatory for the calculation of the power dP, see also Equation 3.24. Here, dT is the infinitesimal torque at the considered position of r and ω the angular velocity.
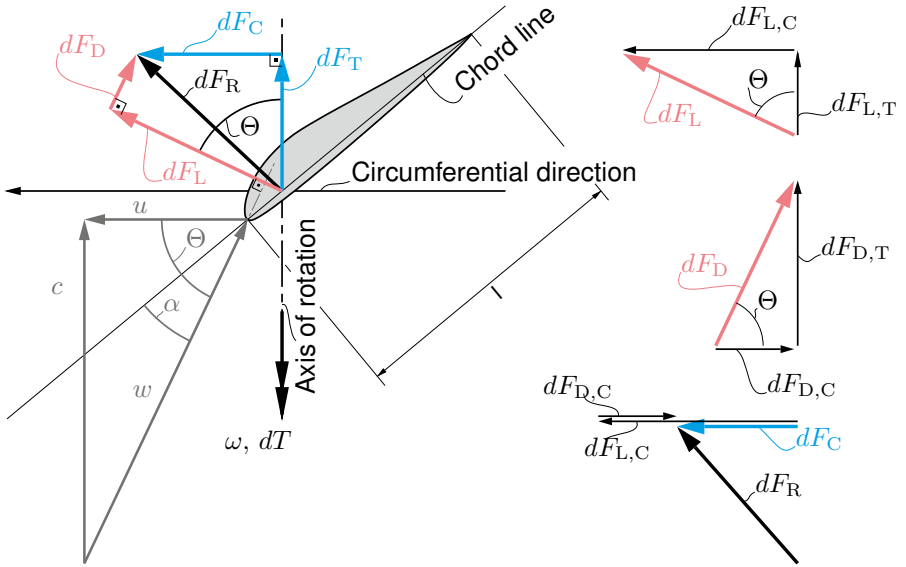
Figure 3.9. *Velocity triangle and force components for an infinitesimal radial section, lift and drag forces are depicted in light red, while thrust and circumferential forces are shown in light blue*

$$dP = \omega \cdot \left| \left(\overrightarrow{dF}_{\mathrm{R}} \cdot \overrightarrow{n}_{\mathrm{C}} \right) \overrightarrow{n}_{\mathrm{C}} \times \overrightarrow{r} \right| = \omega \cdot dF_{\mathrm{C}} \cdot r = \omega \cdot dT \tag{3.24}$$

Hence, as depicted in Figure 3.9, the axial force dF_{T} and the circumferential force dF_{C} have to be expressed as their vector sum, which is composed of the related axial and circumferential components of lift and drag. Thus, Equations 3.25 and 3.26 can be formed.

$$dF_{\mathrm{T}} = dF_{\mathrm{L,T}} + dF_{\mathrm{D,T}} = \cos \Theta \cdot dF_{\mathrm{L}} + \sin \Theta \cdot dF_{\mathrm{D}} \tag{3.25}$$

$$dF_{\mathrm{C}} = dF_{\mathrm{L,C}} - dF_{\mathrm{D,C}} = \sin \Theta \cdot dF_{\mathrm{L}} - \cos \Theta \cdot dF_{\mathrm{D}} \tag{3.26}$$

With respect to the loads as depicted in Figure 3.9 and taking the number

of blades n_z into account, for a rotating impeller with the relative angle Θ between the circumferential velocity u and the effective velocity w, the infinitesimal thrust and torque, as cited by Glauert [77], give the final result of the *blade element theory*, see Equations 3.27 and 3.28.

$$\frac{dF_T}{dr} = \frac{\rho}{2} \, w \, (r)^2 \cdot l \, (r) \left[\cos \Theta \cdot C_L \, (\alpha) + \sin \Theta \cdot C_D \, (\alpha) \right] n_z \qquad (3.27)$$

$$\frac{dT}{dr} = \frac{\rho}{2} \, w \, (r)^2 \cdot l \, (r) \cdot r \left[\sin \Theta \cdot C_L \, (\alpha) - \cos \Theta \cdot C_D \, (\alpha) \right] n_z \qquad (3.28)$$

Finally, the disadvantages of the above approach should be outlined: in actual fact, the *blade element theory* in its primitive form, is very unsatisfactory for machines with high blade numbers. Wood et al. [242] investigated airfoils aligned in a cascade and discovered a normalised deviation in thrust between theoretical calculations and their experimental results of about $3\,\%$ for all the discovered variations of the blade number. The deviation in the torque was estimated at about $4\,\%$. Note that the non-normalised results were much higher for both parameters. These unsatisfactory results are caused by the blades interferring with each other. Thus, the assumptions outlined above are not valid for impellers with a high number of blades.

A further problem comes with the axial velocity, as presumed in the primitive *blade element theory* discussed above. The theory underwent many enhancements, such as by Betz [15] and de Bothezat [48]. While Drzewiecki erroneously an undisturbed axial velocity assumed in his considerations, the authors of enhanced blade element theories applied the axial velocity using the *axial momentum theory*, as discussed in Chapter 3.2.1. The first connections between *axial momentum theory* and *blade element theory* can be recognised as a result. Note that this enhancement will be applied in this research work too, see Chapter 7.1.

However, in the scope of this research, a propeller with a low number of blades will be designed and further enhancements of the *blade element theory* are not relevant[78].

Notes

[1] In Equations 3.1 and 3.2, the coefficients for the lift and drag of an airfoil are given. These parameters are the dimensionless form of their related force. The mentioned equations can be found by applying Buckingham's π theorem, as discussed in Chapter 5.3.1.

[2] The mandatory calculations to plot the dimensionless coefficients of Figures 3.3 to 3.5 were performed using the tool JavaFoil from Hepperle [95]. With the exception of Figure 3.3, the data was taken from the AID Airfoil Investigation Database [4]. The results of Figure 3.3 were calculated by the author of this thesis, utilising the tool JavaFoil.

[3] The pressure coefficient C_{p} may also be analysed for beginning flow separation. For rising C_{p} at the suction side, flow separation becomes more and more probabile and can be expected as a consequence. Hence, the late onset of rising C_{p} is aimed for, especially for gliders.

[4] In Figure 3.3, a sudden rise of the plotted curves can be found at $x/l = 1$. This is because of the value $C_{\mathrm{p}} = 1$ for the trailing edge as required from the theoretical background of potential flow, as applied in the calculation tool. Measurement values would decline otherwise.

[5] Instead of the stream tube, as shown in Figure 3.6, Rankine assumed a sudden change in axial velocity over the propeller plane. This was in line with the state of knowledge of those times and a subject of controversy later. Indeed, the physics of the propeller flow was discussed by Froude in 1889 in a correct manner, while the mistake of Rankine was repeated by Parsons in 1911 [68, p. 158, Discussion] and led to the Lanchester' mistake in estimating the theoretical limit of wind turbines [148].

[6] The interference factor a, as conceived by Glauert [77], leads to different formulations of Froude-Rankine's theorem. When calculating the Betz-Joukowsky maximum (see Chapter 4.2.1), the differences lead to different mathematical derivations: consequently, both theoretical approaches lead to the same final result, see e.g. Gasch and Twele [72] for details.

[7] Modern airfoil theory has a similar approach to the *blade element theory* but is related to a different basis. For machines with high blade numbers in particular, it is sufficient to consider the *vortex theory*, which considers the vortex system of the propeller and thus the induced velocities. Because of the low number of blades for propeller mixers under consideration in this research work, a low deviation due to interference can be expected. This assumption is in line with the investigations of Wood et al. [242].

[8] It should be mentioned that even the assumption of the equality of the flow around an airfoil and a blade element with infinitesimal thickness may be wrong. The reason can be found in the finite span of the investigated airfoils. Either the measured airfoil has to be dimensioned by a ratio of 5 or 6 or the measured values have to be corrected – see Glauert [77] for related formulae.

4. Wind turbine design methods

Although the goal of this research project is to find a design method for optimum propeller mixers, a brief overview of the contemporary design process for wind turbines is provided. These procedures are relevant for this research topic due to the adoption of this design process as a part of the desired design process of propeller mixers.

4.1. Principles of wind turbines

In general, the physical principles of utilising wind speed in wind turbines can be subdivided into two different principles:

- The utilisation of the stagnation pressure of the wind speed at a flat plate or similar bodies as shown in Figure 4.1a

- The principle of aerodynamic lift at a streamline-shaped body. Figure 4.1b shows an example for the second principle.

While the principle of stagnation pressure is very suitable for wind speed anemometers, this principle is not relevant for wind energy power plants. For industrial purposes, only the principle of aerodynamic lift is utilised.
This is because of the maximum tip speed. Typically, the tip speed is given as the ratio of the maximum circumferential speed to the wind speed: $\Lambda = \omega\,R/c$. While the tip speed ratio of rotors based on stagnation pressure can reach the maximum values of $\Lambda = 1$, which is only possible for idle speed, rotors based on aerodynamic lift can reach higher tip speed ratios up to $\Lambda = 12$ for one-bladed turbines [72].
Considering the velocity triangles at the leading edge of a single blade of the wind turbine as sketched in Figure 4.1, it is clear that the effective velocity at the blade is given by the relative velocity w. The relative velocity is the vector addition of the wind speed c on the rotor plane and the circumferential velocity of the rotor $u = \omega \cdot r$. Hence, the value of the relative velocity is always larger than the wind speed. Thus, the physics of the aerodynamic principle

(a) Wind speed anemometer based on stagnation, Photographer: Stefan Kühn

(b) Wind turbine for industrial use, Photo: Nordex SE

Figure 4.1.   Wind energy principles

is more suitable for industrial purposes, and only this type of machine will be considered in the following.

To design a wind turbine based on aerodynamic principles, the most convenient method is to apply *blade element momentum theory*, as conceived by Glauert [77], see Chapter 3.2. Although *blade element momentum theory* was conceived to design the shape of a propeller, the method provides no guidance as the maximum power output. This mandatory optimisation was investigated by Betz [17] and Joukowsky [108] simultaneously. Both Betz and Joukowsky discovered the maximum power output of an ideal working rotor with one-dimensional methods.

With *blade element momentum theory*, it is possible to identify the necessary overlap of a stream tube with a rotor to obtain the ideal power identified by Betz and Joukowsky. Both theories are combined in the *momentum method*

and will be discussed in Chapter 4.2.

Due to the problems of the *momentum method*, Chapter 4.3 briefly outlines the more general *vortex methods*. However, the *momentum method* is still the preferred design process in practice [89; 104; 212; 213].

4.2. Momentum method

The *momentum method* of wind turbine design consists in the principle of two theoretical models. The main theory is the *blade element momentum theory*, which was discussed in detail in Chapter 3.2. The fundamentals of this theory are combined with the theory of Betz and Joukowsky to find a certain impeller shape to extract the maximum possible power from the wind.

4.2.1. Betz-Joukowsky maximum

Betz [17] and Joukowsky [108] both developed the theory independently of each other. They conducted their research at a time when wind turbines were used for water pump systems or even to grind corn. Using wind energy machines to generate electricity was of minor importance, yet was a topic of discussion at the time [18]. Therefore, they could not have foreseen wind energy power plants having a major role in the energy sector. All the same, their theory is still the basis of the contemporary design process [89; 104; 212; 213].

The theory is based on the *axial momentum theory* by Rankine and Froude and has similarly approximate assumptions:

- The flow around the wind turbine is reduced to a two-dimensional stream tube that contains an arbitrary geometrical shape to withdraw power from the fluid flow, as depicted in Figure 3.6. Note that Figure 3.6 shows a propulsion task, as opposed to the case under consideration: the principles are valid for both considerations, as cited by Glauert [77].

- The geometrical shape of the impeller was chosen by Betz and Joukowsky as a hypothetical rotating disc, with this already being de-

fined by *axial momentum theory* by Rankine and Froude. This means that the real contour of the machine is still unknown and therefore without any further influence for the whole method, except for withdrawing power.

- Furthermore, the fluid flow needs to be ideal and the fully developed velocity profile of the incompressible fluid is ideally rectangular without any time-dependent effects.

From *axial momentum theory*, the velocity at Position $\textcircled{1}$ on the disc plane is known by Equation 3.20, and the change of the kinetic energy from the inflow at $\textcircled{0}$ to the outlet at $\textcircled{2}$ can be calculated while performing an energy balance with respect to the relevant plane in $\textcircled{1}$. The first law of thermodynamics can be applied and leads to Equation 4.1. Taking continuity into account produces Equation 4.2.

$$\frac{dE}{dt} = \dot{m}_{\mathrm{m}} \, g \, (z_2 - z_0) + \frac{\dot{m}_{\mathrm{m}}}{2} \left(v_2^2 - v_0^2 \right) + P \tag{4.1}$$

$$\dot{m}_{\mathrm{m}} = \rho \, v_1 \, A_1 = \rho \, \frac{v_0 + v_2}{2} \, A_1 \tag{4.2}$$

Because of the stationary conditions, there is no time dependency. Furthermore, the potential quantities are ignored because of the horizontal aligned stream tube filament, and finally, with Froude-Rankine's theorem, the power P is found, according to Equation 4.3.

$$P = \frac{\dot{m}_{\mathrm{m}}}{2} \left(v_0^2 - v_2^2 \right) = \rho \, \frac{v_0 + v_2}{4} \, A_1 \left(v_0^2 - v_2^2 \right) \tag{4.3}$$

It is obvious that a complete deceleration of the flow in the stream tube by the disc would withdraw all the kinetic energy of the wind, and one could assume that this should be the aim of the turbine. However, this would cause a flow velocity of $v_2 = 0 \, m/s$ behind the disc, and the mass flow rate $\dot{m}_{\mathrm{m}}$ would be stopped. Thus, the total conversion of kinetic energy in the wind turbine is not suitable due to the blocking of the stream tube. On the other hand, it is

also clear that without deceleration, no power can be withdrawn because of the equality of the inlet and outlet velocities. Hence, from Equation 4.3, it is clear that the withdrawn power cannot be equal to the kinetic energy of the wind. There must be a point of optimum energy transformation.

To identify this point of optimum energy transformation, Betz and Joukowsky separated the relevant wind energy $P_{\mathrm{Wind}} = \rho/2 \cdot A_1\, v_0^3$ of the propeller plane and Equation 4.3 can be transduced to Equation 4.4 using a brief calculation.

$$P = \underbrace{\frac{\rho}{2}\, A_1\, v_0^3}_{P_{\mathrm{Wind}}} \cdot \underbrace{\left[\frac{1}{2} \left(1 + \frac{v_2}{v_0} \right) \left(1 - \left(\frac{v_2}{v_0} \right)^2 \right) \right]}_{C_P} \qquad (4.4)$$

Equation 4.4 can be subdivided into two factors. Since the first factor corresponds to the total power of the wind P_{Wind} on the disc plane, the second factor is the coefficient of power C_P of the ideal fluid energy machine under consideration. The coefficient C_P is often interpreted as aerodynamic efficiency.

In the case of the assumed ideal conditions, the coefficient of power is a function of the velocity ratio v_2/v_0, which is drawn in Figure 4.2. The course of the curve shows a clearly distinguished maximum value. Performing a simple curve sketch, the maximum value for the coefficient can be identified as $C_P = 16/27$ and is named the Betz-Joukowsky maximum after its creators. To reach the point of maximum power, a velocity ratio of $v_2/v_0 = 0.\bar{3}$ must be established, see Equation 4.5.

$$C_{P,\mathrm{max}} = C_P \left(\frac{v_2}{v_0} = \frac{1}{3} \right) = \frac{16}{27} \approx 0.593 \qquad (4.5)$$

These results show that no machine can utilise more than about $59\,\%$ of the wind energy, provided the control room and all assumed conditions as described above are correctly set. In reality, a lower aerodynamic efficiency can be expected because of the rough assumptions included in the fundamentals
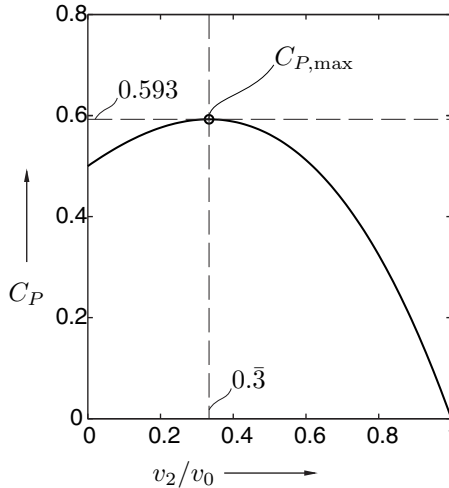
Figure 4.2. *Course of ideal power coefficient C_P over velocity ratio v_2/v_0 with the maximum point of power*

of the theory, as discussed above.

Note that there are theoretical considerations when creating a ducted flow around the disc [88]. This would enable the extraction of a larger amount of wind energy by raising the coefficient of power. Nevertheless, these methods are not relevant in practice and will not be considered here.

4.2.2. Optimum blade dimension

The principle of the Betz-Joukowsky limit alone is not sufficient to design the geometrical shape of a wind turbine, but only provides information about the maximum power output.

Thus, the design process must aim to find a geometrical shape that fulfils the conditions proposed by Betz and Joukowsky and can achieve the maximum power output. Typically, *blade element momentum theory*, which was discussed in Chapter 3.2, is applied to identify the geometrical shape.

Under the assumption of sufficient incidence, the lift coefficient C_L is typically much bigger than the drag coefficient C_D, and the drag force can be ignored

[72], especially under ideal conditions, as required by Betz and Joukowsky. Hence, together with Equation 3.22, Equation 4.7 follows from Equation 4.6 for the circumferential component dF_C of a single blade of an impeller on the rotating plane ① according to Figure 3.6.[1]

$$dF_C = dF_{L,C} - \underbrace{dF_{D,C}}_{\ll dF_{L,C}} \tag{4.6}$$

$$dF_C \approx \sin\Theta \cdot \frac{\rho}{2}\, w_1\, (r)^2 \cdot C_L\, (\alpha) \cdot l\, (r)\ dr \tag{4.7}$$

The circumferential component dF_C of the resulting force will cause loads at all blades. Thus, Equation 4.7 has to be multiplied by n_z. While impellers with up to 32 blades or just one blade were built in the past [2], the blade number of modern impellers is typically set to $n_z = 3$. This value does not (only) result from aerodynamics, but also from structural strength, low noise development, and also experience. [3]

Furthermore, to obtain the power, Equation 4.7 must be multiplied by the rotation frequency and the rectangular distance from the origin. This leads to the infinitesimal power of a radial section, see Equation 4.8. Equation 4.9 follows from Equation 4.7. Figure 4.3 illustrates the procedure for a three-bladed impeller.

$$dP\, (r) = dF_{C,\, i} \cdot n_z \cdot \omega\, r \tag{4.8}$$

$$dP\, (r) = \frac{\rho}{2}\, w_1\, (r)^2 \cdot C_L\, (\alpha) \cdot l\, (r)\ dr \cdot n_z \cdot \omega\, r \tag{4.9}$$

Although Equation 4.9 provides an analytics-based method for calculating the power at an infinitesimal section, by integrating it to the total power of the impeller, Equation 4.9 cannot be solved yet. Either the geometrical length l or the infinitesimal power dP are unknown. The other quantities of Equation 4.9 are typically provided within the design process.

The aim of the described procedure is to identify a geometrical shape to withdraw power from the wind at maximum efficiency as deduced by Betz
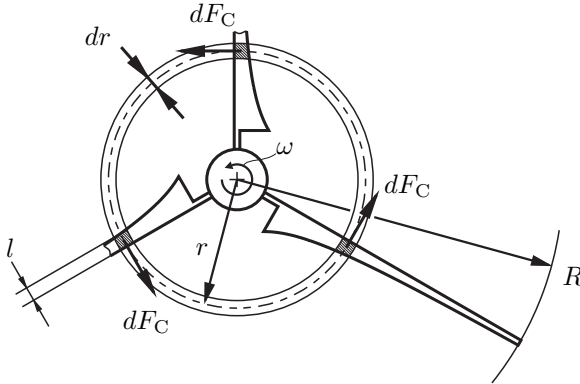
Figure 4.3. *Circumferential forces at infinitesimal radial section, three-bladed impeller*

and Joukowsky, see Equation 4.5. To solve this problem, the ideal maximum power will be linearly distributed over the whole propeller. Hence, the power, according to Equation 4.4 and with respect to the ideal aerodynamic efficiency of $C_P = 16/27$, is expressed as an integral of r for an annulus, see Equation 4.10. As outlined by Glauert, this procedure is valid under the given assumptions.

$$P_{\mathrm{Ideal}} = \int\limits_0^R \frac{\rho}{2} \, c_0^3 \, \frac{16}{27} \cdot 2\,\pi\,r\,dr \tag{4.10}$$

The infinitesimal ideal power dP_{Ideal} can now be equated with the infinitesimal power dP at the radial section according to Equation 4.9. This leads to Equations 4.11 and 4.12.

$$\boxed{dP\,(r) \equiv dP_{\mathrm{Ideal}}} \tag{4.11}$$

$$\frac{\rho}{2}\,w_1^2 \cdot C_{\mathrm{L}} \cdot l\,dr \cdot \omega\,r \cdot n_{\mathrm{z}} \equiv \frac{\rho}{2}\,c_0^3\,\frac{16}{27} \cdot 2\,\pi\,r\,dr \tag{4.12}$$

At this point, the infinitesimal power of a radial section is related to the amount

of ideal power that can be withdrawn by the considered section. Hence, only chord length l is unknown and can subsequently be derived from Equation 4.12.

After brief calculation, Equation 4.13 can be found. Here, $\Lambda_{\mathrm{Des}} = \omega R / c_1$ is the tip speed ratio for the design point of the wind turbine. Note that even the coefficient C_{L} is a function of r. This is due to its dependency on the flow angle α, which depends on the relative velocity w_1 of the considered radial section.

$$l\left(r\right) = \frac{8}{9\,C_{\mathrm{L}}\,n_{\mathrm{z}}} \, \frac{2\,\pi\,R}{\sqrt{\frac{4}{9} + \left(\Lambda_{\mathrm{Des}}\,\frac{r}{R}\right)^2}\,\Lambda_{\mathrm{Des}}} \tag{4.13}$$

Not only does the chord length l change with the radial coordinate r, but also the mounting angle φ that defines the angular position of the airfoil of each radial section. The change occurs due to the change of the flow angle α, as mentioned above.

To obtain the mounting angle φ, the flow angle α has to be subtracted from the relative angle Θ, as shown in Equation 4.14. From Figure 3.9, for the relative angle Θ, the following is directly derived: $\tan\Theta = c_1/u_1$. Together with Froude-Rankine's theorem and the definition of Λ_{Des}, Equation 4.15 can be established.

$$\varphi\left(r\right) = \Theta - \alpha \tag{4.14}$$

$$\varphi\left(r\right) = \arctan\left(\frac{2}{3}\,\frac{R}{r}\,\frac{1}{\Lambda_{\mathrm{Des}}}\right) - \alpha \tag{4.15}$$

Within the rough requirements, assumed by Betz and Joukowsky, Equation 4.13 calculates the chord length of a blade; with Equation 4.15, its torsion can be calculated – the course of both parameters is shown in Figure 4.4 for selected design parameters. Thus, in principle, the geometrical shape of the blade is known when choosing suitable airfoil profiles for each considered radial section from a database. For a more detailed explanation of the design

(a) *Chord length*   **(b)** *Relative angle*
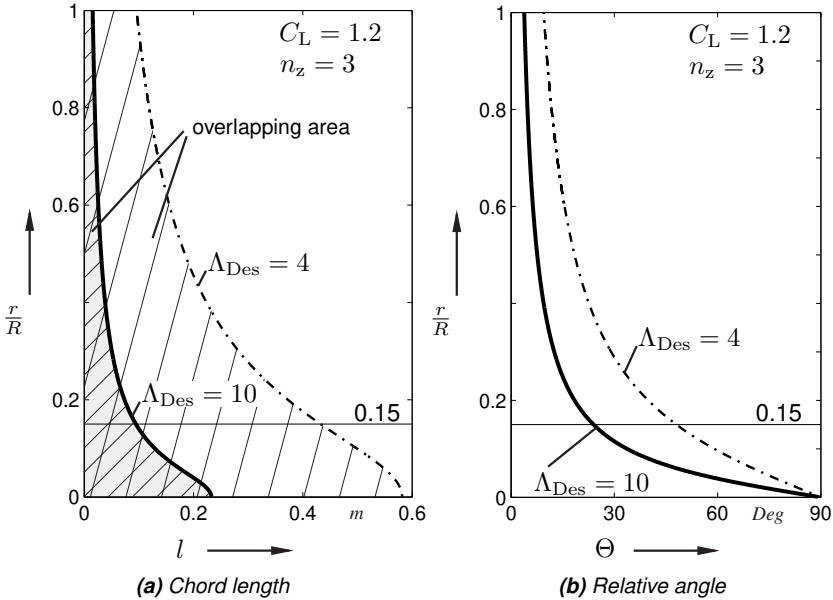
Figure 4.4.   *Chord length $l\,(r)$ and relative angle $\Theta\,(r)$ for **ideal blade design**, as shown for the tip speed ratio $\Lambda = 4$ (broken line) and $\Lambda = 10$ (continuous line) for a hypothetical three-bladed machine with a constant lift coefficient of $C_{\mathrm{L}} = 1.2$ and a hub radius of $r/R = 0.15$, the hatching marks the area of the stream tube, which is overlapped by a single blade*

process, refer to Chapter 4.2.5.

The current state of design

At this point, the results found up to this point will be discussed with a view to evaluating the current state of the design process:

While the course of the chord length l is shown in Figure 4.4a as a plausible curve, the mounting angle φ is not easy to illustrate because of its dependence on a specific impeller design. For identically chosen design points and different chosen profiles, the geometrical shape of an impeller may vary – this is because of the change in the glide angle δ when changing the profiles. Therefore, Figure 4.4b illustrates the relative angle Θ instead of the mount-

ing angle φ. For better understanding, the ratio r/R is drawn over the chord length l and therefore the relative angle Θ to illustrate the overlapping area of the stream tube by a single blade as the projection into the theoretical rotating plane. This region is given by the area under the chord line distribution, as shown in Figure 4.4a.

Figure 4.4 was generated as a hypothetical example. For this, a blade number of $n_z = 3$ and a lift coefficient of $C_L = 1.2$ were assumed. While three is a suitable number of blades, a constant value for the lift coefficient is not relevant for practical purposes. Typically, the lift coefficient changes with the radius from low to high values. To achieve a useful distribution, an iterative design process or even experience is necessary. In the given example, the course of the chord length and the relative angle alone are the focus of discussion. So, the practical usability of the graphs was not of relevance, but their simplicity was taken into consideration.

Besides the elements discussed above, both figures contain two lines: The continuous curve is for a modern high-speed wind turbine and represents a tip speed ratio of $\Lambda_{\mathrm{Des}} = 10$, while the broken curve is for a slow running machine characterised by $\Lambda_{\mathrm{Des}} = 4$. Both lines for both figures decrease monotonically.

The effect of the tip speed ratio Λ_{Des} on both characteristic parameters is clearly distinguished in the figure, especially for the chord length. For rising tip speed ratios, the whole curve of the chord length changes to lower values. Thus, the projection of the impeller to the section of the stream tube decreases. This means that the overlap of the crossing area of the stream tube by the turbine becomes lower. But Figure 4.4 shows that the closer the radial coordinate to the hub, the larger the chord length.

Even the course of the relative angle changes with the tip speed ratio. For low tip speed ratios, the slope changes slowly, but not for high tip speed ratios. Considering low relative angles for $\Lambda_{\mathrm{Des}} = 10$, the slope is very low, while the slope suddenly changes to higher values for the relative angles of $\Theta \approx 25\,°$. It means that at the tip, the change in the radial position of the blade and thus the relative angle is very low and almost constant. As the distance to the symmetry line gets closer, the angular position changes first slightly and then

rapidly to $\Theta = 90\,°$.

There is an additional line in the diagram. The line is positioned at $r/R = 0.15$. This region is where the hub structure begins, and the further course of the geometrical parameters is no longer of any practical relevance.

Nevertheless, both parameters still rise to higher, albeit theoretical values. While the region of the tip and the middle of the blade are well designed, the continuous increasing chord length in particular would lead to a large axial hub length. Together with the rising mounting angle, the torsion of the blade would cause huge problems in manufacturing such a blade.

The technical disadvantages arise due to the errors in modelling the fluid flow. As mentioned before, the theoretical fundamentals of the recent state are quite rough. In particular, the neglected swirl causes a huge mismatch between model and reality. Therefore, the theoretical consideration of swirl and the associated phenomena are discussed in Chapter 4.2.3.

Even the requirement for frictionless conditions will lead to mismatches, but for the design point considered here, drag forces are significantly smaller than lift forces and therefore the mistake in assuming frictionless conditions is relevant only in a minor way, see Equation 4.6. Also, tip-losses caused by the finite extrusion of a blade are not considered at this point. Compared to swirl losses, both losses are of minor importance and will be discussed together in Chapter 4.2.4.

4.2.3. Rotational wake enhancement

One of the major requirements of the *axial momentum theory* is the requirement for two-dimensional flow. Though this assumption is suitable for a theoretical approach, as performed by Rankine [170] and Froude [67], these requirements lead to modelling errors for real fluid machinery: since a structure in the fluid domain will be affected by the moments caused by the fluid, the fluid will also be affected by these moments caused by the structure due to the principle of the action–reaction law. Because of the rotation of the machine, the loads will be caused by an angular momentum, and this will lead to swirl in the stream tube as qualitatively illustrated in Figure 4.5.
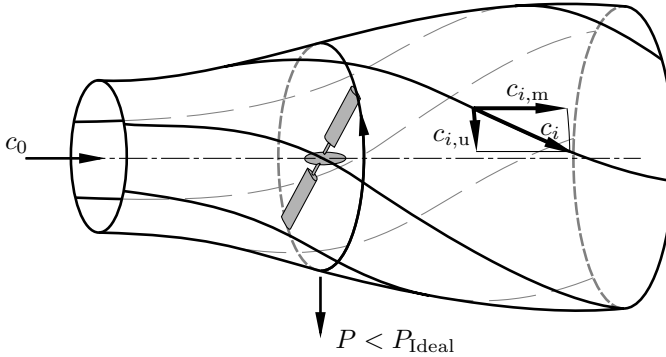
Figure 4.5. *Stream tube around swirl-affected fluid machine with axial ($c_{i,\mathrm{m}}$) and radial ($c_{i,\mathrm{u}}$) component of the absolute velocity c_i at an arbitrary point with power output P, author's own representation based on Hau [90]*

To take swirl into account, Schmitz [204] enhanced the common design method by applying the *lifting line theory* of Lanchester [122] and Prandtl [164, 165]. The theory is based on the *vortex theory*, investigated by Helmholtz [92], and involves the circulation Γ. *Lifting line theory* is well established in practice and can be found in many references, such as in Schlichting and Truckenbrodt [202, 203], Wieghardt [239], and many others. However, allthough *lifting line theory* can be adopted for the design of fluid machinery, here only the caused swirl is of interest. A brief overview of the design process applying *lifting line theory* is given in Chapter 4.3, among other vortex-based methods.

Under the assumption of the *vortex theory*, the relative velocity changes from its ideal value w_1^* to the real value of w_1 due to the induction of drag. Thus, the velocity component $\frac{w_\Gamma}{2}$, which is perpendicular to the relative velocity w_1, has to be considered. The vector addition of the velocity components lead to a change of the absolute velocity c and the velocity triangle according to Figure 4.6 is found.

As can be seen in Figure 4.6, the absolute velocity c is no longer parallel to the axis of rotation, and the velocity components c_{m} and c_{u} occur. While the latter can be understood as swirl, the meridional component of the absolute
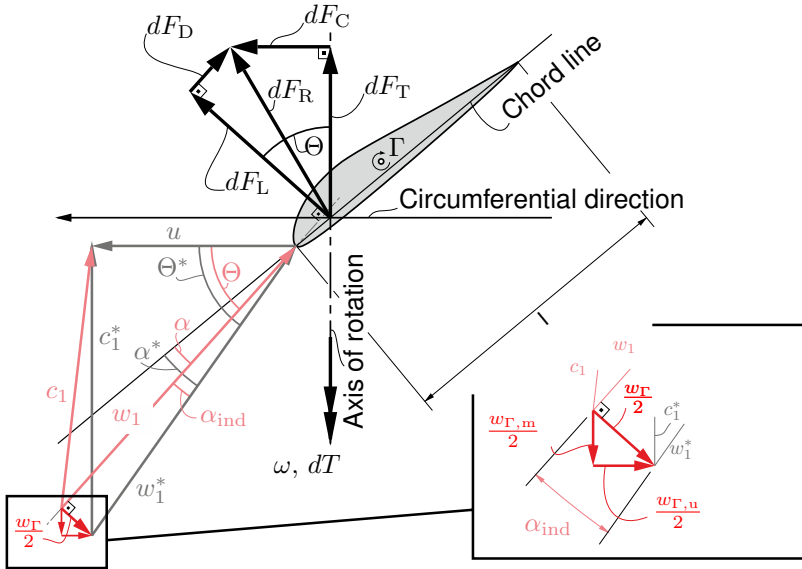
Figure 4.6. *Velocity triangle and force components for an infinitesimal radial section under the conditions of circulation, induced velocity $\frac{w_\Gamma}{2}$ additionally shown as component assembly, deviations from ideal conditions marked in red*

velocity in the propeller plane becomes Equation 4.16.

$$c_{1,\mathrm{m}} = c_1^* - \frac{w_{\Gamma,\mathrm{m}}}{2} \tag{4.16}$$

Thus, the power according to Equation 4.10 is not appropriate. Balancing the angular momentum and neglecting acceleration under the assumption of fully developed flow, leads, together with Equation 4.16, to the infinitesimal power at the blade as written in Equation 4.19[4].

$$dT = \left| \vec{r} \times d\vec{I}_{\mathrm{C}} \right| = \left| \vec{r} \times (\vec{v} \cdot \vec{n}_{\mathrm{C}}) \, \vec{n}_{\mathrm{C}} \right| \cdot d\dot{m} \qquad (4.17)$$

$$\Rightarrow dT = r \, c_{1,\mathrm{u}} \cdot \rho \, c_{1,\mathrm{m}} \, 2\pi r \, dr \qquad (4.18)$$

$$dP = dT \, \omega = 2\pi r^2 \rho \left(c^* - \frac{w_{\Gamma,\mathrm{m}}}{2} \right) w_{\Gamma,\mathrm{u}} \, \omega \cdot dr \qquad (4.19)$$

Note that the consideration of the *lifting line theory* would lead to the same result, as shown by Schmitz. However, in the scope of this research project, the above-presented method was adopted to calculate swirl in the wake of the propeller.

As with Betz and Joukowsky, the findings of Schmitz for the infinitesimal power at the section can be equated with the infinitesimal power deduced from the *blade element theory*. Finally, the resulting equation can be solved for the chord length and Equation 4.20 follows.

$$l\left(r \right) = \frac{16\pi}{n_{\mathrm{z}} \, C_{\mathrm{L}}} \, r \, \sin^2 \left[\frac{1}{3} \cdot \arctan \left(\frac{R}{\Lambda_{\mathrm{Des}} \, r} \right) \right] \qquad (4.20)$$

In addition to the chord length, the flow angle α and the relative angle Θ have to be recalculated to obtain the mounting angle φ. The resulting relationships are given by Equation 4.22.

$$\varphi\left(r \right) = \Theta - \alpha \qquad (4.21)$$

$$\varphi\left(r \right) = \frac{2}{3} \arctan \left(\frac{R}{r} \, \frac{1}{\Lambda_{\mathrm{Des}}} \right) - \alpha \qquad (4.22)$$

In comparison with the results of Betz and Joukowsky, the distribution of the chord length l and the relative angle Θ is calculated differently. Thus, the course of both functions, according to Schmitz, is outlined in Figure 4.7. The underlying assumptions of Figure 4.7 are a blade number of $n_{\mathrm{z}} = 3$ and a hypothetical lift coefficient of $C_{\mathrm{L}} = 1.2$ – they are the same as for the example results according to Betz and Joukowsky, as shown in 4.4. Besides the two
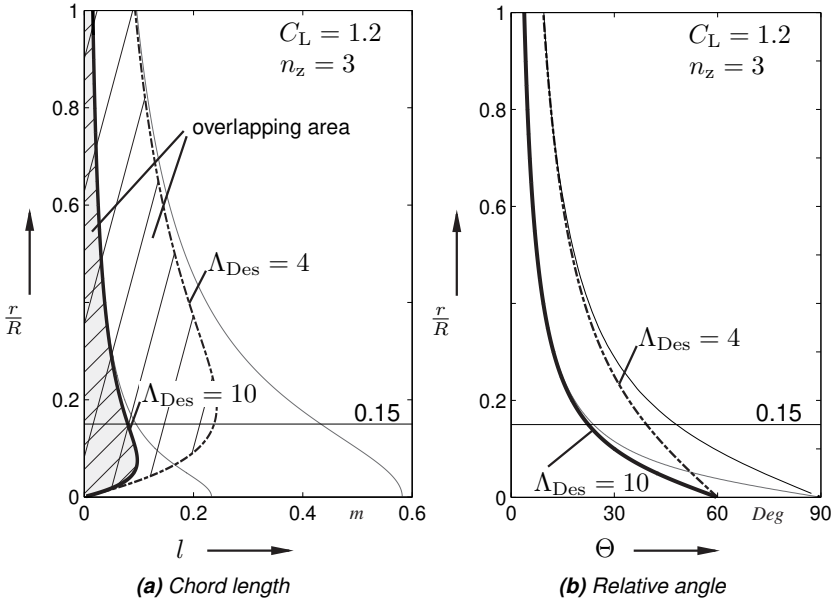
Figure 4.7. *Chord length $l\,(r)$ and relative angle $\Theta\,(r)$* **according to Schmitz [204]** *to take swirl into account, as shown for tip speed ratio $\Lambda = 4$ (broken line) and $\Lambda = 10$ (continuous line) for a hypothetical three-bladed machine with a constant lift coefficient of $C_{\mathrm{L}} = 1.2$ and a hub radius of $r/R = 0.15$, the hatching marks the area of the stream tube, which is overlapped by a single blade*

examples, both diagrams contain the former results as a faint slight line for comparison.

Regarding the course of the curves, in the region of the tip, good agreement can be found between the ideal design and the more practical design by Schmitz. But the closer the curve is to the hub, the more obvious the differences are. While the relative angle of Figure 4.7b is in general lower, it is less so with a rising tip speed ratio. When taking swirl into account, the course of the chord length changes its characteristics near the hub. Figure 4.7a clearly shows a turning point, which means that the chord length has a maximum value in the lower part of the blade near the hub. This is more plausible than the results of Betz and Joukowsky which lead to a very large chord length

directly at the hub.

As already mentioned, swirl will be considered within this research project. Thus, the developed design process, see Chapter 7, contains the method to calculate the swirl by a momentum balance. Owing to the utilisation of a high viscous fluid, *lifting line theory* is not suitable due to the requirement of a non-viscous fluid flow within this theoretical approach. In Chapter 8, the influences of the swirl will be investigated in detail.

4.2.4. Further losses

Besides the losses due to swirl, many other losses may occur in the complex structure of modern wind turbines. But in the field of aerodynamics, only losses caused by friction and tip flow are of further relevance.

Friction losses

In Chapter 4.2.2, the outlined procedure to design wind turbines comes with the rough assumption of neglecting friction and thus viscous stresses, see Equation 4.6. It is obvious that this may cause errors when regarding either aerodynamically high-loaded profiles or a high-viscous fluid flow.

To take friction into account, it is sufficient to calculate the power ratio in accordance with Equation 4.23 – it means considering the ratio of a real machine's power with the power of the ideal machine, as given by Equation 4.9.

$$\eta_{\text{Friction}} = \frac{dP}{dP_{\text{ideal}}} \tag{4.23}$$

Hence, with Equations 4.6 and 4.9, Equation 4.24 can be found, and finally, Equation 4.25 is formed while taking the velocity triangle of Figure 3.9 into account.

$$\eta_{\text{Friction}} = 1 - \frac{C_{\text{D}}}{C_{\text{L}}} \cdot \tan^{-1} \Theta \tag{4.24}$$

$$\eta_{\text{Friction}} = 1 - \frac{3r}{2\epsilon R} \Lambda_{\text{Des}} \tag{4.25}$$

By Equation 4.25, it becomes clear that the neglect of friction will cause errors if either the fundamental assumption for the insignificance of drag forces is violated or the profiles are aerodynamically high-loaded – both can be optimised by selecting profiles with a high lift-to-drag ratio ϵ.

Tip losses

In the fundamentals of *blade element momentum theory*, it is essential that no mass flow passes the stream tube, except at inflow and outflow. In addition to this requirement, only single cross-sections of a blade and thus infinite airfoils without hub or tip are regarded. However, the tip of a finite blade in particular will be affected by the secondary flow because of the pressure compensation effects and the ideal assumptions are not valid [5].

To take tip losses into account, it is sufficient to introduce the effective but reduced diameter D_{reduced}. The method was investigated by Betz [16, with remarks by Prandtl] and is elucidated in detail in Gasch and Twele [72][6]. Here, only the resulting efficiency η_{Tip} is shown by Equation 4.26. Note that tip losses are not included in the design method, as discussed in Chapter 7.

$$\eta_{\text{Tip}} = \left(\frac{D_{\text{reduced}}}{D} \right)^2 = \left(1 - \frac{\frac{4}{3} \ln 2}{n_z \sqrt{\Lambda_{\text{Des}}^2 + \frac{4}{9}}} \right)^2 \tag{4.26}$$

4.2.5. Final design process

Following the design steps of Chapter 4.2.2 and including the losses according to Chapters 4.2.3 and 4.2.4 will produce several well-designed sections. Note that the typical design process is characterised by a few iteration steps.
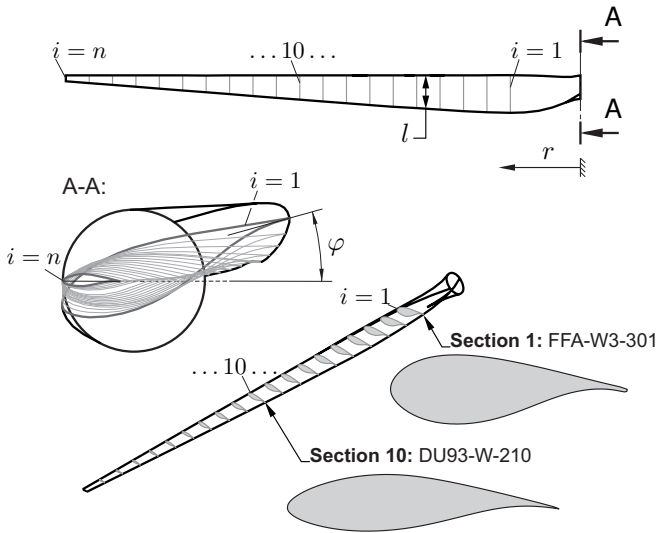
Figure 4.8. *Typical blade with multiple airfoil profiles, characterised by decreasing chord length l and changing the mounting angle φ with the rising radius r, as realised by several different airfoils represented by Schubel and Crossley [209]*

As the last step of the design process, the considered sections have to be mounted on a spar in an appropriate manner. As an example, Figure 4.8 shows the final design of a blade comprising a multiple, finite number of different sections.

In Figure 4.8, the considered sections are aligned by their leading edges, but sections are often aligned by their centre of pressure [72]. As can be seen, the presented blade consists of multiple sections – an optimum profile was chosen for each section. Typically, a single blade is designed with airfoils from different profile series. While the profiles near the hub are relatively thick for reasons of rigidity, those near the tip become thinner as they are more aerodynamically loaded than the profiles close to the hub. Besides the thickness of the profiles, Figure 4.8 also shows the chord length distribution $l(r)$ and the twist of the mounting angle $\varphi(r)$ over the radius. To illustrate both functions, Figure 4.9 shows a photo of a wind turbine type E-101 from Enercon.

Figure 4.9. *Single-blade of a wind turbine type E-101 from Enercon, detailed view of the trailing edge from hub to tip to illustrate the course of the chord length distribution and the change of the blade angle, photographer: Marc-André Aßbrock*

4.3. Vortex methods

As mentioned in Chapter 3.2, the *blade element momentum theory* – introduced by Glauert – is established in practice and in the literature. The method can be found in many references, e.g. in Gasch and Twele [72]; Hansen [88]; Hau [90]; Schlichting and Truckenbrodt [202]; Wilson and Lissaman [240]. However, by using one-dimensional methods as in *blade element momentum theory*, some physical effects are neglected.

Complex fluid machinery is often related to three-dimensional flow phenomena, especially at the hub and tip, see Figure 4.10. Thus, the method based on Betz and Joukowsky is not suitable to describe these phenomena. These effects can be described by considering the circulation Γ on vortex filaments, as already mentioned in Chapter 4.2.3. The *vortex methods* are based on the theorems conceived by Helmholtz and were first formulated as the *lifting line theory* by Lanchester [122] and Prandtl [164, 165]. They will be briefly summarised in an overview below. For further details of this theoretical approach, refer for instance to Schlichting and Truckenbrodt [202, 203], Wieghardt [239] or Spurk and Aksel [217].
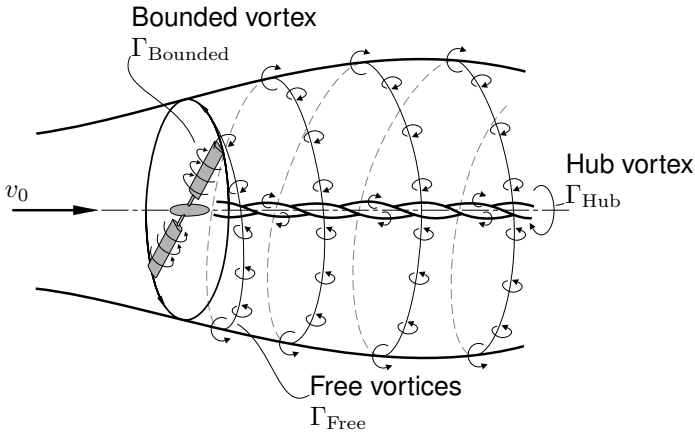
Figure 4.10. *Vortices for rotating propellers, author's own representation based on Hau [90] and Wilson and Lissaman [240]*

Lifting line method

As already mentioned, because of the pressure compensation effects at the tip of finite airplane wings or wind turbine blades, *blade element momentum theory* produces unsatisfactory results. Thus, the *lifting line theory*, as formulated by Prandtl [164, 165], can be applied to solve the problems of the former approaches.

Lifting line theory is based on the vortex theorems developed by Helmholtz [92]. Based on this approach, Prandtl claimed that a bounded vortex at the wing affects the lifting force. Since a vortex filament either has to be a closed loop, expire at a wall, or be infinite, a free vortex filament merges the bounding vortex filament at the tip. A horseshoe-like vortex results – in the case of a starting aircraft, the free vortex filaments on both sides merge with the starting vortex and the vortex filament becomes a closed loop, as depicted in Figure 4.11. The circulation Γ is a measure for the intensity of the vortex filament itself.

To apply *lifting line theory*, a distribution of the circulation is provided on the wing. The simplest case is to assume a constant value for Γ, but it is more suitable to assume an elliptic distribution $\Gamma(y) = \Gamma_0 \sqrt{1 - (2y/b)^2}$. The rea-
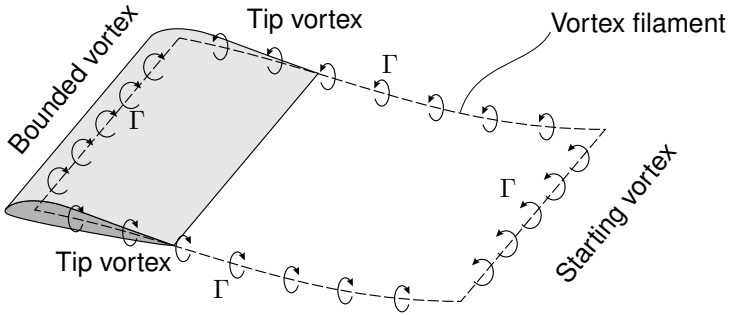
Figure 4.11. *Circulation and vortex filament, schematic view for 2D-extruded airfoil*

son can be found in the induced downward velocity[7] w_{ind}, which becomes a constant value for an elliptic distribution of the circulation, as can be seen in Figure 4.12.

Based on the Kutta-Joukowsky relationship according to Equation 4.27 and Equation 3.22, the effective flow angle α results, see Equation 4.28 and Figure 4.6.

$$dF_{\mathrm{L}} = \rho w \Gamma\left(y\right)\, dy \tag{4.27}$$

$$\Rightarrow \alpha = \frac{2\,\Gamma\left(y\right)}{w\, l\left(y\right)\, C_{\mathrm{L}}} \tag{4.28}$$

Finally, by applying the Biot-Savart law to the infinitesimal vortex filament $-d\Gamma$ at y' according to Figure 4.12, Equation 4.29 can be found for the induced flow angle α_{ind} due to the relationship $\alpha_{\mathrm{ind}} = w_{\mathrm{ind}}/w$.

$$\alpha_{\mathrm{ind}} = \frac{1}{4\pi\, w} \int\limits_{-b/2}^{b/2} \frac{d\Gamma}{dy'}\frac{dy'}{y-y'} \tag{4.29}$$

The flow angle $\alpha^*\left(y\right)$ of the ideal flow can be found by adding together the effective flow angle α and the induced flow angle α_{ind}, as in Equation 4.30.
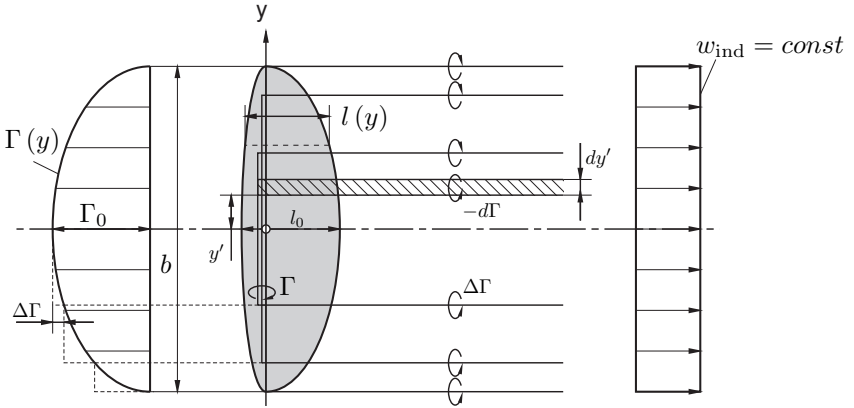
Figure 4.12. *Circulation vortex filament for elliptic distribution of circulation, author's own representation based on that of Schlichting and Truckenbrodt [203]*

$$\alpha^*(y) = \frac{2\,\Gamma(y)}{w\,l(y)\,C_\mathrm{L}} + \frac{1}{4\pi\,w} \int\limits_{-b/2}^{b/2} \frac{d\Gamma}{dy'}\frac{dy'}{y-y'} \tag{4.30}$$

From Equation 4.30, either the distribution of the flow angle, or, as is required in this research project, the chord length distribution $l(y)$ can be calculated, see Equation 4.31.

$$l(y) = l_0\sqrt{1 - \left(\frac{2y}{b}\right)^2} \tag{4.31}$$

Note that for Equation 4.31 a constant total flow angle was assumed as well as an eliptic distribution of the circulation.

Equation 4.31 provides an alternative approach to creating a potential shape for the shape of an aircraft wing or a propeller blade. Because of the consideration of induced drag as a consequence of the vortex system, the *lifting line theory* approach leads to highly qualitative results.

Disadvantages of the vortex methods

Technical flow in rotating fluid machinery is often associated with complex vortex structures, such as tip and hub vortices, as can be seen in Figure 4.10. As elucidated above, the *vortex methods* allow the calculation of these 3-dimensional flow phenomena to a high degree of accuracy. The method can easily be combined with numerical methods, such as CFD for instance, and is very important for design processes in practice.

However, the theory is based on the Helmholtz theorems, which are in turn based on the assumption of negligible viscous effects. In the scope of the technical fluid flow, it is mainly turbulence effects that dominate and thus the molecular viscosity is relatively small and although the theorems are suitable in one sense, they are not within the scope of this research project. This research topic deals with the treatment of high viscous fluid flow under low-Re conditions. And thus, the aforementioned requirements for negligible viscous forces are not at hand and it is not suitable to apply the *vortex methods*. Hence, the desired method to design propeller mixers for this kind of fluid flow, as discussed in Chapter 7, is based on the *momentum methods*, as discussed in Chapter 4.2.

Notes

[1] The procedure of combining *blade element theory* with *axial momentum theory* to describe the absolute velocity c at a specific blade section by the velocity magnitude v_1 on the rotating plane of the stream tube, is what leads to *blade element momentum theory* and was done by Betz [15] to enhance *blade element theory*. Thus, all further equations in this thesis with any relationships to *blade element momentum theory* are given with respect to the indices of *axial momentum theory* and the formula symbols of *blade element theory* as defined in Chapters 3.2.1 and 3.2.2.

[2] There is a strong connection between the number of blades on the impeller and the aerodynamic efficiency of the wind turbine. While high numbers of blades were used in early wind pump systems, single-blade machines were only built in modern times for research purposes.

[3] As a new trend in the late 2010s, the utilisation of two-bladed turbines for off-shore wind farms was discussed due to the superior efficiency and dispensable noise character, but this concept is yet to be established in practice.

[4] Taking swirl into account also gives rise to a relationship of the infinitesimal power at a single section, which can be equated with results using *blade element theory*. But separating the wind power dP_{Wind} from Equation 4.19 reveals that the resulting coefficient of power C_P is no longer a constant, but a function of the tip speed ratio Λ_{Des}:

$$C_P = \int\limits_0^1 4\Lambda_{\mathrm{Des}} \left(\frac{r}{R}\right)^2 \frac{\sin^3 \frac{2}{3}\Theta}{\sin^2 \Theta} \, d\left(\frac{r}{R}\right) \tag{4.32}$$

[5] The tip losses are caused by the tip vortices. Considering a vortex filament, it is clear that not only tip vortices, but also hub vortices have to exist. This is, of course, true, but typically the hub vortex is calculated by means of CFD, while this vortex system is neglected in the design process [72].

[6] To consider an effective but reduced diameter is sufficient because of the radial distribution of circulation over the blade: circulation and thus the lifting force will suddenly decrease close to the tip. The idea is to choose the effective diameter in such a way that it correlates to an ideal machine without decreasing circulation while the integral value remains the same for the real machine with decreasing circulation. For details, refer to the notes by Prandtl in [16]. With the known value of the ideal diameter, the machine can be designed with the method discussed in Chapter 4.2.2. Subsequently, the ideal power can be reduced by multiplying with the tip efficiency according to Equation 4.26 to obtain the correct power.

[7] *Lifting line theory* predicts the induction of drag, even for the most ideal flow of non-viscous fluids. The reason can be found in the free vortex, which starts at the tip of the wing due to pressure compensation effects. This free vortex has to be supplied by energy continuously and thus the kinetic energy of the wing is reduced. In practice, the induced drag comes with the induction of the downwards velocity.

5. High viscous fluid flow

The flow of high viscous fluids is of major importance in this project. This type of flow is often characterised by complicated non-linear material properties. Hence, considering the classic field of fluid mechanics alone is mostly insufficient, and the field of rheology should also be considered. But the field of rheology handles the flow of all matter. Since this research field is very broad and complex, only a short overview of the relevant topics will be given here.

5.1. Flow of matter

The field of rheology investigates the flow properties of matter and thus also fluids. But within the field of rheology, there is no strict distinction between fluids and bodies. All real matter, however complex it is, will have an arbitrary state between two ideal conditions, which are based on simple, yet theoretical models: the ideal fluid and the ideal body. Therefore, in the following, both ideal models are explained briefly before the general fluid flow is introduced. Then, non-Newtonian fluid flow is described, which is often connected with high viscous liquids and related to the present work.

5.1.1. Ideal constitutive laws

Ideal viscous fluids

First, an ideal fluid flow will be considered. This type of fluid flow can be described by Newton's law.

As is commonly known, Newton found in 1714 that there is a proportional relationship between the force F and the state of deformation. For two-dimensional shear flow, as shown in Figure 5.1, the state of deformation can be defined as the ratio of the maximum velocity v_{max} to the distance of the gap ΔH, which can be easily reduced to the shear rate $\dot{\gamma}$ for infinitesimal quantities, see Equation 5.1. For infinitesimal quantities, the force F
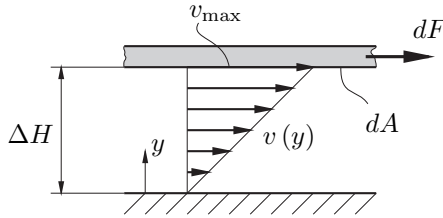
Figure 5.1. *Newton's law*

becomes dF and can be transferred to the wall shear stress τ via dividing dF by the infinitesimal area dA.

$$\frac{v_{\mathrm{max}}}{\Delta H} = \frac{dv}{dy} = \dot{\gamma} \tag{5.1}$$

Finally, the dynamic shear viscosity μ can be applied as a constant proportional factor. Taking the density ρ into account, the kinematic shear viscosity $\nu = \mu/\rho$ can be derived from the dynamic shear viscosity. Thus, Newton's law is commonly formulated according to Equation 5.2.

$$\tau = \dot{\gamma} \cdot \mu = \dot{\gamma} \cdot \nu \cdot \rho \tag{5.2}$$

Frictionless fluid flow is often considered within the field of classic fluid mechanics. This is because of the negligible low friction outside the boundary layer, as it is typical for high-Re problems and modelled by the theory of potential flow. Enhancing the theoretical considerations by viscous flow effects, for simple Newtonian fluids like air or water, Equation 5.2 is very suitable for modelling these effects.

While Equation 5.2 represents the most ideal fluid behaviour, the law can only be adopted for a small number of fluids, as mentioned above. Owing to the complexity of many technical fluids, Equation 5.2 is not suitable for modelling their rheological behaviour, especially for a low-Re fluid flow. Many

technical fluids, even those in the processing industry, are characterised by high viscous and mostly non-Newtonian behaviour.

Ideal elastic bodies

In keeping with Newtonian fluid, a body is considered to model an ideal elastic body. This body is stressed by an infinitesimal load, dF, as shown in Figure 5.2.

The force dF leads to the stress τ in the body, thereby causing the strain Δx in the x-direction. Together with the distance ΔH, the shear strain γ can be derived according to Equation 5.3.

$$\frac{\Delta x}{\Delta H} = \frac{dx}{dy} = \gamma \tag{5.3}$$

For ideal elastic bodies, the shear stress τ and the shear strain γ are proportionally related, and the shear modulus G can be found as the proportionality factor. For this ideal linear-elastic body, first described by Hooke in 1678, Equation 5.4 can be found.

$$\tau = \gamma \cdot G \tag{5.4}$$

Although Equation 5.4 is only valid for ideal bodies and infinitesimal strain, Hooke's law is highly important in the field of material science. For small
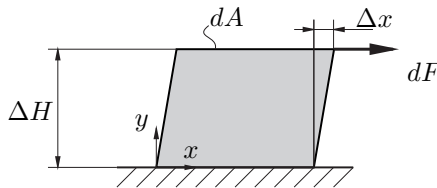
Figure 5.2. *Hooke's law*

strains, many materials can be modelled in very good agreement by Equation 5.4 until the onset of plastic deformation.

Ideal viscoelastic fluid

As previously mentioned, real matter cannot be explicitly classified as a fluid or body within the field of rheology, except for materials with ideal conditions. It means that all real matter can be classified as being in a state between Newton's fluid and Hooke's body without ever reaching one of these ideal states. Nevertheless, matter is either characterised by more viscous or more elastic properties, with viscosity properties dominating for fluids. Only fluids are of interest in this project and hence the focus of explanation.

$$\dot{\gamma} = \dot{\gamma}_{\text{visc.}} + \dot{\gamma}_{\text{elast.}} \tag{5.5}$$

When shearing a fluid probe, the response has to occur on a viscous and an elastic component, as shown in Equation 5.5. When expressing the response as an equilibrium of loads, the factor $\lambda = \mu/G$ appears, as can be seen in Equation 5.6. This factor is a time-dependent property of the fluid and is often referred to as the relaxation time.

$$\dot{\gamma} = \frac{\tau}{\mu} + \frac{\dot{\tau}}{G}$$
$$\Leftrightarrow \tau + \underbrace{\frac{\mu}{G}}_{\lambda} \dot{\tau} = \mu \dot{\gamma} \tag{5.6}$$

This model, which represents the simplest way to describe a fluid with viscoelastic properties, is called Maxwell fluid[1] after its creator, Maxwell, who established this relationship in 1867. The model takes place on a viscous damping element, which follows a spring element, see Figure 5.3a. Both elements are stressed simultaneously. Since the simple Maxwell element is not able to model real fluids, it is more convenient to consider several parallelised

(a) simple *(b) generalised*
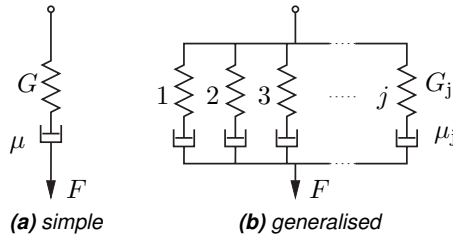
Figure 5.3. *Maxwell model*

simple Maxwell elements. This creates the generalised Maxwell model, as illustrated in Figure 5.3b.

The generalised Maxwell model can be applied with the enhancements of Baumgaertel and Winter [10] to identify the necessary number of simple Maxwell elements and is utilised to model the melts of macromolecules [21; 135], but also for aqueous polymer solutions [180]. The application of this model has been extensively described by Reviol et al. [180] and performed for different aqueous polymer solutions.

5.1.2. General fluid flow

With Newton's and Hooke's law, and Maxwell's proposal to model viscoelastic fluids, linear material properties were considered using the relaxation time λ. Summarising all materials with linear material properties, they lie on a single number line, given by the expression $\omega \cdot \lambda$,[2]. On the left of this line, the starting point is given by Newton's fluid and its value is 0, while the ending point on the right is given by Hooke's body and continues to ∞.

However, in reality, all materials are characterised by more or less distinguished non-linear material properties and the mentioned number line of ideal matter cannot be achieved by real matter, but real matter can come very close to achieving it. The more distinct the non-linearity, the larger the distance to the line and both ideal extremes. Pipkin [161] suggested a diagram to combine all ideal and real states in one single chart when the matter
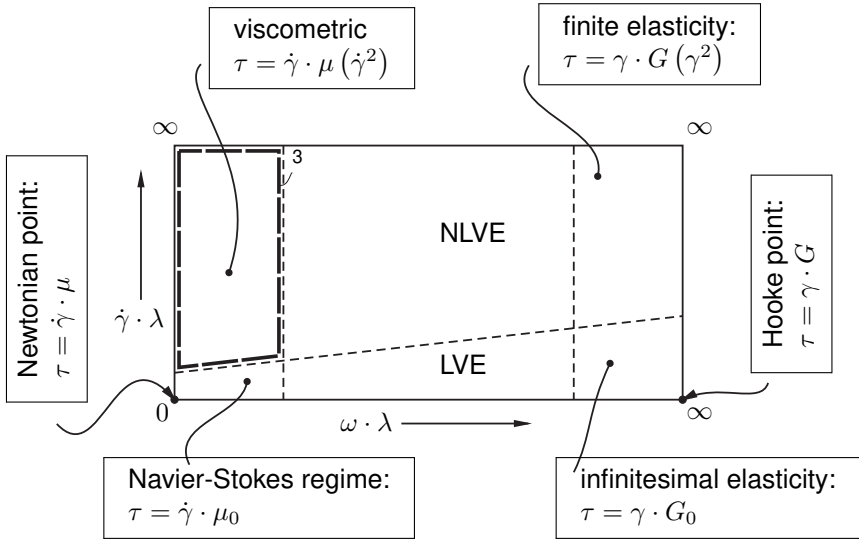
Figure 5.4. *Pipkin's diagram*

is subjected to shear stress, irrespective of how linear or non-linear they are, see Figure 5.4.

As already mentioned, the Newtonian point can be found in the left corner. At this point, the shear viscosity μ is a constant, but this state is absolutely ideal. Enlarging this single point to a larger regime, which can be found in reality, leads to the Navier-Stokes regime. This regime assumes that the shear time is low compared to the relaxation time and the shear stress is a steady load. Because of this, the limit value consideration for low shear rates of the viscosity function leads to the dynamic zero-shear-rate-viscosity μ_0, which is consequently a constant Newtonian viscosity. For a detailed explanation of the viscosity function, see Chapter 5.2. In the case of a short relaxation time, e.g. $\lambda = 1 \cdot 10^{-12}$ s for water [135], the Navier-Stokes regime is appropriate to model simple fluid flow, as considered in the field of classic fluid mechanics.

Above the Navier-Stokes regime, for rising shear rates, the regime of viscometric flow can be found. This kind of flow is characterised by shear-dependent fluid properties, while the shear rate is independent of time [102].

Thus, in this region, the viscosity cannot be reduced to a single value and the whole viscosity function $\mu\left(\dot{\gamma}^2\right)$ has to be taken into account. However, viscoelastic effects are of minor importance and the fluid can be assumed as purely viscous but non-linear viscous (see also Chapter 5.1.3 and 5.2 respectively). Many technical fluids in the processing industry are in this regime and thus this kind of fluid is of major interest in the scope of this work.

Raising the shear frequency ω instead of the shear rate will make the response more and more viscoelastic. This regime is called the linear viscoelastic regime (LVE). In its simplest formulation, this regime is modelled by Maxwell's model[4], as illustrated in Figure 5.3. Above the LVE-regime, the non-linear viscoelastic (NLVE) regime can be found. This region consists of materials that are very hard to achieve by mathematical models due to the non-linear character of both viscous and elastic properties with different distinct characteristics of each property.

As an extreme, for rising frequency, the product $\omega \cdot \lambda$ reaches ∞. If the shear rate is simultaneously low, the state is represented by the most ideal body, meaning that the shear modulus G is a constant value. In keeping with Newton's fluid, Hooke's body cannot be achieved by real matter but can be close to it. The region around the ideal extreme is the infinite elastic regime, which is valid for real materials. If the strain is low in this region, the shear modulus is given by G_0. Steel and other metals are characterised by a distinct elastic regime for low strain.

Above the infinite elastic regime, matter with distinctly non-linear but elastic behaviour can be found. This is the region of rubber-like materials, also called finite elastic, while the shear modulus becomes a function of the shear strain: $G(\gamma^2)$.

Note that Pipkin [161] discussed his diagram, as depicted here in Figure 5.4, from the perspective of a fluid by considering the shear rate $\dot{\gamma}$ and the shear frequency ω. However, Pipkin and Pipkin and Tanner [162] carried out further considerations for solids. Owing to the insignificance of bodies in the scope of this work, this will not be considered from the perspective of solids.

5.1.3. Introduction of generalised Newtonian fluid flow

In many cases of technical flow, a fluid's elasticity is of minor relevance[5] because of a dominating viscous flow process. Thus, in agreement with Pipkin's diagram, viscometric flow is the most relevant type of flow, provided that the Navier-Stokes regime is invalid either due to the length of relaxation time λ of the considered fluid or due to the actual amount of the shear rate $\dot{\gamma}$. Hence, the elasticity is mostly negligible for practical use and the fluid is considered fully viscous.

However, technical fluids show a more or less distinct dependence on viscosity[7] in the state of deformation, as will be explained in Chapter 5.2.2. Hence, considering a fluid as purely viscous but with varying viscosity is sufficient in practical use. This fluid type is described in the literature as *generalised Newtonian fluid*. For further details, refer to [21; 76; 102]. The *generalised Newtonian fluid flow* model includes all non-Newtonian fluid flow without any distinct elastic properties. Following the proposal by Pipkin to consider a number line with Newton's fluid on the left and Hooke's body on the right, Figure 5.5 can be derived to classify the matter. Since the number line contains an infinite number of imaginable fluids, *generalised Newtonian fluids* are a very special kind of theoretical fluid, but they are, as mentioned above, very suitable to model technical flow. In Figure 5.5, *generalised Newtonian fluids* are marked by a bold, broken line.
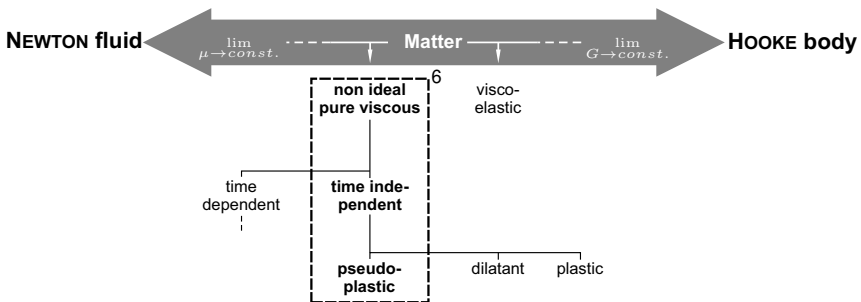
Figure 5.5. *Classification of matter*

As illustrated in Figure 5.5, *generalised Newtonian fluids* can be further sub-divided into time-independent and time-dependent fluids – examples of time-dependent effects are rheopexy (shear-thickening effect over shear time) and thixotropy (shear-thinning effect over shear time).

In line with the above-mentioned considerations, viscoelasticity will not be considered in the scope of this work and the model of *generalised Newtonian fluids* will be applied. Additionally, as will be shown in Chapter 9.1 and 9.2, only time-independent fluids were applied in the scope of this work and hence time-dependent effects, such as rheopexy and thixotropy, will not be considered[8].

Owing to its relevance for this research work, some relevant points about *generalised Newtonian fluids* will be discussed below in more detail.

5.2. Generalised Newtonian fluids

Technical fluids are mostly characterised by a more or less pronounced variability of viscosity. The variability can be caused by temperature, pressure, or by the recent state of deformation, as well as by moisture and concentration [74]. Since the dependence on moisture and concentration comes with the change of the initial fluid, they will not be considered here. Furthermore, changes in the viscosity of liquids due to pressure appear only for high-pressure differences [105; 107; 129; 157]. Though the dependence of the viscosity on temperature may exist for slight thermal differences, they are typical (but not only) for Newtonian fluids [74; 129] – the higher the viscosity, the more pronounced the dependence [66] – and it is obvious that these effects are negligible for (almost) isothermal processes, as considered here. However, for technical flow, the most important influence on the viscosity of non-Newtonian fluids is related to the state of deformation [76].

5.2.1. Phenomenology

While the state of deformation causes changes in the viscosity, the change can range from shear-thinning to shear-thickening, or even plasticity can oc-
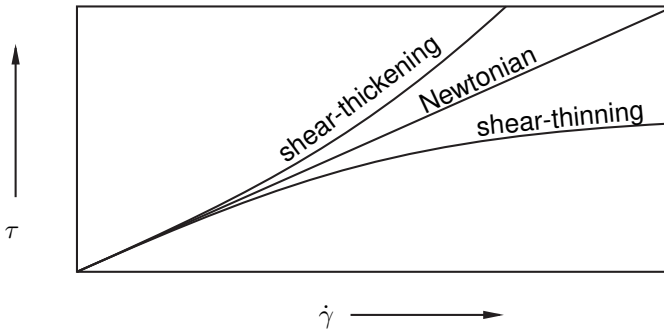
Figure 5.6. *Purely viscous and time independent fluids*

cur. A schematic overview of these types of fluids is illustrated in Figure 5.6. As summarised by Giesekus [76], most non-Newtonian fluids are characterised by shear-thinning behaviour and thus, as already mentioned, only this kind of matter will be discussed in detail.

As outlined, considering technical flow, the viscous properties of the fluid are of major interest. Thus, in the following, the characteristic aspects of pseudoplastic fluid flow will be discussed.

Pseudoplastic media are characterised by shear-thinning fluid patterns, but the shear-thinning effect is not infinite. Typically, the pseudoplastic matter shows Newtonian behaviour, but only for very low and very high shear rate. Both regimes show a plateau-like course of the viscosity and are quantified by the zero-shear-rate-viscosity μ_0 and the infinite-shear-rate-viscosity μ_∞, as illustrated in Figure 5.7a for the flow function and in Figure 5.7b for the viscosity function. Note that both diagrams of Figure 5.7 show double-logarithmic axes. Hence, in the regime of the plateau-like course for the viscosity function, the slope amounts to $\partial \tau / \partial \dot{\gamma} = 1$ for the flow function due to the constant values of the zero-shear-rate-viscosity μ_0 and the infinite-shear-rate-viscosity μ_∞. The shear-thinning region lies between both plateau-like regions.

As outlined by Chhabra and Richardson [38], microstructures may influence the rheological behaviour of a fluid and thus cause shear-thinning behaviour, as discussed above. Ebert [59] discussed two vivid approaches of shear-
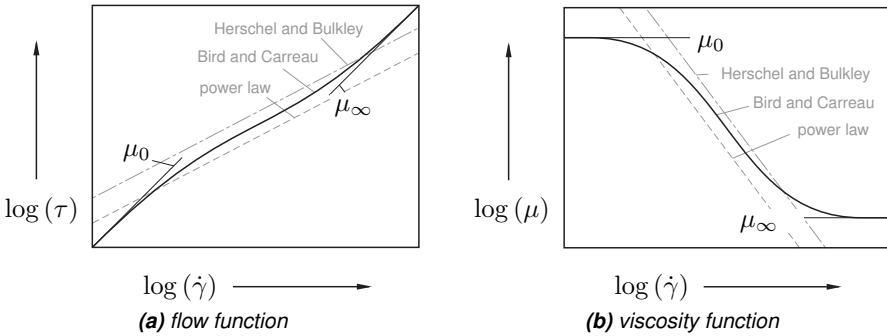
Figure 5.7. *Typical flow characteristics of a shear-thinning fluid (black, continuous line) with zero-shear-rate-viscosity μ_0 and infinite-shear-rate-viscosity μ_∞, also shown are the power law approximation function (grey, broken line) and the functions according to Herschel and Bulkley (grey, dash-dotted line) and Bird and Carreau (hidden by the characteristics) – deviations of approximations from characteristics are overstated*

thinning behaviour which are presented in the following due to their clarity[9]:

1. In the case of the liquid dispersion of slender particles like fibres or macromolecules, there is an entanglement of these particles that looks like a connection, provided that the dispersion is at rest or under infinitesimal slow shear. Under this condition, the viscosity of the dispersion is relatively high and nearly constant. For rising shear rates, connections break with greater frequency and the viscosity decreases. This effect holds until all particles are oriented in the flow direction and the viscosity reaches its minimum, which also has to be a constant value.

2. Liquid dispersions of small particles can be considered as colloidal systems. At low shear rates, water is bounded as a hydrate shell around the particles, and hence, the viscosity is relatively high and nearly constant. Increasing the shear rate causes solvation of the hydrate shell and the lubricant effect of the surrounding water increases, while the viscosity of the dispersion increases. At some time, most of the water is transferred out of the hydrate shell and the viscosity reaches a minor constant value.

The above mechanisms are reversible for time-independent fluids and irreversible for time-dependent fluids. For many practical fluids, both approaches have a very plausible explanation and thus, they are very suitable but only phenomenological.

Hence, an overview of the state of deformation will be provided in Chapter 5.2.2. The constitutive law of *generalised Newtonian fluid flow* will be presented in Chapter 5.2.4. Some more practical, and yet empirical, models will be discussed in Chapter 5.2.5.

5.2.2. State of deformation

Arbitrary fluid flow must be characterised by a wide range of fluid properties, as outlined in Chapter 5.1.2. However, it was emphasised in Chapter 5.1.3 that only a purely viscous fluid flow is of interest in the scope of this research work. Therefore, only the state of deformation has to be considered while taking into account the variability of the viscosity.

To discuss an arbitrary state of deformation, the fluid element, according to Figure 5.8, is considered. Owing to simplicity, the deformation is discussed for a two-dimensional fluid element only.

The edge lengths of the element are given by dx and dy, respectively. As a consequence of the fluid flow, the vortices P, Q, R, and S of the element will be moved within the time dt in an arbitrary manner, and P will be transformed to P' due to the velocity vector $v = (v_\mathrm{x}, v_\mathrm{y})$ at the point P. When the location of the point P in the x-direction is changed to $v_\mathrm{x} \cdot dt$ in the time dt, the location of the point Q changes to $\left(v_\mathrm{x} + \frac{\partial v_\mathrm{x}}{\partial x} dx\right) dt$. Thus, the change of the edge length in the x-direction amounts to $\frac{\partial v_\mathrm{x}}{\partial x} dx\, dt$, while Equation 5.7 results in the longitudinal strain rate $\dot{\varepsilon}_\mathrm{x}$ in this direction.

$$\dot{\varepsilon}_\mathrm{x} = \frac{\partial v_\mathrm{x}}{\partial x} dx\, dt \cdot \frac{1}{dx \cdot dt} = \frac{\partial v_\mathrm{x}}{\partial x} \tag{5.7}$$

Similarly, Equation 5.8 results in the y-direction and Equation 5.9 when considering the z direction.
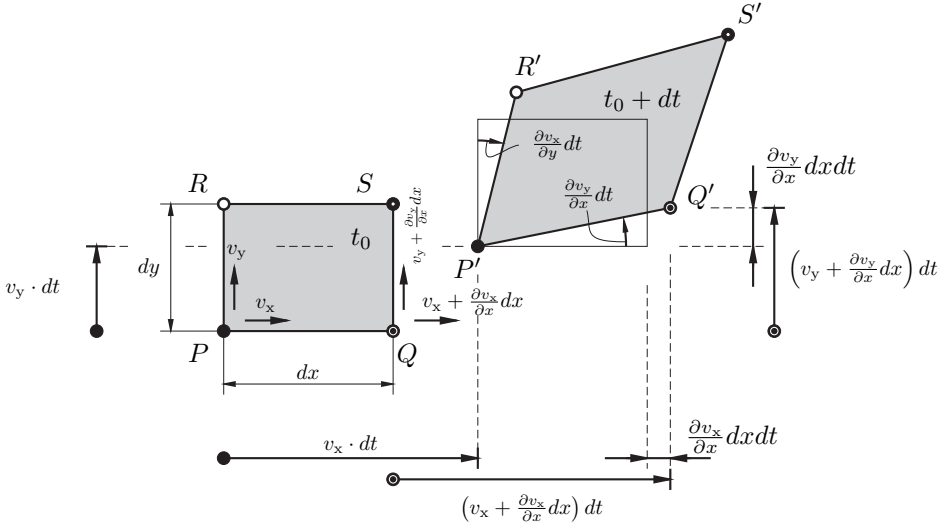
Figure 5.8. *Deformation of a fluid element*

$$\dot{\varepsilon}_y = \frac{\partial v_y}{\partial y} \tag{5.8}$$

$$\dot{\varepsilon}_z = \frac{\partial v_z}{\partial z} \tag{5.9}$$

Taking the change in the y direction of the points P and Q into account, the location of the transformed point P' is $v_y \cdot dt$, while the location of Q' is $\left(v_y + \frac{\partial v_y}{\partial x} dx\right) dt$, see Figure 5.8. Hence, not only can the longitudinal rate of strain $\dot{\varepsilon}$ be estimated, but also the rate of shear strain $\dot{\gamma}$. The rate of shear strain $\dot{\gamma}_{x,y}$ of the xy-plane consists of the shear rates of the edge dx and the edge dy. Both rates of shear strain lead to Equation 5.10.

$$\dot{\gamma}_{x,y} = \frac{\partial v_x}{\partial y} dy dt \cdot \frac{1}{dy \cdot dt} + \frac{\partial v_y}{\partial x} dx dt \cdot \frac{1}{dx \cdot dt} = \frac{\partial v_x}{\partial y} + \frac{\partial v_y}{\partial x} \tag{5.10}$$

As already performed for the longitudinal strain, the shear strain can also be

calculated similarly for the remaining directions, see Equations 5.11 to 5.13.

$$\dot{\gamma}_{x,y} = \dot{\gamma}_{y,x} \tag{5.11}$$

$$\dot{\gamma}_{x,z} = \frac{\partial v_x}{\partial z} + \frac{\partial v_z}{\partial x} = \dot{\gamma}_{z,x} \tag{5.12}$$

$$\dot{\gamma}_{y,z} = \frac{\partial v_y}{\partial z} + \frac{\partial v_z}{\partial y} = \dot{\gamma}_{x,y} \tag{5.13}$$

Note that the matrix of the shear rate is symmetrical, hence $\dot{\gamma}_{i,j} = \dot{\gamma}_{j,i}$.
By summarising all strain components in one single tensor, Equation 5.14 is formed.

$$\mathbf{D} = \begin{pmatrix} \dot{\varepsilon}_x & \frac{1}{2}\dot{\gamma}_{x,y} & \frac{1}{2}\dot{\gamma}_{x,z} \\ \frac{1}{2}\dot{\gamma}_{y,x} & \dot{\varepsilon}_y & \frac{1}{2}\dot{\gamma}_{y,z} \\ \frac{1}{2}\dot{\gamma}_{z,x} & \frac{1}{2}\dot{\gamma}_{z,y} & \dot{\varepsilon}_z \end{pmatrix} \tag{5.14}$$

Together with Equations 5.7 to 5.13, Equation 5.14 becomes Equation 5.15.

$$\mathbf{D} = \begin{pmatrix} \frac{\partial v_x}{\partial x} & \frac{1}{2}\left(\frac{\partial v_x}{\partial y} + \frac{\partial v_y}{\partial x}\right) & \frac{1}{2}\left(\frac{\partial v_x}{\partial z} + \frac{\partial v_z}{\partial x}\right) \\ \frac{1}{2}\left(\frac{\partial v_y}{\partial x} + \frac{\partial v_x}{\partial y}\right) & \frac{\partial v_y}{\partial y} & \frac{1}{2}\left(\frac{\partial v_y}{\partial z} + \frac{\partial v_z}{\partial y}\right) \\ \frac{1}{2}\left(\frac{\partial v_z}{\partial x} + \frac{\partial v_x}{\partial z}\right) & \frac{1}{2}\left(\frac{\partial v_z}{\partial y} + \frac{\partial v_y}{\partial z}\right) & \frac{\partial v_z}{\partial z} \end{pmatrix} \tag{5.15}$$

Tensor $\mathbf{D}$ is called the deformation rate tensor and can fully describe the state of deformation of a fluid element. It can be used to describe the variability of the viscosity under the previous assumptions.
As can be seen in Equation 5.15, all components are partial derivatives of the velocity vector. Calculating the Jacobian matrix J_v of the velocity vector v leads to Equation 5.16, containing all required partial derivatives of the velocity vector.

$$J_{\mathrm{v}} = \begin{pmatrix} \partial v_{\mathrm{x}}/\partial x & \partial v_{\mathrm{x}}/\partial y & \partial v_{\mathrm{x}}/\partial z \\ \partial v_{\mathrm{y}}/\partial x & \partial v_{\mathrm{y}}/\partial y & \partial v_{\mathrm{y}}/\partial z \\ \partial v_{\mathrm{z}}/\partial x & \partial v_{\mathrm{z}}/\partial y & \partial v_{\mathrm{z}}/\partial z \end{pmatrix} = \mathbf{L} \tag{5.16}$$

The Jacobian matrix J_{v} of the velocity vector v is also called the velocity gradient tensor $\mathbf{L}$. From the gradient tensor $\mathbf{L}$, the deformation tensor $\mathbf{D}$ can be calculated according to Equation 5.17.

$$\mathbf{D} = \frac{1}{2} \left(\mathbf{L} + \mathbf{L}^T \right) \tag{5.17}$$

Equation 5.17 means that only the velocity gradient tensor $\mathbf{L}$ has to be known to calculate the state of deformation.

Note that the deformation tensor $\mathbf{D}$ is characterised by three principle invariants[10], given by Equations 5.18 to 5.20:

$$I = \mathbf{tr}\,(\mathbf{D}) \tag{5.18}$$

$$II = \frac{1}{2} \left((\mathbf{tr}\,(\mathbf{D}))^2 + \mathbf{tr}\,(\mathbf{D}^2) \right) \tag{5.19}$$

$$III = \mathbf{det}\,(\mathbf{D}) \tag{5.20}$$

In Equations 5.18 to 5.20, $\mathbf{tr}\,(\mathbf{D})$ is the trace of the deformation tensor $\mathbf{D}$, while $\mathbf{det}\,(\mathbf{D})$ is its determinant. The principle invariants will be important for Reiner-Rivlin's constitutive law, as discussed in Chapter 5.2.4.

5.2.3. State of stress

In continuum mechanics, an infinitesimal part of a body is typically considered. In fluid mechanics, an infinitesimal control volume is analysed instead. In Figure 5.9, the control volume of an arbitrary fluid flow is illustrated.

The flow causes stresses in the fluid and therefore on the surfaces of the control volume. The state of stress can be separated into normal components
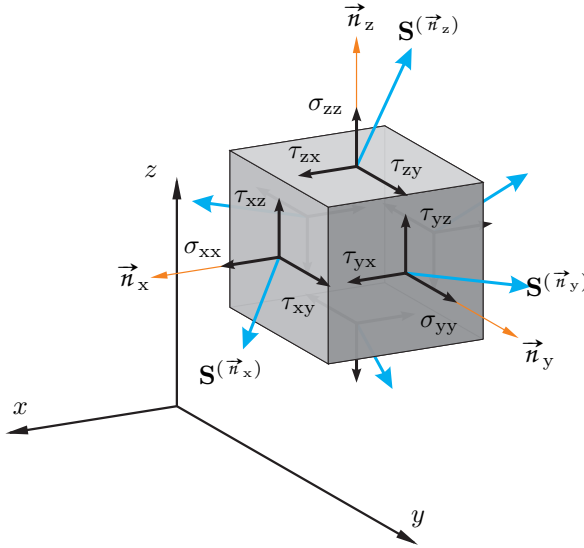
Figure 5.9. *State of stress of a fluid element*

σ_{ii} and tangential components τ_{ij}. In Figure 5.9, the indices of the stress components follow the convention that the first index marks the considered plane, while the second index gives the direction of the axis. Thus, for each single surface of the control volume, one normal and two tangential stresses are present and therefore nine different components can be identified while neglecting the reaction forces.

Each component can be added to Cauchy's stress tensor $\mathbf{S}$, resulting in Equation 5.21.

$$\mathbf{S} = \begin{pmatrix} \sigma_{xx} & \tau_{xy} & \tau_{xz} \\ \tau_{yx} & \sigma_{yy} & \tau_{yz} \\ \tau_{zx} & \tau_{zy} & \sigma_{zz} \end{pmatrix} \tag{5.21}$$

When discussing the state of stress at a fluid element, as shown in Figure 5.9, the hydrostatic pressure entities p_i, which are normal to the considered surface, have to be considered. Owing to the direction of the pressure on the

shape of the control volume, in turn, the pressure has to affect the normal vectors $\vec{n}_i$ of each surface and the normal components can be set to $\sigma_{ii} = -p_i + \tau_{ii}$.

Typically, the hydrostatic pressure p_i is understood as isotropic pressure [76; 102]. Strictly speaking, this is a mistake because of the variability of the hydrostatic pressure over the spatial structure of a volume, especially for compressibility, as originally discussed by Stokes [219][11]. However, in the scope of this research, the (relatively) slow fluid flow of liquids is the focus and thus compressibility is not considered. Nevertheless, to obtain isotropic pressure, it is more correct to consider the thermodynamic pressure p. Following this concept, the pressure p can be separated from Cauchy's stress tensor and $\mathbf{S}$ becomes 5.22.

$$\mathbf{S} = \begin{pmatrix} -p & 0 & 0 \\ 0 & -p & 0 \\ 0 & 0 & -p \end{pmatrix} + \underbrace{\begin{pmatrix} \tau_{xx} & \tau_{xy} & \tau_{xz} \\ \tau_{yx} & \tau_{yy} & \tau_{yz} \\ \tau_{zx} & \tau_{zy} & \tau_{zz} \end{pmatrix}}_{\mathbf{T}} \qquad (5.22)$$

Introducing the extra stress tensor $\mathbf{T}$ for the second summand of Equation 5.22, Cauchy's stress tensor can be defined as follows in Equation 5.23.

$$\mathbf{S} = -p\mathbf{1} + \mathbf{T} \qquad (5.23)$$

5.2.4. Reiner-Rivlin constitutive law

The previous chapter introduced the state of deformation and the state of stress. However, the relationship between the state of deformation and the state of stress is given by the matter. As outlined before, pure but non-linear viscous fluid flow and thus *generalised Newtonian fluid flow* is of major interest in this thesis.

Hence, the relationship between both the mentioned states must be formulated with respect to the considered fluid. The mathematical formulation of

such a fluid was first formulated by Reiner [175] and Rivlin [191], and thus, this kind of fluid is called Reiner-Rivlin liquid[12].

Since Reiner-Rivlin liquids are the most general form of *generalised Newtonian fluids*, they have to fulfil the four criteria of a viscous fluid for the relationship between stress and velocity field, as outlined by Stokes [219]:

> *"1. The stresses are continuous functions of the rates of deformation* [$\mathbf{D}_{ij}$, T.R.].
>
> *2. The fluid is homogeneous in such a way that the stresses are explicitly independent of the particle coordinates* [x_i, T.R.].
>
> *3. When the rates of deformation are zero, i.e.* [$\mathbf{D}_{ij} = 0$, T.R.]*, the stresses are given by the isotropic thermodynamic pressure* $p = p(\rho, \theta)$.
>
> *4. Viscosity is an isotropic property, or in other words, the fluid is isotropic."* [102, p. 153, chapter 8.2]

In a strict sense, Stokes' fourth criterion can be neglected because of the implicit formulation of this criterion by the others. The reason can be found in the principle of material objectivity while defining a constitutive law.

This principle requires that the state of stress on the surface of a particle, given by $\mathbf{S}$, has to be independent of the chosen reference system to which the constitutive law is actually related. As an example, an arbitrary state of stress $\mathbf{S}_{(1)}$ with the reference (1) has to be equal to the state of stress $\mathbf{S}_{(2)}$ with the reference (2), provided that both states are regarded for the same particle at the same time. For a more detailed explanation of the principle of material objectivity, refer to Ebert [59]; Giesekus [76]; Irgens [102].

Thus, if the principle of material objectivity is valid, the related quantities are called objective quantities – for instance, the stress tensor $\mathbf{S}$ and the deformation tensor $\mathbf{D}$ are objective quantities. Therefore, the relationship between state of stress and state of deformation consists of objective quantities and thus the relationship has to be objective as well – this can only be valid for isotropic fluids, as suggested above as Stokes fourth criterion. Note that the

mentioned criteria can be found in a slightly different formulation in Ebert [59] and Giesekus [76].

Underlying the mentioned assumptions, Reiner [175, 176] found Equation 5.24 for a purely viscous fluid flow.

$$\mathbf{S} = [-p\mathbf{1} + \chi_0] + \chi_1 \mathbf{D} + \chi_2 \mathbf{D}^2 \tag{5.24}$$

Rivlin [191] also discussed this constitutive law, but in the simpler form of Equation 5.25.

$$\mathbf{S} = -p\mathbf{1} + \chi_1 \mathbf{D} + \chi_2 \mathbf{D}^2 \tag{5.25}$$

Equation 5.24 and 5.25, are almost identical, except for the function χ_0. The scalar functions χ_0, χ_1, and χ_2 are related to the properties of the fluid. While χ_0 can be understood as bulk viscosity, χ_1 is connected with the shear viscosity μ and χ_2 with the second normal stress coefficient ψ_2 of the fluid. Hence, Equation 5.25 is valid for neglecting bulk viscosity only and therefore for incompressible fluid flow.

Note that the scalar functions χ_i only depend on the density ρ and so on the temperature θ, as well as on the three principle invariants according to Equations 5.18 to 5.20: $\chi_i = \chi_i(\rho, \theta, I, II, III)$.

Assuming incompressible flow, the bulk viscosity χ_0 and thus the first principle invariant I disappears because of $\mathbf{tr}(\mathbf{D}) = \dot{\varepsilon}_i = 0$. Hence, the remaining scalar functions only depend on the second and third principle invariants, resulting in Equation 5.26 while only considering the extra stress tensor $\mathbf{T}$, as stated in Böhme [21].

$$\mathbf{T} = 2\mu(II, III) \cdot \mathbf{D} + 4\psi_2(II, III) \cdot \mathbf{D}^2 \tag{5.26}$$

Equation 5.26 can easily be transformed into both *generalised Newtonian* and Newtonian fluids. In both cases, only viscous fluid properties are required

and thus ψ_2 disappears. For the latter fluid assumption, the viscosity also has to be a constant and the Newtonian fluid according to Equation 5.2 follows directly from Equation 5.26. It is clear that the Reiner-Rivlin fluid contains the most general formulation of a *generalised Newtonian fluid* as considered in this research work.

Nevertheless, a fluid according to Reiner and Rivlin has never been observed in practical considerations. So this kind of fluid does not have any practical relevance. However, owing to its general formulation of purely viscous fluids and its possibility to be transformed into Newton's fluid, the constitutive law of Reiner and Rivlin is a very important basis, and the fundamental assumptions, mentioned for this type of flow, also have to be valid for the considered flow in the scope of this research topic.

5.2.5. Empirical laws

In the literature, many mostly complex models can be found which describe several types of fluid flow. One of these models is briefly described in Chapter 5.2.4, but there are more complex and more specific models like the Oldroyd or Giesekus constitutive laws. Since these models are associated with enormous expenses in modelling rheological parameters, they are not suitable for practical utilisation. A detailed mathematical description can be found in Böhme [21]; Ebert [59]; Giesekus [76] or Irgens [102], but they will not be discussed here due to their complexity.

For the application of more practical models, many different empirical laws have been presented in the literature to describe the fluid properties for a special but small sub-field of non-Newtonian fluid flow. Hence, they are mostly very appropriate for modelling *generalised Newtonian fluids*. Many of these laws are only valid for a special region of interest and cause severe mistakes when applied outside the intended region. Thus, they have to be applied carefully.

Furthermore, empirical laws were invented to be applied on measurement values, performed in viscometers – for instance, in rotational viscometers, as utilised in the recent research project, see Chapter 9.2. In these measure-

ment devices, a simple shear flow is typically achieved by the geometrical shape and thus the state of the deformation tensor $\mathbf{D}$ can be reduced to a two-dimensional tensor. Because of the symmetry of $\mathbf{D}$, the remaining entries are equal – note that the trace disappears for the *generalised Newtonian fluid flow* as a result of the purely viscous character – and the indices of the shear rate can be omitted. Therefore, instead of the deformation tensor $\mathbf{D}$, the shear rate $\dot{\gamma}$ will be stated in the outlined laws.

In the following, only three well-known models will be explained due to their practical relevance and wide applicability:

Power law approximation

A very simple, but often suitable law is the *power law* according to Equation 5.27. This law is suitable for approximating shear-thinning and shear-thickening fluids as well. Furthermore, for the case of a Newtonian fluid, Equation 5.27 becomes Newton's law. The law is also named Ostwald and de Waele's law after its creators Ostwald [150, 151] and de Waele [49, 50] [177].

$$\tau\left(\dot{\gamma}\right) = k \cdot \dot{\gamma}^{m}$$
$$\mu\left(\dot{\gamma}\right) = k \cdot \dot{\gamma}^{m-1}$$

(5.27)

$$m \begin{cases} < 1, & \text{for shear-thinning fluids} \\ = 1, & \text{for Newtonian fluids} \\ > 1, & \text{for shear-thickening fluids} \end{cases}$$

The model fits the shear-thinning or the shear-thickening region with a simple potential function comprising a factor and an exponent. Both parameters have to be understood as mathematical curve fit parameters rather than as physical material properties. The factor of the regression function is often called consistency and is described by k, while the exponent is named flow index m. The consistency has the dimension $[k] = Pa\,s^{m}$ and depends there-

fore on m, while m itself is dimensionless. For shear-thinning fluids, m is less than 1 but positive, while m is larger than 1 for shear-thickening fluids. As a special case, m becomes 1 for Newtonian fluids.

Owing to the potential character of the regression function, the variable course of the viscosity function becomes a straight line in double-logarithmic diagrams, as can be seen in Figure 5.7b. The validity of the law can be found between the zero-shear-rate-viscosity μ_0 and the infinite-shear-rate-viscosity μ_∞, but excluding both crossover areas. Hence, the *power law* is only valid for a small portion of the characteristics.

A common mistake in this approximation is its application for shear rates out of the region of validity, which leads to over- or underestimation of the apparent viscosity. Thus, the application of Equation 5.27 to a measurement series to identify the parameters k and m must be done very carefully. Including the crossover areas or even the limiting Newtonian viscosity regions into the fitting algorithm[13] may cause significant deviations of the regression curve from the desired measurement region. Figure 5.7 shows such a deviation from the characteristic curve, but note that the deviation shown is quite large due to the clarity of the illustration.

However, most technical fluid flow is in the area of validity and thus this kind of approximation is mostly very suitable [21; 76].

Herschel and Bulkley approximation

Another well-known regression function was formulated by Herschel and Bulkley [96] in 1926. The mathematical formulation of this law is given by Equation 5.28. In principle, the Herschel and Bulkley law is very similar to the *power law*, except for the yield stress τ_0, that is added to the shear stress τ of the function according to Equation 5.27.

$$\tau = \tau_0 + k \cdot \dot{\gamma}^m \quad , \text{resp.}$$
$$\mu = \frac{\tau_0}{\dot{\gamma}} + k \cdot \dot{\gamma}^{m-1} \tag{5.28}$$

Table 5.1. *Parameter range of the Herschel and Bulkley regression, representation based on Ehrentraut [61]*

fluid character	τ_0	m
shear-thinning	$= 0$	< 1
Newtonian	$= 0$	$= 1$
shear-thickening	$= 0$	> 1
visco-plastic	> 0	< 1
Bingham-plastic	> 0	$= 1$

The consideration of the yield stress τ_0 enables the *power law* not only to approximate shear-thinning and shear-thickening fluids, besides Newtonian fluids, but also the plastic fluid flow. Table 5.1 shows the five different fluid characteristics the Herschel and Bulkley law is able to approximate, together with each parameter range of the yield stress τ_0 and the flow index m respectively. Note that the Bingham-plastic fluid is characterised by a constant and thus by Newtonian viscosity, but the fluid has to be treated as a solid if the shear stress remains lower than τ_0.

Owing to the strong relationship between the *power law* and Herschel and Bulkley's law, the advantages and disadvantages are also very similar, and this model has to be understood as a mathematical curve fit as well.

Carreau approximation

As outlined above, power laws come with the problem of non-physical predictions for the region of the zero-shear-rate-viscosity μ_0 and the infinite-shear-rate-viscosity μ_∞. Carreau [32] solved this problem by including both parameters in a new approach. This approach was intensively investigated [23; 33; 34] and enhanced by Yasuda [244]. The Carreau-Yasuda approximation is given by Equation 5.29.

$$\mu = \mu_\infty + (\mu_0 - \mu_\infty)\left[1 + (\lambda \cdot \dot{\gamma})^a\right]^{\frac{m-1}{a}} \qquad (5.29)$$

Here, the time-related parameter λ and the two dimensionless parameters a and m are included alongside the mentioned Newtonian parameters μ_0 and μ_∞. While the time-related value λ and the dimensionless parameter m are characteristic values for the considered fluid, the parameter a is often set to 2 (referred to as the Bird and Carreau approximation in this form). Only with the Yasuda enhancement does Carreau's approximation become Equation 5.29. In this case, a influences the starting point of the first crossover region and thus is sometimes referred to as stiffness.

As can be seen in Figure 5.7, Carreau's approximation fits the character of a shear-thinning fluid better than the *power law* or the Herschel and Bulkley regression, and hence, this law should be applied preferentially. However, the law consists of five parameters which have to be determined for each fluid. The measurement of both the zero-shear-rate-viscosity μ_0 and the infinite-shear-rate-viscosity μ_∞ are particullary challenging because of the wide shear-rate range that exists between both values. Typically, this range extends over several decades, and different measurement principles have to be utilised to measure both values. Therefore, the *power law* according to Equation 5.27 is preferred to the Carreau approximation.

It should be mentioned that further empirical laws have been established in the literature, such as the approximations according to Ree and Eyring[14], Cross[15] or Casson[16] and many more, see Böhme [21], Mezger [135] or Irgens [102]. Mostly, these regression functions were defined for very special fluids or applications, and thus, they are neither utilised nor explained in this work.

Table 5.2 summarises all mentioned research-relevant fluid models with their mathematical formulation and the area of their application.

Table 5.2. *Laws to model pure viscous fluid flow*

Model	Equation	Type
Reiner-Rivlin	$\mathbf{T} = \chi_1 \mathbf{D} + \chi_2 \mathbf{D}^2$	theoretical
Newton	$\tau = \mu \dot{\gamma}$	ideal
Power law	$\mu = k \cdot \dot{\gamma}^{m-1}$	nonlinear
Carreau-Yasuda	$\mu = \mu_\infty + \dfrac{\mu_0 - \mu_\infty}{\left[1 + (\lambda \cdot \dot{\gamma})^a\right]^{\frac{1-m}{a}}}$	nonlinear
Herschel and Bulkley	$\mu = \dfrac{\tau_0}{\dot{\gamma}} + k \cdot \dot{\gamma}^{m-1}$	plastic

5.3. Similarity mechanics

As a major part of this research project, the profile polar curves of non-Newtonian fluid flow of different profiles will be investigated and stored in a polar database, see Chapter 7.2. Subsequently, the most sufficient profile will be selected for specific operation conditions by comparing the polar curves with each other. Unfortunately, the polar curves cannot be compared in their dimensional form and thus the concept of similarity mechanics is necessary.
The field of similarity mechanics goes back to the work by Buckingham [29], which was published in 1914 and is not only important for the mixing of non-Newtonian fluid flow. Typically, the method is named Buckingham's theorem after its creator.
However, in the scope of this research work, this theory need only be applied to the mixing of the non-Newtonian fluid flow in principle. But owing to the challenging nature of the non-Newtonian character of the considered fluid flow, the method will not only be applied, but briefly introduced by way of an example related to mixing. For more details, refer to the original publication of Buckingham [29] or, for instance, to Pawlowski [155], Spurk [216] and Zlokarnik [247].

5.3.1. Introduction to Buckingham's theorem

Figure 5.10 shows a random mixing vessel with a vertically aligned shaft. The shaft is connected to an engine that requires the power P to drive the shaft at the speed n. At the end of the shaft, a mixing unit is installed. The diameter of the mixing unit is given by D_{P}, while the vessel's diameter amounts to D. The depicted mixing process is designed to agitate a fluid characterised by the density ρ and the dynamic viscosity μ. The free surface of the mixed fluid is located in the height H_{F} and is influenced by the gravity g. Altogether, eight quantities are found to describe the mixing process.

The principle of Buckingham's theorem is that every problem, comprising an arbitrary amount of quantities $\mathfrak{X}_{\mathrm{k}}$, is connected by its dimensions. In the mentioned example, an amount of $k = 8$ quantities describes the problem, but it is more general to consider $k = 1, 2, 3, \ldots, n_{\mathrm{z}}$. Owing to the connection of these quantities, they can also be written in relation to each other, as proved by Equation 5.30.
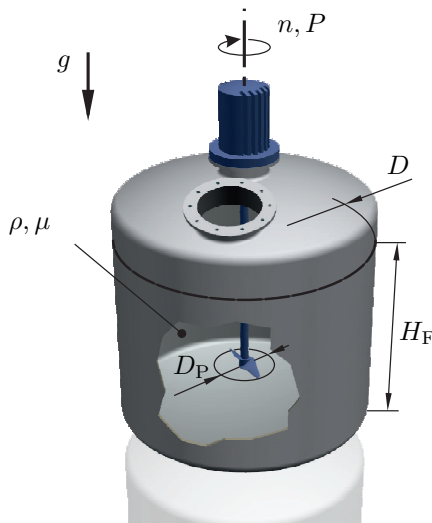
Figure 5.10.   *Relevant quantities of a mixing process*

$$f\left(\underline{\mathfrak{X}}_k\right) = f\left(\mathfrak{X}_1, \mathfrak{X}_2, \ldots \mathfrak{X}_{n_z}\right) = 0 \tag{5.30}$$

The quantities $\mathfrak{X}_k$ are gathered in the subset $\underline{\mathfrak{X}}_k$ and can be separated into two further nonempty subsets: the first subset only contains quantities with dimensions that are linearly independent – named $\underline{\mathfrak{X}}_i$ – while the dimensions of the entities of the second subset linearly depend on the first subset. The second subset is given by $\underline{\mathfrak{X}}_j$. Next, the relationship according to Equation 5.30 can be reformulated and results in Equation 5.31.

$$f\left(\underline{\mathfrak{X}}_i, \underline{\mathfrak{X}}_j\right) = 0 \tag{5.31}$$

Considering the dimensions of each quantity, the potential relationship according to Equation 5.32 has to be valid due to the linear dependence of $\underline{\mathfrak{X}}_j$ on $\underline{\mathfrak{X}}_i$. Note that the exponent p_{ij} is taken from the dimensional matrix, as discussed by Pawlowski [155], see Equation 5.34.

$$\text{Dim}\left(\underline{\mathfrak{X}}_j\right) = \prod_i \left(\text{Dim}\left(\underline{\mathfrak{X}}_i\right)\right)^{p_{ij}} \tag{5.32}$$

Then, the relationship of Equation 5.33 can be found, as stated by Pawlowski [155].

$$\pi_j = \mathfrak{X}_j \prod_i \mathfrak{X}_i^{-p_{ij}} \tag{5.33}$$

Pawlowski [155] also described a vivid formulation based on the consideration of $\underline{\mathfrak{X}}_k$ as a dimensional matrix. As was shown in Equation 5.31 for the set $\underline{\mathfrak{X}}_k$, the dimensional matrix can also be divided into two matrices: the core matrix containing the entities of $\underline{\mathfrak{X}}_i$ and the residual matrix with the linearly dependent $\underline{\mathfrak{X}}_j$ entities.

$$
\begin{array}{c|cc}
 & \underline{\mathfrak{X}}_{\mathrm{i}} & \underline{\mathfrak{X}}_{\mathrm{j}} \\
\hline
\mathrm{Dim}(\mathfrak{X}_1) & 1 & \\
\vdots & \ddots & p_{\mathrm{ij}} \\
\mathrm{Dim}(\mathfrak{X}_r) & \quad 1 &
\end{array}
\tag{5.34}
$$

Pawlowski [155] suggests organising the quantities $\mathfrak{X}_{\mathrm{i}}$ and $\mathfrak{X}_{\mathrm{j}}$, respectively, as columns of the dimensional matrix. Thus, the number of rows is given by the number of the dimensions of the quantities – in Equation 5.34 given by r. The total number of rows was chosen as n_{z}. Since the core matrix is a square matrix, the number of rows is also r. Hence, the number of rows of the residual matrix is $m_{\mathrm{z}} = n_{\mathrm{z}} - r$. This means that a number of m_{z} dimensionless π quantities can be identified by applying Buckingham's theorem. As can be read in Pawlowski [155], the core matrix must be transformed into the unity matrix before applying Equation 5.33 – this is already performed in Equation 5.34.

$$
\begin{array}{c|ccc|ccccc}
 & \rho & D_{\mathbf{P}} & n & \mu & P & g & H_{\mathbf{F}} & D \\
\hline
\mathbf{M} & 1 & 0 & 0 & 1 & 1 & 0 & 0 & 0 \\
\mathbf{L} & 0 & 1 & 0 & 2 & 5 & 1 & 1 & 1 \\
\mathbf{T} & 0 & 0 & 1 & 1 & 3 & 2 & 0 & 0
\end{array}
\tag{5.35}
$$

When applying Pawlowski's approach to the mixing task of Figure 5.10, Equation 5.35 follows, when selecting the density ρ, the diameter of the propeller D_{P}, and the shaft speed n to set the linearly independent SI-dimension system comprising mass (**M**), length (**L**), and time (**T**). Note that Equation 5.35 obtains the unity matrix for the core matrix $\underline{\mathfrak{X}}_{\mathrm{i}}$.

As explained, $m_{\mathrm{z}} = 5$ dimensionless π quantities can be found for the considered example, as can be found in Equations 5.36a to 5.36e. These quantities fully describe the characteristics of the considered example. Since π_4 and π_5

only describe geometrical ratios, they will not be considered due to the requirement for fixed geometry. Moreover, π_3 can be transformed into Froude's number, which does not influence the power of a mixing process [247], at least for low-Re flow [196; 197], as considered here and only π_1 and π_2 are assumed to influence the mixing process.

$$\pi_1 = \frac{\mu}{\rho\, D_\mathrm{P}^2\, n} \tag{5.36a}$$

$$\pi_2 = \frac{P}{\rho\, D_\mathrm{P}^5\, n^3} \tag{5.36b}$$

$$\pi_3 = \frac{g}{D_\mathrm{P}\, n^2} \tag{5.36c}$$

$$\pi_4 = \frac{H_\mathrm{F}}{D_\mathrm{P}} \tag{5.36d}$$

$$\pi_5 = \frac{D}{D_\mathrm{P}} \tag{5.36e}$$

Equation 5.36a can be transformed into Equation 5.37 through inversion and results in the Reynolds number Re. This quantity is crucial to this research work and thus the Reynolds number will be discussed in detail in Chapter 5.3.2 and 5.3.3.

The remaining π quantity according to Equation 5.36b is commonly known as the Newton number Ne; it gives the dimensionless power of the considered mixing process.

5.3.2. Common Reynolds number calculation

In 1883, Reynolds published the relationship which is nowadays known as the Reynolds number Re [183; 184]. Reynolds studied the development of eddies in the pipe flow by performing experimental investigation with dye filaments that are applied to the flow through a trumpet-shaped inlet. As one of the consequences of his effort, Reynolds found Equation 5.37.

$$Re = \frac{\rho\, v\, L}{\mu} \tag{5.37}$$

Equation 5.37 quantifies the ratio of the inertia force $F = \dot{m}\, v$ and the friction force $F = \mu\, \frac{v}{L}\, A$. A further fact, discovered by Reynolds [183], is that pipe flow is always laminar for $Re < 2300$, otherwise the flow becomes transitional and finally turbulent. As elucidated by Rott [192] and also by Eckhardt [60], Reynolds already assumed that the critical value $Re = 2300$ can be raised for ideal conditions.

The Reynolds number is mostly very suitable for identifying influences caused by friction in the fluid flow. Unfortunately, the Reynolds number is a function of the dynamic viscosity μ and μ is not defined for non-Newtonian fluid flow. Thus, the Reynolds number according to Equation 5.37 is not appropriate for application in this research project and an alternative concept has to be identified to investigate and analyse the characteristics of friction in the fluid flow considered here.

5.3.3. Rheological adjusted Reynolds number

As mentioned, to specify the flow character, the Reynolds number according to Equation 5.37 is not suitable here, but some studies of the flow character of the non-Newtonian fluid flow, as well as the investigation of representative Reynolds numbers, based on the apparent viscosity instead of the Newtonian dynamic viscosity, can be found in the literature.

One of the first investigations was performed by Metzner and Reed [132] in 1955, and it was based on the fluid-independent formulation of the shear rate, discovered by Rabinowitsch [168] and Mooney [137]. An alternative suggestion was found by Chhabra and Richardson [38], which is based on the considerations of the shear rate of a *power law* fluid, elucidated by Coulson et al. [44]. Both definitions can be transformed into each other because both are derived from a pipe flow problem and are related to the assumption of the validity of the friction factor $f = 16/Re$ for both Newtonian and non-Newtonian

fluid flow.

Besides the mentioned concepts, other definitions have been presented in the literature, such as those by Rudman et al. [194], Güzel et al. [82], and Haldenwang et al. [86]. Since Haldenwang et al. emphasised the definition of Metzner and Reed as the most convenient, only the definition by Chhabra and Richardson known from the literature will be applied in this work because it is identical to Metzner and Reed's definition. Additionally, a representative Reynolds number will be derived by applying Buckingham's π theorem.

Note that Kluck [115] also found the definition of a representative Reynolds number by theoretical considerations of a propeller flow problem. Kluck started with the consequent dimensional analysis of all relevant parameters of an arbitrary mixing task. For this, the method is only suitable for this kind of mixing task, but not for a single radial section, such as the profiles considered in Chapter 7.2. So, Kluck's definition will not be explained here, though the definition could be suitable for the finally designed propeller mixer; the definition, however, is not convenient for the design process.

Reynolds number according to Chhabra and Richardson

The Reynolds number according to Chhabra and Richardson [38] can be introduced by Equation 5.38.

$$Re_{\mathrm{CR}} = \frac{\rho \cdot v^{2-m} \cdot L^m}{8^{m-1} \cdot k \cdot \left(\frac{3 \cdot m + 1}{4 \cdot m}\right)^m} \tag{5.38}$$

As already outlined, the Reynolds number according to Chhabra and Richardson is based on pipe flow problems. In its original form, the characteristic length is given as diameter. But owing to the application on flow profiles here, the characteristic length L in Equation 5.38 is given by the chord length l.

To derive the representative Reynolds number, Chhabra and Richardson analysed the velocity distribution and the shear rate in a pipe, and found a function for the axial velocity, depending on the flow index m of the considered
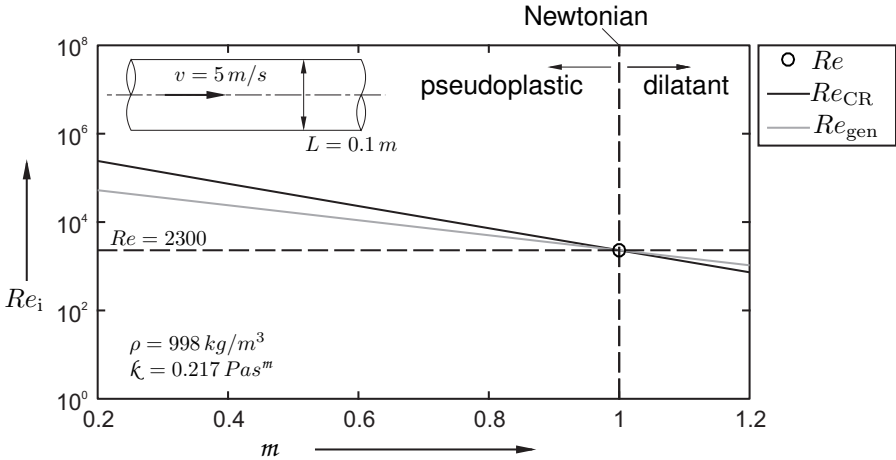
Figure 5.11. *Differences in the definition of the Reynolds number according to Equations 5.37, 5.38, and 5.41, shown for an exemplarily chosen pipe flow problem with the conditions:* $v = 5\,m/s$, $L = 0.1\,m$, $\rho = 998\,kg/m^3$ *and* $k = 0.217\,Pas^m$

fluid. By integrating this function over the pipe radius and including the pressure gradient, the mean velocity of the flow depends on friction factor results. The procedure is nearly identical to the work of Hagenbach [85] which is based on the research on laminar pipe flow by Hagen [83, 84] and Poiseuille [163]. Assuming the identity of $f = 16/Re_{\mathrm{CR}}$ leads to Equation 5.38.

Because of the similarity of the above derivation to the approach of Hagen's and Poiseuille's law, the procedure of Chhabra and Richardson is logical and very clear. But the general fundamentals of Chhabra and Richardson's definition are related to a pipe flow problem. So, since Chapter 7.2 discusses the flow around a profile, another physical task is analysed. Errors in similarity have to be accepted while applying Equation 5.38.

Nevertheless, assuming identical fluid flow in the far field, Chhabra and Richardson's Reynolds number may be applied, but it is necessary to compare the Reynolds number of several operating points with each other. In this case, the comparison turns occurring errors to systematic errors.

Note that the change of the definition of the Reynolds number will result in values that are not easily to be compared with the original definition by

Reynolds. In Figure 5.11, an exemplarily chosen pipe flow problem is shown to have compared the differences of both definitions. While the velocity v, the characteristic length L, the density ρ, and the consistency k – the latter eventually becomes the dynamic viscosity μ for Newtonian fluids – were set to be constant, the value of the flow index m was varied. As can be seen, for $m = 1$, the definition given by Chhabra and Richardson [38] becomes the origin definition. The course of the Reynolds number is over-predicted for $m < 1$ and under-predicted for $m > 1$.

Generalised Reynolds number

In Chapter 5.3.1, Buckingham's π theorem was introduced. Since this theorem was conceived to derive dimensionless numbers to characterize a problem and also because of the simple derivation of the Reynolds number, while applying this theorem (see Equation 5.36a), it is a logical consequence to also apply the π theorem for non-Newtonian fluid flow around a profile. The more complex the method to model the fluid, the more challenging the application of the mentioned theorem. Fortunately, a very convenient, simple fluid model was introduced in Chapter 5.2, which can in practice mostly be reduced to a *power law* fluid. Thus, the application of Buckingham's theorem is quite simple.

A flow problem, shown in Figure 5.12, leads to the lifting force F at the profile, prompted by the velocity v and the dimensional matrix according to Equa-
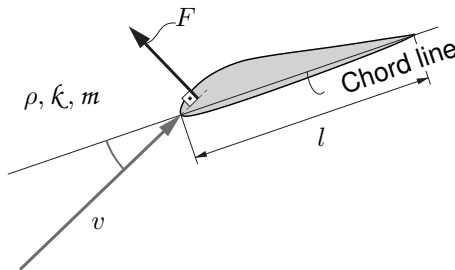
Figure 5.12. *Relevant quantities at an airfoil*

tion 5.39 results when applying the π theorem.

	ρ	l	v	k	m	F
M	1	0	0	1	0	1
L	0	1	0	m	0	2
T	0	0	1	$2 - m$	0	2

(5.39)

From Equation 5.39, three independent and dimensionless numbers can be identified, see Equation 5.40. In Equation 5.40, π_1 is the inverse of the representative Reynolds number which can be calculated by the π theorem. π_2 is identical to the flow index m of the considered fluid and hence the flow index itself is a dimensionless number to characterize the problem. In fact, the non-Newtonian character of the problem is described by m: the closer m is to 1, the less non-Newtonian fluid behaviour while the fluid becomes Newtonian for $m = 1$. The third π entity characterises the lifting force of the flow problem.

$$\pi_1 = \frac{k}{\rho \cdot l^m \cdot v^{2-m}}$$
(5.40a)

$$\pi_2 = m$$
(5.40b)

$$\pi_3 = \frac{F}{\rho \cdot l^2 \cdot v^2}$$
(5.40c)

Equation 5.41 gives the definition of the Reynolds number, calculated by the theorem.

$$Re_{\text{gen}} = \pi_1^{-1} = \frac{\rho \cdot l^m \cdot v^{2-m}}{k}$$
(5.41)

In keeping with the definition given by Chhabra and Richardson, Equation 5.41 is applied on the chosen pipe flow problem to demonstrate the differences in calculation results, see Figure 5.11. As can be seen, the principle devia-

tion of Equation 5.41 from the original definition is the same as derived from the definition given by Chhabra and Richardson, but the deviations are less pronounced.

In Equation 5.40, substituting the velocity magnitude v by the maximum circumferential velocity $u_{\max}/\pi = n \cdot D_{\mathrm{P}}$ at the propeller and the chord length l by the diameter of the propeller D_{P}, the problem is directly transformed into a mixing task and Equation 5.42 follows.

$$Re_{\mathrm{gen,P}} = \pi_1^{-1} = \frac{\rho \cdot D_{\mathrm{P}}^2 \cdot n^{2-m}}{k} \tag{5.42a}$$

$$m = \pi_2 \tag{5.42b}$$

$$Ne = \pi_3 \cdot \frac{u_{\max}}{u_{\max}} = \frac{P}{\rho \, D_{\mathrm{P}}^5 \, n^3} \tag{5.42c}$$

Owing to the general use of the representative Reynolds number derived by Buckingham's theorem the Reynolds number according to Equations 5.41 and 5.42a is defined here as the *generalised Reynolds number*.

Notes

[1] The parallel assembly of damping and spring elements leads to a viscoelastic body, instead of a viscoelastic fluid and is called a Kelvin-Voight body. Because this is not relevant for fluids, it is not considered here. Details can be found in Ebert [59]; Giesekus [76]; Irgens [102]; Phan-Thien [159]

[2] The product of the frequency ω and the relaxation time λ is utilised to scale the abscissa of Pipkin's diagram. The product can be interpreted as the Deborah number $De = \omega \cdot \lambda$.

[3] In Pipkin's diagram, the region of viscometric flow is the region of interest in this thesis.

[4] To approximate the linear viscoelastic flow, models which are more detailed and even more complex than Maxwell's model can be applied. Refer to Giesekus [76] for details.

[5] Overlooking elasticity may be mistaken for moulding processes with macromolecule melts. In the scope of the present work, only water-based liquids are of interest and it is sufficient to assume a purely viscous fluid flow. This assumption is also proven in Chapter 9.1 for the applied model fluids.

[6] The scope of this research is related to non-ideal but pure viscous fluid flow.

[7] Because other rheological effects are not considered, other than the state of deformation, the expression *shear viscosity* is reduced to *viscosity* from this point due to the uniqueness of the expression.

[8] In this thesis, only time-independent fluid flow is considered. For a detailed discussion of time-dependent effects, refer to Ebert [59], Giesekus [76] and Irgens [102]

[9] Utilised model fluids refer to the approach of entangled slender particles, while the modelled fluids of biogas and waste-water treatment plants refer to the approach of hydrate shells, see also Chapter 9.2 for a detailed description of the applied test fluids.

[10] The principle invariants of the deformation tensor $\mathbf{D}$ always remain the same, even when changing the reference of the tensor.

[11] In the discussion of the state of stress, compressibility is often neglected, as has also been done in this thesis. Taking compressibility into account, the bulk viscosity has to be considered, see e.g. Giesekus [76].

[12] The Reiner-Rivlin fluid goes back to an idea, suggested by Stokes, but Stokes only formulated a linearised model [76]. However, sometimes this kind of fluid is also called Stokes liquid.

[13] The approximation of the viscosity function is calculated by empirical models. The method of least squares is commonly applied to calculate the regression parameters of these models.

[14] As an alternative for the *power law*, the Ree and Eyring function is also suitable for non-plastic fluids.

[15] To approximate fluids with zero-shear-rate-viscosity μ_0 and infinity-shear-rate-viscosity μ_∞, the model by Cross can be applied instead of the approximation by Carreau.

[16] Casson's empirical law was developed for printing ink, but it is also recommended for chocolate melts [135].

6. Introduction to jet theory

As outlined in Chapter 3.2, *blade element momentum theory* can only be applied to design a propeller while setting the velocity of the propeller plane, taken from *axial momentum theory*, as the absolute velocity at a blade element according to *blade element theory*. Thus, the inflow velocity into the stream tube should be known to calculate the absolute velocity at the blade element. However, *blade element momentum theory* regards the propulsion of an airplane or a ship. So, by changing the kinematics, the inflow condition, as illustrated in Figure 3.6, is known, but not so in the considered case of a fixed installed propeller mixer.

For mixing tasks, this gap can be closed by considering the mass flow rate carried by the propeller mixer. Hence, this parameter can be required as the inlet parameter of the design process – this is in line with the common mixing tasks, as mentioned in Chapter 2.1. Though this assumption leads to a mean velocity, a more detailed knowledge of the velocity distribution is desired, especially because the jet generated by the propeller will accelerate the surrounding fluid, thereby leading to an increase in the carried mass flow at the outflow of the stream tube.

Hence, jet theory is essential for the considered mixing task of a propeller mixer. The necessary basics will be discussed in this chapter. Initially, the general theory of a turbulent jet, as first elaborated by Tollmien [223], will be briefly discussed in Chapter 6.1. Chapter 6.2 will explain the semi-empirical jet theory for propeller propulsion, as investigated by Oebius [146, 147], in detail.

In both concepts, the geometric characteristics of the jet are similar. Hence, before discussing the theoretical approaches, the geometrical characteristics are shown by Figure 6.1.

As can be seen in the figure, a fluid flowing out of a gap with an opening length of b causes a diverging jet. If the direction of divergence is equal to the direction of propagation, the divergence is approximately linear and can be extrapolated backwards to a virtual origin. The jet is initialised in the flow development region. Here, a core is located with constant velocity conditions.
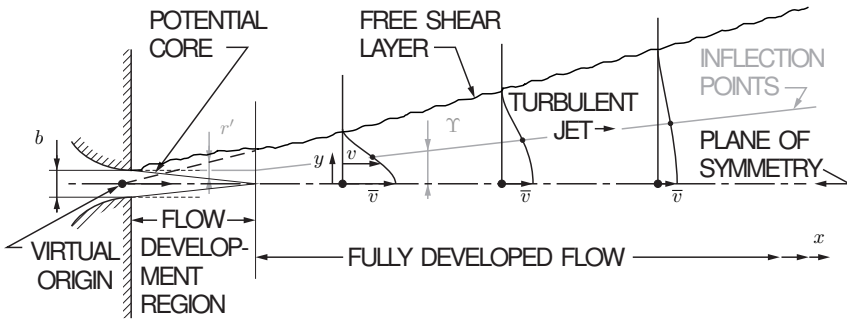
Figure 6.1. *Definition sketch of plane turbulent jets, author's own representation based on Rajaratnam [169]*

After this zone, the fully developed flow region is connected. Outside the core of the initial zone and in the fully developed flow region, the velocity distribution can be approximated by a Gaussian curve.

6.1. General theory

In the literature, many studies on jet theory can be found, e.g. Zimm [245], Tollmien [223], Schlichting [200], Andrade [6]; Andrade and Tsien [7], Görtler [81], Reichardt [174], Rajaratnam [169], Vollmers and Rotta [231], and Schlichting and Gersten [201].

These studies mostly consider a turbulent jet, but a jet may even be laminar [200]. Nevertheless, only the turbulent jet theory will be discussed here – it was first investigated by Tollmien [223]. The decision to only consider the turbulent propagation of a jet is based on the very low values for the critical Reynolds number of $Re = 30$ for the flow characteristics of a jet [201][1].

To outline the theoretical background, the basic concept will be discussed below. Since the theory by Oebius [146] utilised in this research project applies another approach, the description of the general jet theory is only superficial in nature and only a brief overview is provided.

In principle, all jet studies start with the boundary equations in the direction of propagation, mostly given by x, as depicted in Figure 6.1. Owing to the rel-
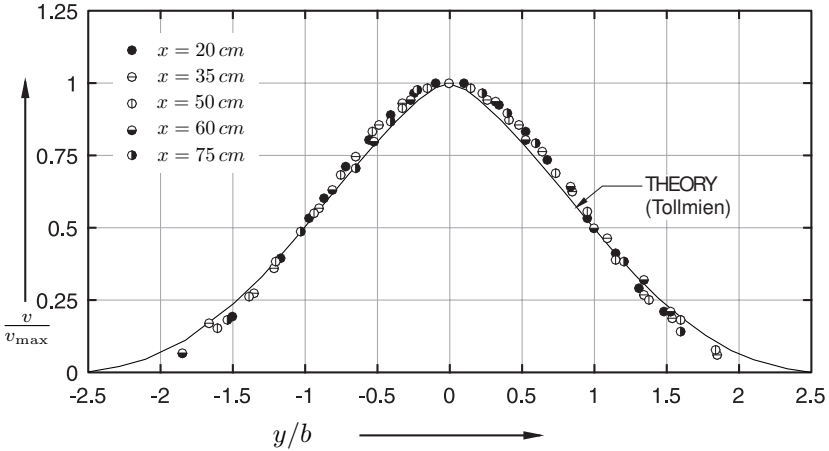
Figure 6.2. *Dimensionless velocity distribution of a plane jet, author's own representation based on Rajaratnam [169] and Förthmann [65]*

ative low velocity of a jet, the pressure can be neglected in a first evaluation, and the boundary equations result in Equation 6.1.

$$v_{\mathrm{x}} \frac{\partial v_{\mathrm{x}}}{\partial x} + v_{\mathrm{y}} \frac{\partial v_{\mathrm{x}}}{\partial y} = -\frac{1}{\rho} \frac{\partial p}{\partial x} + \frac{1}{\rho} \frac{\partial \tau_{\mathrm{xy}}}{\partial y} \tag{6.1}$$

To calculate the derivative of shear stress $\partial \tau_{\mathrm{xy}}/\partial y$ in Equation 6.1, Tollmien applied the apparent shear stress assumption of Boussinesq [26], in combination with the theory of the mixing length formulated by Prandtl [166]. But other procedures for considering turbulence were also applied, such as the utilisation of the $k\text{-}\epsilon$ turbulence model by Jones and Launder [106].

Subsequently, a potential flow consideration is applied to derive the equations of motion. Depending on the different assumptions of the studies and the different investigated geometrical cases, the equations of motion differ from one theoretical approach to another, see Tollmien [223] and Görtler [81]. Afterwards, a momentum balance is carried out and the velocity distribution is derived. As a result, Tollmien [223] obtained a Gaussian curve, see Figure 6.2. Note that similar results were found in every study mentioned

above.

The theoretical consideration by Tollmien was validated experimentally by Förthmann [65]. In Figure 6.2, the results of this study are drawn too. Förthmann performed experimental investigations for different distances between $x = 20\,cm$ and $x = 75\,cm$. It should be noted that Figure 6.2 shows the normalised velocity distribution. For normalisation, the velocity v is divided by its maximum value of v_{max} at each considered x position, while the y coordinate is divided by the opening length of the gap b. Owing to the normalisation, all experimental results can be approximated in good agreement with the theoretic curve by Tollmien, and for the following, the assumption of a Gaussian curve for the velocity distribution is in line with the analytical approaches.

6.2. Jet theory for propeller propulsion

The fundamentals of jet theory, as described above, are not appropriate for defining the velocity distribution in the wake of a propeller. Because of propeller propulsion, the momentum is not unidirectional and evenly distributed, as in the case of a homogeneous jet out of a gap. The theoretical consideration of a jet, generated by a marine-type propeller with subsequently performed experimental validation, as investigated by Oebius [146][2], can remedy the previously mentioned problem of the general jet theory. This theory will be explained below.

6.2.1. Introducing the assumptions

Even though *blade element momentum theory* is a proven method of designing a propeller, the method is not suitable for calculating the velocity distribution in the wake. By observing jets from marine-type propellers, Oebius found that this kind of jet diverges immediately after passing the propeller plane, but the fundamentals of *blade element momentum theory* predict contraction due to acceleration of the fluid. Hence, Oebius started his investigations by considering a rotational jet and by analysing the analogies between this jet and a propeller jet.

Based on the analogies between both types of jets, he proposed several assumptions to derive the jet theory for propeller propulsion, such as

- the decrease in kinetic energy with the propagation of the jet due to friction,

- the equality of momentum for every cross-sectional plane because of negligible differences in pressure and

- the presence of an additional entrainment mass flow rate accelerated by the free turbulent shear-layer of the jet.

Finally, he concluded that the velocity distribution in a propeller jet and the geometrical characteristics of its propagation have to be similar to those for general turbulent jets, as shown in Figure 6.1. He therefore expected a Gaussian curve and formulated Equation 6.2 as the general form of velocity distribution[3].

$$v\left(x,r\right) = v_{\mathrm{max}} \exp\left(-\frac{1}{2}\left(\frac{r'}{\Upsilon}\right)^2\right) \tag{6.2}$$

In principle, Equation 6.2 is the mathematical definition of an arbitrary Gaussian curve adapted to a propeller jet. Thus, the factorisation of the base of the Gaussian distribution is given by the maximum velocity v_{max} of a considered cross-sectional plane in the x direction, while the exponent is multiplied by $1/(2\,\Upsilon^2)$. The function Υ is auxiliary. In the initial region, Υ is identical to Υ_{Co} and corresponds to the length between the inflection point of the velocity distribution on the considered x plane and the outer diameter of the potential core. In the fully developed region, Υ is given by Υ_{Dev} and is equal to the distance between the inflection point and the symmetry axis. The variable quantity r' of the considered section is given by the distance between the outer shape and the potential core in case of the initial region and the symmetry axis for the fully developed zone, respectively. In Figure 6.1, the mentioned functions and variables are illustrated.

Based on the assumptions, as required above, Oebius claims that the general form of Equation 6.2 is valid for all fluids, provided that the density is similar. This is also in agreement with R. E. Froude [67], who remarked in 1889 that propulsion depends only on inertia forces due to fluid acceleration. This is an important point for this research project, see also Chapter 7.1.1, and thus, the theoretical background of this claim has to be discussed in more detail:

It is obvious that turbulence affects the generation of the jet considered here – this is the fundamental recognition which led Tollmien to the utilisation of the boundary layer equations, even though the problem is that this does not include a wall, only free and turbulent shear layers in a surrounding fluid. The critical Re number is quite low, and thus, a turbulent jet can be assumed in most cases, allthough Schlichting [200] outlined the existence of laminar jets. In turbulent processes, the apparent turbulent viscosity is much larger than the molecular viscosity, and hence, the latter is negligible. Since turbulence comes with momentum transport perpendicular to the main direction of the fluid flow, inertia forces have to be of major relevance. Thus, differences in density are much more important than differences in viscosity.

Hence, for fluids with similar density, a similar solution according to Equation 6.2 can be expected.

6.2.2. Universal law of propeller jets

In a further step, Oebius adapted the general law for propeller flow according to Equation 6.2. To do this, he first identified the differences in both jet types:

- Instead of a single momentum, starting at the outflow, several origins of various momentums are generated by a propeller. Each blade generates a single momentum, which additionally depends on the number of revolutions of the propeller.

- Rotational acceleration may cause radial velocity components.

- The action-reaction law will cause swirl in the wake, and hub and tip-vortices will be generated.
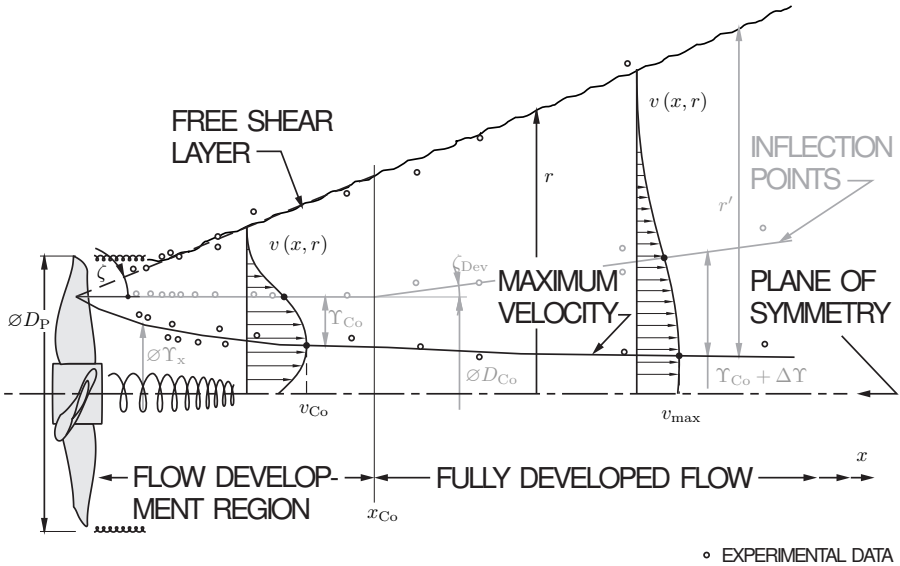
Figure 6.3. *Schematic view of the geometry of a propeller jet for undisturbed and free-moving flow conditions, author's own representation based on Oebius [146]*

However, many characteristics of both types of jets are similar. For propeller propulsion, the jet can also be separated into two zones, see Figure 6.3, for a schematic view.

A flow-development region can be observed, which reaches from the propeller plane to x_{Co} in the x direction. Within the core of this region, the maximum velocity v_{max} is equal to the maximum velocity of the propeller plane. It must be mentioned that the point of maximum velocity is not equal to the outer radius, but to the point of maximum circulation on the blade as given by D_{Co}. Therefore, the variation of this point for different propellers is possible. As mentioned before, the divergence of the jet can be observed immediately on the propeller plane. The divergence is approximately linear and described by the divergence angle ζ according to Equation 6.3.

$$\tan \zeta = \frac{r - D_{\text{Co}}/2}{x_{\text{Co}}} = C_1 \tag{6.3}$$

Oebius also recognised that the location of the maximum velocity, starting with the maximum velocity on the propeller plane at the position D_{Co}, converges degressively with the propagation of the jet. While the starting point D_{Co} and the diameter Υ_{x} both depend on the geometry, the differential quotient $\Delta\Upsilon_{\text{x}}/\Delta x$ was found by Oebius to be a universal law, see Equation 6.4. The function Υ_{x} matches the distance between the course of the location of the maximum velocity and the symmetry axis, as depicted in Figure 6.3.

$$\frac{\Delta\Upsilon_{\text{x}}}{\Delta x} = f(x, r) = C_2 \tag{6.4}$$

In contrast to the rotational jet, as considered in the assumptions of Oebius's theory, for the propeller jet, the distance r' is defined as the length between the turbulent shear layer and the course of the point of the maximum velocity. Thus, Equation 6.5 can be found for r'.

$$r' = r - \frac{\Upsilon_{\text{x}}}{2} \tag{6.5}$$

Owing to the dependence of Υ_{x} on the course of the points of the maximum velocity, the distance between inflection points and points of maximum velocity Υ_{Co} is also a changing function – as given in Equation 6.6 – though the course of the inflection points does not change in the initial region.

$$\Upsilon_{\text{Co}} = \frac{D_{\text{Co}}}{2} - \frac{\Upsilon_{\text{x}}}{2} = f(\Upsilon_{\text{x}}) \tag{6.6}$$

As a final important parameter of the initial region, Oebius defined the length of the initial region x_{Co} as universal, but it depends on the diameter D_{Co}, see Equation 6.7.

$$x_{\mathrm{Co}} = f\left(D_{\mathrm{Co}}\right) \tag{6.7}$$

Behind the initial region, the zone of the fully developed flow is connected. This region is characterised by a further divergence of the jet. While the angle of divergence ζ is still constant, the course of the inflection points of velocity distribution diverges with the angle ζ_{Dev} in keeping with Equation 6.8.

$$\tan \zeta_{\mathrm{Dev}} = \frac{\Delta \Upsilon}{x - x_{\mathrm{Co}}} \tag{6.8}$$

Hence, the distance $\Delta \Upsilon$ must be added to the auxiliary function Υ_{Co} to take the further divergence into account. Finally, Υ_{Dev} is found for the fully developed zone, as given in Equation 6.9.

$$\Upsilon_{\mathrm{Dev}}\left(x\right) = \Upsilon_{\mathrm{Co}} + \Delta \Upsilon = C_3 \tag{6.9}$$

6.2.3. Semi-empirical law of propeller jets

To adapt the general law according to Equation 6.2 on propeller propulsion, and to estimate the constant parameters of the specifications according to Equations 6.3 to 6.9 , Oebius performed an experimental study. He investigated eight different marine-type propellers with differing geometrical parameters. Within this study, the diameter of the propellers varied from $D_{\mathrm{P}} = 103.6\,mm$ to $150.4\,mm$ – the hub diameter ratio $D_{\mathrm{P}}/D_{\mathrm{Hub}}$ was mostly between 5 and 6, but also 4 for some propellers. In addition to the diameter, Oebius varied the number of blades of the utilised propellers from $n_{\mathrm{z}} = 3$ to 5 to obtain a broad field of geometrical variations and to prevent influences due to geometry. The considered revolution speed of the propellers was changed in four variations from $n = 375\,min^{-1}$ to $1250\,min^{-1}$. To measure the velocity distribution in different axial distances, at least 10 planes between $35\,mm$ and $1500\,mm$ downwind from the propeller plane were chosen. The utilised

velocity measurement was performed by traversing a pitot-static tube. As an extract of the experimental data, selected results are shown in Figure 6.3 and Figure 6.4.

The experimental data, as drawn in Figure 6.3, gives an overview of the topology of the jet. It is striking that the origin of the jet is not positioned at the outer radius of the propeller, but rather at approximately $67\,\%$ of the diameter D_P of the propeller. Taking the diameter D_Hub of the hub into account for the diameter of the core D_Co in the propeller plane, Equation 6.10 follows.

$$D_\mathrm{Co} = 0.67 \cdot D_\mathrm{P} + D_\mathrm{Hub} \tag{6.10}$$

The value $0.67 \cdot D_\mathrm{P}$ highlights the origin of the momentum, which affects the jet. Oebius recognised that this has to be the point of the maximum circulation Γ. Then, the point of maximum circulation gives the point of maximum lift and thus of maximum thrust[4]. Based on this recognition, it is clear that this point depends on the geometry – this point may change from one propeller to another. But in practice, a well-designed propeller is mostly near this value due to similar aerodynamic qualities for well-designed blades. All propellers investigated by Oebius had a point of maximum thrust of about $65\,\%$ to $70\,\%$, although they were quite different in geometry. Hence, the error in choosing a value of $67\,\%$ is quite small.

In addition to the point of maximum thrust, Oebius found in his experiments that a divergence angle of about $\zeta \approx 18.78\,^\circ$ can be estimated for all propellers and Equation 6.3 becomes Equation 6.11.

$$\zeta = \frac{r - D_\mathrm{Co}/2}{x_\mathrm{Co}} \approx 18.78\,^\circ \tag{6.11}$$

The inflection point of velocity distribution is required to fully describe the Gaussian curve and was thus analysed in the experimental survey. In the flow development region, the course of these points is parallel to the symmetry axis and equal to the diameter D_Co of the initial core in the propeller plane,

(a) Relocation of the course of maximum velocity

(b) Decrease of the maximum velocity
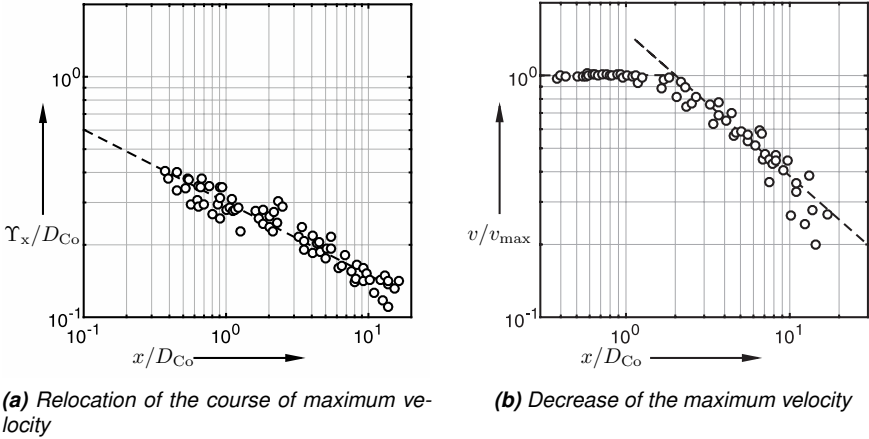
Figure 6.4. Change in the maximum velocity of a propeller jet with increasing propagation, double logarithmic scale, experimental data represented by circles (○), and curve fit by the dashed line, author's own representation based on Oebius [146]

see Equation 6.6, while in the development region, the curve of the inflection points diverges with the propagation of the jet, as can be seen in Figure 6.3. In his investigations, Oebius found a constant factor for this divergence of $\zeta_{\mathrm{Dev}} \approx 5°$, and the distance Υ_{Dev} according to Equation 6.9 can be rewritten as Equation 6.12 by taking Equation 6.8 into account[5].

$$\Upsilon_{\mathrm{Dev}} = \frac{D_{\mathrm{Co}}}{2} - \frac{\Upsilon_{\mathrm{x}}}{2} + 0.0875 \cdot (x - x_{\mathrm{Co}}) \tag{6.12}$$

To calculate the function Υ_{x}, Oebius analysed the relocation of the course of the maximum value. A detailed view of his results can be found in Figure 6.4a. In the double logarithmic diagram, the experimental dataset is represented by circles, while the curve fit is drawn as a dashed line. The function of the curve fit is represented by Equation 6.13.

$$\Upsilon_{\mathrm{x}}(x) = 0.6 \cdot D_{\mathrm{Co}} \cdot (x/D_{\mathrm{Co}})^{-0.3} \tag{6.13}$$

As mentioned above, the maximum velocity v_{max} is constant for the development region and equal to the velocity of maximum circulation and thrust respectively. But in the fully developed region, the value of v_{max} decreases with the propagation of the jet. To obtain a mathematical relationship for this behaviour, Oebius performed experimental investigations – the results of these investigations can be found in the double logarithmic diagram in Figure 6.4b. Experimental data is again depicted as circles, while the curve fit is given by a broken line. The nearly constant course of the maximum velocity v_{max} in the initial zone is clearly represented by the experiments, and therefore, the decrease of the course for distances is larger than $x/D_{\mathrm{Co}} = 1$. The curve fit for the fully developed region can be found as Equation 6.14.

$$\frac{v}{v_{\mathrm{max}}} = \frac{3}{2} \left(\frac{x}{D_{\mathrm{Co}}} \right)^{-0.6} \tag{6.14}$$

Combining the general law for a jet according to Equation 6.2 and the derivatives given in Equations 6.3 to 6.9, the semi-empirical approaches found in Equation 6.10 to 6.14 lead to the velocity distribution $v(x, r)$, as given in Equation 6.15.

$$v(x, r) = \begin{cases} v_{\mathrm{max}} \exp\left[-\frac{1}{2} \left(\frac{r - \Upsilon_{\mathrm{x}}(x)/2}{D_{\mathrm{Co}}/2 - \Upsilon_{\mathrm{x}}(x)/2} \right)^2 \right], \text{for } x < x_{\mathrm{Co}} \\ v_{\mathrm{max}} \exp\left[-\frac{1}{2} \left(\frac{r - \Upsilon_{\mathrm{x}}(x)/2}{\Upsilon_{\mathrm{Dev}}(x)} \right)^2 \right], \text{for } x \geq x_{\mathrm{Co}} \end{cases} \tag{6.15}$$

Note that the velocity distribution is defined by cases due to the increased diverging character in the fully developed region. Thus, Equation 6.16 gives the definition of the maximum velocity v_{max} for both cases.

$$v_{\mathrm{max}} = \begin{cases} v_{\mathrm{Co}}, & \text{for } x < x_{\mathrm{Co}} \\ v_{\mathrm{Co}} \cdot \frac{3}{2} \left(\frac{x}{D_{\mathrm{Co}}} \right)^{-0.6}, & \text{for } x \geq x_{\mathrm{Co}} \end{cases} \tag{6.16}$$

It also has to be said that the maximum velocity v_{max} depends on the velocity at the point of maximum circulation, which is given by Equation 6.17.

(a) Isolines

(b) Velocity in cross-sectional planes
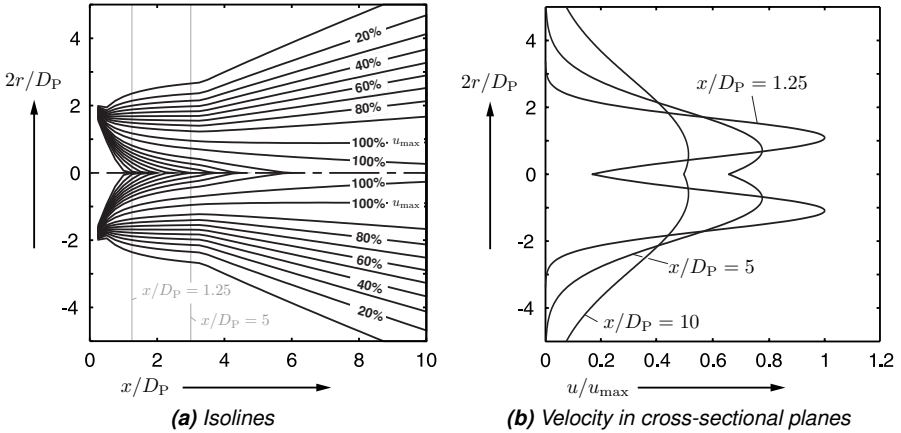
Figure 6.5. *Calculation of the velocity distribution in a propeller jet, calculated using Equation 6.15, shown as isolines of different values to demonstrate the propagation of the jet and as velocity distribution depending on different cross-sectional planes*

$$v_{Co} = \pi \cdot n \cdot D_{Co} \tag{6.17}$$

Based on Equation 6.15, it is now possible to estimate the velocity distribution for jet propulsion. Figure 6.5 shows the application of such velocity distribution as an example.

6.2.4. Jet theory for non-Newtonian fluid flow

The focus of the investigation performed by Oebius was the identification of erosion in harbour basins caused by marine-typed propellers. Thus, it is obvious that Oebius only considered water. High viscous or even non-Newtonian fluids were never the focus of his investigation. However, Oebius explicitly claimed that the method did not depend on the fluid used. He clearly emphasised the universal character of the law for propeller jets.

Because of the claimed universal character of the propeller jet theory, the theory will be applied to high viscous and non-Newtonian fluid flow in this
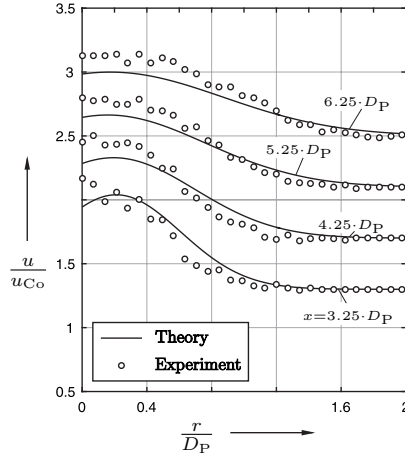
Figure 6.6. *Comparison of experiment (1.1 Ma.-% Xanthan gum) with jet theory, performed with a gear-driven mixer according to Urban [228], taken from Reviol et al. [181]*

study. To prove the validity of the theory, the investigation performed by Urban [228] was analysed and compared with Oebius' jet theory.

Urban investigated a gear-driven mixer. The mixer agitated an aqueous solution with 1.1 Ma.-% Xanthan gum. Subsequently, he applied Oebius' theory. Both the experiment and theory are depicted in Figure 6.6. The results are shown as local axial velocity, normalised by the maximum velocity in the core. The abscissa shows the local radius normalised by the outer diameter of the mixer. Figure 6.6 contains four different axial positions. The experimental data is drawn as circles, while the theoretical results are given as a continuous line. As can be seen, the theoretical curves fit the experimental data very well.

Oebius emphasised the general validity of the propeller jet theory without any detailed explanation. Hence, the reason for the good agreement is missing and will be explained in this thesis: Despite Oebius claiming general validity, the propeller theory cannot be valid for all fluids but only for fluids with similar densities. As described by Tollmien, the surrounding fluid is accelerated by the free turbulent shear layer. This means that turbulence is the most dominant effect in the kinematic process and viscous effects are smaller than

turbulence. Therefore, only the acting inertia forces, which are related to the density of the fluid, are relevant. Thus, Oebius' claim of universality is only correct in part, but sufficiently so for this research project, as will be described in Chapter 9.2.

Notes

[1]Laminar jet theory follows directly from the boundary layer equations, see Schlichting [200] for details – the mathematical procedure is quite similar to the procedure for a turbulent jet, but without taking the mixing length or similar approaches into account. Owing to the change of the flow characteristics for low Reynolds numbers of $Re = 30$, it is assumed that all jets considered in this work are fully turbulent. Note that the Reynolds number for a non-Newtonian fluid flow is not easy to calculate, see Chapter 5.3.3.

[2]The aim of the investigations performed by Oebius was the identification of the influence of the jet of a propeller on the sole erosion in harbour basins.

[3]In his further fundamental considerations of a rotational jet, Oebius [146] derived some empirical constants by experimental investigations. The values of these constants are in very good agreement with the theoretical derived values, as performed by Zimm [245] and Tollmien [223].

[4]Oebius [146] recognised that the origin of the momentum depends on the circulation. Lilienthal [125] found a point of maximum lift which correlates with the point of maximum circulation. Lilienthal also stated this value to be $67\,\%$ of the blade length for most blades.

[5]The constant factor of 0.0875 in Equation 6.12 directly follows from Equation 6.8, when setting $\zeta_{\mathrm{Dev}} = 5\,°$. Note that for a rotational jet out of a cylindrical gap, a value of 0.0807 was estimated by Oebius. This is in very good agreement with the theoretically calculated value of 0.08 for a plane jet as performed by Zimm [245] and Tollmien [223].

Part III.

Method development and validation

7. Method development

The previous part of this thesis introduced the mandatory fundamentals to develop the desired design method for propeller mixers. As suggested by Reviol et al. [181], the different fundamentals are merged and finally applied in Part III and especially in Chapter 7.

Before the design technique is presented in Chapter 7.3, the analytical deduction of the method is presented first in Chapter 7.1 and then the underlying profile database is discussed in Chapter 7.2.

7.1. Analytical approach

7.1.1. Kinematic conditions in a jet

As mentioned in Chapter 1.3, parts of the solution concept of the desired design technique are taken from the field of wind turbines. Adopting these parts on propeller mixers lead to the problem of the absence of a defined inflow condition, as given by the wind speed in the field of wind turbines. Additionally, the fundamentals of the mentioned approaches are defined for low viscous fluid flow with high Reynolds numbers only and are not valid for high viscous fluid flow and low Reynolds numbers as given for non-Newtonian media. Thus, the kinematics around a jet – as generated by a propeller mixer – are considered again, to adjust the state of the art methods for the purpose considered here.

Figure 7.1 illustrates the schematics of such a jet. The agitator is positioned at ①and rotates with the shaft speed n about the symmetry line. The propeller is driven by the power P_{PP} which leads to the mass flow rate $\dot{m}$ at the inflow zone, which is chosen in a sufficient distance upstream from the propeller, indicated by ⓪. Following the theoretical approaches of Oebius [146], between the propeller plane at Position ①and an arbitrary outlet position, given by ②, the jet diverges. Position ②is also chosen at a sufficient distance to the propeller plane. In the following, the positions defined in Figure 7.1 are utilised to describe the position in the jet, while the volume,
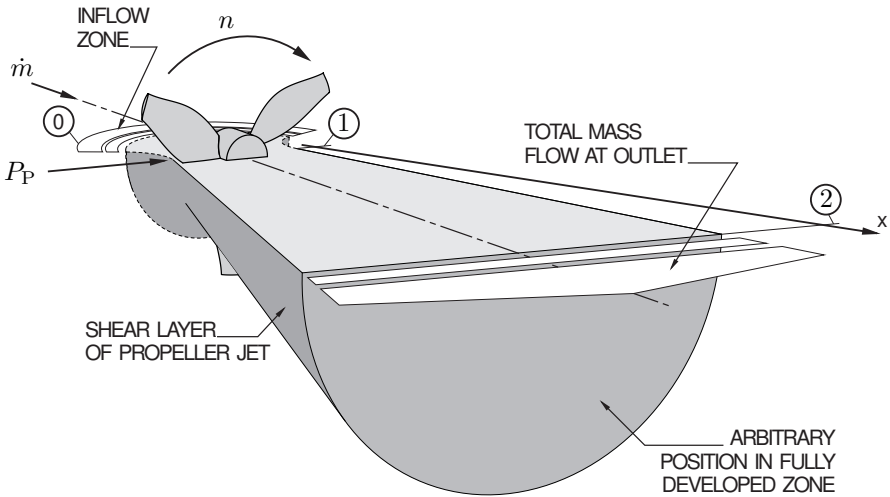
Figure 7.1. *Sectional view of a propeller jet with relevant process parameters, contour line calculated according to Oebius [146]' thoery – illustration of inflow zone (dashed curve) not included in Oebius' theory, inflow indicated with ⓪, propeller position marked with ① and outflow position for arbitrary x coordinate with ②*

enclosed by the shear layer of the jet is understood as the control volume for balancing conserved quantities.

Mass flow balance

The conservation of mass requires equal mass flow rates at in- and outflow, provided there is no increase or decrease in mass within the control volume. This means Equation 7.1 has to be valid in principle.

$$\dot{m} = \dot{m}_0 = \dot{m}_1 = \dot{m}_2 = const \tag{7.1}$$

However, Equation 7.1 is only valid if the surrounding surface of the control volume consists of solid material – or the velocity field in the surface must not have a component normal for this surface. For a jet, the surrounding surface is identical to the free shear layer and for a viscous fluid, the absence of
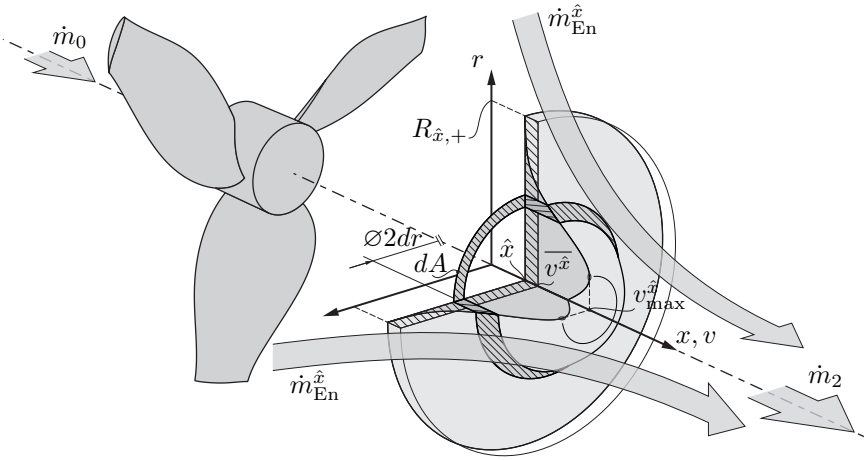
Figure 7.2. *Mass flow rates in the jet downstream from the propeller, depicted for an arbitrary position, representation according to Reviol et al. [181]*

normal velocity components cannot be assumed due to friction. This means, for a jet, the outflow mass flow rate has to be larger than the inflow mass flow rate because of the entrainment mass flow rate, which is accelerated by friction in the shear layer of the jet.

Thus, the entrainment mass flow rate has to be taken into account. For this, the propeller jet is intersected at an arbitrary position $\hat{x}$ downstream from the propeller, as illustrated in Figure 7.2. The figure illustrates the flow through an arbitrary propeller mixer and the acceleration of entrainment by the jet. Note that the radial velocity profile and the parameters of its geometrical distribution as calculated by the propeller jet theory according to Oebius [146] (see Chapter 6.2) is sketched together with the local mean velocity $\overline{v^{\hat{x}}}$ in axial direction.

To calculate the conservation of mass, as a simplification for low Re and high viscous fluid flow, incompressible conditions can be assumed. Thus, Equation 7.2 can be given for the outflowing mass flow rate $\dot{m}_2^{\hat{x}}$ at position $\hat{x}$. Herein, $A^{\hat{x}}$ is the area of the section through the jet, perpendicular to the symmetry line at $\hat{x}$.

$$\dot{m}_2^{\hat{x}} = \rho \cdot \overline{v^{\hat{x}}} \cdot A^{\hat{x}} \tag{7.2}$$

As described above, the entrainment mass flow rate $\dot{m}_{\mathrm{En}}^{\hat{x}}$ which occurs between inflow at $\textcircled{0}$ and outflow at $\textcircled{2}$ has to be taken into account and Equation 7.3 results.

$$\dot{m}_2^{\hat{x}} = \dot{m}_{\mathrm{En}}^{\hat{x}} + \dot{m}_0 \tag{7.3}$$

The entrainment mass flow rate $\dot{m}_{\mathrm{En}}^{\hat{x}}$ at $\hat{x}$ can be understood as the integral of the local entrainment mass flow rate $\dot{m}_{\mathrm{En}}(x)$ from $\hat{x}_{-\infty}$ to the considered position $\hat{x}$, see Equation 7.4. The position $\hat{x}_{-\infty}$ marks the starting point of the jet.

$$\dot{m}_{\mathrm{En}}^{\hat{x}} = \frac{1}{\hat{x} - \hat{x}_{-\infty}} \int_{\hat{x}_{-\infty}}^{\hat{x}} \dot{m}_{\mathrm{En}}(x) \cdot dx \tag{7.4}$$

With Equation 7.4, the mass flow rate $\dot{m}_2^{\hat{x}}$ at the outflow position becomes Equation 7.5.

$$\dot{m}_2^{\hat{x}} = \frac{1}{\hat{x} - \hat{x}_{-\infty}} \int_{\hat{x}_{-\infty}}^{\hat{x}} \dot{m}_{\mathrm{En}}(x) \cdot dx + \dot{m}_0 \tag{7.5}$$

Combining Equations 7.1 to 7.5 creates the general formula for the whole mass outflow rate $\dot{m}_2$, see Equation 7.6. In Equation 7.6, $\hat{x}_{+\infty}$ describes the axial position of fully dissipated momentum forces – this means the position, where the velocity field of the jet is equal to the velocity of the far field. The analogue for the radial position is described by $R_{x,+\infty}$. It should be noted that Equation 7.6 is mostly not solvable in practice.

$$\dot{m}_2 = \frac{1}{\hat{x}_{+\infty} - \hat{x}_{-\infty}} \int\limits_{\hat{x}_{-\infty}}^{\hat{x}_{+\infty}} \dot{m}_{\mathrm{En}}(x) \ dx + \dot{m}_0$$

$$= \frac{\rho}{\hat{x}_{+\infty} - \hat{x}_{-\infty}} \int\limits_{\hat{x}_{-\infty}}^{\hat{x}_{+\infty}} \int\limits_{0}^{R_{x,+\infty}} \int\limits_{0}^{2\pi} v(x,r) \cdot r \ d\vartheta \ dr \ dx \qquad (7.6)$$

Axial flow velocity at inlet and outlet

To apply *blade element theory*, as discussed in Chapter 3.2.2, the axial flow velocity c_1 in the plane of the propeller is required. Assuming Froude-Rankine's theorem according to Equation 3.20, this velocity can be calculated using the inflow velocity c_0 and the outflow velocity c_2.

Regarding a control room according to Figure 7.3 and applying continuity, Equation 7.7 and 7.8 follow respectively.

$$c_0 = \frac{\dot{m}_0}{\rho \cdot A_0} \qquad (7.7)$$

$$c_2 = \frac{\dot{m}_2}{\rho \cdot A_2} \qquad (7.8)$$

However, due to entrainment, it is not allowed to apply continuity – the flow perpendicular to the stream tube must not be neglected, as discussed before. Thus, the mass flow rate at Position $\textcircled{2}$ has to be larger than at the inflow. Taking entrainment as formulated by Equation 7.5 into account, Equation 7.7 changes and Equation 7.9 results.

$$c_0 = \frac{\dot{m}_2 - \frac{1}{\hat{x}_2 - \hat{x}_{-\infty}} \int \dot{m}_{\mathrm{En}} \ dx}{\rho \cdot A_0} \qquad (7.9)$$

Equation 7.9 depends on the mass outflow rate and therefore on the still unknown outflow velocity c_2. Assuming a mixing time $\mathcal{T}$, which is necessary

to circulate the whole fluid exactly one time, c_2 can be estimated for a known mixing volume V and Equation 7.10 is found for the inflow velocity c_0 and Equation 7.11 for the outflow position respectively.

$$c_0 = \frac{V/\mathcal{T}}{A_0} - \frac{\int \dot{m}_{\mathrm{En}}\, dx}{\rho \cdot A_0\, (\hat{x} - \hat{x}_{-\infty})} \tag{7.10}$$

$$c_2 = \frac{V/\mathcal{T}}{A_0} \tag{7.11}$$

Taking both the inflow velocity c_0 and the outflow velocity c_2 into account, Froude-Rankine's theorem can be applied in principle to calculate the velocity in the propeller plane – provided the required assumptions are fulfilled, which is not valid in the considered case. Equation 3.20 and so the origin *axial momentum theory* is only valid for low viscous fluid flow and for the absence of entrainment, see Chapter 3.2.1 for details. Hence, Froude-Rankine's theorem has to be enhanced for non-Newtonian fluid flow.

Froude-Rankine's theorem for high viscous fluid flow

From Equation 7.6, it is obvious that the entrainment mass flow rate $\dot{m}_{\mathrm{En}}^{\hat{x}}$ can not be calculated precisely under practical conditions. However, the mass flow rate of the entrainment may be modelled in a simple manner in accordance with the *axial momentum theory* of Froude [67] and Glauert [77]:

Following the approach to subdivide the mass outflow rate into an entrainment mass flow rate $\dot{m}_{\mathrm{En}}^{\hat{x}}$ and an undisturbed mass outflow rate $\dot{m}_2^*$, which is equal to the mass inflow rate $\dot{m}_0 = \dot{m}_2^*$ as performed in Equation 7.3, a characteristic velocity can be identified for each mass flow rate.

Under these assumptions, c_{En} is the characteristic velocity of the entrainment mass flow rate at Position ② and can be estimated by Equation 7.12 and 7.13.
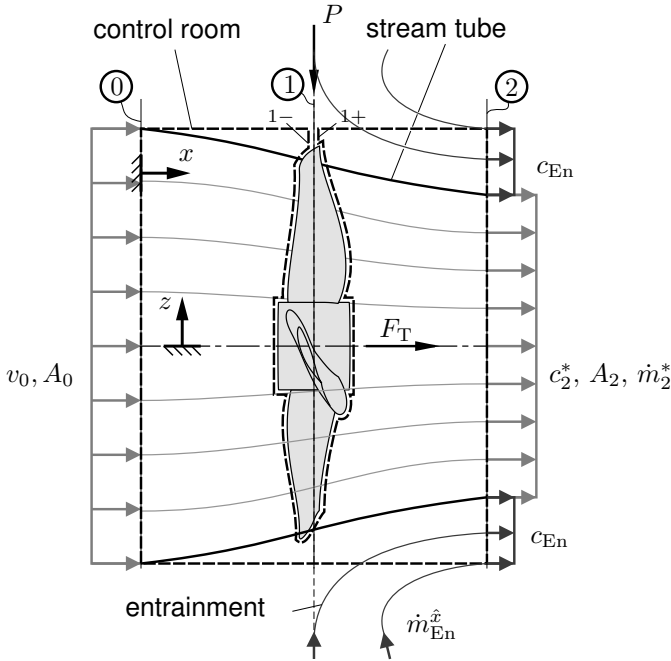
Figure 7.3. *Stream tube to derive the axial momentum theory for high viscous fluid flow with characteristic entrainment mass flow rate due to friction, ⓪ marks the entrance, ① the propeller plane and ② the outflow*

$$c_{\text{En}} = \overline{\dot{m}_{\text{En}}}/\rho A_0 \tag{7.12}$$

$$\overline{\dot{m}_{\text{En}}} = \int\limits_{\hat{x}_{-\infty}}^{\hat{x}_2} \frac{\dot{m}_{\text{En}}}{\Delta x}\,dx \tag{7.13}$$

Herein, the mass flow rate $\overline{\dot{m}_{\text{En}}}$ is the mean value of the entrainment from the starting point $\hat{x}_{-\infty}$ to the outflow position, which is indicated by $\hat{x}_2 = \Delta x + \hat{x}_{-\infty}$. Thus, Δx gives the considered length of the jet.

Similarly, for the ideal mass outflow rate, the hypothetical velocity c_2^* can be identified. Under these circumstances, continuity still applies and the inflow

velocity c_0 is equal to c_2^*. Hence, c_2^* can be understood as characteristic for the part of the mass flow rate which occurs under frictionless conditions.

In Figure 7.3, the entrainment mass flow rate $\dot{m}_{\mathrm{En}}^{\hat{x}}$ is sketched qualitatively together with the ideal and undisturbed mass outflow rate $\dot{m}_2^*$. Note that the control room is chosen in a way that every velocity component is either parallel to the x-axis or to the z-axis of the control room. Because of this, the pressure distribution becomes complex – but pressure is assumed to be constant due to incompressible fluid flow and due to the distance of the boundaries to the considered propeller. Hence, pressure components will vanish, and only horizontal and vertical aligned velocity components occur.

The fundamentals of the original *axial momentum theory* are based on Bernoulli's principle. Introducing characteristic velocities, as described above, enables the principle to be applied to the present problem. In analogy to Chapter 3.2.1, total pressure is balanced. This leads to Equation 7.14 for the fluid flow from Position ⓪ to the point $_{1-}$ infinitesimal in front of the propeller. Note, that Equation 7.14 is equal to Equation 3.9 because of the onset of entrainment mass flow rate not occuring before the propeller plane is reached. Thus, Equation 7.15 takes the whole entrainment mass flow rate from $_{1+}$ to Position ② into account. Finally, Equation 7.16 gives the difference of both values for the total pressure balances, which has to be equal to the difference in pressure over the propeller.

$$p_0 + \frac{\rho}{2}\, {c_0}^2 = p_{1-} + \frac{\rho}{2}\, {c_{1-}}^2 \tag{7.14}$$

$$p_{1+} + \frac{\rho}{2}\, {c_{1+}}^2 = p_2 + \frac{\rho}{2}\, c_2^2 = p_2 + \frac{\rho}{2}\, \left(c_2^* + c_{\mathrm{En}}\right)^2 \tag{7.15}$$

$$\Delta p = \frac{\rho}{2}\left[{c_0}^2 - \left(c_2^* + c_{\mathrm{En}}\right)^2 \right] \tag{7.16}$$

Subsequently, the momentum balance in axial direction has to be considered. As explained before, the control room is chosen in such a way that only horizontal and vertical aligned velocity components are present. For incompressible flow, Equation 7.17 results.

$$F_T = \dot{m}_0 \, c_0 - \dot{m}_2 \, c_2 \tag{7.17}$$

Note, that Equation 7.17 and Equation 3.17 are quite similar but not identical. In contrast to the original *axial momentum theory*, the mass flow rate rises due to the entrainment. Introducing the hypothetical entrainment mass flow rate $\overline{\dot{m}_{En}}$ for entrainment and the hypothetical mass flow rate $\dot{m}_2^*$ for the ideal stream tube, the total mass flow rate at the outflow can be calculated by Equation 7.18.

$$\dot{m}_2 = \dot{m}_2^* + \overline{\dot{m}_{En}} \tag{7.18}$$

For the ideal case, the mass outflow rate $\dot{m}_2^*$ can be substituted by the mass inflow rate $\dot{m}_0$. Then, from Equation 7.17 and Equation 7.18, the thrust F_T according to Equation 7.19 is found.

$$F_T = \dot{m}_0 \, (c_0 - c_2) - \overline{\dot{m}_{En}} \cdot c_2 \tag{7.19}$$

Equating the pressure load $\Delta p \cdot A_1$ (see Equation 7.16) and the reaction force $\check{F}_T$ leads to Equation 7.20, which represents Froude-Rankine's theorem for high viscous fluids. As can be seen, neglecting the entrainment mass flow rate in Equation 7.20, Froude-Rankine's theorem follows directly, see Equation 3.20.

$$c_1 = \frac{c_0 + c_2}{2} + \frac{\overline{\dot{m}_{En}} \cdot c_2}{\rho \, A_1 \, (c_0 - c_2)} \tag{7.20}$$

Modelling the entrainment flow rate

Equation 7.20 can be utilised to calculate the absolute axial velocity c_1 in the propeller plane – provided the cumulated entrainment mass flow rate $\overline{\dot{m}_{En}}$

is known. In practice, $\overline{\dot{m}_{\mathrm{En}}}$ is very hard to predict by analytical methods. Considerable effort and the use of experimental methods would be necessary to estimate the mass flow rate. The direct calculation of the outlet velocity c_2 is also challenging. For given mixing volume and time, c_2 can be derived, see Equation 7.15. However, the cross section of the jet at the inflow is also necessary, but unknown.

Thus, in the scope of this research project, the entrainment mass flow rate $\dot{m}_{\mathrm{En}}$ and also the outflow velocity c_2 will be modelled by a semi-analytical method. For this, Oebius' propeller jet theory, as discussed in Chapter 6.2, will be utilised. Oebius estimated the velocity distribution downstream from the propeller as a function of radial and axial distance to the propeller, see Equation 6.9 and 6.15. Note that the validity of the method for use on high viscous fluid flow was proven in Chapter 6.2.4.

As elucidated above, the mass outflow rate – including the entrainment mass flow rate – can be calculated using Equation 7.6. Taking Equation 6.15 into account, the velocity distribution is known as mathematical function and the total mass flow rate can be calculated by integration. Based on this principle, the mean entrainment mass flow rate $\overline{\dot{m}_{\mathrm{En}}}$ can be estimated by Equation 7.21. Equation 7.22 gives the velocity distribution c_2. It has to be said, that entrainment is assumed to only occur downstream from the propeller.

$$\overline{\dot{m}_{\mathrm{En}}} = D \cdot \left(\int_0^\infty v\left(\hat{x}, r\right) \cdot 2\,\pi\,r \cdot dr - \int_0^\infty v\left(0, r\right) \cdot 2\,\pi\,r \cdot dr \right) \tag{7.21}$$

$$c_2 = \overline{v}\left(x = \hat{x}, r\right) = \frac{1}{\pi\,R_{\hat{x},+\infty}^2} \int_0^\infty v\left(x = \hat{x}, r\right) \cdot 2\,\pi\,r \cdot dr \tag{7.22}$$

The integration point $\textcircled{2}$ downstream from the propeller has to be chosen appropriately[1]. Additionally, the inlet velocity c_0 at Position $\textcircled{0}$ has to be calculated. For an ideal flow field, the inflow velocity has to be $c_0 = 0$ due to the infinite distance between the starting point of the jet and the propeller. In practice, c_0 is expected to be larger than 0 and has to be estimated first.

This can be done either by experimental measurements or by the utilization of Equation 7.9 and 7.10. Subsequently, the axial velocity c_1 in the propeller plane can be calculated by Equation 7.20.

As a more practical formulation, the simplified velocity in the propeller plane $\widetilde{c}_1$ can be identified, see Equation 7.23. The reason for the good agreement of Equation 7.23 can be found in the utilization of the diameter D_{Co}, which correlates with the point of maximum velocity in radial distance within the core region. Furthermore, the influence of entrainment is still low at this position – entrainment is assumed to start at this point. Thus, the estimation of the axial velocity with Equation 7.23 seems to be plausible, even though the formula is not physically correct.

$$\widetilde{c}_1 \approx \frac{4V/\mathcal{T}}{\pi \, D_{\mathrm{Co}}{}^2} \tag{7.23}$$

It should be noted that the procedure above can be utilised without the application of the jet theory by Oebius, provided the velocity distribution as a function of radius and distance $v\,(x, r)$, as can be seen in Figure 7.2, is established by alternative methods, such as theoretical models or experimental data. However, the velocity c_1 in the propeller plane can be identified by Equation 7.20.

Velocity triangles

Until this point of the considerations, the origin *axial momentum theory* has been adopted for the agitation of high viscous fluid flow. As a next step, *blade element theory* will be applied in analogy to Chapter 3.2.2. For this, the velocity triangles in the propeller plane (1) are analysed. Figure 7.4 shows a schematic view of the velocity components at all relevant positions in the stream tube.

The utilization of *blade element theory* requires an effective velocity at the profile, which is identified here by the relative velocity w. The absolute velocity c is commonly defined as the sum of circumferential $u = \omega \cdot r$ and relative

velocity w. Hence, the magnitude of the relative velocity can be calculated by both the magnitude of the absolute velocity and the circumferential velocity. However, it should be noted that Equation 7.20 was formulated for axial flow conditions, so for neglected swirl. Hence, only the meridional component c_{m} of the absolute velocity c can be estimated by Equation 7.20. For rotating fluid machinery, neglecting swirl can cause huge errors in the design process. The rotating structure, e.g. a propeller, causes momentums in radial direction, which can be identified as swirl in the fluid flow – and swirl requires kinetic energy too. Therefore, not only the already known meridional component c_{m}, but also the circumferential component c_{u} is essential for the full description of the absolute velocity c. As can be seen in Figure 7.4, the circumferential velocity u is enlarged by the circumferential component c_{u} of the absolute velocity. And for the calculation of the relative velocity w, the vector sum has to be calculated with the meridional component c_{m} of the absolute velocity. The magnitude of the relative velocity can be calculated using Equation 7.24.

$$|w_1|^2 = |c_{1,\mathrm{m}}|^2 + (|u_1| + |c_{1,\mathrm{u}}|)^2 \tag{7.24}$$

The circumferential component of the absolute velocity c_{u} results from the momentum balance in an angular direction. The derivation of the loads from this balance is performed in the following chapter. Owing to didactic reasons, an early intermediate result, which leads to c_{u}, is given by Equation 7.25 before the momentum balance is explained in more detail.

$$c_{1,\mathrm{u}} = \frac{dF_{\mathrm{C}}}{\rho \cdot c_{1,\mathrm{m}} \cdot dA_1} \tag{7.25}$$

The calculation of the relative angle Θ is simple and can be performed according to Equation 7.26, whereas the flow angle α depends on the considered flow profile – thus, the position of a selected profile has to be adjusted until α has reached a desired value.
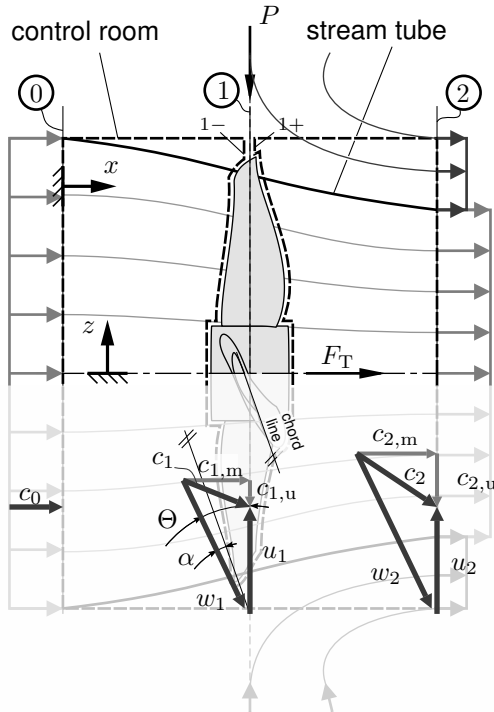
Figure 7.4. *Velocity triangles upstream from the propeller ⓪, in the propeller plane ① and downstream from the propeller ②, author's own representation based on Reviol et al. [181]*

$$\Theta = \arcsin \frac{c_{\mathrm{m}}}{w} = \arccos \frac{u}{w} \qquad (7.26)$$

7.1.2. Loads caused by the flow

At this point of the considerations, all relevant velocity components for a momentum balance are known. And thus, the infinitesimal forces at the section can be calculated by applying *blade element theory* as discussed in Chapter 3.2.2. For this, Figure 7.5 shows a schematic view of the relevant forces at an exemplary chosen radial section.
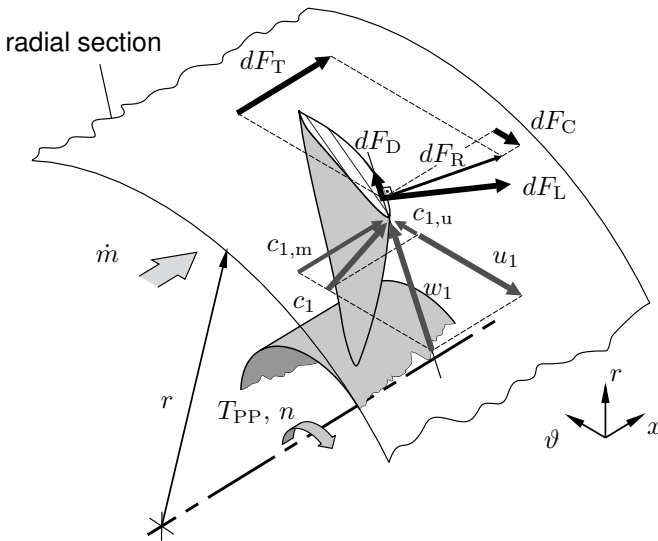
Figure 7.5. *Relevant forces, torque and velocity components at a radial section, author's own representation based on Reviol et al. [181]*

As depicted, the infinitesimal resulting force dF_R is caused by the infinitesimal forces for lift dF_L and drag dF_D. Additionally, dF_R can be separated into its components in axial and circumferential direction. As a result, dF_T can be obtained for infinitesimal thrust, while dF_C gives the infinitesimal circumferential force. The circumferential component leads directly to the drive torque $T_{PP} = dF_C \cdot r$. As with the original *blade element theory*, the mentioned forces can be calculated by Equation 3.22, 3.23, 3.25 and 3.26, see Chapter 3.2.2. It is worth mentioning that in contrast to Chapter 3.2.2 and Chapter 4.2.2, swirl is taken into account here, as illustrated in Figure 7.5. This is in accordance with the more complex design technique of considering circulation Γ, as briefly discussed in Chapter 4.3, despite the fact that circulation is also not taken into account explicitly in this chapter. Hence, the relative velocity w_1 has to be calculated according to Equation 7.24.

An alternative approach to estimate the resulting force dF_R is the consideration of the acting momentums. The momentum load $\dot{I}$ which occurs over the

infinitesimal time period ∂t is given by Equation 7.27. For steady state conditions – as typically required in the design process – the acceleration $\partial c / \partial t$ becomes zero and only the mass flow rate $\dot{m}$ has to be taken into account.

$$\dot{I} = \frac{\partial I}{\partial t} = \frac{\partial m}{\partial t} c + \frac{\partial c}{\partial t} m = \dot{m} \cdot c \qquad (7.27)$$

Applying Equation 7.27, the circumferential force dF_C and the thrust force dF_T can be derived directly and Equation 7.28 and 7.29 follow respectively. Note that dF_C is caused by perpendicular and dF_T by parallel vectors. Hence, Equation 7.28 and Equation 7.29 are given in vectorial lettering.

$$dF_\mathrm{C} = d\dot{I}_\vartheta = d\dot{m} \cdot |(\overrightarrow{n}_\vartheta \cdot \overrightarrow{c}) \cdot \overrightarrow{n}_\vartheta| \qquad (7.28)$$

$$dF_\mathrm{T} = d\dot{I}_x = d\dot{m} \cdot |(\overrightarrow{n}_x \cdot \overrightarrow{c}) \cdot \overrightarrow{n}_x| \qquad (7.29)$$

Considering the velocity triangle, the vectors can be substituted by scalar quantities and Equation 7.30 and 7.31 are as follows.

$$dF_\mathrm{C} = \rho \cdot c_{1,\mathrm{m}}\, c_{1,\mathrm{u}} \cdot dA_1 \qquad (7.30)$$

$$dF_\mathrm{T} = \rho \cdot c_{1,\mathrm{m}}{}^2 \cdot dA_1 \qquad (7.31)$$

As mentioned in Chapter 7.1.1, Equation 7.30 can be applied to calculate the swirl losses within the design process (see Equation 7.24 and 7.25)[2].

7.1.3. Derivation of the propeller shape

For the design process of wind turbines, as in Chapter 4.2.2 the shape of the blade can be derived from the integral forces – provided that a criterion for optimisation is defined. In the field of wind turbines, the Betz-Joukowsky limit is typically chosen as the criterion for ideal fluid flow. Here, this approach is not appropriate: on the one hand, the utilization of a high viscous and non-Newtonian fluid means that the ideal conditions as required for the Betz-

Joukowsky limit are not at hand. On the other hand, for the design process of wind turbines, a maximum conversion of wind energy is desired, while here, the opposite, a minimum of drive power, is desired. Thus, the target quantities are differing in general and an alternative criterion to optimise a propeller mixer must be chosen for the case under consideration.

As mentioned, an optimised propeller mixer is desired which consumes a minimum of power, which can also be considered as the effort P_{PP} to drive the propeller. Furthermore, the mixer is expected to generate a maximum of thrust, because a maximum of thrust leads to a maximum of mass flow rate, which was defined as the desired purpose of the propeller mixer, see Chapter 1. The kinetic energy, transported by the jet is given by power P_{Jet} of the jet. Thus, the relationship between benefit and effort defines the propeller efficiency η_P, see Equation 7.32 as already presumed by Glauert [77].

$$\eta_P = \frac{P_{Jet}}{P_{PP}} = \frac{F_T \cdot c_m}{T_{PP} \cdot \omega} \tag{7.32}$$
$$\Rightarrow F_T = max \quad \wedge \quad T_{PP} = min$$

With Equation 7.20, 7.30 and 7.31, Equation 7.32 is easy to solve and enables the propeller mixer to be optimised. Instead of considering the drive power, the thrust force can be chosen as an alternative criterion for optimisation. In a similar manner to the derivation of the chord length and thus to the design of the shape of the blade of a wind turbine, the shape of the propeller mixer can be designed by the derivation of the chord length as a function of thrust. This means, the chord length of each considered radial section is adjusted to the infinitesimal thrust and thus, the mixing task of the propeller mixer will be fulfilled best with this procedure.

The chord length can be obtained by combining the infinitesimal thrust dF_T according to Equation 3.25 with the infinitesimal lift and drag forces, see Equation 3.25 and 3.26 respectively. The mentioned forces are deduced from *blade element theory* as discussed in Chapter 3.2.2. Note that the infinitesimal thrust dF_T is additionally known by Equation 7.31. When isolating

the chord length l, Equation 7.33 results. The quantity n_z defines the number of propeller blades and must be chosen.

$$l = \frac{2 \cdot dF_T}{n_z \, \rho \, w_1{}^2 \, \left(C_L \, \cos \Theta - C_D \, \sin \Theta\right) \, dr} \tag{7.33}$$

Unfortunately, the chord length according to Equation 7.33 is a function of a large number of initially dependent and unknown quantities as can be seen in Equation 7.34.

$$l = f\left(dF_T, dr, w_1, c_{1,u}, C_L, C_D, \Theta, \alpha\right) \tag{7.34}$$

Furthermore, additionally to the chord length $l = f\left(\ldots\right)$, the mounting angle φ has to be known too. Since the mounting angle not only depends on the relative angle Θ but also on the flow angle α, the mounting angle can not be determined a priori due to the implicit character of Equation 7.33. Initially, the profiles to be selected for each considered radial section are unknown, and hence, the ideal flow angle is unknown too. Additionally, it is clear that φ has to be a function of the radius r, see Equation 7.35.

$$\varphi = \Theta\left(r\right) - \alpha\left(\ldots\right) = f\left(r, \ldots\right) \tag{7.35}$$

To solve the above problem, an iterative procedure is required. This is performed by a numerical algorithm, which can be found in Chapter 7.3 and in Figure 7.16 respectively. However, before the numerical procedure can be applied, the essential profile data of selected hydro- and airfoils has to be investigated. This is done in the following chapter.

7.2. Underlying polar plot database

As discussed in the overview of this work (see Part I), the procedure presented in Chapter 7.1 closely resembles the design process of wind turbines, which is well researched and understood. However, based on the theoretical consideration in Chapter 7.1, it is clear that the method is only sufficient if high quality profile polar data for a huge number of profiles is known - but this data is not available for non-Newtonian fluid flow. In consequence, flow profiles have to be investigated under non-Newtonian fluid flow conditions in order to generate a database.

Typically, profile polar data is investigated by experimental surveys. These studies include a manifold variation of the flow parameters. To derive a single polar curve, at least ten different measurement positions have to be analysed depending on the accuracy of the desired results. Mostly, polar plot data is given for varied velocity magnitude. In total, more than about 50 measurement positions have to be investigated for a single flow profile.

In the scope of this research work, not only do the flow conditions have to be changed but also the fluid conditions. Investigating only a few fluids would directly increase the number of measurements enormously – for just one single flow profile. Hence, in this research work, the polar data is generated by a numerical survey[3]. This allows extensive parameter studies.

7.2.1. Selected profiles

First, the investigated profiles will be introduced. It is clear that there are too many different flow profiles to examine them all. An appropriate preselection must first be performed, to reduce all the available flow profiles to those related to the present topic. To do this, several conventional databases were examined to obtain a representative overview of relevant profiles. Finally, a small number were selected for thorough examination.

The flow profiles were selected according to the following criteria:

- suitability of the profile as a low-Re-profile and/or

- suitability for use in a liquid
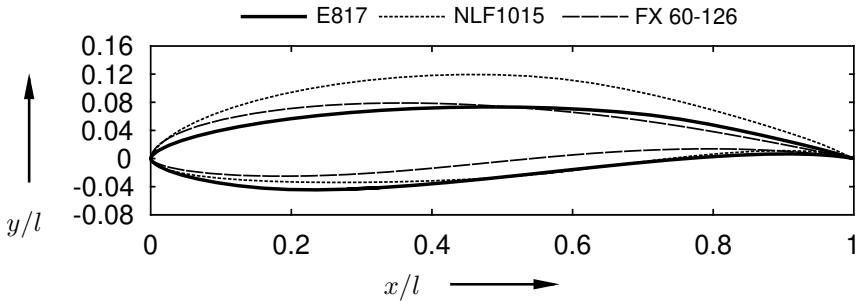
Figure 7.6. *Normalised plot of the three preselected flow profiles*

Three different profiles were selected: the Eppler E817 profile, due to its suitability as a hydrofoil, the Natural-Laminar-Flow (NLF) 1015 profile from NASA, because of the special development for laminar flow patterns and finally the Wortmann FX60 profile, because of its suitability as a low-Re profile. All profiles are depicted together in Figure 7.6 as a normalised plot to highlight the geometrical differences. As elucidated in Chapter 3.1.1, the profiles can be characterised by different parameters. These are shown in Table 7.1 and are separated into geometrical data and polar characteristics - for a detailed explanation of these parameters, refer to the fundamentals of this research work. The polar data is of major importance for the application of *blade element momentum theory*. Note that the data given in Table 7.1 concerns an experimental survey in Newtonian fluids and is therefore not relevant for the related research project and have to be recalculated for non-Newtonian fluid flow instead.

7.2.2. Numerical setup

As described above, the numerical investigations are performed with numerical studies. Owing to the large number of necessary investigations, the Lattice-Boltzman method (LBM) is applied. In the present research project, the relevant advantage of LBM compared to the RANS method is given by the numerical procedure. LBM only calculates the local collisions and the resulting propagation of the density distribution functions at every node, meaning that all calculations are carried out locally. Furthermore, no nonlinear sys-

Table 7.1. *Parameters for geometrical description of the investigated flow profiles including the polar characteristics for optimum flow conditions under Newtonian fluid flow for a Reynolds number of $Re = 1 \cdot 10^6$, data taken from the AID Airfoil Investigation Database [4]*

		E817	NLF1015	FX60-126
Geometrical data	Thickness	$10.9\,\%$	$15\,\%$	$12.5\,\%$
	Camber	$2.9\,\%$	$4.7\,\%$	$3.6\,\%$
	Trailing edge angle	$8.1\,°$	$11.8\,°$	$4.1\,°$
	Leading edge radius	$1.9\,\%$	$2.4\,\%$	$2.6\,\%$
	Lower flatness	$8.4\,\%$	$11\,\%$	$10.9\,\%$
	Efficiency	$25.3\,\%$	$46\,\%$	$41.3\,\%$
Polar characteristics[4]	max C_L	0.911	1.66	1.491
	max C_L angle	$7\,°$	$8\,°$	$10\,°$
	max $\mathrm{L/D}$	62.175	56.523	145.519
	max $\mathrm{L/D}$ angle	$2.5\,°$	$5\,°$	$5\,°$
	max $\mathrm{L/D}\ C_\mathrm{L}$	0.815	1.284	1.149
	Stall angle	$2.5\,°$	$-0.5\,°$	$10\,°$
	Zero lift angle	$-4\,°$	$-7\,°$	$-4.5\,°$

tems of equations are necessary. These two advantages significantly reduce the duration of a single calculation run. The almost linear scalability of the solving process is particulary noteworthy, due to the MPI-possibilities.

In this work, all CFD calculations were performed with the in-house code SAM-Lattice of the Institute of Fluid Mechanics and Turbomachinery of the Technical University of Kaiserslautern. The code is not only an LBM-based solver but includes an automatic mesh-generator too. The whole code was developed by Conrad and Schneider and has been comprehensively validated [40; 206; 207]. For a propeller mixer test case, Conrad et al. [41] have shown that even the agitation of non-Newtonian fluid flow can be calculated using the in-house code.

A detailed explanation of the relevant aspects of the LBM and in particular the in-house code SAM-Lattice are discussed by Conrad [40] and Schneider [206].
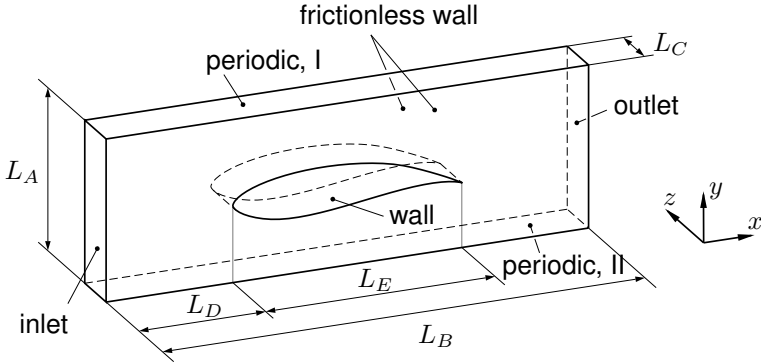
Figure 7.7. *Schematic view of the fluid domain*

Fluid domain

To calculate the profile polar characteristics, it is sufficient to consider only a small profile segment regarded as an element with infinite span by setting appropriate boundary conditions. This comes with two advantages: the costs of the numerical procedure are kept low and, more importantly, any influence of the aspect ratio on the polar characteristics as discussed by Glauert [77] is not present.

In Figure 7.7, a schematic view is shown. Note that the figure is not drawn to scale. The fluid enters the fluid domain through the boundary **inlet** on the left and exits on the right via the **outlet**. The boundary type of the inlet is set to *equilibrium velocity* with a fixed turbulence intensity of 10%, while the outlet is set to *equil./gauge pressure* and the pressure in this plane is considered as equal to ambient pressure. Only the boundary **wall** which represents the flow profile has a physical wall. Thus, the boundary chosen is the *Bouzidi bounce back* type. Owing to the assumption of a constant in-plane velocity, the whole numerical problem will also be two-dimensional. Thus, in y-direction, periodical (**periodic, I** and **periodic, II**, both set to *periodic*) and in z-direction, symmetrical conditions (**frictionless wall**, type *frictionless*) are applied. Conditions are adjusted at the inlet and outlet boundaries to generate the amount and the direction of the desired flux. The dimensions L_i are

constant for all numerical investigations and are set to prevent influences on the numerical procedure. The relevant parameters of the fluid domain are shown in Table 7.2.

Mesh

In contrast to the RANS method, the requirements related to computational grid are significantly less restrictive. In particular, the points do not have to represent the geometry exactly. In fact, the computational grid of an LBM simulation consists on a relatively simple rectangular and equidistant grid of points.

All grids utilised in this project were generated by an in-house tool implemented within the in-house LBM code. The resulting grids for each profile consists of about $16 \cdot 10^6$ nodes. An exemplary grid for the LBM is depicted for the E817 profile in Figure 7.8.

As well as an overview in the lower part of the illustration, Figure 7.8 shows a detailed view of the leading edge (1), the boundary layer region in the middle of the suction side (2) and the trailing edge (3). As can be seen, the grid does not exactly match the geometry because of the low restrictive requirements of the method on the computational grid. Furthermore, the boundary layer seems to be unrefined – although due to the short time duration of a single simulation run, the whole fluid domain can be chosen in an equal and high refinement level that includes a sufficient resolved boundary layer region. Hence, the numerical investigations are performed without taking wall functions into account.

Parameter study

To generate a single polar curve with sufficient accuracy, the variation of the flow angle must be extensive. Furthermore, a variation of the velocity is required to generate several polar curves. The considered flow angle varies from $-6\,°$ to $+12\,°$. The flow angle is increased by $2\,°$, while the velocity rises from $0.1\,m/s$ to $5\,m/s$ in steps of $0.5\,m/s$.
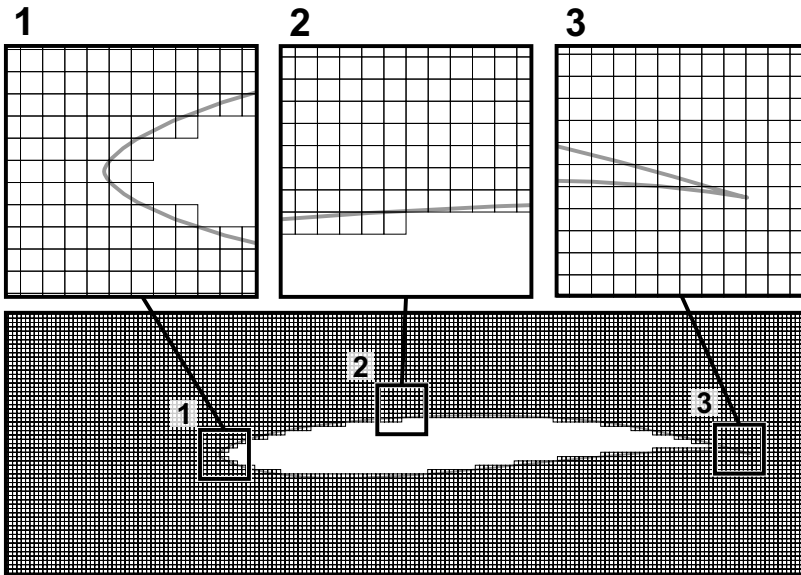
Figure 7.8. *Exemplarily computational grid for the E817 profile as utilised for LBM simulations, including detailed view of the leading edge (1), the boundary layer region at the suction side (2) and the trailing edge (3)*

As a further very important parameter, the non-Newtonian character of the fluid under consideration has to be changed within the study. The mathematical modelling of the fluid properties is carried out using the *power law* according to Equation 5.27, see Chapter 5.2.5. With regard to validation experiments, rheological parameters of aqueous carboxymethylcellulose (CMC) solutions and xanthan-gum (XG) solutions will be considered, due to the suitability of these solutions for experimental investigations, see Chapter 9.2.

The consistency factors of the applied fluids vary from $0.45\,Pa\,s^m$ to $31.31\,Pa\,s^m$. The physics of the regarded fluids result in a corresponding *power law* index variation from 0.85 to 0.27. Note that the *power law* index decreases in general with increasing consistency, while the pseudoplastic character increases.

Solver properties

As mentioned before, the utilised calculation grids consist of an overall node number of about $16 \cdot 10^6$ nodes. All simulations were performed within an automatically started process in parallelised CFD runs with typically 32 and at most 128 CPUs on a high-capacity computer. Each run was performed over at least 120000 time steps with the Multiple Relaxation Time (MRT) solver mode. The MRT is selected due to better numerical stability. Oscillations can be damped by adjusting the bulk viscosity [206].

With these settings, a simulation run requires $24\,GB$ RAM and takes about $14\,h$. Owing to the parallelisation capability with a large number of CPUs, the LBM is very suitable for generating a profile polar database for several hydrofoils, taking non-Newtonian fluid flow into account.

For all numerical investigations, the forces in x- and y-direction were analysed to calculate lift and drag forces and their dimensionless coefficients. Owing to the transient character of an LBM calculation, as emphasised by Conrad [40], the forces have to be evaluated as a mean value. The mean value was calculated as the arithmetic average of the last 5000 iteration steps.

Table 7.2 contains the significant solver parameters.

7.2.3. Validation study

Although the utilised LBM code was validated by Conrad et al. [41]; Schneider [206]; Schneider and Böhle [207]; Schneider et al. [208] for several cases, the applied code is an in-house code. Thus, experiences are yet limited in applying the code for special situations or certain problems. Hence, a short validation study is performed to show the validity of the in-house code by comparing the LBM results with the commercial CFD tool CFX v14.5 from ANSYS[6]. Note that the CFD method of CFX is the popular RANS method.

Owing to the fact that two different CFD methods will be applied, it is necessary to set up both solvers under similar conditions, especially at the boundaries. Apart from the differences in the fundamentals of the methods, the properties of the boundaries are set up identically. However, the plane **frictionless wall** is set as *symmetry* in the RANS simulations. The differences

Table 7.2. *Boundary and solver conditions for the numerical investigations, performed with the LBM and the RANS methods*

|	LBM	RANS
CFD tool		
	SAM-Lattice	ANSYS CFX v14.5
Investigated profiles		
Profile type	Eppler E817, NASA NLF1015, Wortmann FX60-126	
Fluid domain		
$L_A\ [m]$	7	
$L_B\ [m]$	15	
$L_C\ [m]$	0.064	1
$L_D\ [m]$	7	
$L_E\ [m]$	1	
Boundary types		
Inlet	Equilibrium velocity	vel. components
Outlet	Equil./gauge pressure	Opening
Periodic, I	Periodic	
Periodic, II	Periodic	
Wall	Bouzidi bounce back	No slip wall
Frictionless wall	Frictionless	Symmetry
Boundary conditions		
Velocity $v\ [m/s]$	$\{0.1:0.5:5\}$	5
Angle $\alpha\ [°]$	$\{-6:2:12\}$	
Pressure $p\ [Pa]$	$1 \cdot 10^5$	
Intensity $Tu\ [\%]$	10	
Consistency $k\ [Pa\,s^m]$	$\{0.45, 2.3, 2.8, 5.8, 8.3, 31.3\}$	$\{0.45, 2.3, 8.3\}$
Flow index $m\ [-]$	$\{0.85, 0.73, 0.40, 0.37, 0.61, 0.27\}$	$\{0.85, 0.73, 0.61\}$
Grid & solver properties		
No. nodes	$16 \cdot 10^6$	$2 \cdot 10^6$
Wall function	-	automatic
No. iterations	120000	min 500, max 1000
Solver mode	MRT	high resolution
CPU time	$14\,h$	$8\,h$
Memory	$24\,GB$	approx. $4\,GB$
No. CPUs	32	4
Turbulence	-	SST γ-Θ-model[5]
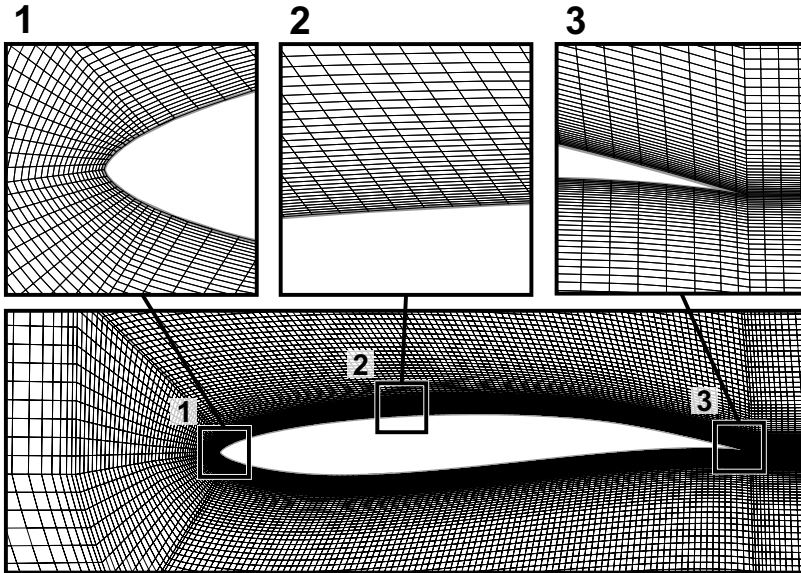
Figure 7.9. *Exemplarily computational grid for the E817 profile as utilised for the RANS simulations, including detailed views of the leading edge (1), the boundary layer region at the suction side (2) and the trailing edge (3)*

in modelling this plane lead to differences in generating the dimensions of the fluid domain. For CFX-runs, the length L_C is set to 1.

The mesh for the RANS-method was generated as a block-structured hexahedron dominant grid with the tool ICEM CFD. Since the logarithmic law for the wall is potentially unsuitable, the boundary layer was fully discretised. The resulting dimensionless wall distance y^+ of all grids reaches values of $y^+ < 4$ as its maximum. A mesh independency study was performed to ensure that no dependencies exist between results and mesh topology. The final grid of each profile consist of about $2 \cdot 10^6$ nodes. In Figure 7.9, the computational grid for the validation study of the E817 profile is shown. Besides an overview of the profile, a detailed view of the leading edge (1), the boundary layer region at the suction side (2) and the trailing edge (3) is shown. The figure illustrates the distribution of the cell elements to obtain the desired y^+ values.

The solver was run in *high resolution* mode over at least 500 and at most 1000 iteration steps. For the chosen number of 4 CPUs and a selected RAM size of $4\,GB$, the time duration of a single run was about $8\,h$. Although this time duration is almost half of time duration of the LBM, it should be noted that the utilised computational grids differ in size by a factor of eight and thus, the LBM is still preferred due to the better resolution of the results.

As a further aspect in quality, the LBM code does not need to model turbulence with two-equation turbulence models. While CFX is utilised in the application of the SST γ-Θ-model, the LBM code SAM-Lattice can be started using LES models with low usage of time and memory.

To reduce the effort to validate the LBM tool, the comparison will be performed for the E817 profile only. Note that the flow conditions are restricted to three different pseudoplastic fluids and only to the velocity of $5\,m/s$.

The validation study is performed for the derived quantities C_L and C_D to plot the polar curve as discussed in Chapter 3.1.1. However, before presenting the polar plot, the local distribution of the field parameters velocity, static pressure and viscosity near the profile are presented as a basis for the explanation of the differences in the numerical results, performed with the different CFD methods.

Velocity and pressure distribution

As an example, one unique operating point is considered. The flow conditions of the chosen operating point are given by a fluid flow with a velocity magnitude of $v = 5\,m/s$ and a flow angle of $\alpha = 8\,°$. The applied viscous properties of the fluid are given by the consistency $k = 8.3\,Pa\,s^m$ while the flow index is set to $m = 0.61$. The results of the operating point are shown as array of various contour plots. Results from the first row were performed using LBM and the second using CFX with the RANS method. In the third row, the results from the first two rows were subtracted from each other and normalised. Hence the resulting contour plot illustrates the differences of both methods. While Figure 7.10 shows the results for the velocity, in Figure 7.11 results for the relative static pressure are shown.
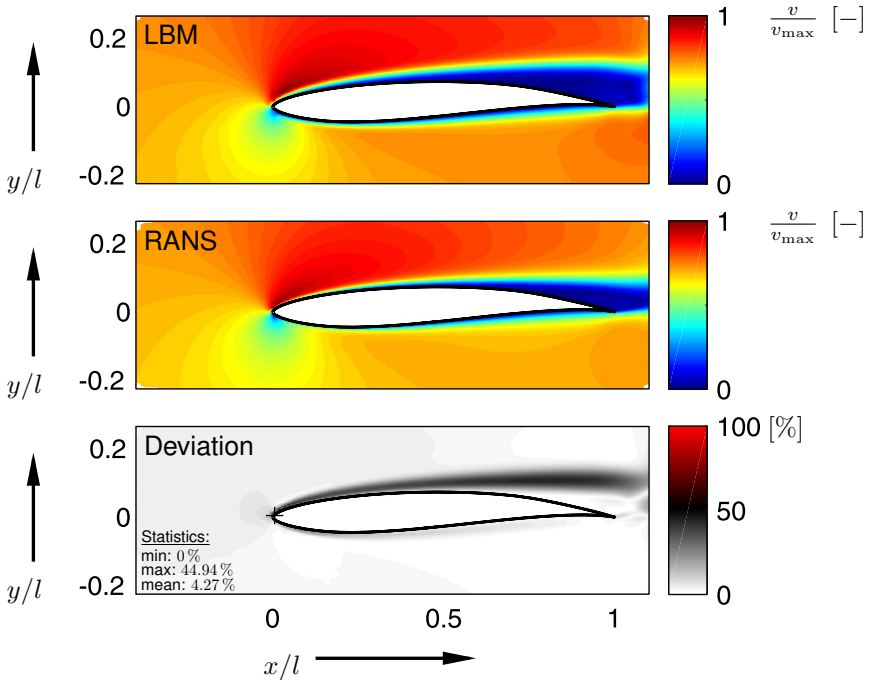
Figure 7.10. *Flow field around E817 profile: **velocity distribution**, performed with the LBM (top) and RANS methods using CFX (middle) including the normalised deviation from each other (bottom), flow conditions: inflow velocity $v = 5\,m/s$, flow angle $\alpha = 8\,°$, consistency $k = 8.3\,Pa\,s^m$, flow index $m = 0.61$*

It can be expected that both methods will produce very similar results. And in fact, the deviations are very low. Despite the maximum deviation reaching values of about $45\,\%$ for velocity, the mean values are much lower and reach values of only $5\,\%$, as can be seen in Figure 7.10. Even for the pressure distribution, which is shown in Figure 7.11, the mean deviation is lower than $5\,\%$, but the maximum value rises locally to about $32\,\%$.

In both figures, the distribution of velocity and static pressure come to their highest deviations due to the same computational reasons. The region of higher deviations is quite narrow but oblong and is positioned at the end of the suction side of the profile. This is caused by the differences in calculating the starting point for stall in the LBM and RANS methods. Because of the small
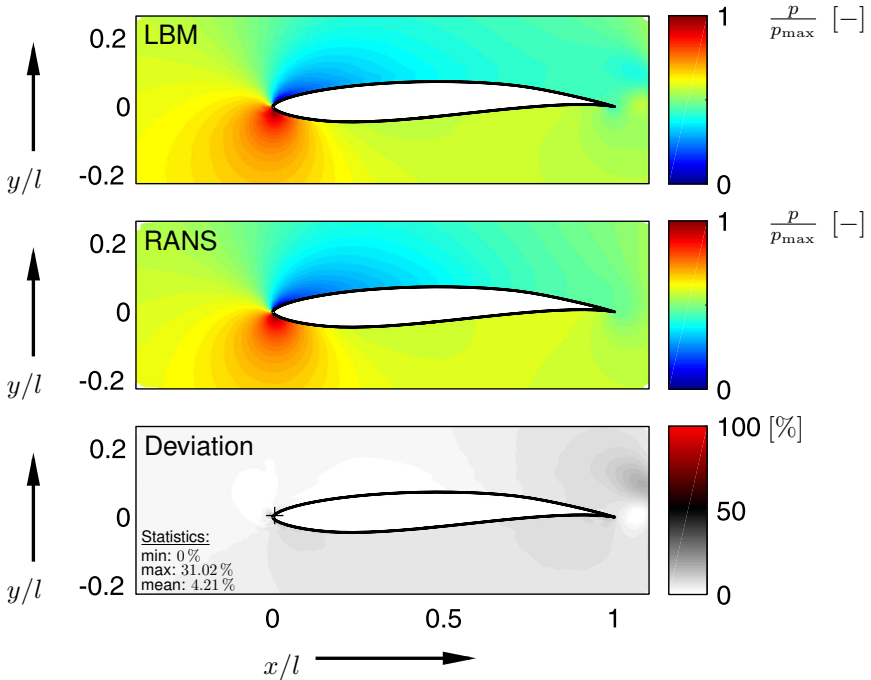
Figure 7.11. *Flow field around E817 profile: **static pressure distribution**, performed with the LBM (top) and RANS methods using CFX (middle) including the normalised deviation from each other (bottom), flow conditions: inflow velocity $v = 5\,m/s$, flow angle $\alpha = 8\,°$, consistency $k = 8.3\,Pa\,s^m$, flow index $m = 0.61$*

region of deviation, it can be assumed that the distribution of velocity and static pressure are calculated in good agreement and without any significant influence on the coefficients C_L and C_D.

Viscosity

However, drag is not only caused by the conditions of the fluid flow but also by fluid friction. Thus, in the scope of this thesis, the viscosity and especially the ability of the CFD to calculate this value in an appropriate manner is of utmost importance. In both CFD codes, identically models to predict the pseudoplastic fluid behaviour have to be chosen. Here, the *power law* was
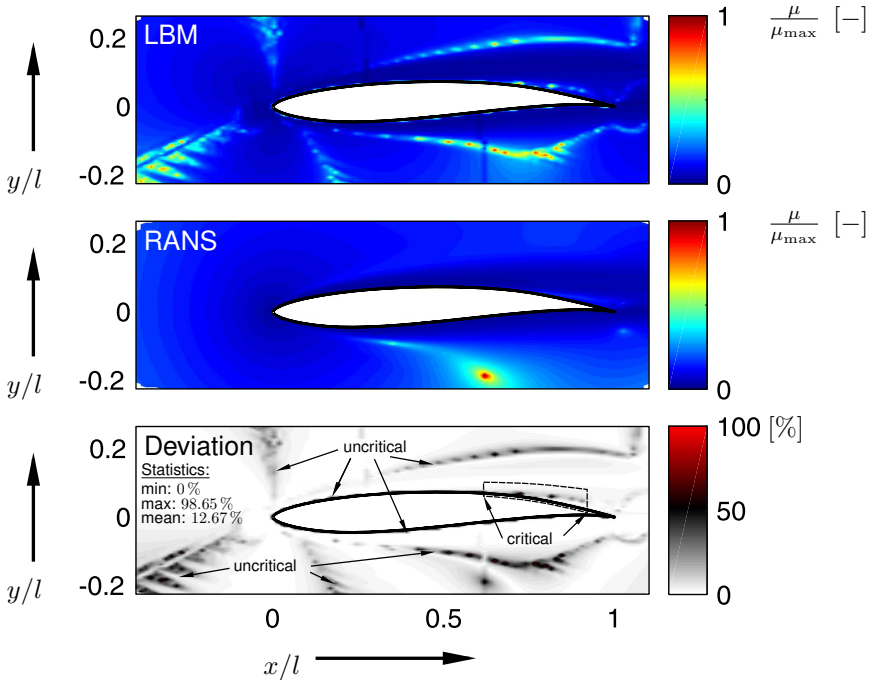
Figure 7.12. *Flow field around E817 profile:* **dynamic viscosity distribution**, *performed with the LBM (top) and RANS methods using CFX (middle) including the normalised deviation from each other (bottom), flow conditions: inflow velocity* $v = 5\,m/s$, *flow angle* $\alpha = 8\,°$, *consistency* $k = 8.3\,Pa\,s^m$, *flow index* $m = 0.61$

chosen, see Equation 5.27.

As shown in Figure 7.10 and 7.11 respectively, Figure 7.12 shows the identical operation point as chosen before in the example - but for the distribution of the viscosity field. To illustrate the normalised deviations for the local distribution of the apparent dynamic viscosity around the profile between the LBM and RANS methods, the third row shows the difference of the results from both methods.

As can be seen in Figure 7.12, the mean value of deviation reaches about $12.7\,\%$. Although this is a high value, the results are very good, due to the very low deviations in the boundary layer, which is relevant to the investigations. In this region, the deviation is nearly zero. Only a small area at the end of
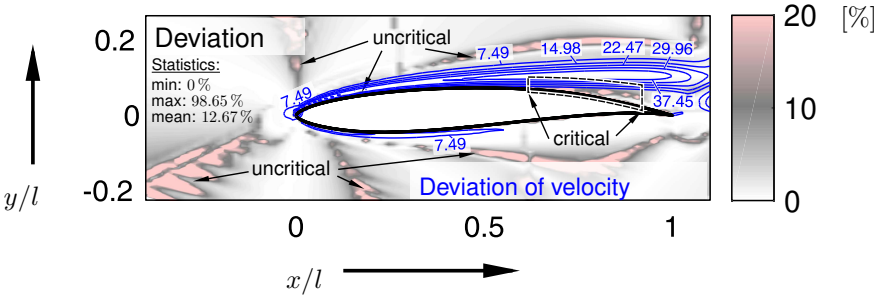
Figure 7.13. *Flow field around E817 profile: **deviation of velocity and viscosity**, performed with the LBM and RANS methods using CFX and depicted as normalised deviation from each other, velocity deviation as superposed isocurves (blue), flow conditions: inflow velocity $v = 5\,m/s$, flow angle $\alpha = 8\,°$, consistency $k = 8.3\,Pa\,s^m$, flow index $m = 0.61$*

the suction side shows higher deviations. This is caused by the differently estimated break-off-points, as described above. In Figure 7.12, this region is marked as *critical*. The remaining regions with identified deviations can be assumed as *uncritical* because of the high distance between these positions and the boundary layer of the profile. Ultimately, only the boundary layer is relevant for drag and thus for the calculation of the coefficient C_D.

Plotting the normalised deviation of the distribution of the velocity field and the distribution of the apparent viscosity field in a single illustration results in Figure 7.13. The distribution of the differences in apparent viscosity is shown as a contour plot, while the deviation of the velocity field is depicted as an isoline plot. Around the region of highest computational differences in velocity, it is clear that differences in viscosity must also occur. Since the upper region of deviations in viscosity is far from the boundary layer, no influence in the calculation of the coefficient C_D should be expected here, but the lower region of the velocity errors is directly connected to the boundary layer. This region is marked as *critical* in Figure 7.12 and 7.13. Thus, Figure 7.13 clearly proves the influence of the velocity field on the apparent viscosity and the quality of the numerical calculation of the coefficient C_D has to be observed in particular.
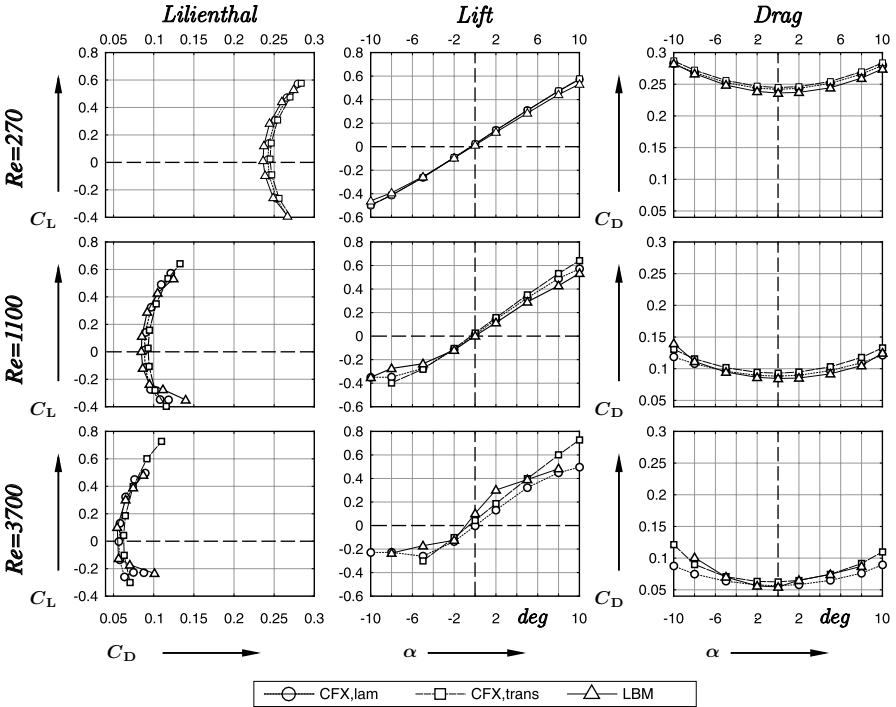
Figure 7.14. *Profile polar plots accordingly to Lilienthal of the validation study, lift and drag polar curve for the LBM and RANS methods (CFX: laminar and turbulence modelling with $\gamma\Theta$-model), profile E817, consistency $\mathcal{k} = 8.3\,Pa\,s^m$, flow index $m = 0.61$, velocity $v = 5\,m/s$*

Coefficients of lift and drag

Figure 7.14 shows the polar plot according to Lilienthal, as well as the polar plots for lift and drag. In analogy to the previous discussion, the figure is referred to a *power law* fluid with consistency $\mathcal{k} = 8.3\,Pa\,s^m$ and flow index $m = 0.61$ but includes a variation of the flow angle α from $-10\,°$ to $+10\,°$. The velocity was set to $v = 5\,m/s$. Note that the given Reynolds numbers Re_{MR} are calculated with Equation 5.38 accordingly to Chhabra, as well as Metzner and Reed.

As discussed above, a good agreement with all CFD solvers can be expected. Although Figure 7.14 illustrates differences in the results of both methods, these differences occur especially for high flow angles and high Reynolds

numbers. This effect is absolutely clear because of its relationship to beginning stall - and due to calculation mismatches in predicting the break-off-point between the applied methods.

Nevertheless, for the intended utilization of the database, the results are perfectly adequate. This is because of the good agreement for flow angles between $+6\,^\circ$ and $+10\,^\circ$. It should be noted that this region is particularly important because of its relevance for the design process: here the glide angle δ rises to its optimum value.

As a consequence of the validation study, the LBM is taken as the most sufficient CFD method to calculate the polar plot database.

7.2.4. Results of the database

The intended method to design a propeller mixer requires a huge number of profile polar datasets. To obtain this data, a wide-ranged parameter variation is necessary. Table 7.2 contains all investigated variables and their variation range. As mentioned above, the LBM is very suitable for performing this huge number of numerical investigations in a short time with high accuracy.

The results of the parameter study performed with the LBM is shown as an overview in Figure 7.15. The figure shows all performed numerical investigations and illustrates the results as plot diagrams for all three profiles. The parameter of the array curves is the Reynolds number according to Chhabra and Richardson, see Equation 5.38. Because the figure provides as an overview, the range of the Reynolds number, which is related to the marker symbols of the single curves, is not given in the figure. For reasons of clarity, the detailed view of each single investigated profile can be found in the appendix in Figures E.1 to E.3 – nevertheless, the figures will be explained here too. Figure E.1 contains all data for the Eppler E817 profile. Figure E.2 summarises all data for the NASA NLF1015 profile, and Figure E.3 shows the data for the Wortmann FX60-126 profile.

The first column of each figure shows the specific results as the polar data curve, as suggested by Lilienthal. The second column shows the lift and the last column the drag data of the investigated profiles. The rows of Fig-

ure 7.15 represent the investigated profiles, while, in the first row, the detailed figures E.1 to E.3 show an overview of all performed investigations for profile analysed in the figures. The rows, except the first one, show the curves for different Reynolds numbers. The second row contains all data between $Re = 0$ and $Re = 11 \cdot 10^2$, while the third row contains all profile polar data for $Re = 11 \cdot 10^2$ to $Re = 3.33 \cdot 10^3$. The fourth row contains all data for $Re = 3.33 \cdot 10^3$ to $Re = 1 \cdot 10^4$. In the last row, all data with higher Reynolds numbers is shown.
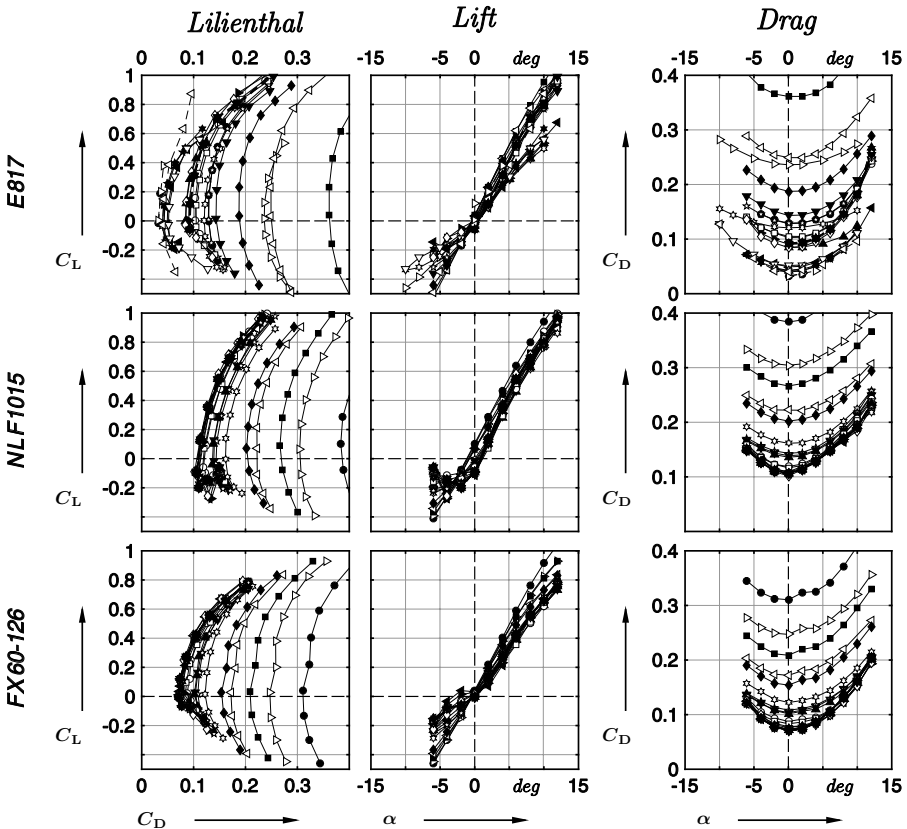
Figure 7.15. *Resulting profile polar plots accordingly to Lilienthal, lift and drag polar curves as array curves with Reynolds number according to Chhabra and Richardson [38] as array parameters, all investigated parameter variations*

155

For all investigations, the velocity is increased in steps of $\Delta v = 0.5\,m/s$ from $v = 0.1\,m/s$ over $v = 0.5\,m/s$ to at least $v = 5.0\,m/s$. In some investigations, even a velocity of $v < 0.1\,m/s$ is analysed. But when choosing such a low velocity, the Reynolds number becomes also very low. The estimated minimum Reynolds number was $Re = 27.5$. The drag coefficients in this regime rise to very high values and C_D becomes higher than 1. These values are not suitable for designing an optimised propeller mixer. Therefore, the figures only obtain polar datasets with drag coefficients minor than $C_D = 0.4$.

The qualitative behaviour of all discovered hydrofoils is very similar. The lift polar curve of each hydrofoil is characterised by a clearly pronounced and almost linear rising regime in the range of $-5\,°$ to $+10\,°$, as one can expect. The drag polar curves rise quickly with decreasing Reynolds numbers. This means that with rising Reynolds numbers, the values of the drag polar curves become lower. The higher the Reynolds number is, the more distinct this characteristic is. At one certain point, all drag polar curves only vary in a small range and the curves become nearly identical. This was be expected given the rising friction with decreasing Reynolds number.

Taking the polar data plot according to Lilienthal into account, the above findings are even reflected in the course of the polar data curves. For low Reynolds numbers in particular, the curves are quickly shifted to high drag coefficients.

As described above, no undisclosed effects and phenomena were identified with the numerical study. The results are clear, fully understood and in accordance with *blade element momentum theory*. Therefore, *blade element momentum theory* is in principle suitable for the design of propeller mixers to agitate non-Newtonian fluid flow. However, the investigation reveals a very quick increase of the drag coefficient for low Reynolds numbers. Hence, when applying *blade element momentum theory* to design a propeller mixer, a well-considered and accurate selection of several profiles is necessary.

7.3. Developed algorithm

As explained in Chapter 1.2, the aim of this research project is to design a flow-optimised propeller. The analytical deduction to obtain this target is explained in Chapter 7.1. However, this procedure has to be implemented in an algorithm to generate the flow-optimised propeller mixer in a fully automatic procedure. For this, the algorithm must be able to identify the most appropriate profile from the database generated in Chapter 7.2.

Since a further goal of the new design process is to calculate the power characteristics in the design process, the algorithm must be able to fulfil both of the following: the design point calculation for predefined operating conditions, which is presented in Chapter 7.3.1 and the calculation of the power characteristics for further and even arbitrary operating conditions. The latter is described in Chapter 7.3.2.

7.3.1. Design point calculation

The design point calculation is the initial step of the design process and includes the geometrical design of the propeller. The procedure handles the theoretical fundamentals as described in Chapter 7.3.1, but arranges them in a logical structure which can be processed in a numerical algorithm.

This structure was first presented by Reviol et al. [181] and is illustrated as a flow chart in Figure 7.16. The flow chart is subdivided in several categories (**A.** to **E.**), that will be described below:

A. Read and calculate specifications: In the first sequence, the algorithm reads the relevant input data to generate the desired propeller mixer. This data can be separated into three categories:

The first category contains data related to the design point conditions, consisting of shaft speed n, consistency k of the fluid and its flow index m. In the second category, geometrical parameters are queried. These parameters are the diameter of the propeller D_P and its hub radius R_{Hub}, the estimated volume flow rate $\dot{V}$ or tank diameter D_T, fill level H_F and mixing
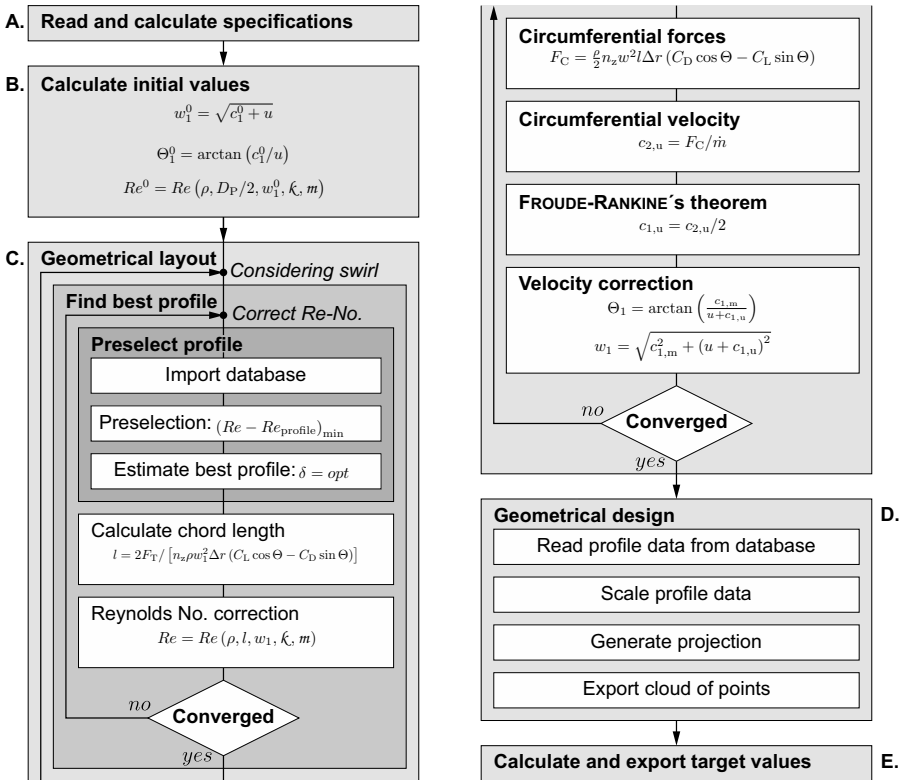
Figure 7.16. *Flow chart of the algorithm logics for the design of a propeller mixer for predefined operating conditions, representation according to Reviol et al. [181]*

time $\mathcal{T}$ and the number of blades n_z. Furthermore, the number of the considered sections has to be given. The last category contains only one entry: the method for how to calculate the Reynolds number. Some methods are known in literature, see Equation 5.38 and 5.42a, and are implemented in the algorithm. Table 7.3 shows all required input variables.

B. Calculate initial values: As a next step, the initial velocity triangles are calculated. To perform this, an initial estimation is calculated for the absolute velocity c_1^0 according to Equation 7.20 or 7.23. Subsequently the initial relative velocity w_1^0 and the initial circumferential velocity u_1^0 are calculated

Table 7.3. *Required input parameters for design point calculation, separated into three categories to describe the design point of the propeller, its geometrical properties and the method for how to calculate the Reynolds number*

Des. pt.	Shaft speed n
	Consistency $\underline{k}$
	Flow index $\underline{m}$
Geom. parameters	Propeller diameter D_P
	Hub radius R_Hub
	Volume flow rate $\dot{V}$ (or tank diameter D_T, fill level H_F and mixing time $\mathcal{T}$)
	Blade number n_z
	Number of radial sections
Misc.	Reynolds number calculation method

using Equation 7.24 and 7.26 respectively. For the later selection of a flow profile, the Reynolds number is also necessary, thus, the initial Reynolds number Re_1^0 according to Equation 5.38 or 5.42a is computed.

In addition to the initial velocity triangle, the thrust that has to be produced by the propeller is estimated. Afterwards, the integral value is distributed over the chosen number of radial sections. This is performed to deduce the hydrodynamic properties of the desired propeller shape.

Owing to the fact that the chord length l is not known at the beginning of the process, it is clear that the procedure has to be solved within an iteration process. Thus, initially, the chord length is set to the diameter D_P of the propeller as an upper estimate. In the following numerical procedure, an iteration loop is performed to compute the geometrical layout of the propeller.

C. Geometrical layout:

To resolve the major problem of the design process, which is to find an appropriate chord length and mounting angle distribution, an iterative procedure is necessary. This procedure is performed in this subsequence and is explained below. Note, that the sequence also considers swirl correc-

tion, but for reasons of simplicity, swirl may be neglected first in the following explanation.

In the first iteration step, the given initial conditions are utilised to derive the value of the required lift (C_L) and drag (C_D) coefficients. A profile is selected from the database using these parameters. Note that not only the coefficients for lift and drag are taken into account but also the glide angle δ to ensure that the most appropriate profile is chosen for profiles with similar coefficients of performance. Then, based on the polar data of the chosen profile, the chord length l can be calculated using Equation 7.33. However, by changing the chord length, the initial Reynolds number is changed too. Hence, a Reynolds number correction has to be performed in the last operation of the iteration step. At the beginning of the next step, the initial Reynolds number and the corrected Reynolds number, both taken from the last step, are compared. If the difference of both Reynolds numbers is smaller than a previously defined convergence criterion, the iteration is defined as converged and the loop is interrupted. Otherwise, the corrected Reynolds number of the last iteration step is taken as the new initial Reynolds number – as for the other derived and calculated quantities – and the iteration procedure is performed again, until either the convergence criterion is fulfilled or a maximum number of iteration steps is reached.

As mentioned above, the sequence also takes the correction of swirl into account. For this correction, the circumferential component c_u of the absolute velocity c has to be considered. This velocity component is derived from balancing the affected momentums, see Equation 7.25. Thus, the circumferential force F_C has to be calculated first as in Equation 3.26. Owing to the dependency of F_C on the chord length, it is necessary to perform the above iteration procedure first before swirl can be corrected. Once the chord length and thus the circumferential force is known, the circumferential component of the absolute velocity can be calculated – but only for a position downstream from the propeller. To resolve this problem, Froude-Rankine's theorem can be utilised. It should be noted that this theorem is found to be not appropriate in literature, if *"...rotation also occurs in the slipstream."*

[77, p. 194, §2]. Although this claim is true, Glauert only considered the magnitude of the velocity. Regarding only the components of the different directions, the validity of Froude-Rankine's theorem can be expected for the components, as applied in this thesis. Subsequently, the correction of the velocity can be computed based on Equation 7.25 and 7.26. However, due to the dependency of the Reynolds number not only on the chord length, but also on the relative velocity w, a further correction of the Reynolds number is necessary and therefore swirl correction has to be handled in an iterative structure too. In analogy to the previous iteration structure, the convergence and stop criteria are defined.

In the last step of the sequence, the calculated relative angle Θ of each considered section is changed by the flow angle α of the selected profile to obtain the mounting angle φ, see Equation 7.35.

D. Geometrical design: In the previous sequence, no true geometrical layout was designed, but only the mathematical distribution of the chord length l and the mounting angle φ. Based on these quantities, the geometrical data of the selected profiles can be imported and transformed. Specifically, this leads to a profile which is positioned correctly in the radial direction, scaled, and rotated about the mounting angle and projected to cylindrical coordinates. This is performed for every considered radial section. In addition to this procedure, the profiles are arranged around a fictive spar to ensure that a useful geometrical layout is designed.

As the result of this sequence, a point cloud is generated which can be exported to any CAD tool. An example point cloud can be seen in Figure 8.2 and 8.6.

E. Calculate and export target values: In the above sequences, several quantities and parameters are calculated. Based on these calculations, not only the geometrical layout is computed, but also the loads and momentums at each regarded profile. All infinitesimal circumferential forces, the total force and thus the expected torque and also power can be evaluated. Finally, the expected efficiency of the designed propeller mixer can be cal-

culated according to Equation 7.32.

The algorithm described above can be performed without any experimental investigations, provided a database with sufficient entries is available. For this research project, the database entries were generated by numerical investigations, which were demonstrated to be similarly robust to experimental investigations. Nevertheless, the procedure is purely analytical and produces a geometrical layout for a specified operating point, represented by the design point. All relevant engineering data for this design point such as thrust, torque and power, is known at the end of the design process.

The final results of the design process fulfil all conditions specified in the objective of this thesis, see Chapter 1.2. Therefore, the goal of developing a transparent and comprehensible design method for propeller mixers is achieved.

However, the design method leads to a fluid machine that is valid for a single operating point only, which was defined at the beginning of the design process – as it is typical in the field of fluid machinery. But instead of the common design processes in the field of fluid machinery, the fluid is also part of the design point and thus changing the mixed fluid without changing the operating conditions will render the design process invalid – and it is obvious that changing the operating conditions will also render the process invalid. In technical processes, a fluid machine often operates beyond its design point and, the fluid properties of the considered fluid may change over the process, especially in the processing industry. Hence, it is necessary not only to design a propeller mixer for a predefined operating point, but also to calculate the power characteristics of this mixer for differing operating conditions – including the change of the fluid properties.

7.3.2. Inverse calculation of characteristics

Because of the application of *blade element momentum theory* in the design process, all relevant data is present at the end of the process, and not only can the design point be calculated, but also alternative operating points. For

this, a procedure is developed to estimate the power characteristics for these operating conditions.

The procedure for deriving the power characteristics is quite similar to the original design process but starts with a given geometry. Hence, beforehand, a valid propeller has to be generated by the design process outlined above. Then, analogue sequences are computed in a reverse order – lastly, the algorithm handles the sequences in an inverse manner, see also Reviol et al. [182].

In Figure 7.17 the principle of the inverse algorithm is depicted. As can be seen, the algorithm is subdivided in three major sequences (**A.** to **C.**), which are explained in detail below:

A. Set initial data: In a similar way to the design process, the method for inverse calculation requires initial parameters too. In fact, these are the same parameters as for the design process and are related to the geometric parameters, to the process parameters of the origin design point and to the method of calculating the Reynolds number. For details, refer to Table 7.3.

Additionally, the parameters of the desired operating point are required. To specify the new point, the *power law* parameters of a certain fluid and a new value for the shaft speed are necessary – note that it is possible to set a shaft speed interval to calculate not only a single point but also a characteristic curve for power over shaft speed. Furthermore, the previously calculated drive torque T_{PP} of the design point is required to compare the torque of the newly regarded operating point with the originally estimated value.

It should be noted that the procedure can also be used for arbitrary propeller geometry that is not designed according to the procedure described here, as long as the required initial data according to Table 7.3 and 7.4 are known.

B. Calculation process: After reading all input data, the main sequence of the algorithm is started. This sequence performs several calculations which depend on each other and thus, these calculations are performed by recursive iteration procedures. Although these subsequences are connected to each other, they can be subdivided into three clearly separated tasks. Owing
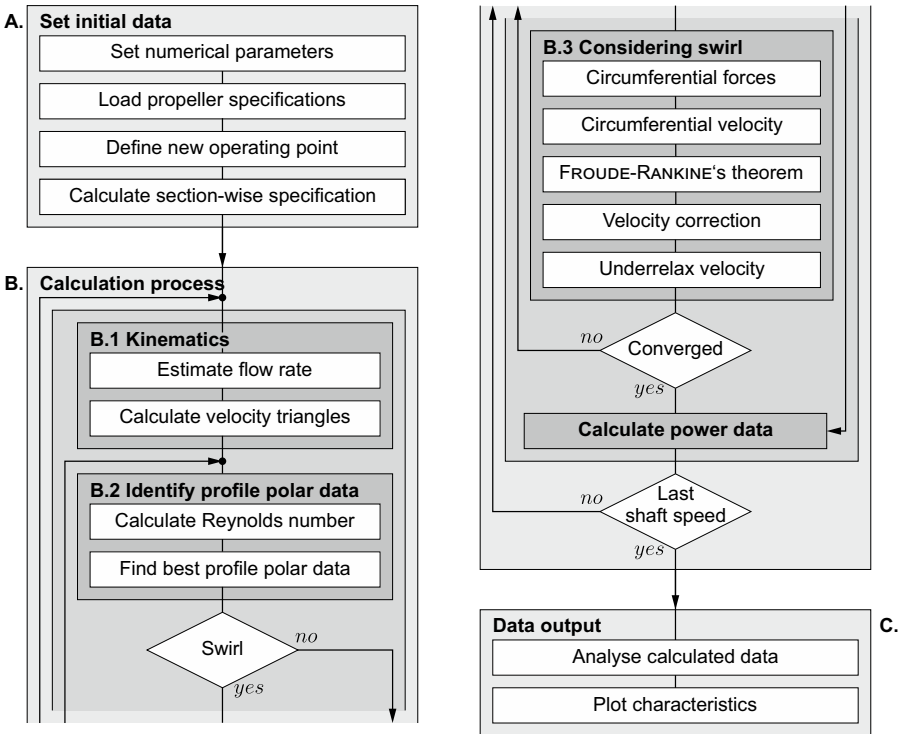
Figure 7.17. *Flow chart of the algorithm logics for the inverse calculation of power characteristics of a propeller mixer for arbitrary operating conditions, representation according to Reviol et al. [182]*

to the change of the shaft speed n, it is necessary to adjust the kinematics of the flow for each iteration step. This is handled in subsequence B.1. Afterwards, for each radial section, in subsequence B.2, a valid polar curve is requested from the database. And finally, the correction of swirl is computed in the last subsequence B.3.

B.1. Kinematics: The overall iteration loop of sequence B handles the shaft speed variation. Thus, over the iteration steps, the kinematic conditions change and before any calculations can be performed, the velocity triangles of the recently considered shaft speed have to be known. It should be noted that the change of the shaft speed not only causes a

Table 7.4. *Input parameters for inverse calculation required in addition to those listed in Table 7.3*

Add. parameters	
	Previously calculated torque T_{PP}
	Interval of interest for shaft speed n
	Profile type of each section
	Chord length l of each section
	Angle α of each section

variation in the circumferential velocity u, but also in the absolute velocity c – due to the relationship between shaft speed and volume flow rate $\dot{V}$. This means that the flow rate is required before calculating the recent velocity triangle.

However, the flow rate is only defined for two points on the power characteristics. One point is defined by the design point and known after the design process. The second point is simple: it is obvious that for a standing propeller, the flow rate falls to zero. Between these two points, the course of the flow rate over the shaft speed has to be approximated. The simplest method of approximation is to assume a linear distribution.

In fact, it is appropriate to assume a linear distribution of the flow rate. Regarding the theoretical approaches of Oebius [146], see Chapter 6.2, it becomes obvious that there is a linear dependency of the axial flow velocity on the shaft speed.

Based on these considerations, a linear course of the flow rate is supposed. Furthermore, the course of the curve must intersect the origin point as well as the design point. Now, it is possible to calculate the velocity triangles within the shaft speed variation once this subsequence is completed.

B.2. Identify profile polar data: The power characteristics of the propeller are directly linked to the coefficients for lift C_{L} and drag C_{D} and thus to the polar data of the underlying flow profiles. So, identifying the correct polar data is the key task of the whole algorithm.

The selected profiles, their chord length and the related mounting angles are defined during the design process and only the velocity triangles are missing to calculate the Reynolds number and the flow angle, which are mandatory to identify the correct polar data. Although the method is suitable for arbitrary propellers too, the underlying flow profiles have to be part of the database. If this is not the case, the database has to be updated for the required profiles – typically, this can be done by a simple numerical investigation. For a propeller mixer designed by method developed here, it is easier to identify the correct polar data. Note that even for known propellers, the polar data may be interpolated because of differences between the flow data of the database and the flow conditions for several operating points. Hence, the more data is stored in the database, the better the results of the inverse calculation.

It should be noted that this subsequence has to be computed with a recursive iteration procedure due to the chained dependency of the Reynolds number on swirl. Furthermore, the flow angle may also be changed if swirl is taken into account. For a suitable detection of the polar data, Reynolds number and flow angle are both very important. Nevertheless, because of the possibility of ignoring swirl in the computational method, this procedure will be explained separately in subsequence B.3.

When the polar data and the flow angle are identified correctly, based on lift and drag forces, the infinitesimal torque and thrust of each regarded radial section can be determined.

B.3. Considering swirl: As mentioned, swirl may be neglected in the calculation procedure. But in fact, it is not physical for rotating fluid machinery and especially not for the low-Re conditions considered here. To take swirl into account, subsequence B.3 can be enabled in the calculation procedure.

As outlined in the design process, swirl is computed by analysing the momentum balance of each radial section. The mandatory coefficients are taken from subsequence B.2. This analysis leads to an adjustment of the relative velocity which is necessary to recalculate the Reynolds number.

But by changing the Reynolds number, the previously selected polar data may be adjusted too, which leads to a variation in the momentum balance again. As can be seen, the procedures influence each other.

Because of the demonstrated link between Reynolds number and swirl, the subsequence for swirl is coded as a recursive while loop. Although this enables the code to solve the problem, the robustness of the algorithm decreases and instability may occur. To avoid these numerical instabilities, the procedure of adjustment is under-relaxed. Note that the under-relaxation is performed in line with the field of CFD.

Following the procedure described above, within the iteration procedure, the Reynolds number and the relative velocity will gradually reach an asymptotic value. To guarantee a highly qualitative result, a residual control is applied for the convergence procedure. Either a predefined convergence criterion has to be reached to end the while loop, or a maximum number of iterations has to be performed.

C. Data output: The last sequence is the post-processing step of the algorithm and generates user-friendly data. Specifically, the characteristic curve is plotted and compared with the origin design point. Furthermore, all data is cumulated to integral values. In Figure 8.9 and 8.10 example views of the final plot are depicted.

Based on the fundamentals described in this chapter and by the developed algorithm, a flow-optimised propeller mixer can be designed by transparent and comprehensible methods. The method is able to calculate the drive power for a given design point and for arbitrary operating conditions. Thus, a complete power characteristic can be deduced from the method at an early point in the development of new propeller mixer.

However, up to this point, all considerations are in fact purely theoretical and the method has to be validated in an experimental survey for at least one example propeller. To do this, in Chapter 8, two different prototypes are designed. Both prototypes are investigated experimentally and assessed in Chapter 9.

Notes

[1]In the scope of this research, the distance between the propeller plane and downstream position is selected to be equal to the diameter of the test bench [see 233], since this is the biggest distance in the test setup.

[2]To take swirl into account, the circumferential component $c_{1,\mathrm{u}}$ of the absolute velocity is required. However, this component is given by Equation 7.25 but cannot be solved directly. Instead, an iterative procedure has to be performed, refer to Chapter 7.3 and Figure 7.16.

[3]The application of a numerical procedure requires a final experimental study. This is performed by the investigation of the developed and manufactured propeller mixer, see Chapter 9.

[4]The data of the polar characteristics presented here (see Table 7.1) is taken from the AID Airfoil Investigation Database [4] and calculated by JavaFoil from Hepperle [95] under the assumption of Newtonian fluid flow for a Reynolds number of $Re = 1 \cdot 10^6$

[5]To investigate the influence of the turbulence, several CFX-runs were performed with the assumption of laminar fluid flow.

[6]The comparison of LBM with the RANS-based code CFX is appropriate. With intensive experimental and numerical investigations of the scalability of different mixer types, Kluck [115] shows the accuracy of CFX under the restriction that all pre-processing conditions, especially the rheological parameters, are well-chosen. The better the modelling of the rheological parameters, the higher the accuracy of the CFD-calculation. Therefore, as shown by Kluck [115], CFX can be taken to validate the LBM results.

8. Application of the method

To validate the method discussed in Chapter 7, the method was applied to design two different propellers. Although both the propellers are designed by the same design process, the first propeller is designed under the assumption of negligible swirl. This means that the fluid is viscous but irrotational. The aim of this very theoretical assumption is to identify whether it is possible to neglect swirl within the design process to achieve a simpler, more robust algorithm. In contrast to this high level of abstraction, which underlies the design of the first propeller, the second propeller is designed after taking viscous and rotational flow into account.

In the following, the underlying design parameters for both the propellers will be presented. Subsequently, the resultant propeller geometry will be discussed. Note that the utilised fluid is of major importance to the design process and, so, is discussed. The test configuration of each propeller is only introduced in a conceptual manner and will be discussed in Chapter 9.2.

8.1. Deriving the geometrical shape

In the typical design process of an arbitrary turbomachine, a design point is given by the requirements the machine has to fulfil and is often identical with the point of best efficiency. This point consists mostly of information about pressure rise, mass flow rate, and shaft speed of the impeller – or on quantities coupled to these. This typical procedure is characteristic for all types of turbomachinery and can be found in many common pieces of literature such as Gülich [78]; Lewis [124]; Pfleiderer and Peterman [158] and many others. Note that in the case of thermal fluid machinery, such information is insufficient; information about density and temperature is also important.

In the present case, it would not be sufficient to define the above quantities, as in the field of thermal turbomachinery. This is because of the significant influence of the non-Newtonian characteristics of the fluid. Hence, a dataset

which includes the rheological behaviour of the utilised fluid is necessary. Hence, in this chapter, first of all, the operating point of both the propellers will be examined in detail. Subsequently, the resultant propeller shape is presented when the design process is applied. Finally, the inverse calculation of the power curve is performed.

8.1.1. Propeller A

The first propeller is designed under the assumption of neglectable swirl. This propeller is referred to as Propeller A and is discussed below.

Design point

Propeller A is designed for laboratory-scaled purposes and is engaged by a shaft speed of $n = 160\,min^{-1}$. To define the volume flow rate, the fluid volume of the test stand and the mixing time are combined. Via the geometrical parameters of the laboratory vessel, see Chapter 9.2.1, a volume flow rate of $\dot{V} = 5.08\,l/s$ is calculated for a mixing time of $T = 5.1\,s$.

As carried out in Chapter 5.1.3, non-Newtonian fluid flow in technical processes is mostly in good accordance with *generalised Newtonian fluids*. Hence, in the following design process, only purely viscous fluid flow is taken into account. Furthermore, the viscosity function of the flow under consideration can be reduced to moderate shear rates because of the application of a mixing process. It can, therefore, be assumed that the dynamic zero-shear-rate-viscosity μ_0 and the infinity-shear-rate-viscosity μ_∞ are not reached, and only the so-called power law regime is of interest for the process considered. For this level of abstraction, the *power law* model according to Equation 5.27 is very appropriate. The consistency of the utilised model fluid amounts to $k = 8.75\,Pa\,s^m$ and the flow index to $m = 0.14$. The density is assumed to be a constant value of $\rho = 1000\,kg/m^3$. This value is chosen on the basis of experience and is in good accordance with the experiments; see Chapter 9.2.1.

Propeller shape

In addition to the above design point, some geometric restrictions have to be taken into account. Since Propeller A is utilised in a laboratory-scaled test stand with a diameter of $D_{\mathrm{T}} = 0.29\,m$, the diameter of Propeller A is set to $D_{\mathrm{P}} = 0.18\,m$ to ensure an appropriate diameter ratio. The hub radius R_{Hub} is set to $0.015\,m$ and the blade number of the propeller is $n_{\mathrm{z}} = 3$.

The subsequently performed design process calculates the chord length distribution and acquires the most adequate flow profiles from the database to fulfil the predefined mixing task. This is done for the previously given number of radial sections. For Propeller A, five radial sections are considered. From the database, as discussed in Chapter 7.2, the Wortmann FX60-126 profile was found to be the most appropriate profile for the first three sections. For the remaining sections near the tip, an Eppler E817 profile is found each time. In detail, the algorithm computed a chord length l_{i} and a flow angle α_{i} in the interval of $l = [0.05,\, 0.13]\,m$ and $\alpha = [20,\, 60]\,°$ respectively. The maximum values of each quantity are located near the hub. This intermediate result is depicted in Figure 8.1. In Figure 8.1a, the chord length distribution $l\,(r)$ is shown as a broken line. The data points in the subfigure represent the radial sections under consideration and are labelled with the names of the flow profiles that have been selected. The subfigure shows a strikingly long chord length for the hub radius – this is similar to the design of wind turbines, if swirl is neglected: see Chapter 4.2.2 and Figure 4.4a. The distribution of the mounting angle $\varphi\,(r)$ is illustrated in Figure 8.1b – the radial sections are also marked and labelled with the designation of the applied profiles. In

Table 8.1. *Calculated process parameters of Propeller A*

Estimated jet power P_{Jet}	$0.70\,W$
Estimated torque T_{PP}	$0.21\,Nm$
Estimated power P_{PP}	$3.46\,W$
Efficiency η_{P}	0.20
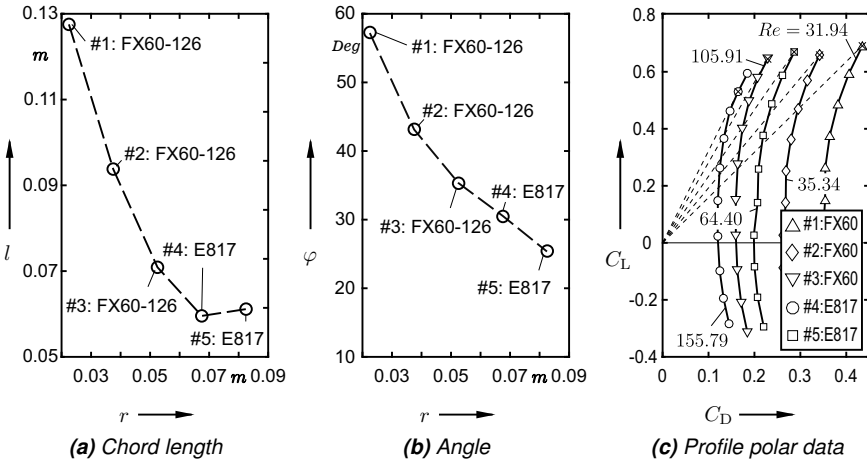
Figure 8.1. *Distribution of chord length, angle, and profile polar data of Propeller A, Reynolds number calculated in accordance with the generalised formulation of Equation 5.41, underlying data according to Reviol et al. [182]*

Figure 8.1c, the polar plot – according to Lilienthal – is shown for the flow profiles. Note that the given Reynolds number is calculated in accordance with Equation 5.41. Table 8.1 contains all the relevant parameters computed in the design process. For the parameters defined and calculated previously, Propeller A is expected by the design process to require a drive torque of $T_{\mathrm{PP}} = 0.21\,Nm$ and a power of $P_{\mathrm{PP}} = 3.46\,W$ in the design point. The jet power is estimated at $P_{\mathrm{Jet}} = 0.70\,W$ and an efficiency of $\eta_{\mathrm{P}} = 0.20$ is the result. Note that the predefined and derived parameters above for the design point are revived in the calculation of the power characteristics for arbitrary operating conditions and, so, these quantities are summarised later with the parameters for the inverse calculation in Table 8.3.

Afterwards, the algorithm transforms the selected flow profiles. For each radial section, the profile considered is scaled pursuant to the computed chord length and transferred from a flat plane to the corresponding cylindrical plane. Simultaneously, the profiles are rotated about the machine axis to obtain a useful arrangement of the profiles around a fictitious spar. As a result, a point cloud is generated, consisting of the geometrical data of the considered and
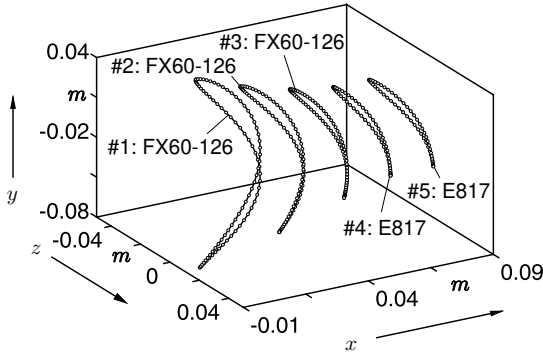
Figure 8.2. *Point cloud for the example design process to derive the shape of Propeller A, each profile is marked with a continuous curve, its section and name, presentation according to Reviol et al. [181]*

transformed flow profiles. Figure 8.2 shows this result for Propeller A as 3D-plot. For better understanding, the points are clustered in accordance with their flow profiles and connected by a continuous line. Furthermore, the designations of the flow profiles are added. This point cloud is the final geometric result of the computing procedure.

As can be seen in Figure 8.3, the blades of the propeller can be obtained by connecting the point cloud with a free-form surface and rotating the surface n_z-times. These can be easily combined with a model of the hub. The construction can be done in any arbitrary 3D-CAD tool. Figure 8.3 shows the 3D-CAD-model of Propeller A in isometric view, top view, front view, and side view.

The final step of the design process for Propeller A is the manufacture of the propeller. This is done by rapid prototyping. The prototyping process was performed by photopolymer technology – with this technology, horizontal layers are printed and hardened by UV light. The reachable precision in the thickness of each layer amounts to $16\,\mu m$ in high-quality mode, but for a full-scale model, a resolution of $200\,\mu m$ is obtained. The machine used was an Eden250 3D-printer from Objet. In Figure 8.4, a photography of Propeller A is depicted.

(a) Isometric view   *(b) Front view*

(c) Side view   *(d) Top view*
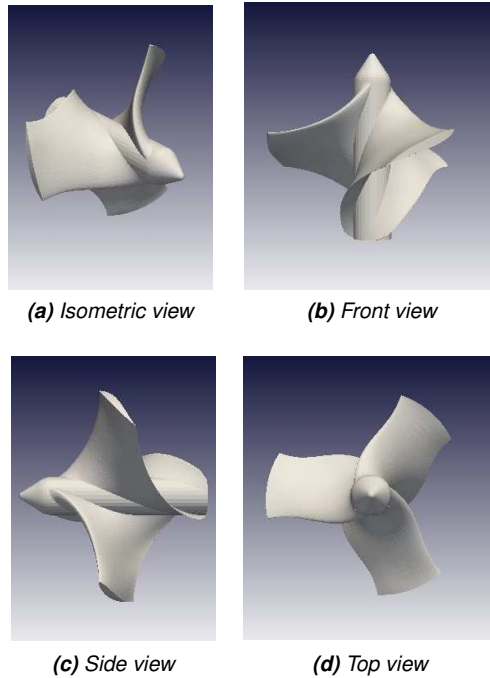
Figure 8.3. *Different views of Propeller A, presentation according to Reviol et al. [181]*

8.1.2. Propeller B

The second prototype propeller is referred to as Propeller B; it was designed taking swirl into account. Note that the propeller was previously designed and investigated in a perfunctory manner by Reviol et al. [181]. In the present thesis, Propeller B is presented in greater detail. But first all the predefined parameters to derive the propeller shape are elucidated as was also done for Propeller A.

Design point

The shaft speed of Propeller B is chosen as $n = 380\,min^{-1}$ and the volume flow rate is defined as $\dot{V} = 54.5\,l/s$. The utilised test stand to investigate

Figure 8.4.   *Propeller A, manufactured prototype, presentation according to Reviol et al. [182]*

Propeller B has a maximum volume of about $12.5\,m^3$, but for the experimental survey, a reduced fill level is applied, so that the effective volume of $V = 6.87\,m^3$ results; see Chapter 9.2.2 for details. Hence, a mixing time of $\mathcal{T} = 126\,s$ can be calculated.

Because the mixed fluid is part of the design point, the fluid properties have to be fixed in the design process. For simplification, a *generalised Newtonian fluid* is assumed. Hence, any viscoelasticity is neglected, and the fluid is regarded as purely viscous but shear-thinning. As will be explained in Chapter 9.2.2, for the shear rate region occurring here, this practical approach is in quite good accordance with theoretical considerations. The *power law* model is applied to model the rheological parameters of the fluid. These are $k = 14.50\,Pa\,s^m$ for consistency and $m = 0.29$ for flow index. As an additional simplification, the fluid is assumed to be incompressible. As also done for Propeller A, the density of the fluid is simplified to a value of $\rho \approx 1000\,kg/m^3$.

Propeller shape

To find the shape of the propeller, the algorithm requires the outer diameter, the hub radius, and the number of blades. For Propeller B, these parameters
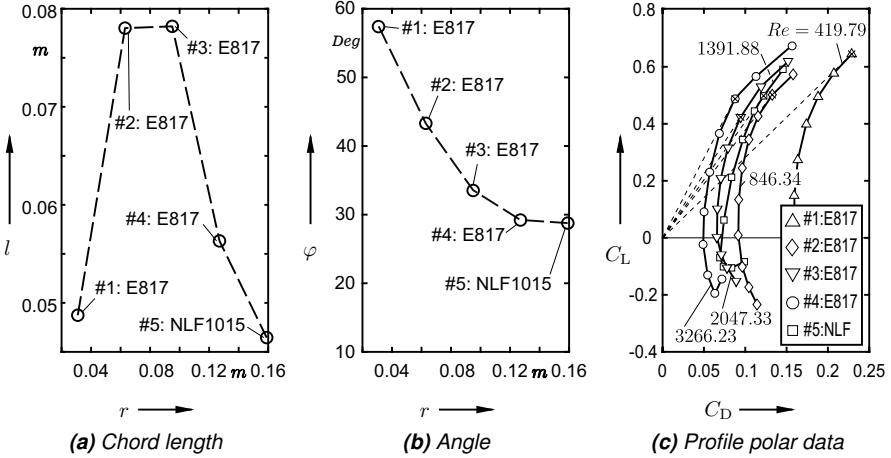
Figure 8.5. *Distribution of chord length, mounting angle, and profile polar data of Propeller B, Reynolds number calculated in accordance with the generalised formulation of Equation 5.38, the underlying data is according to Reviol et al. [182]*

are predefined as $D_{\mathrm{P}} = 0.35\,m$ for the outer diameter, $R_{\mathrm{Hub}} = 0.015\,m$ for the hub radius and $n_{\mathrm{z}} = 3$ for the number of blades. The algorithm is applied to take five different radial sections into account.

After defining all input parameters, the algorithm is started. The chord length distribution is estimated as the intermediate result, and every considered radial section is filled with the most suitable flow profile. In the case of Propeller B, the algorithm identifies the Eppler E817 profile as the most suitable profile for all sections, except for the section at the tip. The tip section is filled with the NASA NLF1015 profile. The computed chord length distribution $l\,(r)$ is in the interval of $l = [0.03,\ 0.08]\ m$. The intermediate results are illustrated by Figure 8.5. While Figure 8.5a shows the chord length distribution $l\,(r)$, in Figure 8.5b, the course of the mounting angle $\varphi\,(r)$ is drawn. Figure 8.5c depicts Lilienthal's polar plot data of the selected profiles. The Reynolds number stated here was calculated on the basis of the suggestion of Chhabra and Richardson according to Equation 5.38. The designations of the intended profiles are labelled in all subfigures.

Concerning the chord length, it needs to be highlighted that the course of
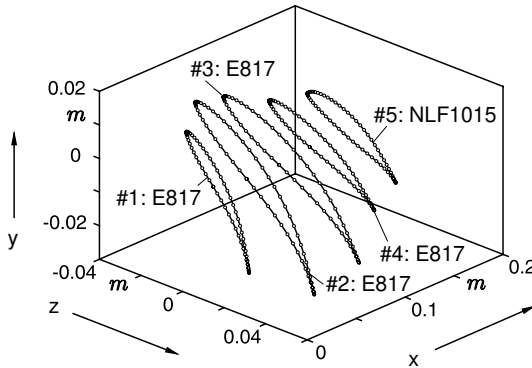
Figure 8.6. *Point cloud for example design process to derive the shape of Propeller B, each profile is marked with a continuous curve and its section and name, presentation according to Reviol et al. [181]*

the curve initially rises over the first two radial sections. Following the rising regime, the course becomes horizontal, and finally decreases. The change in monotonicity is in analogy with the chord length distribution according to Schmitz – see Chapter 4.2.3 – and is caused when swirl is taken into account. Regarding the mounting angle, it can be seen that this quantity amounts to $\varphi = 42.95\,°$ at the hub and decreases, initially quickly, over $31.60\,°$ to $23.85\,°$ until the middle of the blade is reached. The course of the curve flattens more and more the closer the considered section lies to the hub. The mounting angle of the last section is calculated with $\varphi = 22.02\,°$. The interval of the mounting angle can be specified by $\varphi = [20,\ 45]\,°$.

The following step of the algorithm procedure computes the transformations of the profile coordinates to obtain a three-dimensional blade. To do this, the profile data is scaled and transferred into different cylindrical planes that have a radius of each considered radial section. For the manufacturing process performed later, each profile is aligned to a fictive spar. As a result, a point cloud of all the profiles considered is obtained. This result is depicted in Figure 8.6. For better understanding, the points of each profile are connected by a continuous curve. Furthermore, the profiles are labelled with their designations.

All relevant operating parameters are calculated at the end of the design

(a) Isometric view   *(b) Front view*

(c) Side view   *(d) Top view*
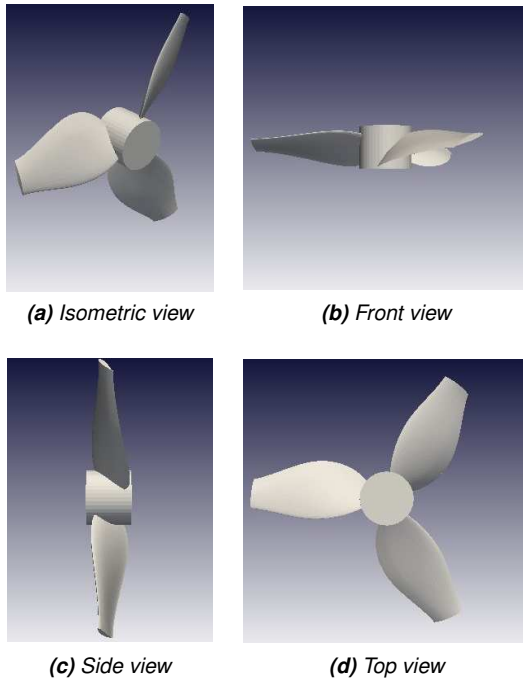
Figure 8.7. *Different views of Propeller B, presentation according to Reviol et al. [181]*

processs. For the predefined parameters of $n = 380\,min^{-1}$ for shaft speed and $\dot{V} = 54.5\,l/s$ for the mass flow rate, a drive power of $P_{\mathrm{PP}} = 296.06\,W$ is estimated. This is equal to a torque of $T_{\mathrm{PP}} = 7.44\,Nm$. In addition, the power of the jet is calculated with $P_{\mathrm{Jet}} = 75.60\,W$ and, so, the efficiency amounts to $\eta_{\mathrm{P}} = 0.26$. In Table 8.2, all relevant target parameters are summarised. Note that all previously defined and estimated quantities are considered again for the calculation of the power characteristics. Hence, all mandatory parameters of Propeller B are shown in Table 8.4.

The geometrical result of the design process in the form of the point cloud, according to Figure 8.6, can be handled in any 3D-CAD tool. By connecting the points first with spline curves and subsequently the curves with free-form surfaces, the shape of one single blade can be designed. Rotating the surface

Figure 8.8. *Propeller B, manufactured prototype, presentation according to Reviol et al. [182]*

n_{z} times about the symmetry axis of the machine and adding a hub geometry produces the final 3D-CAD model of the designed propeller. Propeller B was constructed with a similar procedure. The resultant 3D-CAD model is shown in Figure 8.7. In this figure, Propeller B is depicted in isometric view and also in top view, front view, and side view.

After performing the design process and designing a 3D-CAD model of the developed propeller, the manufacturing process of Propeller B can be started. Figure 8.8 shows a photograph of the propeller finally created.

Table 8.2. *Calculated process parameters of Propeller B*

Estimated jet power P_{Jet}	$75.60\,W$
Estimated torque T_{PP}	$7.44\,Nm$
Estimated power P_{PP}	$296.01\,W$
Efficiency η_{P}	0.26

8.2. Predicting characteristics

The design process only includes the calculation of the design point, but in many cases, a fluid machine is not applied at its intended operating point. Hence, the design process is enhanced by the inverse calculation method – see Chapter 7.3.2 for details. This procedure has to be performed subsequently for the design process and requires the parameters of the desired operating point as well as the parameters of the design point.

8.2.1. Propeller A

As explained in Chapter 7.3.2, the inverse calculation of the characteristics requires a range of data. In general, the data includes the design point as well as the geometrical specifications defined within the design process. Both are described in detail in Chapter 8.1.1. In addition, the procedure calls for the operation point, which has to be considered. Hence, shaft speed n_{OP}, consistency k_{OP}, flow index m_{OP}, and density ρ_{OP} of the operation point must be specified. With regard to the shaft speed, it is possible to set a single value, but it is more appropriate to choose an interval of interest, as done in this research project. Table 8.3 gives an overview of all data.

Running the algorithm produces the characteristic data for power and efficiency. Note that the procedure can either be computed to calculate the behaviour of a designed propeller for partial and overload – this means for the intended design fluid – or for an arbitrary fluid. In the first case, apart from the shaft speed, the operating data is identical to the design data.

The inverse calculation algorithm is computed for the shaft speed range of $n_{\mathrm{OP}} = [0, 300] \, min^{-1}$ and for the design fluid. The numerical results of the inverse calculation procedure are plotted in Figure 8.9. The estimation for torque T_{PP} is shown by a continuous line, while the efficiency η_{P} is drawn in a broken line. Furthermore, the design parameters torque, specified as $T_{\mathrm{PP,Des}} = 0.21 \, Nm$, efficiency calculated as $\eta_{\mathrm{P,Des}}$, and shaft speed, given as $n_{\mathrm{Des}} = 160 \, min^{-1}$, are marked in Figure 8.9.

The plausibility of torque can be assumed because of the intersection with

		1	2	3	4	5
Operation	Shaft speed range n_{OP} $\left[min^{-1}\right]$			[0, 300]		
	Consistency k_{OP} $\left[Pa\,s^m\right]$			8.75		
	Flow index m_{OP} $[-]$			0.14		
	Density ρ_{OP} $\left[kg\,m^{-3}\right]$			1000		
Design point	Shaft speed n $\left[min^{-1}\right]$			160		
	Consistency k $\left[Pa\,s^m\right]$			8.75		
	Flow index m $[-]$			0.14		
	Density ρ $\left[kg\,m^{-3}\right]$			1000		
	Torque T_{PP} $[Nm]$			0.21		
	Efficiency η_{P} $[-]$			0.20		
Geometrical parameters	Propeller diameter D_{P} $[m]$			0.18		
	Hub radius R_{Hub} $[m]$			0.015		
	Tank diameter D_{T} $[m]$			0.29		
	Fill level H_{F} $[m]$			0.392		
	Mixing time $\mathcal{T}$ $[s]$			5.1		
	Blade number n_{z} $[-]$			3		
	Radial sections			5		
	Mean section radius $[m]$	0.0225	0.0375	0.0525	0.0675	0.0825
	Profile type	FX60	FX60	FX60	E817	E817
	Chord length l $[m]$	0.128	0.094	0.071	0.060	0.061
	Angle α $[°]$	57.20	43.14	35.34	30.55	23.35
Misc.	Reynolds number calculation			Generalised		

Table 8.3. *Operating point and design parameters of Propeller A*

both the origin of the diagram and the design point. The course of the efficiency is also plausible, because of the intersection of the curve with the design point. However, the very discontinuous course (marked in the diagram with *unclear*) of the curve for both torque and efficiency and the still rising efficiency for overload is striking. Note that this fact is caused by the profile database. This issue will be discussed intensively in Chapter 10. However, it has to be said that only an experimental validation is able to verify the numerical procedures. This validation has to be performed for fluid properties which differ from those of the design fluid. In this chapter, the application of the method is performed. Hence, the characteristic curve of the propeller for the design fluid is of interest and the fluid data is chosen identically to this point. Later, in Chapter 9.3.1, the propeller is investigated experimentally, and the method of inverse calculation is examined for the utilised test fluid.
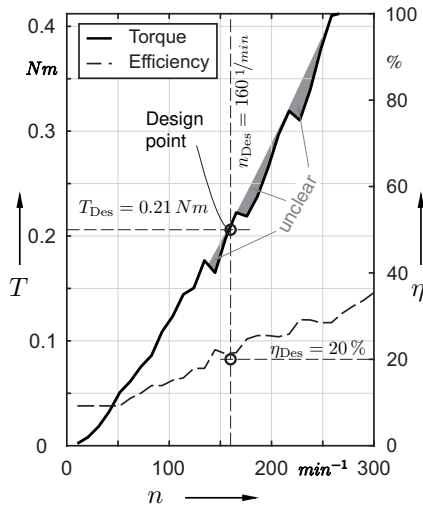
Figure 8.9. *Calculated characteristics of Propeller A as torque over shaft speed (continuous line) and efficiency (broken line), containing the numerical results of the design point, presentation according to Reviol et al. [181]*
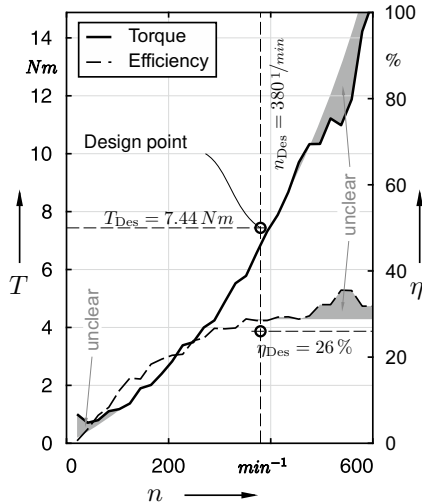
Figure 8.10. Calculated characteristics of Propeller B as torque over shaft speed (continuous line) and efficiency (broken line), containing the numerical results of the design point, presentation according to Reviol et al. [181]

8.2.2. Propeller B

In analogy to Propeller A, the second propeller is considered here for the design fluid only. Hence, the parameters k_{OP}, m_{OP}, and ρ_{OP} are equal to the design point and only the shaft speed n_{OP} is varied in the interval of $[0,\,600]\,min^{-1}$. Table 8.4 contains all data of Propeller B to perform the calculation procedure.

Running the algorithm for inverse calculation, the characteristics for torque and efficiency – according to Figure 8.10 – can be found. The course of torque T_{PP} is drawn as a continuous line and the efficiency η_{P} is drawn as a broken line. In addition to the derived parameters, the input parameters to specify the design point are added to the diagram. This point is given by the torque of $T_{\mathrm{PP,Des}} = 7.44\,Nm$ for a shaft speed of $n_{\mathrm{Des}} = 380\,min^{-1}$. The efficiency in this point reaches a value of $\eta_{\mathrm{P,Des}} = 0.26$.

As can be seen in Figure 8.10, both curves intersect the origin of the diagrams. The calculated design point fits the estimated curves quite well – but the efficiency only reaches a plateau range at the design point and starts

		1	2	3	4	5
Operation	Shaft speed range n_{OP} $[min^{-1}]$			[0, 600]		
	Consistency k_{OP} $[Pa\,s^m]$			14.50		
	Flow index m_{OP} $[-]$			0.29		
	Density ρ_{OP} $[kg\,m^{-3}]$			1000		
Design point	Shaft speed n $[min^{-1}]$			380		
	Consistency k $[Pa\,s^m]$			14.50		
	Flow index m $[-]$			0.29		
	Density ρ $[kg\,m^{-3}]$			1000		
	Torque T_{PP} $[Nm]$			7.44		
	Efficiency η_{P} $[-]$			0.26		
Geometrical parameters	Propeller diameter D_{P} $[m]$			0.35		
	Hub radius R_{Hub} $[m]$			0.015		
	Tank diameter D_{T} $[m]$			2.50		
	Fill level H_{F} $[m]$			1.4		
	Mixing time $\mathcal{T}$ $[s]$			126		
	Blade number n_{z} $[-]$			3		
	Radial sections			5		
	Mean section radius $[m]$	0.031	0.036	0.095	0.127	0.159
	Profile type	E817	E817	E817	E817	NLF1015
	Chord length l $[m]$	0.049	0.078	0.078	0.056	0.039
	Angle α $[°]$	42.95	31.60	23.85	20.37	22.02
Misc.	Reynolds number calculation			Metzner-Reed		

Table 8.4. Operating point and design parameters of Propeller B

8. Application of the method

rising again for high overload. In addition to this implausible behaviour of the efficiency, the course of torque is discontinuous again. Both regions are marked in the figure as *unclear* – if these regions are ignored, the course of both parameters would appear very plausible: the torque would rise continuously and the efficiency would reach its highest value in the design point, which starts a plateau-like region of nearly equal efficiency. Note that this implausible course of the curves can be neglected, not because of a deficiency in the calculation method, but in the profile database. This will be discussed in greater detail in Chapter 10. In the next step, Propeller B – and, so, Propeller A – have to be examined by an experimental study to verify both the design process and the method of inverse calculation.

9. Experimental investigations

In this chapter, the experimental validation of the design process discussed above and the calculation procedure will be presented. Initially, the test configuration of both the hydraulic systems developed will be explained – each hydraulic system consists of one of the previously discussed propellers, see Chapter 8.1.1 and 8.1.2 respectively, and a vessel is related to each propeller. Not only the geometrical specifications, but also the fluid intended for each system is important, and so these are explained in the description of the test configuration. This includes a study of available model fluids to select a suitable test fluid.

The experimental explorations are presented in the second part of this chapter. Before detailed experimental investigations are discussed, the performance characteristics of both the propellers are examined in a preliminary experimental study.

9.1. Model fluid study

In Chapter 8.1, the influence of the rheology of the fluid on the operation point of the propeller was emphasised. To investigate the designed propeller, it is obvious that the propeller has to be examined under known conditions – especially for the design point that includes the design fluid. Hence, model fluids with distinct rheological properties have to be created.

Preselection of additives

In the literature, a broad variation of additives is known to establish model fluids with different fluid patterns. In this thesis, only *generalised Newtonian fluids* (see Chapter 5.2) especially purely shear thinning fluids are of interest. Fluids with clear distinct shear thinning behaviour can be obtained by mixing different additives with water. As a preselection, four additives are chosen. These are carboxymethyl cellulose (CMC), polyacrylamide (PAA), xanthan
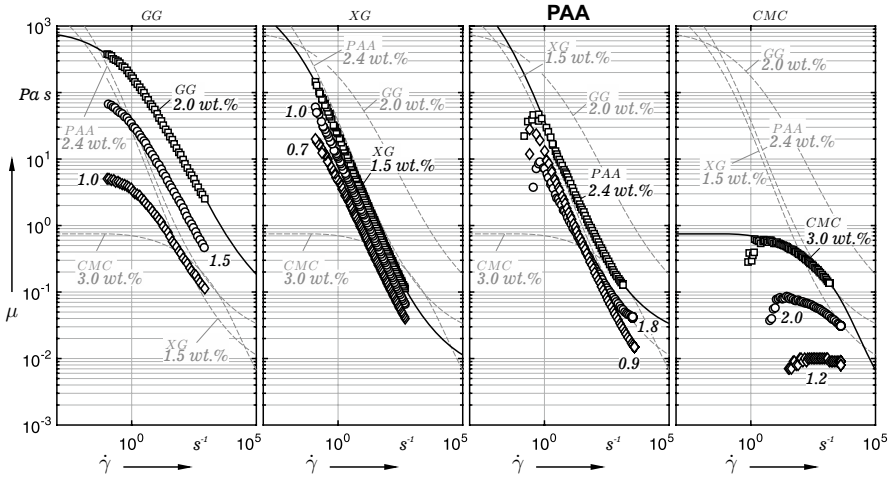
Figure 9.1. *Viscous characteristics of **guar gum** (GG: $2.0\,wt.\%$ ($\square$), $1.5\,wt.\%$ ($\circ$), $1.0\,wt.\%$ ($\diamond$), data taken from Torres et al. [225]), **xanthan gum** (XG: $1.5\,wt.\%$ ($\square$), $1.0\,wt.\%$ ($\circ$), $0.7\,wt.\%$ ($\diamond$)), **polyacrylamide** (PAA: $2.4\,wt.\%$ ($\square$), $1.8\,wt.\%$ ($\circ$), $0.9\,wt.\%$ ($\diamond$)) and **carboxymethyl cellulose** (CMC: $3.0\,wt.\%$ ($\square$), $2.5\,wt.\%$ ($\circ$), $1.2\,wt.\%$ ($\diamond$)) as aqueous solutions with different concentration of each specimen*

gum (XG), and guar gum (GG). Their principal rheological behaviour will be assessed to select the final model fluids.

Aqueous solutions of the aforementioned additives were examined in numerous investigations. Often, the viscous behaviour of different concentrations was of interest. The aforementioned additives were examined in different concentrations – for example, by Torres et al. [225] for GG, by Klein and Kulicke [113, 114] for PAA, by CPKelco [45] for XG, and by Ghannam and Esmail [73] for CMC, but also in preliminary tests within this research project. In Figure 9.1, the viscous behaviour of different aqueous solutions of these additives in water is shown. Each specimen was applied in different concentrations. All measurements were performed in a Searle-typed coaxial cylinder measuring system from Brookfield, except the examinations of GG, which were taken from Torres et al. [225]. These were performed in a parallel plates system. As can be seen, the viscous patterns of each type of solution differ from each other. In the examined shear strain regime, the considered concentrations of GG and CMC reach their zero-shear-rate viscosity μ_0, while
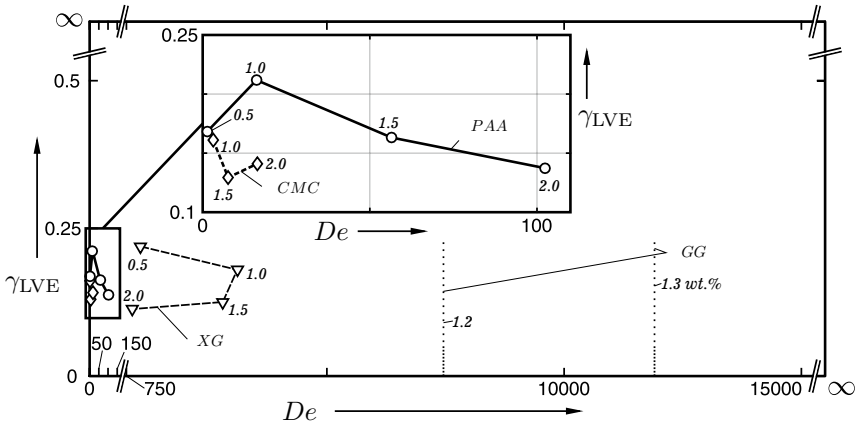
Figure 9.2. *Viscoelastic characteristics of* **carboxymethyl cellulose** *(CMC: ⬦),* **polyacrylamide** *(PAA: ○),* **xanthan gum** *(XG, ▽) and* **guar gum** *(GG: dotted line, taken as relaxation time λ from Patel et al. [153]) as aqueous solutions with different concentration of each specimen, depicted as LVE-range limit γ_{LVE} over $De = \lambda \cdot 10 \, rad/s$ in Pipkin's diagram*

PAA and XG reach almost their infinity-shear-rate viscosity μ_∞. For each mixture, the power law range can be identified. In principle, therefore, the viscous properties of the above additives are suitable for the planned experimental investigations of both propellers.

The requirement for *generalised Newtonian fluids* is strictly connected to the viscoelastic properties of the model fluid – the model fluid must not have any pronounced elastic behaviour. Therefore, in Figure 9.2, mixtures of the four additives are plotted in Pipkin's diagram to assess their viscoelastic behaviour. To obtain these results, frequency and amplitude sweeps were performed in a parallel plate measuring system[1]. As a result, the border of the LVE regime γ_{LVE} and the relaxation time λ of each probe were calculated. The Deborah number was computed by multiplying the relaxation time with the frequency of the amplitude sweep. This frequency was set to $\omega = 10 \, rad/s$. This does not apply to the results of GG. These were taken from Patel et al. [153] – because of the unclear parameters of the LVE region in the publication, these results are marked as a dotted line in Pipkin's diagram. From all the samples examined, GG is the fluid with the most viscoelastic properties. For CMC, PAA, and XG, only slight viscoelastic pat-

terns could be identified, while XG has more pronounced, though still low, viscoelastic behaviour.

For further examinations, CMC and XG were chosen on account of their good viscous properties and their low elastic behaviour. Hence, only these two types of additives are discussed in greater detail below.

Xanthan gum

Xanthan gum is a natural, widely-used polysaccharide [110; 152], and widely-used in the food industry, e.g. as a thickening agent, but also in the pharmaceutical and drilling industries [110; 152; 193; 198]. The state of aggregation is solid, and XG is typically processed to a cream-coloured and odourless powder. When XG is mixed with water, the powder swells and the viscosity of the solution increases. The rheology of aqueous XG solutions has been discussed by many researchers, such as e.g. by Cauvelier and Launay [37]; García-Ochoa et al. [71]; Sanderson [198]; Son et al. [214] and many others. Figure 9.3 shows a sample of xanthan gum powder (on the left).

Because of its distinctly non-Newtonian behaviour and the easy change of this behaviour by changing the concentration of xanthan gum, aqueous XG solutions are also utilised in the research of process industry and fluid machinery to model the required rheological parameters of the fluid in the process under consideration [178; 179; 228]. However, XG solutions are found to be viscoelastic, allthough the elastic behaviour is described as highly dependent on the concentration of XG [37; 214]. Hence, XG solutions can be considered quasi-viscoinelastic, provided a low concentration of XG is used. As an additional rheological aspect, initial yield stress has to be regarded for aqueous XG solutions. The amount of this initial stress also depends on the concentration of XG but rises quickly. Nevertheless, for low concentrations of XG of above $c \approx 15 \, g/l$ the yield stress is lower, than $\tau_0 \approx 3 \, Pa$, as discovered by García-Ochoa and Casas [70]; Hannote et al. [87]; Torres et al. [224]. In line with the viscoelastic effects, initial yield stress is also negligible for low XG concentrations.

In this thesis, aqueous XG solutions with slight XG concentrations were

Figure 9.3. *Additives used to produce the applied model fluids: xanthan gum (XG) (left) and carboxymethyl cellulose (CMC) (right), photographer: Christian Landfester*

utilised. Hence, all samples are regarded as viscoinelastic and non-plastic. The applied XG powder is the KELZAN type distributed by CPKelco – see Appendix C.1.

Carboxymethyl cellulose

Carboxymethyl cellulose is an important industrial polymer and is a derivative of cellulose resulting from the reaction of cellulose with chloroacetic acid [24; 99]. Different types of CMC exist [193], but in the present study, sodium carboxymethyl cellulose SCMC was used, and is referred to as CMC in the following.

Carboxymethyl cellulose is solid aggregated and typically processed to a granulate or powder. CMC is almost totally white and odourless. Figure 9.3 shows a sample of CMC powder (sample on the right side). When CMC

powder is added to water, the powder swells, and, depending on the concentration of added CMC, the viscosity of the mixture rises.

As mentioned, CMC is a widely-used industrial polymer and is applied in aqueous solutions in the food and pharmaceutical industry, and also in engineering processes like drilling or the fuel industry, see Abdelrahim and Ramaswamy [2]; Boylu et al. [27]; Rowe et al. [193]. Because of the wide distribution and the different utilisations of aqueous CMC solutions, knowledge of the rheology is important and has been investigated by a various number of researchers, such as by Abdelrahim and Ramaswamy [2]; Benchabane and Bekkour [11]; Ghannam and Esmail [73] and others.

Furthermore, the viscoelastic properties of aqueous CMC solutions have been investigated in detail. Hence, it is known that CMC solutions become more and more viscoelastic for rising CMC concentrations. Benchabane and Bekkour [11] discovered a critical concentration of $c \approx 3.0\,wt.\%$ for suddenly rising viscoelastic effects. This means that for lower concentrations, elasticity is of minor importance. This is in good accordance with a study outlined by Reviol et al. [180]. The authors investigated aqueous CMC solutions with concentrations of at most $c = 2.0\,wt.\%$ and did not find any significant elastic, but only viscous, fluid behaviour.

Owing to the application of mixtures with CMC concentrations of $c < 3.0\,wt.\%$, in the scope of this work, aqueous CMC solutions will be considered to be viscoinelastic. The CMC powder used is the WALOCEL CRT 40000 PV from Dow Construction Chemicals; see Appendix C.2.

9.2. Test configuration

As mentioned, the first part of this chapter provides an overview of the test configuration. Because two different propellers are designed, two different test configurations have to be described. The configuration of the first propeller, referred to as Propeller A, which was designed for viscous but irrotational fluid flow, is discussed first.

9.2.1. Propeller A

Test stand

Propeller A was designed to operate in the laboratory scaled test bench in accordance with Figure 9.4. For details of the design process, refer to Chapter 8.1.1. The test stand has a modular design and, so, all relevant components can be changed with little effort. The most important components will be described below.

(a) Schematic view   *(b)* Photograph
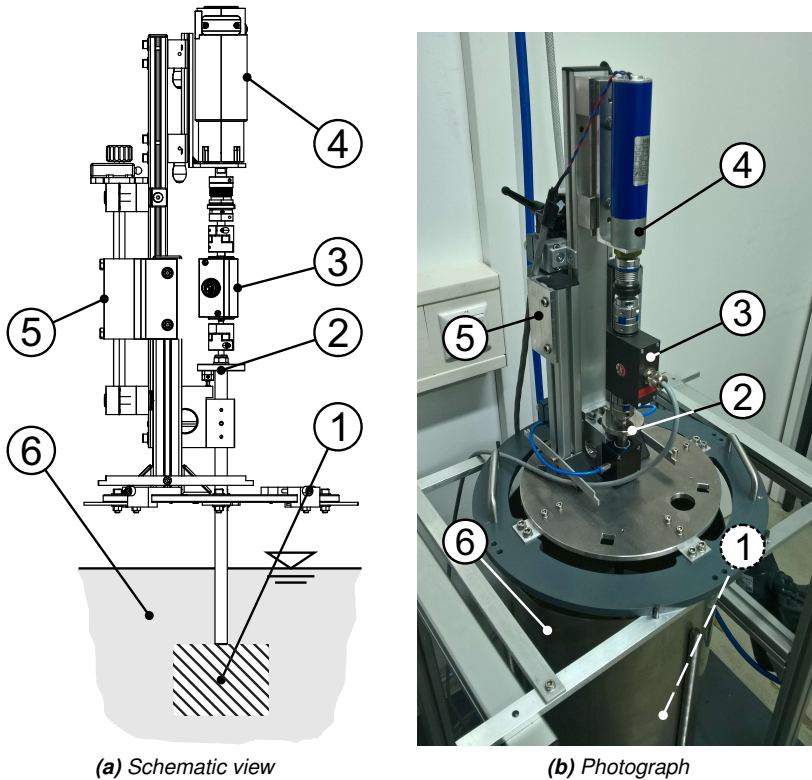
Figure 9.4.   *Test stand for Propeller A, shown as schematic view and photograph, representation according to Reviol et al. [182]*

At Position $\left(1\right)$, the propeller or any other test specimen is located and driven by a vertical shaft, which is connected to a DC motor $\left(4\right)$. To investigate fluid flow with low as well as with high viscous properties, two different motors with different power outputs can be utilised. The specifications of these can be found in Appendix B.1. The parameters, which are of major interest in the present investigations, are torque and shaft speed. Both parameters are measured by a single device, located at Position $\left(3\right)$. Two torque-/shaft speed-meters are available, which should be selected on the basis of the maximum value of the expected torque range. The test stand is designed to be equipped with DRWPL-I torque meters from ETH-Messtechnik GmbH. The data sheet of this sensor type can be found in Appendix A.2.

Owing to the low forces, especially for slow fluid flow and slow shaft speed, bearing friction has a huge impact on the quality of the measurement. To reduce this influence, the whole drive chain is mounted by precision air bearings. The bearing unit is positioned at $\left(2\right)$ between the test specimen and the torque sensor. The technical specifications of both the axial and the radial bearing can be found in Appendix B.3.

To change the position of the test specimen in relation to the surface of the probe, the test bench is equipped with an axial displacement unit $\left(5\right)$. This is important, in particular, for the use of different vessels. All investigations were performed in a cylindrical vessel with an inner diameter of $D_{\mathrm{T}} = 0.29\,m$, while the fill level was $H_{\mathrm{F}} = 0.392\,m$ for all measurement series. Figure 9.4a shows only a schematic view of the vessel because of the possibility of using different tanks, while Figure 9.4b depicts the utilised vessel at Position $\left(6\right)$.

A measurement device – an NI USB-6259 BNC from National Instruments – was applied to record the measurement data of the observed parameters. To analyse this data, a desktop PC with the tool Matlab from MathWorks was utilised. These devices are not shown in Figure 9.4 for reasons of simplicity.

Modelled fluid flow

In the context of this work, aqueous solutions with low XG concentrations are used. Aqueous XG solutions are suitable to model fluids with *generalised*
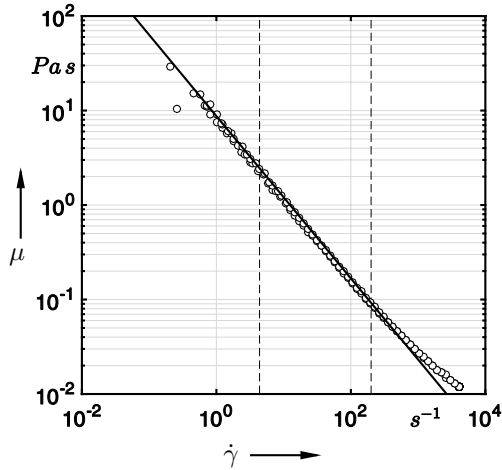
Figure 9.5. *Apparent viscosity of aqueous xanthan gum mixture,* $0.75\,wt. - \%$, *model fluid of Propeller A, illustration according to Reviol et al. [182]*

Newtonian fluid behaviour, as claimed in the fundamentals of the design procedure in Chapter 7 and demonstrated in Chapter 9.1.

The design point of Propeller A is discussed in Chapter 8.1.1, where the design fluid was set to the rheological parameters $k = 8.75\,Pa\,s^m$ and $m = 0.14$ according to the *power law* viscosity model, see Equation 5.27. The density is assumed to be near that of pure water because of the slight addition of XG and is estimated at $\rho = 1000\,kg\,m^{-3}$. A fluid with these properties can be produced using an aqueous solution with a concentration of $c = 0.75\,wt.\%$ xanthan gum powder.

After processing the aqueous XG mixture in the test facility, the mixture was allowed to rest for a defined period of time to allow the whole powder to swell. The time period was set to one day. After this time period, a sample from the test stand was taken and investigated in a Searle-type viscometer from Brookfield with a predefined measurement protocol. The data sheet of the applied test device can be found in Appendix A.1.

In Figure 9.5, the viscous properties of the XG solution under investigation are plotted as the apparent viscosity μ over the shear rate $\dot{\gamma}$. In addition to the viscosity function, the figure also contains the regression of the design fluid

according to the *power law* in accordance with Equation 5.27. The approximation is indicated by a continuous line. For the mathematical fit of the measurement data, only valid measurement points were taken into account, while statistical outliers and data points outside of the power law region are ignored. As can be seen in Figure 9.5, for shear rates under $\dot{\gamma} = 7.5 \cdot 10^0 \, s^{-1}$, some outliers can be found, while the power law region ends at about $\dot{\gamma} = 1.9 \cdot 10^2 \, s^{-1}$. Hence, the applied shear rate interval lies between these two values and is qualitatively marked by two broken lines. The courses of both the measurement data and the regression reveal very good agreement.

For statistical certainty, five measurement series were performed. The first measurement series is ignored because of the destruction of long polymer chains by initial shear stresses, as suggested by Mezger [135]. Performing this procedure guarantees similarity between all measurements independent of the measurement time. Aqueous XG solutions are prone to a natural ageing effect. Hence, all examinations are carried out promptly in relation to each other. In preliminary investigations, the ageing effect could be avoided – or at least reduced, for a few weeks by using a preservative agent. To prevent influences caused by ageing over the subsequently performed power examinations, isocil acid was added as a stabiliser.

As a result of the viscosity measurements, the averaged power law parameters were determined as $\overline{k} = 8.462 \, Pa \, s^m$ for mean consistency and $\overline{m} = 0.136$ for mean flow index. To observe the quality of the measurement, the standard deviation was considered. For the consistency, the standard deviation amounts to $\varsigma_k = 0.492 \, Pa \, s^m$ (relative value: $\varsigma_k = 5.81 \, \%$), while for the flow index, a value of $\varsigma_m = 0.01$ (relative value: $\varsigma_m = 7.35 \, \%$) is calculated. Comparing both averaged parameters with each parameter of the design fluid, a deviation of $\Delta k = -3.26 \, \%$ for consistency and $\Delta m = -3.55 \, \%$ for flow index resulted. Table 9.1 summarises the viscosity parameters of the applied model fluid and compares them with the design values.

Among the investigation of viscous properties, the density was also examined. Owing to the low mass of added XG, the density was slightly changed in contrast to pure water and amounted to $\overline{\rho} = 998.00 \, kg/m^3$. The density was measured by visibly observing hydrometers, type L 50-095, compliant

Table 9.1. *Rheological parameters of the applied model fluid in comparison with the design fluid, parameters according to power law*

	$c\,[wt.\%]$	$k\,[Pa\,s^m]$	$m\,[-]$	$\rho\,[kg\,m^{-3}]$
Design fluid	-	8.747	0.141	1000
XG1	0.75	8.462 ± 0.49	0.136 ± 0.01	998.00 ± 0.5
Uncertainty		$-3.26\,\%$	$-3.55\,\%$	$-0.20\,\%$

with ISO387:1977-09 [103] (DIN12790:2019-12 [51] and DIN12791-1:2019-12 [52]) and, so the calculation of the standard deviation is not appropriate because of the measurement uncertainty of $\pm0.5\,kg/m^3$ given by the scale. Hence, for density, the measurement error is indicated instead of the standard deviation.

The processed model fluid is named **XG1**. As can be seen in Table 9.1, the uncertainty of all parameters is under $3.55\,\%$ and the model fluid fits the design fluid very well.

9.2.2. Propeller B

The second propeller is named Propeller B. The test facility and the applied model fluids are described in the following.

Test stand

Since Propeller A was designed for investigations in laboratory-scaled dimensions, Propeller B is designed to be one dimension larger to investigate not only the power characteristics, but also the velocity field of the jet.

The test facility for Propeller B is shown in Figure 9.6 as a schematic overview, in Figure 9.7 as a detailed view, and in Figure 9.8 as photographs.

In principle, the test stand is a rectangular basin with a squared base area. The length of each side of the base area amounts to $L = 2.5\,m$. The height of the basin is approximately $H = 2\,m$; hence, for the volume of the test basin, it yields $V = 12.5\,m^3$. To achieve a more practical test configuration,
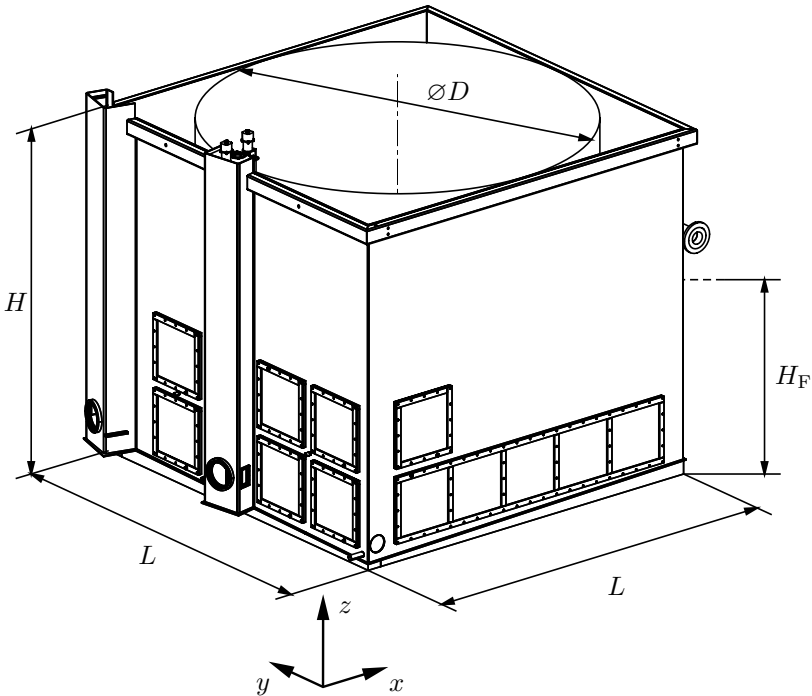
Figure 9.6. *Geometrical overview of the test basin, applied for experimental investigations of Propeller B, schematic view*

a cylindrical sheet is assembled in the test bench. Since all experimental investigations were performed for a fluid elevation of $H_\mathrm{F} = 1.4\,m$, an effective volume of $V \approx 6.87\,m^3$ results.

In Figure 9.7 and Figure 9.8, Position $\textcircled{1}$ marks the position of the propeller. The propeller is driven by a hydraulic motor $\textcircled{3}$. This principle was chosen because of the higher power density of a hydraulic system compared to electric engines – see Appendix B.2 for details about technical specifications. To measure the torque and shaft speed, a measuring device is mounted in a submersible box $\textcircled{2}$. The box is open for the shaft and sealed by two dynamic seals. To avoid water leakage, the box is air-pressured. Inside the box, a DRWPL-II torque/shaft speed sensor from ETH Messtechnik GmbH is installed. The technical data sheet of the sensor can be found in Appendix A.2.
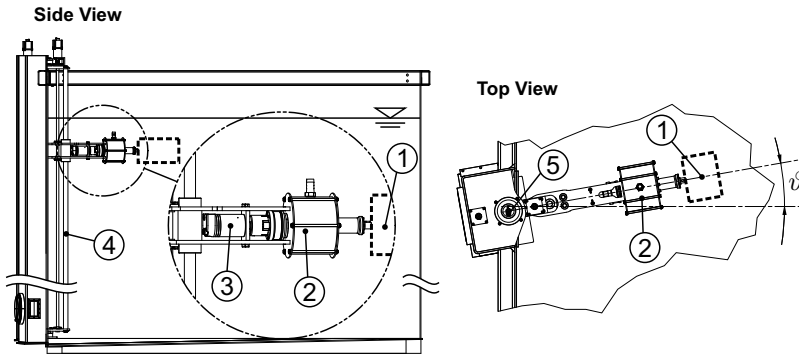
Figure 9.7. *Test setup for Propeller B, schematic view, illustration according to Reviol et al.*
[182]

Positions (1) to (3), which is grouped to the mixing unit, can be rotated
by the angle ϑ over a virtual fixing point that lies just on the sidewall of the
test bench. Simultaneously, the whole mixing unit can be linearly moved in
a vertical direction along a jack screw (4). Both the angular and the verti-
cal position can be controlled by two actuating motors positioned at (5). By
these degrees of freedom, a propeller position – which is commonly found
in biogas power plants and waste water treatment plants – can be achieved,
while different assembly positions can be modelled very easily.

Propeller B is investigated not only for the power characteristics, but also for
the velocity distribution of the propeller's jet. To measure the velocity field,
an automatic linear actuating system is mounted at the top of the test bench
(7). The actuating system is computer-controlled and can reach every point
of the test basin in all spatial coordinates by following a Cartesian grid. The
actuating system is equipped with a measuring probe. At the lowest point
of this probe, a Vector UDA sensor from Nortek AS is mounted (6). This
sensor measures the velocity vector at one single point by interpreting the
sound response. To do this, the emitter – positioned in the centre of the sen-
sor – sends an acoustic signal at a measurement volume of 5–$20\,mm$ height,
positioned approximately $157\,mm$ under the sensor. The response of the sig-
nal is measured by three different receivers, arranged under $30\,°$ against the
perpendicular plane of the emitter, and rotated by $120\,°$ around the emitter.

(a) *Filled vessel*

(b) *Visualisation of mixer position*
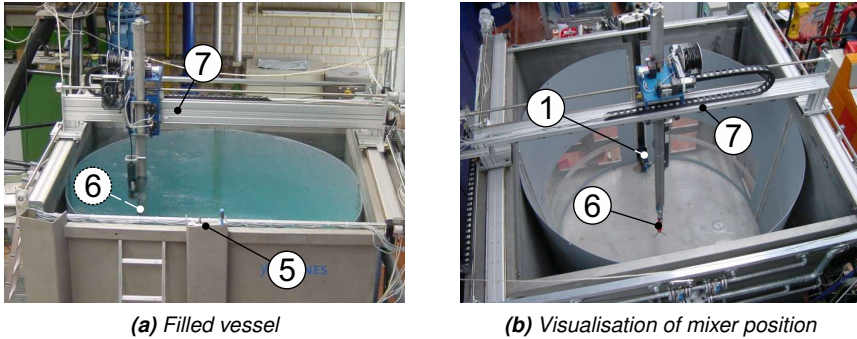
Figure 9.8. *Test setup for Propeller B, photographs, author's own representation according to Urban [228]*

The sensor has an output sampling rate of $64\,Hz$. The accuracy amounts to $\pm0.5\,\%$ of the measured value. Figure 9.9 shows the sensor in detail. Comparing the frequency change of the measured signal with the emitted signal determines the velocity. Since three different positions are observed, the 3D spatial velocity field can be determined. Further details about the sensor are given in Appendix A.3. The principle is a contactless method and, so, influences of the measurement method on the measurement volume are very low. Alternative methods, such as laser Doppler anemometry, are not suitable on account of the opaque nature of the test fluids.

To control the test bench and to acquire the measurement data, a desktop PC is utilised. The desktop PC and the test facility are connected by an NI
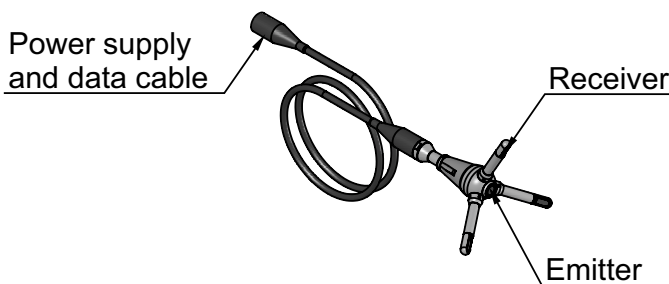
Figure 9.9. *UDA sensor, technical sheet Nortek AS [145]*

PCI-6259 I/O-Module from National Instruments and by the corresponding BNC connector block NI BNC-2090A. Software control and post processing are performed by the software tool Labview from National Instruments and by Matlab from Mathworks respectively. In both Figures 9.7 and 9.8, neither the devices to control the test facility nor the desktop PC to acquire and post-process the measurement data are shown for reasons of simplicity.

Modelled fluid flow

In analogy with Propeller A, a model fluid which closely resembles the design fluid has to be applied to investigate Propeller B at its design point. Instead of using aqueous xanthan gum solutions, aqueous carboxymethyl cellulose (CMC) solutions were used.

A model fluid is required that has the same rheological properties as the design fluid. The desired parameters were fixed by the design point given in Chapter 8.1.2. The *power law* model, according to Equation 5.27, was adopted to characterise the design fluid. The design consistency amounts to $k = 14.50 \, Pa \, s^m$, while the flow index at the design point is $m = 0.29$. The density was assumed to be similar to pure water and was defined as $\rho = 1000 \, kg \, m^{-3}$.

By performing a rheological study, a model fluid closely resembling the design fluid could be found. The final model fluid was achieved with a concentration of approximately $c = 1.25 \, wt. \, \%$ CMC powder. After adding the CMC powder to the test bench, the mixture was allowed to rest for a defined time period to allow all the added CMC powder to swell. However, because of the size of the vessel and, hence, of the water fraction, a relatively high mass of CMC powder was added, and the swelling process was supported by mixing the fluid with a small stirrer, before the aqueous CMC solution was allowed to rest for a few days. Isocil acid was added to stabilise the mixture, as for the XG solution, because of the results of a preliminary study on ageing effects. Because of the relatively high volume of the test stand for Propeller B, a slight deviation in the concentration of CMC leads directly to relatively high changes in the rheological parameter of the utilised fluid. Therefore, a final viscometric

Table 9.2. *Rheological parameters of applied model fluid in comparison with the design fluid, parameters according to power law*

	$c \, [wt.\%]$	$k \, [Pa \, s^m]$	$m \, [-]$	$\rho \, [kg \, m^{-3}]$
Design fluid	-	14.50	0.290	1000
C3	1.25	16.601 ± 1.07	0.302 ± 0.01	989.0 ± 0.5
Uncertainty		$+14.49\,\%$	$+4.138\,\%$	$-1.100\,\%$

test was performed after mixing the model fluid in the test facility. The measured parameters of the model fluid amount to $\overline{k} = 16.601 \, Pa \, s^m$ for consistency and to $\overline{m} = 0.302$ for the flow index, while the density was measured as $\overline{\rho} = 988.7 \, kg \, m^{-3}$. The applied hydrometer conforms with ISO387:1977-09 [103] (DIN12790:2019-12 [51] and DIN12791-1:2019-12 [52]). The values were obtained by averaging five measurement series. The standard deviation of the parameters was calculated as $\varsigma_k = 1.07 \, Pa \, s^m$ (relative value: $\varsigma_k = 6.445\,\%$) for consistency k, respectively $\varsigma_m = 0.010 \, Pa \, s^m$ (relative value: $\varsigma_m = 3.311\,\%$) for flow index m. The density was also measured and amounts to $\overline{\rho} = 989.0 \, kg \, m^{-3}$. Because the applied hydrometer must be observed visually, calculating the standard deviation is not appropriate, and the minimum scale unit of $0.5 \, kg \, m^{-3}$ is given as the quantity for the measurement error.

The relative deviations of the measured parameters from the design parameters are $\Delta k = +14.490\,\%$ for consistency, $\Delta m = +4.138\,\%$ for flow index and $\Delta \rho = -1.100\,\%$ for density. The parameters of the design fluid, the statistical results of the model fluid – referred to as **C3** in the following – and their deviation from each other are shown in Table 9.2.

At first glance, the deviation of the model fluid from the design fluid seems to be very high because of a relative error of about $14.5\,\%$ for the consistency, and even almost $4.2\,\%$ for the flow index. But on comparing the regression curves – as calculated by Equation 5.27 – both fluids are close together with similar viscous characteristics. Figure 9.10 depicts the apparent viscosity over the shear rate. The experimental results of the viscometric test are plotted by diamond symbols ($\diamond$), while the regression of the measurement data is plotted by a continuous line. In addition to both entries, the approximation
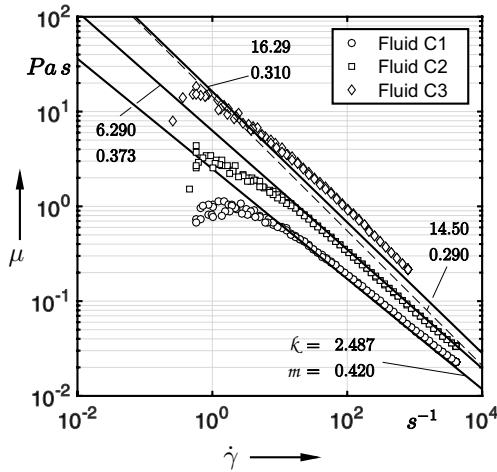
Figure 9.10. *Apparent viscosity of investigated aqueous carboxymethylcellulose-(CMC)-mixtures, C1, C2 and C3 , model fluids of Propeller B, illustration according to Reviol et al. [182]*

of the design fluid is depicted by a broken line. As can be seen, the deviation is slight for the region of moderate shear rates. With rising shear rates, the deviation becomes higher, because of the difference in the flow indices. The flow index is the exponent of the *power law* and represents the slope of a curve in a double logarithmic plot. Hence, the flow index is responsible for the divergence of both regression curves. Hence, the flow index is more important for the quality of the model fluid **C3** than the consistency. The error of the flow index is still in an acceptable region.

To preclude mistakes in comparing the experimental investigations with the predicted power characteristics, according to Chapter 8.2.2, the experimental investigation of Propeller B is enlarged for two further fluids with a minor concentration of CMC. This procedure is used in addition to prove the quality of the method developed for varying fluids, and for varying operating conditions. The supplementary model fluids are named **C1** and **C2** respectively and are processed and analysed in analogy with the test fluid **C3**. The concentrations are $c_{C1} = 0.62\,wt.\%$ and $c_{C2} = 0.83\,wt.\%$ respectively. The resultant consistency of fluid **C1** amounts to $k = 2.509 \pm 0.05\,Pa\,s^m$ (relative error: $1.99\,\%$)

Table 9.3. *Rheological parameters of applied model fluids for different operating points, parameters according to power law*

	$c\,[wt.\%]$	$k\,[Pa\,s^m]$	$m\,[-]$	$\rho\,[kg\,m^{-3}]$
C1	0.62	$2.509_{\pm0.05}$	$0.440_{\pm0.003}$	$991.0_{\pm0.5}$
C2	0.83	$6.122_{\pm0.12}$	$0.365_{\pm0.004}$	$989.5_{\pm0.5}$
C3	1.25	$16.601_{\pm1.07}$	$0.302_{\pm0.01}$	$989.0_{\pm0.5}$

and the flow index $m = 0.440 \pm 0.003$ (relative error: $0.682\,\%$). The density is measured as $\rho = 991.0 \pm 0.5\,kg\,m^{-3}$ (relative error: $0.05\,\%$), while the parameters of fluid **C2** are measured as $k = 6.122 \pm 0.12\,Pa\,s^m$ (relative error: $1.96\,\%$), $m = 0.365 \pm 0.004$ (relative error: $1.096\,\%$) and $\rho = 989.5 \pm 0.5\,kg\,m^{-3}$ (relative error: $0.05\,\%$). The change in the density is striking, but in comparison with the design fluid, the error is still slight, at most $-1.1\,\%$. All statistical parameters of the utilised model fluids are summarised in Table 9.3, while the measurement data of the viscometric tests of both fluids and their approximation curves is plotted in Figure 9.10. Fluid **C1** is plotted by circle symbols ($\circ$) and **C2** by square symbols ($\square$), while the regression of both fluids is drawn as a continuous line.

9.3. Preliminary investigations

Two propellers with different abstraction levels were designed. Both of these were examined in preliminary investigations. The aim of the preliminary study is to identify the necessary abstraction level for the upstream design process. To do this, both propellers are examined in the test facilities described in Chapters 9.2.1 and 9.2.2. The results of these investigations are detailed below. Finally, a brief assessment – which does not include a detailed discussion of the method and the abstraction level – is given. A detailed discussion is included in Chapter 10.1. The discussion is related to both the theoretical background and the detailed experimental investigations.

9.3.1. Propeller A

A software tool for the automatic control of the test stand is used for all examinations of the propeller. The tool varies the shaft speed over a given range and measures the torque. At the same time, the shaft speed is monitored for deviations from the control value. Each observed shaft speed holds for a certain time period. Over this period, both parameters are measured continuously, and finally averaged over the duration. The result is the power characteristic over the specified speed range.

To investigate Propeller A, a measurement survey with three repeating measurement series was performed. Figure 9.11 shows the result of the measurement campaign as torque T over shaft speed n. The measured values for torque are between $T = 0\,Nm$ and $T = 0.35\,Nm$ while the shaft speed was varied from $n = 0\,min^{-1}$ to $n = 300\,min^{-1}$. The recorded series are marked with different symbols: Series 1 with $\diamond$, Series 2 with $\circ$, and Series 3 with $\triangleleft$. In addition to the measurement data, the power curve is calculated. For comparison, the torque is derived from the numerical result and drawn as a continuous line in Figure 9.11. To assess the quality of both measurement and calculation procedures, the given design point consisting of torque $T_{\mathrm{PP}} = 0.21\,Nm$ and shaft speed $n = 160\,min^{-1}$ is depicted as well. The investigations, as explained, were performed by Reviol et al. [182].

The three different measurement series were statistically analysed. A standard deviation of at most $\varsigma_{\mathrm{max}} = 3.29\,\%$ was calculated. Because of the low value for deviation, the illustration does not contain error bars. As can be seen, all measurement series are close together.

Figure 9.11 also contains the results from the numerical procedure in accordance with Figure 8.9 for sake of comparison. The analysis of the course of the experimental results as well as the numerical results shows large differences between the two methods. The numerical results are more plausible on account of the intersection of the curve with the zero point and the design point. However, the discontinuous course of this curve is conspicuous and, therefore not very plausible, as already explained in Chapter 8.2.2. A strictly monotonous rise can be expected, but, for some segments of the curve, the
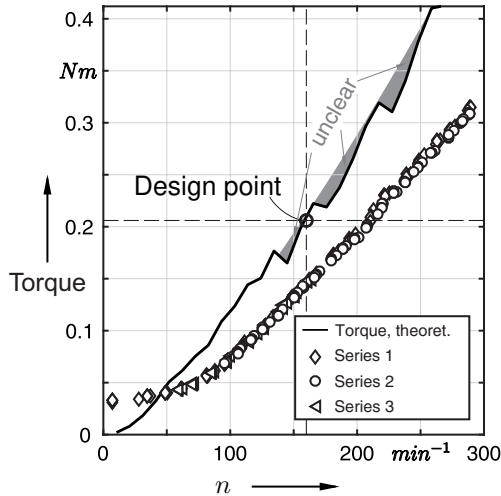
Figure 9.11. *Experimental data of Propeller A as torque over shaft speed (three measurement series, Marker Series 1: ◇, Series 2: ○, Series 3: ◁), compared with calculated characteristics (continuous line), containing the design point (chained line), illustration according to Reviol et al. [182]*

slope becomes negative. These regions are marked as *unclear* in the illustration. In contrast, the measurement results are very unsatisfactory. Despite the very small measuring errors, the course is not plausible, since neither the zero point nor the design point are within the measurement results.

There is a clear explanation for the deviations. The reason can be found in the abstraction level of the design process. For reasons of clarity, these points are discussed together with the results of Propeller B in Chapter 10.1.2.

9.3.2. Propeller B

As will be explained later, only Propeller B is used for supplementary investigations. The explanation for this procedure is given in Chapter 9.3.3. The investigations include the examination of the flow field for the analysis of the jet developed by the propeller. Therefore, Propeller B is not operated with an automatic change of the shaft speed. The investigations are performed by controlling the shaft speed as the target value and by measuring the actual

values of torque and shaft speed. For each controlled shaft speed value, the nominal value is kept constant for a given time period. This duration is applied for averaging. This process was repeated several times for statistical reasons. Afterwards, the standard deviation is calculated to estimate the measurement error. Owing to the different dimensioning of the test bench for Propeller B and because of the simultaneously performed investigation of the jet (see Chapter 9.4), a smaller number of measuring points was observed, but at least the design point and one additional point each for the partial and overload regimes. Table 9.4 indicates all the preliminary investigations conducted in relation to the utilised fluids and the shaft speed variation. Note that the table also contains an indication of the variations for the supplementary investigations.

Figure 9.12 shows the results for torque over shaft speed. All three applied test fluids (left: C1, centre: C2, right: C3) are shown – the rheological parameters related to each test fluid are noted in each diagram. The measured

Table 9.4. *Measurement plan of Propeller B in relation to the utilised test fluid and the operating point investigated in relation to the design point, the plan indicates preliminary (characteristics) and supplementary (jet) investigations*

	Fluid	Design Point	Characteristics	Jet
C1-N065	C1	65 %	✓	✗
C1-N085	C1	85 %	✓	✓
C1-N100	C1	100 %	✓	✓
C1-N115	C1	115 %	✓	✓
C2-N065	C2	65 %	✓	✗
C2-N085	C2	85 %	✓	✓
C2-N100	C2	100 %	✓	✓
C2-N115	C2	115 %	✓	✓
C3-N085	C3	85 %	✓	✓
C3-N100	C3	100 %	✓	✓
C3-N105	C3	105 %	✗	✓
C3-N115	C3	115 %	✓	✗

values are represented by a single marker ($\diamond$) together with the calculated error bars. The measured values are between $T = 2.9\,Nm$ and $T = 9.5\,Nm$ for torque and between $n = 259\,min^{-1}$ and $n = 440\,min^{-1}$ for the shaft speed. For each parameter, the standard deviation is computed. All the measured data is shown in Table 9.5 in greater detail. The error bar in Figure 9.12 is calculated with the standard deviation. As can be seen, the measurement error is small. The maximum value for the relative standard deviation is less than $\varsigma \approx 1.75\,\%$ for torque and shaft speed. In addition, the results of the inverse calculation are displayed for comparison. Torque is drawn as a continuous line and the efficiency is plotted as a broken line in grey. This data is taken from Figure 8.10. To assess the results, the predefined design point is plotted in each subfigure with a broken line for the designed torque of $T_{\mathrm{PP}} = 7.44\,Nm$ and the design shaft speed of $n = 380\,min^{-1}$.

A comparison of the design point with the measurements shows that the course of test fluid C1 (left) and test fluid C2 (middle) does not fit this point. However, test fluid C3 (right) fits the design point very well. This is very plausible, given the fact that only fluid C3 is prepared to match the design
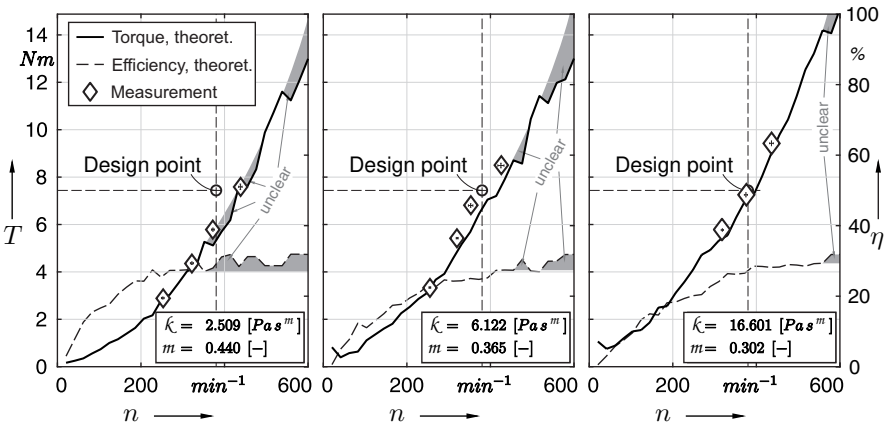
Figure 9.12. *Experimental data of Propeller B as torque over shaft speed (three measurement series, Marker Series 1: $\diamond$, Series 2: $\circ$, Series 3: $\triangleleft$), compared with the calculated characteristics (continuous line), containing the design point (chained line), presentation according to Reviol et al. [182]*

Table 9.5. *Measurement results of Propeller B, includes only preliminary (characteristics) investigations but indicates whether supplementary (jet) investigations are performed*

	$n\ \left[min^{-1}\right]$	$T\ [Nm]$	**Characteristics**	**Jet**
C1-N065	252.24 ± 3.18	2.90 ± 0.04	✓	✗
C1-N085	321.89 ± 3.54	4.37 ± 0.05	✓	✓
C1-N100	372.25 ± 3.31	5.78 ± 0.06	✓	✓
C1-N115	437.95 ± 4.13	7.59 ± 0.12	✓	✓
C2-N065	254.95 ± 2.07	3.34 ± 0.03	✓	✗
C2-N085	320.37 ± 2.27	5.42 ± 0.02	✓	✓
C2-N100	352.59 ± 5.34	6.80 ± 0.07	✓	✓
C2-N115	425.06 ± 7.38	8.49 ± 0.10	✓	✓
C3-N085	318.57 ± 2.68	5.77 ± 0.05	✓	✓
C3-N100	375.03 ± 3.68	7.25 ± 0.09	✓	✓
C3-N115	436.14 ± 4.64	9.43 ± 0.10	✓	✗

fluid. Fluids C1 and C2 were deliberately prepared to be different from the design fluid – hence, the measurements related to these fluids must not fit the design point. Furthermore, a very good agreement of measurement and inverse calculation can be seen.

9.3.3. Assessment of the model assumptions

The results of Propeller A show a clear difference between predicted and measured power characteristics. Considering only these results, the method seems to be invalid. In contrast, Propeller B leads to very plausible results for design process, calculation method, and measurement results. The reason for the mismatch of Propeller A and the match of Propeller B is the difference in the abstraction level of the design process of both propellers. Only Propeller B was designed after taking swirl into account. Hence, a high abstraction level – as chosen for Propeller A – is not suitable, and it is indisputable that swirl must be considered in the design process.

Based on the performance characteristics of Propeller B, both the design

method and the inverse calculation method are considered to have been conclusively verified. Because of the unsuitability of Propeller A, further investigations of this propeller are not worthwhile. Only the second propeller is examined from this point.

9.4. Supplementary investigations

In the preliminary investigations, the validity of the design technique and the inverse calculation procedure were verified. However, not only is the power consumption of the applied propeller a point of interest, but also the generated flow field. It is clear, then, that the jet developed by the propeller is the goal of the process. In the following, Propeller B is examined for the developed flow field of the shaft speed variation considered. In the scope of this work, only the jet, in a horizontal plane of the machine axis of the propeller, and the related velocity distribution in cross-section planes in front of the propeller are presented. A more detailed investigation of the flow field and comparisons with numerical procedures have been published by Wang [232]; Wang et al. [233, 234, 235].

9.4.1. Measurement methodology

The detailed investigations of the flow field are carried out using a UDA probe. The probe is installed on a traverse unit that enables the probe to be positioned at any position in the xy-plane. A detailed description of the test bench can be found in Chapter 9.2.1. An overview of the test stand is shown in Figures 9.6 to 9.8. A measurement computer is used for automatic control of the traverse system. To record the flow field in the xy-plane, the computer requires a user-defined grid for automatic traversing.

The simplest way of defining a grid is to apply a rectangular coordinate system. Hence, in this project, a rectangular grid with a clearance of $\Delta x = 100\,mm$ and $\Delta y = 100\,mm$ between each point is chosen. Because of the circular shape of the test bench, the rectangular grid is trimmed near the wall. In addition, the region of the propeller has to be omitted to avoid the collision
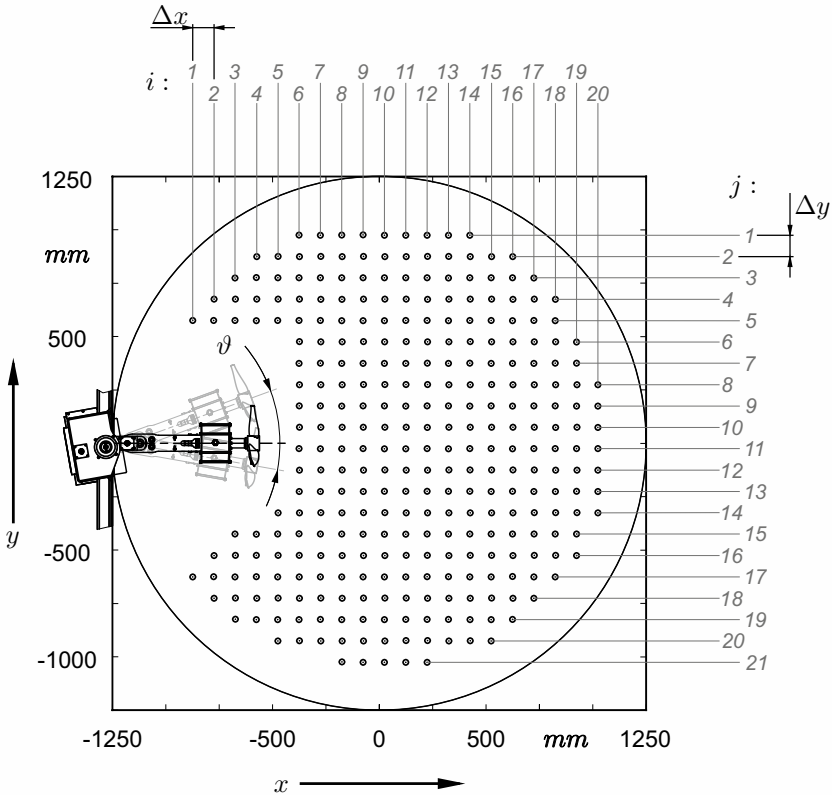
Figure 9.13. *Data acquisition points in relation to the test bench with the clearance Δx and Δy for both varied spatial parameters*

of the UDA probe with the propeller. This result is a reduced rectangular grid with more than 300 data acquisition points. Figure 9.13 shows the final grid. As an overlay, a schematic diagram of the test bench is also provided in the figure.

The variation of the test liquid requires a measurement plan for methodical investigations. The variation is in line with the preliminary investigations, as shown in Table 9.4. Note that only three operating points for each applied fluid are investigated. The investigated operating points always include partial load and overload. The design point is also investigated each time,

however, because of the change of the test fluid, the original design speed was not suitable for test fluids **C1** and **C2**. The shaft speed has, therefore, been set to more suitable values for the aforementioned fluids. Furthermore, for test fluid **C3**, the overload regime was investigated at lower shaft speed. Table 9.4 indicates the differences between preliminary and supplementary investigations. Despite the fact that the test bench is designed to also vary the mounting angle ϑ of the propeller, these investigations are not within the scope of this research project and have been performed by Wang et al. [235]. The result of the UDA measurements is discrete data recorded for each acquisition point of the grid. For better visualisation, the dataset is interpolated using the nearest neighbour method, as proposed by Sandwell [199]. The post-processing of the data is performed in a Matlab routine.

9.4.2. Jet distribution

The detailed investigation of the velocity distribution is carried out for a fill level of $H_{\mathrm{F}} = 1.4\,m$. The immersion depth of the propeller is adjusted and kept constant for all investigations. The z-position of the propeller is set to $z = 0.9\,m$.

This amount has been chosen to achieve a maximum distance between the floor of the test bench and the propeller, without positioning the propeller too close to the surface. If the distance between floor and propeller or surface and propeller is not chosen well, a vortex core may form on the surface or on the ground, which is connected to the propeller by a vortex filament. This vortex filament requires energy, which leads to a higher power consumption of the propeller. This will falsify the measurement results if surface or underwater vortices occur. To avoid vortices, the proposal by Prosser [167] is applied. The proposal is adopted from the field of fluid machinery and requires an immersion depth H_{ID} of at least $H_{\mathrm{ID}} = 1 \cdot D_{\mathrm{In}}$ for the intake in a pump sump. In this proposal, D_{In} is the diameter of the intake, assumed here to be equal to the diameter of the propeller. The immersion depth is almost 1.5 times higher than the propeller diameter and a sufficient distance is assumed.

However, the proposal of Prosser refers to pump sumps instead of mixers. In

particular, the surface of each measurement survey is observed for vortices. Since the distance between the surface and the propeller is smaller than the distance between the base and the propeller, vortices are more likely to occur on the surface. This is in agreement with Rushton et al. [196, 197], who discovered that Froude number effects – and, hence, surface vortices – may be relevant for Reynolds numbers higher than $Re = 300$. No surface vortex was observed for all measurement surveys. Therefore, the distance of $z = 0.9\,m$ is assumed to be appropriate.

In all the measurements performed, only the xy-plane – as shown in Figure 9.13 – is considered. The machine axis of the propeller is chosen for the z-position of the measurement plane. This position is equal to the aforementioned propeller position of $z = 0.9\,m$.

The measurements are performed for the same operating points as selected earlier for the preliminary investigation of the power characteristics. Owing to deviations in the measurements, slight differences in the operating points can occur. Hence, the shaft speed was controlled and measured as the actual value. Table 9.6 contains all measured values for the shaft speed for all considered operating points. In addition to the measurement value, the standard deviation is presented. A comparison of the contents of Table 9.6 with those of Table 9.5 reveals that the differences are negligible. Table 9.6 also indicates whether the power characteristics are investigated for the velocity distribution examined.

In Figures 9.14 to 9.16, the velocity distribution in the measurement plane is depicted as a contour plot. The velocity is normalised by the maximum value of the velocity magnitude measured for the parameter set under consideration. Each figure represents the measurement results for the investigation of the operating point near the design point of one of the different test fluids. In the appendix, the remaining operating points for partial load and overload are shown. For these results, refer to Appendix E.2 and Figures E.4 to E.12. Furthermore, the appendix contains not only the results as normalised illustrations, but also true-to-scale (Figure E.13 to Figure E.21) and scaled to the velocity range of $v = [0, 1.7]\ m/s$ (Figure E.22 to Figure E.30) for better comparison.

In addition to the contour plot of velocity in the xy-plane, the velocity distribution is shown in three cross-sections perpendicular to the measurement plane in all figures. The velocity distribution is plotted as a graph of the velocity magnitude v and its components v_x, v_y, and v_z. The three positions are chosen at $x = -370\,mm$, $x = 0\,mm$, and $x = 370\,mm$. Each graph is normalised with its maximum velocity magnitude.

*Results of test fluid **C1***

Figure 9.14 shows the results of the parameter set **C1-N100** for fluid **C1** normalised with the maximum velocity magnitude of the depicted measurement output. Figure E.5 shows the same dataset true-to-scale. The applied test fluid is not as viscous as fluid **C2** or even fluid **C3**. Therefore, the velocity magnitude reaches its maximum values for this test fluid for all performed measurements. For the operating point near the design shaft speed considered here, the maximum velocity amounts to $v_{max} = 1.7997\,m/s$ (partial load: $v_{max} = 1.5667\,m/s$, overload: $v_{max} = 1.9671\,m/s$).
A clear, distinct velocity field is formed by the propeller, which clearly reaches

Table 9.6. *Operating points of the detailed investigations as the actual value of the shaft speed. Includes only supplementary (jet) investigations, but indicates whether the preliminary (characteristics) investigations are fulfilled*

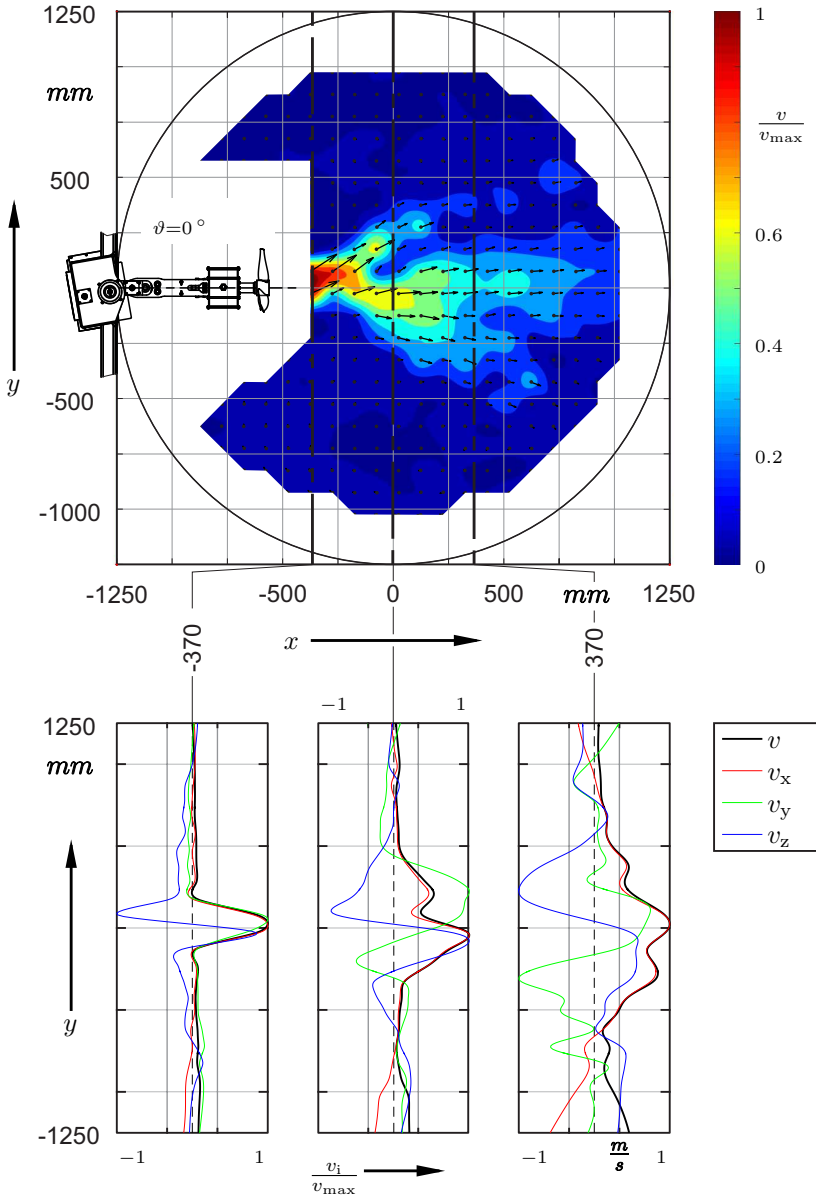|	**Fluid**	$n\,[s^{-1}]$	**Characteristics**	**Jet**
C1-N085	C1	321.85 ± 3.54	✓	✓
C1-N100	C1	372.23 ± 3.30	✓	✓
C1-N115	C1	437.84 ± 4.21	✓	✓
C2-N085	C2	320.36 ± 2.27	✓	✓
C2-N100	C2	352.53 ± 5.34	✓	✓
C2-N115	C2	424.93 ± 7.42	✓	✓
C3-N085	C3	318.57 ± 2.68	✓	✓
C3-N100	C3	375.03 ± 3.68	✓	✓
C3-N105	C3	400.56 ± 5.95	✗	✓

Figure 9.14. *Measurement result C1-N100, normalised velocity contour plot v/v_{max} with vector plot and evaluation of the normalised velocity vector v_i/v_{max} for cross-section planes at $x = -370$, $x = 0$, and $x = 370\,mm$, drawn for machine-level $z = 0.9\,m$, maximum velocity magnitude of contour: $v_{max} = 1.7997\,m/s$, and accuracy of the applied UDA sensor: $\pm 0.5\,\%$*

the wall opposite the propeller. In the upper half of the velocity field, a separation can be observed. This may be related to transient effects. The measurement was performed over a small time duration and averaged afterwards. The duration may not have been long enough to filter out transient effects. In respect of the characteristics of the whole flow field, a diverging jet with a pronounced core is measured. This is in agreement with the theoretical approach of a free jet, as described in Chapter 6.

In addition to the contour plot, the velocity distribution is shown as a set of curve plots. The first plot is close to the propeller ($x = -370\,mm$) and shows, for the magnitude and the three components, a clear peak near the machine axis at $y = 0\,mm$. For this distance, the core of the jet is still intact. At the second distance ($x = 0\,mm$), the former core region is enlarged and the jet has begun to diverge. The velocity v_{x} in x-direction still has its maximum position at $y = 0\,mm$ but is characterised by a secondary maximum. The distributions of v_{y} and v_{z} have started to diverge. For the last position at $x = 370\,mm$, the magnitude of v and v_{x} both still show the propagation of the jet, though no core region can be identified. The remaining components are scattered. As performed for the contour plot, each diagram is normalised by its maximum value.

In summary, it can be said that an effective jet was developed and the power consumption was close to the predicted value. For the test fluid **C1**, Propeller B operated as expected.

Note that no error evaluation was performed for the contour plot. This is because of the application of the biharmonic spline interpolation method. Postprocessing was performed for mathematical grid points instead of data acquisition points. Owing to the size of the mathematical grid, the application of error propagation methods was not appropriate. Therefore, the accuracy of $\pm 0.5\,\%$ of the measurement device is given in the figures instead of applying methods of error propagation. This also applies to all further investigations.

*Results of test fluid **C2***

Test fluid **C2** is characterised by moderate viscous properties. The maximum velocity of the measurements of this fluid for the operating point close to the design speed amounts to $v_{\max} = 1.2681\,m/s$ (partial load: $v_{\max} = 1.0717\,m/s$, overload: $v_{\max} = 1.3557\,m/s$). This value is taken for normalising the contour plot of the considered results of the parameter set **C2-N100**, as depicted in Figure 9.15. For a true-to-scale illustration, refer to Figure E.8. The contour plot shows a distinct jet which reaches the wall opposite the propeller. But the jet is not as clearly pronounced as for the test fluid **C1**. Furthermore, a separation of the jet into two main regions occurs, and only the upper part of the jet reaches the wall in Figure 9.15. A few separations can be observed in the middle between both the main regions of the jet. The jet seems to diverge rapidly because of the increased viscosity. Owing to rising shear stress in the free shear layer, it is clear that the divergence of the jet starts closer to the propeller. The separation regions may be related to transient effects connected to the hub vortex.

Considering the first velocity plot for the cross-section plane at $x = -370\,mm$, the course of all curves is quite similar to the test fluid **C1**. The second cross plane for $x = 0\,mm$ shows two distinct maxima for both the velocity magnitude v and the x-component v_{x}. For the upper maximum, the component v_{y} has a positive peak, while the component v_{z} has a negative peak. For the lower maximum, it is the other way round. All peaks are of a similar quantity, except the peak of the component v_{z} for the upper maximum. The courses of both the component v_{y} and the component v_{z} show the swirl of the flow. It can be assumed that the jet is still diverging evenly at this x position. The contour plot shows the enveloping area that is characterised by the tip vortex. For the last position, no clear structure can be observed in the course of the curves, allthough it can be assumed that the separation regions are related to the dissipation of the whole jet in this distance from the propeller.

In conclusion, it can be said that the jet is still clearly pronounced but starts to diverge closer to the propeller. From the preliminary tests, it is known that the power consumption was calculated correctly. For the test fluid **C2**, Propeller B

Figure 9.15. *Measurement result C2-N100, normalised velocity contour plot $v/v_{\max}$ with vector plot and evaluation of the normalised velocity vector $v_i/v_{\max}$ for cross-section planes at $x = -370$, $x = 0$ and $x = 370\,mm$, drawn for machine level $z = 0.9\,m$, maximum velocity magnitude of contour: $v_{\max} = 1.2681\,m/s$, accuracy of the applied UDA sensor: $\pm 0.5\,\%$*

operated as expected.

*Results of test fluid **C3***

As a final variation, the test fluid **C3** was examined. Fluid **C3** is characterised by having the highest investigated viscosity and is similar to the design fluid. Figure 9.16 illustrates the measurement results **C3-N100** for the test fluid as a normalised dataset for the design speed. The normalisation of the contour plot was performed by dividing the local velocity magnitude v by the maximum value $v_{\mathrm{max}} = 0.6706\,m/s$ of the measurements for the design point (partial load: $v_{\mathrm{max}} = 0.0894\,m/s$, overload: $v_{\mathrm{max}} = 0.4726\,m/s$). The graph plots shown are normalised by the maximum value of velocity magnitude v_{max} of each diagram. A true-to-scale illustration of the measurement set is shown in the Appendix in Figure E.11.

The velocity distribution of the contour plot shows no jet. Only the area near the propeller is significantly accelerated. This is caused by the high viscosity of the fluid. However, as an overlay of the contour plot, a vector field is illustrated. The vector field shows a main flow direction, which is aligned to the wall opposite the propeller. The length of the vectors is related to the velocity magnitude. As can be seen, the velocity magnitude is quite low, but not zero.

To assess the velocity field of the experimental investigation of test fluid **C3**, the velocity graph plot has to be taken into account. On reviewing the first cross-section plane for $x = -370\,mm$, a clear pronounced jet can be seen. It has to be said that the jet is already diverged, and no core can be observed. For the remaining cross-sections, no clear velocity distribution can be identified. However, the velocity magnitude is aligned to the x-axis, which can be seen in the distribution of the x-component of the velocity vector in both the remaining diagrams. Therefore, the main flow direction is still downstream from the propeller, although the magnitude of the velocity is very small.

As a result of the measurements, first of all, it was determined that Propeller B is not able to accelerate the test fluid **C3** to reach the opposite wall. Nevertheless, the velocity graph of the first section plane shows a clearly
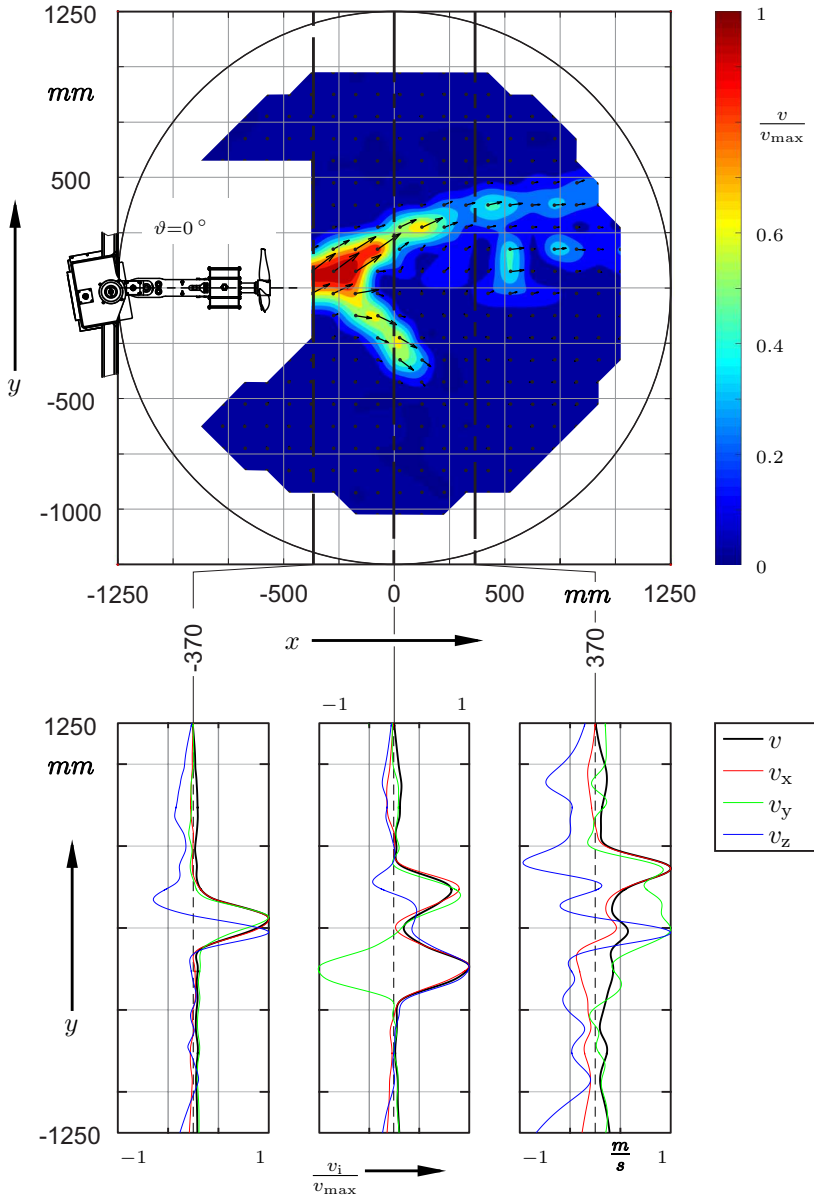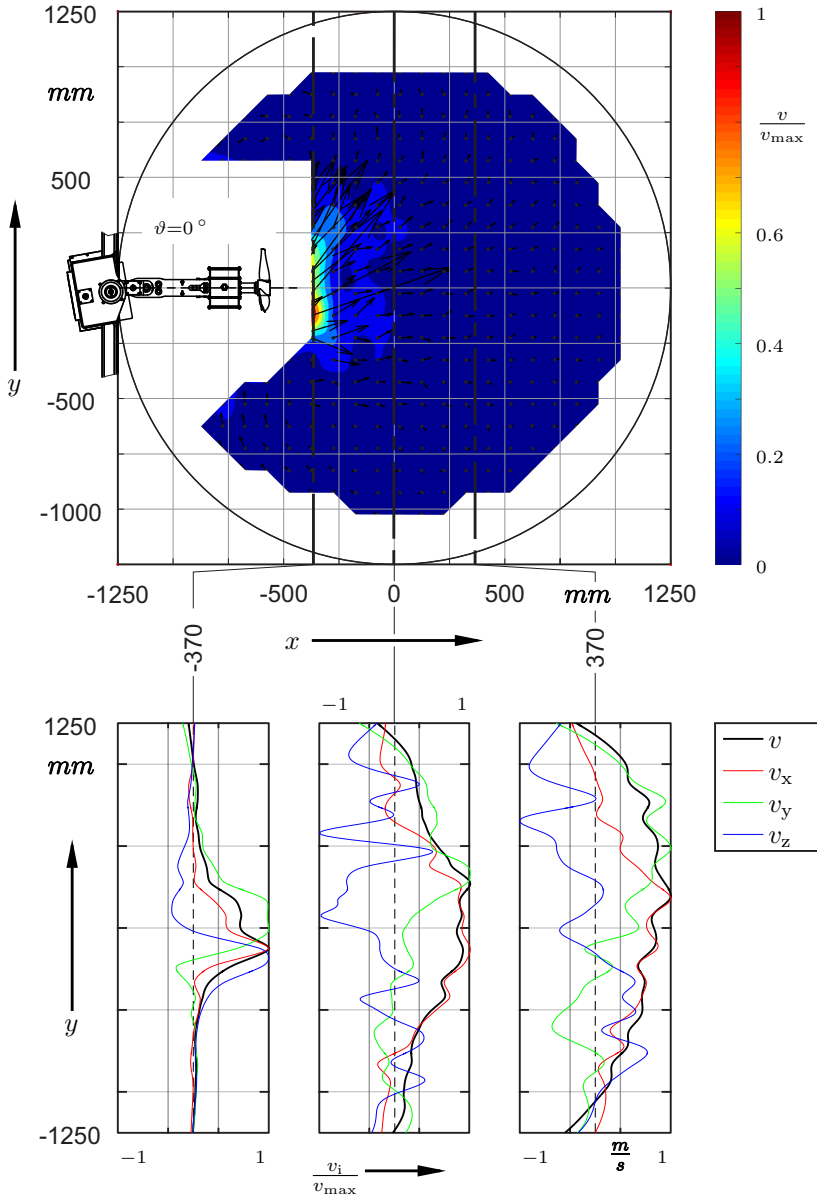
Figure 9.16. *Measurement result C3-N100, normalised velocity contour plot $v/v_{\max}$ with vector plot and evaluation of the normalised velocity vector $v_i/v_{\max}$ for cross-section planes at $x = -370$, $x = 0$ and $x = 370\,mm$, drawn for machine-level $z = 0.9\,m$, maximum velocity magnitude of contour: $v_{\max} = 0.6706\,m/s$, accuracy of the applied UDA sensor: $\pm 0.5\,\%$*

developed but already highly diverged jet. The remaining velocity diagrams have shown a main flow direction of the fluid aligned to the x axis, as also the contour plot. The preliminary investigations were also successful, and the power consumption was predicted with a high degree of accuracy. Although test fluid **C3** is obviously not suitable to be mixed by a propeller agitator, the design process and the reverse calculation method were finally verified for the design fluid as well.

Notes

[1]The measurement device to investigate the viscoelastic properties of possible model fluids was a RheoStress 6000 rheometer from Haake.

Part IV.

Discussion and review of the method

10. Discussion of the method

The application of the design techniques of wind energy turbines to develop a propeller mixer was successful. As required in Chapter 1.2, the new design technique provides both the shape of a propeller and the drive power required. This data can be computed in the design process for arbitrary low-Re conditions, which are mostly associated with non-Newtonian fluid flow.

It is clear, however, that the method is not universally valid. The basis of the new design method was to focus on a clearly defined machine type in order to obtain a comprehensive and transparent theory for the turbomachine considered. In addition to being restricted to a specific machine type, some simplifications or abstractions have been made to apply analytical methods. Hence, the limits of the method have to be discussed in the following.

The verification of the method was carried out by means of experiments. In the last part of this chapter, therefore, the applied measurement methods are critically discussed in order to point out their influence on the verification.

10.1. Disadvantages of the method

The major disadvantages of the method result from the fundamentals of the method. The disadvantages can be subdivided into different main topics. These are the general application range and the assumed simplifications of the approach, which imply the influence caused by non-Newtonian fluid flow. These are discussed in detail below.

10.1.1. Limited application range

As mentioned earlier, the method was developed to create a propeller mixer for a specific design fluid. As explained in Chapter 2.1, the field of mixing is very broad and characterised by various mixing tasks. Propeller agitators are best suited for mass transport tasks, e.g. in biogas power plants or sewage treatment plants. Therefore, it is not possible to use the procedure for alternative mixing applications. Since this was evident from the requirements

of the new design process, the limited application range is known from the beginning, and, so, is not really a disadvantage.

10.1.2. Polar plot database

Since the fundamental basis of the method is the *blade element momentum theory* (see Chapter 3.2), the whole design process depends on polar plot data and its quality. The database data was discussed in Chapter 7.2. The dependence of the new method on the polar data became apparent through the discontinuous course of the predicted power characteristic, as presented in Chapter 9.3.1 and 9.3.2.

When an analytical energy balance is used, a continuous and strictly monotonically increasing course of the characteristic curve can be expected. The power must be a cubic function of the entry speed, while the torque characteristic must have a quadratic curve. If a linear relationship is assumed between inlet velocity and rotational speed, then the above relationship also applies to rotational speed.

Both Figures 9.11 and 9.12 clearly show that the course of the inverse calculated power has a quadratic trend. The calculated curves can, therefore, be considered plausible. However, this does not explain the discontinuous course of the curves, but only proves the plausibility of the curve trend.

The reason for the discontinuity of the characteristic curves must be assumed to be the limited size of the profile database. During the period in which this work is carried out, the database consisted only of discrete individual results; the preservation of which required a great deal of effort. These results were generated by a large, but limited, number of variations; see Chapter 7.2 for details. This also means that results are only available for a limited number of Reynolds numbers. The algorithm uses the Reynolds number to select the best profile. The Reynolds number determined is compared with the results of the database. The database entry closest to the Reynolds number determined by the algorithm is selected for use. In general, it cannot be assumed that the Reynolds number determined by the algorithm has an exact counterpart in the database. The greater the difference between the re-

quired Reynolds number and the existing Reynolds numbers in the database, the greater the negative influence of the profile that is finally selected. The database should, therefore, be systematically expanded in order to improve its quality. In addition, the database must be extended to include physical effects such as stall, flow separation, or transitions.

It is clear that the limited size of the database will have a significant impact. The influence of the aspects discussed above becomes obvious for the characteristics illustrated in the Figures 9.11 and 9.12. Each time a peak occurs, the algorithm estimates a Reynolds number that causes a change of profile. This is associated with a sudden change of the profile polar data; the course of the characteristics is also influenced.

Furthermore, for a narrow rotational speed range of the examples performed, the algorithm selected the datasets with the largest investigated angle of attack. The algorithm may have selected a larger angle if this data had been present in the database. In this case, it is clear that the data for a larger angle of attack would be more suitable. However, these were not examined because of the neglect of stall. Therefore, the database should be extended for higher levels of attack.

Regions that are not clear – either because of a large difference of required and stored Reynolds numbers or because of the limited range of the angle of attack investigated – are marked in Figure 9.11 and 9.12 as *unclear*. By neglecting these regions, a continuous course can be assumed.

Finally, it can be said that these influences are not a disadvantage of the method, but only of the results presented here. Despite the small number of entries, the method works very well, as the accuracy of the results for Propeller B shows. Expanding the database will further improve the method and make the results even more accurate.

10.1.3. Influence of the Reynolds number

In addition to the number of database entries, it can be assumed that the definition of the Reynolds number also has an influence on the calculation of the characteristics.

As explained in Chapter 5.3, the Reynolds number is not defined for non-Newtonian fluids. As can be seen from Equation 5.27, there is no way to give a unique viscosity that fully characterises the viscous patterns of a non-Newtonian fluid. If a representative single value is required, the concept of apparent viscosity can be chosen. In this concept, the Reynolds number depends on the deformation state and, so, is not unique. Therefore, an alternative definition must be used.

Two possibilities are presented in Chapter 5.3.3. The first definition was described by Chhabra and Richardson [38] to compare Newtonian and non-Newtonian pipe flow. The fundamental of Chhabra and Richardson's Reynolds number, according to Equation 5.38, was the assumption of a constant friction coefficient for pipe flow tasks. The second definition of an alternative Reynolds number was deduced by applying Buckingham's π theorem, see Equation 5.41, and is called *generalised Reynolds number*. The power law parameters k and m were adopted for deduction. This means that the physical properties of a fluid are taken into account by applying mathematical regression parameters. Hence, the definition is more mathematical than physical. Both definitions must, therefore, be treated with scepticism.

An analysis of the profile polar data shows that the course of the lift and drag coefficient is discontinuous when plotted as a function of the Reynolds number. The magnitude of the influence depends on the definition chosen for the Reynolds number. A more suitable procedure to compare non-Newtonian fluids as proposed by Kluck [115] should be adopted, but at present there is no clear definition of the Reynolds number for non-Newtonian fluid flow that has been proven in practice.

However, the resultant error in the application of the definitions that have been applied is systematic. Therefore, in the context of this thesis, it is not permissible to calculate a single value with the definition according to Chhabra and Richardson or the application of the *generalized Reynolds number*, but the consideration of the difference of two different states is permissible, since only the relative difference of the Reynolds number is considered. It is a prerequisite, then, that only one definition of the Reynolds number is used during the entire design process and that the absolute values of the Reynolds num-

ber are ignored.

10.1.4. Influence of modelling assumptions

The investigated algorithm works very well, but the model assumptions have to be accurate. The calculation has to take swirl into account. This will be discussed in the following.

If only the results of Propeller A according to Chapter 9.3.1 are considered, the calculation method seems to have failed. The deviation between the preselected design point and the numerical calculation and the experimental data is unacceptably large. In contrast, all results of Propeller B fit together very well – see Chapter 9.3.2.

If Propeller A is analysed in greater detail, it immediately becomes clear that the design point lies on the inverse calculated curve. This means that the design method and the inverse calculation of the power curve provide, in principle, the same results. It may, therefore, be assumed that the differences result from the experimental investigation. However, all three measurement series are almost identical and the experimental investigations can be considered plausible. This suggests that the deviation of Propeller A is not caused by the basics of the calculation method and also not by the measurements, but by the model assumptions applied for reasons of simplicity.

A consideration of the model assumptions of Propeller A and their comparison with Propeller B show that both the algorithm and the investigations are valid. Propeller A was designed under the assumption of negligible swirl, while Propeller B was designed taking swirl into account. The experimental investigation of Propeller A clearly shows the importance of swirl for the design process.

At first glance, it does not seem that swirl is the reason for the numerical overestimation of power. Since swirl requires power, the total power of the experiments should be higher instead of lower. Although this is true, the mistake was made at the beginning of the design process. The method was performed under incorrect, non-physical conditions. Hence, no comparison of the numerical and the experimental results is possible.

Further analysis of Propeller A shows that the calculation of the chord length is responsible for the mismatch of the results. The neglect of swirl causes the overestimation of the chord length, especially near the hub. In Figure 8.1a, the chord length distribution of Propeller A is plotted. Near the hub, striking high values for l occur. For Propeller B, the chord length is more plausible: see Figure 8.5a. Since the chord length is overestimated for Propeller A, the Reynolds number is also overestimated because of the dependence of the Reynolds number on this parameter. As a consequence, non-plausible data was taken from the database to create the shape of Propeller A. The profile taken is characterised by over-estimated lift coefficients C_{L}. In contrast, the drag coefficient C_{D} is assumed to be too low. Finally, the algorithm computes higher values for both the design point and the inverse calculated power characteristics.

10.2. Discussion of the measurements

Despite the fact that the alignments of the shafts of both the investigated propellers are different, no effect on the experimental results is expected. According to Rushton et al. [196, 197] and Prosser [167], the onset of vortices or caverns will cause increased power consumption. For both propellers, the surface was observed, and no air sucking vortices were identified. Therefore, no relevant influence from the test setups is assumed. The alignment of the jet may cause slight differences due to the influence of gravity. But the acceleration in the jet and the inertia forces caused are higher than gravity. Hence, gravity is assumed to be negligible.

Apart from the test bench, the test fluid is also part of the test setup. The rheological properties of the fluid have to be discussed. For Propeller A, the applied test fluid **XG1** was in good accordance to the defined design fluid, see Chapter 9.3.1, Figure 9.3 and Table 9.1. The test fluid of Propeller B was challenging. Between the applied test fluid **C3** and the defined design fluid, a mismatch of $\Delta k = 14.5\,\%$ for consistency was measured. For the flow index, the difference was smaller and was measured at $\Delta m = 4.1\,\%$. However, both parameters are mathematical curve fit parameters. Hence, the deviation was only small, as can be seen in Figure 9.10. The small deviation between the applied test fluid and the design fluid only caused small influences on the experimental results. The accordance between the predefined design point and the measured value is very good.

The accuracy of the measured quantities has to be discussed as well. Some different measurement devices are applied, with each device having a characteristic measurement error. Each sensor is carefully selected with regard to its measuring range – all the measured quantities amount to at least $10\,\%$ of the maximum value of the sensor to avoid the influences caused by the measuring range. For details about the measurement ranges of all applied measurement devices, refer to Appendix A.3. To eliminate statistical errors, each measurement was performed in measurement series with several repetitions. To quantify the statistical dispersion, the standard deviation was calculated. Each measurement series is specified by the mean value of all

datasets of the measurement series. The calculated standard deviation of each measurement series is specified in Chapter 9 together with the mean value of the measurement series. In every case, the standard deviation was satisfactorily low.

11. Conclusion and outlook

11.1. Conclusion

This thesis presented a new design method for axial turbomachinery. The method is intended for propellers for agitating high viscous fluid flow, such as those commonly found in process engineering and energy technology. Typically, this kind of fluid flow is related to non-Newtonian fluid conditions. The design method is based on analytical and transparent methods and determines both the power requirement and the shape of the propeller for a predefined operating point.

Bringing together the above topics, which make up the presented design method, is challenging, and leads to several conflicts in the present fundamentals of fluid mechanics, turbomachinery, process engineering, and energy technology. A major problem is that the present fundamentals to design propellers only take high-Re fluid flow into account, which is typically modelled with potential flow or other simplifications. But agitating high viscous fluid flow causes a more pronounced influence of the friction – and, so, of the shear viscosity of the fluid under consideration. Hence, the above simplifications and their related assumptions are no longer valid in the scope of this research. Therefore, the theoretical fundamentals were analysed for their design techniques and subsequently enhanced for non-Newtonian fluid flow. The fundamentals considered only refer to propeller engines and wind turbines.

Since the approach that has been applied is derived from the design process for axial turbomachinery, such as propeller engines or wind turbines, the method focuses on the aerodynamics of airfoils. Until now, their aerodynamic characteristics are only known for high-Re conditions – mostly for air and sometimes for pure water – but not for non-Newtonian fluid flow. To establish the aerodynamics of airfoils under the conditions of non-Newtonian fluid flow, numerical investigations were performed. The Lattice-Boltzman method was utilised to calculate numerous different flow conditions.

The approach presented in this thesis is combined with the design method of

modern wind turbines to derive the shape of the turbomachine sought. However, the application of the methods that have been considered require the knowledge of the absolute velocity at the inflow of the control room regarded. This velocity was derived from the momentum forces of the propeller to be developed. These forces can be found by adopting the jet theory.

Finally, the combination of the above research topics led to an approach that is able to calculate the optimum shape of a propeller mixer from a given design point to agitate high viscous low-Re fluid flow. The power consumption of the turbomachine is calculated in the design process.

The power consumption of this propeller is known early in the design process. This fact is a key role for suitable design techniques. Nevertheless, the calculated data is only valid for the design conditions. Therefore, in this thesis, the new approach is also investigated for its suitability for application in further operating conditions, such as partial load and overload – or even for agitating other fluids. For this purpose, the algorithm considered was developed in such a way that it can be started in inverse mode. This means that not the design point itself, but a propeller shape is given as the input parameter when the algorithm is operated in inverse mode. The result of the inverse method is the full power characteristics of the propeller for an arbitrary fluid. However, the method is limited to pseudoplastic fluids. Pseudoplastic properties occur most often in combination with highly viscous media.

In the last part of this thesis, the design method was applied and two propeller mixers were designed. The propellers were designed with different abstraction levels: one propeller was designed to neglect swirl, while the second was designed to take swirl into account. The difference was used to establish the influence of the abstraction level on the design approach. The influence of swirl was found to be of high importance for the design. Hence, the second propeller was chosen for detailed experimental investigations. The examinations proved the suitability of the new approach.

As a consequence, the design techniques of propeller engines and modern wind turbines can be adopted under some enhancements to design a flow-optimised propeller mixer for the agitation of high viscous fluid flow.

11.2. Outlook

The new approach worked as expected. But the quality of the method depends on the investigation of profile aerodynamics for non-Newtonian fluid flow. The better the quality of the results of these investigations and the larger the amount of investigated profiles, the better the design technique. The investigation of more profiles is, therefore, highly recommended. Since the investigated profiles were taken from other applications, the design of new profiles, especially for the purpose of the topic under consideration here, will also increase quality. However, the design of flow profiles for high viscous fluid flow may be challenging. Furthermore, the flow conditions considered were not chosen beyond the stall point. For the low-Re conditions regarded, stall is not expected, but cannot be excluded either. The database should be extended for these investigations as well.

Although the method itself was proven in this thesis, validation was performed under laboratory conditions, such as homogeneous fluid flow. The experimental examinations have to be extended for practical use. This type of propeller mixer is commonly applied in waste water treatment or biogas power plants, for instance. In these plants, the agitated fluid is nonhomogeneous sewage with gas fraction. Therefore, the influence of particles and gas fraction have to be taken into account in further examinations.[1]

Notes

[1] The influence of gas fraction has been investigated by Wang [232].

Bibliography

[1] I. H. Abbot, A. E. von Doenhoff, and L. S. j. Stivers. Report No. 824. https://ntrs.nasa.gov/archive/nasa/casi.ntrs.nasa.gov/19930090976.pdf, 1945.

[2] K. A. Abdelrahim and H. S. Ramaswamy. High Temperature/Pressure Rheology of Carboxymethyl Cellulose (CMC). *Food Res. Int.*, 28(3):285–290, 1995. doi: 10.1016/0963-9969(94)00045-A.

[3] G. Agricola. *De Re Metallica Libri XII*. J. Froben and N. Episcopius, Basel, 1556.

[4] AID Airfoil Investigation Database. AID Airfoil Investigation Database. http://www.airfoildb.com/airfoils/863. Accessed: 2019-02-27.

[5] Al-Dimashqi. *Cosmographie, approx. 1300 AD*. M. A. F. Mehren, St. Petersburg, Translated edition, 1866.

[6] E. N. d. C. Andrade. The Velocity Distribution in a Liquid-Into-Liquid Jet. Part 2: The Plane Jet. *Proc. Phys. Soc.*, 51(5):784–793, 1939.

[7] E. N. d. C. Andrade and L. C. Tsien. The Velocity Distribution in a Liquid-Into-Liquid Jet. *Proc. Phys. Soc.*, 51(5):381–391, 1937.

[8] M. E. Aulton and K. M. G. Taylor. *Aulton's Pharmaceutics – The Design and Manufacture of Medicines*. Elsevier, Edinburgh, 2018.

[9] C. J. Baker. Wind Engineering – Past, Present and Future. *J. Wind Eng. Ind. Aerodyn.*, 95(9–11):843–870, Oct. 2007. doi: 10.1016/j.jweia.2007.01.011.

[10] M. Baumgaertel and H. H. Winter. Determination of Discrete Relaxation and Retardation Time Spectra from Dynamic Mechanical Data. *Rheol. Acta*, 28(6):511–519, Nov./Dec. 1989.

[11] A. Benchabane and K. Bekkour. Rheological Properties of Carboxymethyl Cellulose (CMC) Solutions. *Colloid Polym. Sci.*, 286:1173–1180, 2008. doi: 10.1007/s00396-008-1882-2.

[12] K. H. Bergey. The Lanchester-Betz Limit. *J. Energy*, 3(6):382–384, 1979.

[13] D. Bernoulli. *Hydrodynamica: Sive de Viribus et Motibus Fluidorum Commentarii*. Johannis Reinholdi Dulseckeri, Strasbourg, 1738.

[14] J. Bertrand and J. P. Couderc. Agitation de Fluides Pseudoplastiques par un Agitateur Bipale. *Can. J. Chem. Eng.*, 60:738–747, Dec. 1982.

[15] A. Betz. Die wichtigsten Grundlagen für den Entwurf von Luftschrauben. *Zeitschrift für Flugtechnik und Motorluftschiffahrt*, 6(13, 14):97–103, 1915.

[16] A. Betz. Schraubenpropeller mit geringstem Energieverlust. *Göttinger Nachrichten*, pages 193–213, 1919.

[17] A. Betz. Das Maximum der theoretisch möglichen Ausnützung des Windes durch Windmotoren. *Zeitschrift für das gesamte Turbinenwesen*, 26:307–309, 1920.

[18] A. Betz. *Wind-Energie*. Bandenhoeck & Ruprecht, Göttingen, Unchanged reprint edition, 1926.

[19] A. Betz. Die Windmühlen im Lichte neuerer Forschung. *Naturwissenschaften*, 15(46): 905–914, Nov. 1927. doi: 10.1007/BF01506119.

[20] G. Böhme. Consistent Scale-up Procedure for the Power Consumption in Agitated non-Newtonian Fluids. *Chem. Eng. Technol.*, 11(1):199–205, 1988. doi: 10.1002/ceat.270110127.

[21] G. Böhme. *Strömungmechanik nichtnewtonscher Fluide*. Teubner, Stuttgart, 2nd edition, 2000.

[22] E. C. Bingham. *Fluidity and Plasticity*. Mcgraw-Hill Book Company, Inc., New York, 1922.

[23] R. B. Bird and P. J. Carreau. A Nonlinear Viscoelastic Model for Polymer Solutions and Melts – I. *Chem. Eng. Sci.*, 23(5):427–434, 1968. doi: 10.1016/0009-2509(68)87018-6.

[24] D. R. Biswal and R. P. Singh. Characterisation of Carboxymethyl Cellulose and Polyacrylamide Graft Copolymer. *Carbohydr. Polym.*, 57(4):379–387, Sept. 2004. doi: 10.1016/j.carbpol.2004.04.020.

[25] H. Blasinski and E. Rzynski. Mixing of non-Newtonian Fluids with Turbine, Propeller, and Paddle Agitators. *Int. Chem. Eng.*, 16(4):751–754, 1976.

[26] J. Boussinesq. *Théorie de l'Écoulement Tourbillonnant et Tumultueux des Liquides dans les Lits Rectilignes a Grande Section*. Paris, Gauthier-Villars et fils, Paris, 1897.

[27] F. Boylu, G. Ateşok, and H. Dinçer. The Effect of Carboxymethyl Cellulose (CMC) on the Stability of Coal-Water Slurries. *Fuel*, 84(2–3):315–319, Jan./Feb. 2005. doi: 10.1016/j.fuel.2003.12.016.

[28] BROOKFIELD ENGINEERING LABORATORIES, INC. BROOKFIELD R/S RHEOMETER – Operating Instructions, 1998. Rev. 10/9.

[29] E. Buckingham. On Physically Similar Systems. *Phys. Rev.*, 4:345–376, 1914. doi: 10.1103/PhysRev.4.345.

[30] E. Buckingham. Windage Resistance of Steam – Turbine Wheels. *Bulletin of the Bureau of Standards*, 10:191–234, 1914.

[31] P. H. Calderbank and M. B. Moo-Young. The Prediction of Power Consumption in the Agitation of non-Newtonian Fluids. *Trans. Inst. Chem. Eng.*, 37:26–33, 1959.

[32] P. J. Carreau. *Rheological Equations from Molecular Network Theories*. PhD thesis, University of Wisconsin – Madison, 1968.

[33] P. J. Carreau. Rheological Equations from Molecular Network Theories. *Trans. Soc. Rheol.*, 16(1):99–127, Mar. 1972. doi: 10.1122/1.549276.

[34] P. J. Carreau, I. F. MacDonald, and R. B. Bird. A Nonlinear Viscoelastic Model for Polymer Solutions and Melts – II. *Chem. Eng. Sci.*, 23(8):901–911, Aug. 1968. doi: 10.1016/0009-2509(68)80024-7.

[35] N. Casson. A Flow Equation for Pigment Oil Suspensions of Printing Ink Type. In C. Mill, editor, *Rheology of Dispersed System*, pages 84–102. Pergamon Press, Oxford, 1959.

[36] A.-L. Cauchy. Recherches sur l'Équilibre et le Mouvement Intérieur des Corps Solides ou Fluides, Élastiques ou non Élastiques. In *Oeuvres Complètes*. Gauthier-Villars, Paris, 1958.

[37] G. Cauvelier and B. Launay. Concentration Regimes in Xanthan Gum Solutions Deduced from Flow and Viscoelastic Properties. *Carbohydr. Polym.*, 6:321–333, 1986.

[38] R. P. Chhabra and J. F. Richardson. *Non-Newtonian Flow in the Process Industries – Fundamentals and Engineering Applications*. Butterworth-Heinemann, Oxford, 1999.

[39] H. Chmiel, R. Takors, and D. Weuster-Botz, editors. *Bioprozesstechnik*. Springer, Berlin, 2018. ISBN 978-3-662-54041-1. doi: 10.1007/978-3-662-54042-8.

[40] D. Conrad. *A Viscosity Adaptive Lattice Boltzmann Method*. Dissertation thesis, Technische Universität Kaiserslautern, 2015.

[41] D. Conrad, A. Schneider, and M. Böhle. Numerical Investigation of an Extended Propellerviscosimeter by Means of Lattice Boltzmann Methods. In *Proceedings of the ASME 2013 Fluids Engineering Division Summer Meeting*, July 2013.

[42] W. Conrad. Zur Berechnung von Flügeln schnellaufender Windkraftmaschinen. *Forschung im Ingenieurwesen*, 8(1):2–5, Jan. 1937. ISSN 0015-7899. doi: 10.1007/BF02585017.

[43] M. Cortada-Garcia, V. Dore, L. Mazzei, and P. Angeli. Experimental and CFD Studies of Power Consumption in the Agitation of Highly Viscous Shear Thinning Fluids. *Chem. Eng. Res. Des.*, 119:171–182, Mar. 2017. doi: 10.1016/j.cherd.2017.01.018.

[44] J. M. Coulson, J. F. Richardson, J. R. Backhurst, and J. H. Harker. *Chemical Engineering Volume 1: Fluid Flow, Heat Transfer and Mass Transfer*. Elsevier Butterworth-Heinemann, Oxford, 6th edition, 1999. ISBN 9780750644440.

[45] CPKelco. Xanthan Gum Book, 2007.

[46] M. M. Cross. Rheology of non-Newtonian Fluids: A New Flow Equation for Pseudoplastic Systems. *J. Colloid Sci.*, 20(5):417–437, June 1965. doi: 10.1016/0095-8522(65)90022-x.

[47] Danfoss. Technical Information – Orbital Motors OML and OMM, 2014. Rev. BA Feb. 2014.

[48] G. de Bothezat. The General Theory of Blade Screws including Propellers, Fans, Helicopter Screws, Helicoidal Pumps, Turbo-Motors, and Different Kinds of Helicoidal Blades. Technical Report 29, NACA, 1918.

[49] A. de Waele. Viscometry and Plastometry. *Oil Color Chem. Assoc. J.*, 6:33–88, 1923.

[50] A. de Waele. Die Änderung der Viskosität mit der Schergeschwindigkeit disperser Systeme. *Kolloid-Zeitschrift*, 36(6):332–333, June 1925. doi: 10.1007/bf01423231.

[51] DIN12790:2019-12. Laborgeräte aus Glas – Aräometer – Grundlagen für Bau und Justierung.

[52] DIN12791-1:2019-12. Laborgeräte aus Glas – Aräometer – Teil 1: Allgemeine Anforderungen.

[53] DIN28131:09-1992. Rührer und Stromstörer für Rührbehälter: Formen, Benennungen und Hauptmaße.

[54] D. Doraiswamy, R. K. Grenville, and A. W. Etchells. Two-Score Years of the Metzner-Otto Correlation. *Ind. Eng. Chem. Res.*, 33:2253–2258, 1994.

[55] DowDuPont. Walocel CRT 40000 PV, 2010.

[56] R. L. Droste and R. L. Gehr. *Theory and Practice of Water and Wastewater Treatment*. Wiley, Hoboken, 2nd edition, 2018.

[57] S. Drzewiecki. Méthode pour la Détermination des Éléments Mécaniques des Propulseurs Hélicoïdaux. In *Bulletin de l'Association Technique Maritime*, number 3, pages 11–31. Imprimerie Gauthier-Villars et Fils, 1892.

[58] J. M. Ducla, H. Desplanches, and J. L. Chevalier. Effective Viscosity of non-Newtonian Fluids in a Mechanically Stirred Tank. *Chem. Eng. Commun.*, 21(1–3):29–36, 1983.

[59] F. Ebert. *Strömung nichtnewtonscher Medien*. Vieweg, Braunschweig, 1980.

[60] B. Eckhardt. Introduction. Turbulence Transition in Pipe Flow: 125th Anniversary of the Publication of Reynolds' Paper. *Phil. Trans. R. Soc. A*, 367(1888):449–455, Feb. 2009. doi: 10.1098/rsta.2008.0217.

[61] M. Ehrentraut. *Numerische Untersuchungen zur Mischgüte beim Rühren von viskoplastischen Fluiden*. Springer Fachmedien Wiesbaden, Wiesbaden, 2016. doi: 10.1007/978-3-658-14534-7.

[62] ETH Messtechnik. Torque Transducer, Waterproof DRWPL, 2018.

[63] A. Federmann. On some General Integration Methods for the Partial Differention Equations of First Order. *Annalen des Polytechnischen Instituts Peter der Große zu St. Petersburg*, 16:97–154, 1911.

[64] H. Fischer. *Mischen, Rühren, Kneten und die dazu verwendeten Maschinen*. Verlag von Otto Spamer, Leipzig, 1911.

[65] E. Förthmann. Über turbulente Strahlausbreitung. *Ingenieur-Archiv*, 5(1):42–54, Feb. 1934. doi: 10.1007/bf02086177.

[66] T. G. J. Fox and P. J. Flory. Viscosity-Molecular Weight and Viscosity-Temperature Relationships for Polystyrene and Polyisobutylene. *J. Am. Chem. Soc.*, 70(7):2384–2395, July 1948.

[67] R. E. Froude. On the Part Played in Propulsion by Differences of Fluid Pressure. *Trans. Inst. Naval Architects*, 30:390–405, 1889.

[68] R. E. Froude. The Acceleration in Front of a Propeller. *Transactions of the Royal Institution of Naval Architects*, 53:39–82, 1911.

[69] W. Froude. On the Elementary Relation between Pitch, Slip, and Propulsive Efficiency. *Trans. Inst. Naval Architects*, 19:47–57, 1878.

[70] F. García-Ochoa and J. A. Casas. Apparent Yield Stress in Xanthan Gum So-lutions at Low Concentrations. *Chem. Eng. J.*, 53(3):B41–B46, Feb. 1994. doi: 10.1016/0923-0467(93)06043-P.

[71] F. García-Ochoa, V. E. Santos, J. A. Casas, and E. Gómez. Xanthan Gum: Pro-duction, Recovery, and Properties. *Biotechnol. Adv.*, 18(7):549–579, Nov. 2000. doi: 10.1016/S0734-9750(00)00050-1.

[72] R. Gasch and J. Twele. *Windkraftanlagen: Grundlagen, Entwurf, Planung und Betrieb*. Springer, Wiesbaden, 5th edition, 2007.

[73] M. T. Ghannam and M. N. Esmail. Rheological Properties of Car-boxymethyl Cellulose. *J. Appl. Polym. Sci.*, 64(2):289–301, Apr. 1997. doi: 10.1002/(SICI)1097-4628(19970411)64:2<289::AID-APP9>3.0.CO;2-N.

[74] S. G. E. Giap. The Hidden Property of Arrhenius-Type Relationship: Viscosity as a Func-tion of Temperature. *J. Phys. Sci*, 21(1):29–39, 2010.

[75] H. Giesekus. A Simple Constitutive Equation for Polymer Fluids Based on the Concept of Deformation-Dependent Tensorial Mobility. *J. Non-Newtonian Fluid Mech.*, 11(1–2): 69–109, Jan. 1982. doi: 10.1016/0377-0257(82)85016-7.

[76] H. Giesekus. *Phänomenologische Rheologie*. Springer, Berlin, 1994.

[77] H. Glauert. Airplane Propellers. In *Aerodynamic Theory*, pages 169–360. Springer Berlin Heidelberg, 1935. doi: 10.1007/978-3-642-91487-4_3.

[78] J. F. Gülich. *Kreiselpumpen*. Springer, Heidelberg, 2010.

[79] E. S. Godleski and J. C. Smith. Power Requirements and Blend Times in the Agitation of Pseudoplastic Fluids. *AIChE J.*, 8(5):617–620, 1962. doi: 10.1002/aic.690080511.

[80] S. Goldstein. On the Vortex Theory of Screw Propellers. *Proc. R. Soc. Lond. A*, 123(792): 440–465, 1929.

[81] H. Görtler. Berechnung von Aufgaben der freien Turbulenz auf Grund eines neuen Näherungsansatzes. *ZAMM - Zeitschrift für Angewandte Mathematik und Mechanik*, 22 (5):244–254, 1942. doi: 10.1002/zamm.19420220503.

[82] B. Güzel, I. Frigaard, and D. M. Martinez. Predicting Laminar-Turbulent Transition in Poiseuille Pipe Flow for non-Newtonian Fluids. *Chem. Eng. Sci.*, 64:254–264, 2009. doi: 10.1016/j.ces.2008.10.011.

[83] G. Hagen. Ueber die Bewegung des Wassers in engen cylindrischen Röhren. *Annalen der Physik und Chemie*, 122(3):423–442, 1839. doi: 10.1002/andp.18391220304.

[84] G. Hagen. *Ueber die Bewegung des Wassers in cylindrischen, nahe horizontalen Leitun-gen*, pages 1–26. Königliche Akademie der Wissenschaften Berlin, 1869.

[85] E. Hagenbach. Ueber die Bestimmung der Zähigkeit einer Flüssigkeit durch den Aus-fluss aus Röhren. *Annalen der Physik und Chemie*, 185(3):385–426, 1860. doi: 10.1002/andp.18601850302.

[86] R. Haldenwang, A. P. N. Sutherland, V. G. Fester, R. Holm, and R. P. Chhabra. Sludge Pipe Flow Pressure Drop Prediction Using Composite Power-Law Friction Ffactor – Reynolds Number Correlations Based on Different non-Newtonian Reynolds Number. *Water SA*, 38(4):615–622, 2012.

[87] M. Hannote, F. Flores, and E. Galindo. Apparent Yield Stress Estimation in Xanthan Gum Solutions and Fermentation Broths Using a Low-Cost Viscosimeter. *Chem. Eng. J.*, 45 (3), 1991. doi: 10.1016/0300-9467(91)80020-W.

[88] M. O. L. Hansen. *Aerodynamics of Wind Turbines*. Earthscan, London, 2nd edition, 2010.

[89] M. O. L. Hansen, J. N. Sørensen, S. Voutsinas, N. Sørensen, and H. A. Madsen. State of the Art in Wind Turbine Aerodynamics and Aeroelasticity. *Prog. Aerosp. Sci.*, 42(4): 285–330, June 2006. doi: 10.1016/j.paerosci.2006.10.002.

[90] E. Hau. *Windkraftanlagen – Grundlagen, Technik, Einsatz, Wirtschaftlichkeit*. Springer, Berlin, 2008.

[91] H. Höcker, G. Langer, and U. Werner. Der Leistungsbedarf von Rührern in nichtnewtonschen Flüssigkeiten. *Chem. Ing. Tech.*, 52(11):916–917, 1980. doi: 10.1002/cite.330521118.

[92] H. Helmholtz. Über Integrale der hydrodynamischen Gleichungen, welche den Wirbelbewegungen entsprechen. *Journal für die reine und angewandte Mathematik*, 55:25–55, 1858. URL `http://eudml.org/doc/147720`.

[93] H.-J. Henzler. Auslegung von Rührfermentern – Berücksichtigung der nichtnewtonschen Eigenschaften von Fermentationslösungen. *Chem. Ing. Tech.*, 79(7):951–965, Apr. 2007. doi: 10.1002/cite.200600112.

[94] H. J. Henzler and G. Obernosterer. Effect of Mixing Behaviour on Gas-Liquid Mass Transfer in Highly Viscous, Stirred non-Newtonian Liquids. *Chem. Eng. Technol.*, 14:1–10, 1991. doi: 10.1002/ceat.270140102.

[95] M. Hepperle. JavaFoil 2.28 [Software]. http://www.mh-aerotools.de, Dec. 2017. Accessed: 2017.

[96] W. H. Herschel and R. Bulkley. Konsistenzmessungen von Gummi-Benzollösungen. *Kolloid-Zeitschrift*, 39(4):291–300, Aug. 1926. doi: 10.1007/bf01432034.

[97] J. L. Hess. Calculation of Potential Flow about Arbitrary Bodies. Technical report, Douglas Aircraft Company, 1972.

[98] A. W. Hixson and G. A. Wilkens. Performance of Agitators in Liquid-Solid Chemical Systems. *Industrial & Engineering Chemistry*, 25(11):1196–1203, Nov. 1933. doi: 10.1021/ie50287a005.

[99] C. B. Hollabaugh, L. H. Burt, and A. P. Walsh. Carboxymethylcellulose. Uses and Applications. *Industrial and Engineering Chemistry*, 37(10):943–947, 1948. doi: 10.1021/ie50430a015.

[100] R. Hooke. *Lectures De Potentia Reflituvia or of Spring Explaining the Power of Springing Bodies*. John Martyn, London, 1678.

[101] B. Hundt. *Energie- und Klimaeffizienz von Biogasanlagen mit Biogasaufbereitung und -einspeisung unter Nutzung von Silomais – Untersuchungen am Beispiel der Biogasanlage der HSE AG in Darmstadt-Wixhausen*. Dissertation thesis, Justus-Liebig-Universität Gießen, 2010.

[102] F. Irgens. *Rheology and non-Newtonian Fluids*. Springer, Heidelberg, 2014.

[103] ISO387:1977-09. HydrometersPrinciples of construction and adjustment.

[104] P. Jamieson. *Innovation in Wind Turbine Design*. John Willey & Sons Ltd, Chichester, 2nd edition, 2018.

[105] W. G. Johnston. A Method to Calculate the Pressure-Viscosity Coefficient from Bulk Properties of Lubricants. *ASLE Transactions*, 24(2):232–238, Jan. 1981. doi: 10.1080/05698198108983016.

[106] W. P. Jones and B. E. Launder. The Calculation of Low-Reynolds-Number Phenomena with a Two-Equation Model of Turbulence. *Int. J. Heat Mass Transfer*, 16(6):1119–1130, June 1973. doi: 10.1016/0017-9310(73)90125-7.

[107] W. R. Jones, R. L. Johnson, W. O. Winer, and D. M. Sanborn. Pressure-Viscosity Measurements for Several Lubricants to 5.5×10^8 Newtons Per Square Meter (8×10^4 PSI) and 149 C (300 F). *ASLE Transactions*, 18(4):249–262, Jan. 1975. doi: 10.1080/05698197508982767.

[108] N. E. Joukowsky. Windmill of the NEJ Type. *Transactions of the Central Institute for Aero-Hydrodynamics of Moscow*, 1:57, 1920. (In Russian). Reprinted in: Joukowsky, N. E. Collected Papers. VI, 405–424, Moscow-Leningrad, 1937.

[109] M. Kaltschmitt and H. Hartmann. *Energie aus Biomasse – Grundlagen, Techniken und Verfahren*. Springer, Berlin, 2001.

[110] B. Katzbauer. Properties and Applications of Xanthan Gum. *Polym. Degrad. Stab.*, 59 (1–3):81–84, Jan. 1998. doi: 10.1016/S0141-3910(97)00180-8.

[111] J. V. Kelkar, R. A. Mashelkar, and J. Ulbrecht. On the Rotational Viscoelastic Flows around Simple Bodies and Agitators. *Trans. Inst. Chem. Eng.*, 50:343–352, 1972.

[112] J. V. Kelkar, R. A. Mashelkar, and J. Ulbrecht. Scale-Up Method for the Power Consumption of Agitators in the Creeping Flow Regime. *Chem. Eng. Sci.*, 28(2):664–668, 1973. doi: 10.1016/0009-2509(73)80071-5.

[113] J. K. Klein and W.-M. Kulicke. Rheologische Untersuchungen zur Struktur hochmolekularer Polyacrylamide in wäßrigen und nichtwäßrigen Lösungen. *Rheol. Acta*, 15(10):558–567, 1976. doi: 10.1007/BF01515879.

[114] J. K. Klein and W.-M. Kulicke. Rheologische Untersuchungen zur Struktur hochmolekularer Polyacrylamide in wäßrigen und nichtwäßrigen Lösungen. *Rheol. Acta*, 15(10):568–576, 1976. doi: 10.1007/BF01515880.

[115] S. Kluck. *Erweiterung des Konzepts der rheologischen Ähnlichkeit und Einführung eines geeigneten Scale-Up Verfahrens für nichtnewtonsche Rührprozesse*. Dissertation thesis, TU Kaiserslautern, May 2016.

[116] A. Knoch. Einfluß des nichtnewtonschen Fließverhaltens auf die charakteristischen Größen eines Rührprozesses. *Chem. Ing. Tech.*, 69(10):1426–1432, Oct. 1997. doi: 10.1002/cite.330691010.

[117] A. N. Kolmogorov. Equations of Turbulent Motion in an Incompressible Fluid. In *Dokl. Akad. Nauk SSSR*, volume 30, pages 299–303, 1941.

[118] A. N. Kolmogorov. Die Energiedissipation für lokalisotrope Turbulenz. In *Dokl. Akad. Nauk SSSR*, volume 32, pages 16–18, 1941.

[119] M. Kraume. *Mischen und Rühren – Grundlagen und moderne Verfahren*. Wiley-VCH, Weinheim, 2003.

[120] M. Kraume. Die Entwicklung der Rührtechnik von einer empirischen Kunst zur Wissenschaft. *Chem. Ing. Tech.*, 86(12):2051–2062, Dec. 2014. doi: 10.1002/cite.201400124.

[121] M. Kraume. The Development of Stirring Technology from an Empirical Art to Science. *ChemBioEng Reviews*, 2(4):279–289, Aug. 2015. doi: 10.1002/cben.201500009.

[122] F. W. Lanchester. *Aerodynamics*. Archibald Constable & Co. Ltd., London, 1907.

[123] F. W. Lanchester. A Contribution to the Theory of Propulsion and the Screw Propeller. *Trans. Inst. Naval Architects*, 3:98–116, 1915.

[124] R. I. Lewis. *Turbomachinery Performance Analysis*. Elsevier, London, 1996.

[125] O. Lilienthal. *Der Vogelflug als Grundlage der Fliegekunst – Ein Beitrag zur Systematik der Flugtechnik*. Gaertners Verlagsbuchhandlung, Berlin, 1889.

[126] B. Lukasch, editor. *Otto Lilienthal - Der Vogelflug als Grundlage der Fliegekunst*. Springer Berlin Heidelberg, Berlin, 2014. doi: 10.1007/978-3-642-41812-9.

[127] Maedler. Maedler Catalogue 03/2018, 2018.

[128] K. Magnusson. Effektbehovets Beroende av den Effektiva Viskositeten vid Omröring av Strukturviskösa Vätskor. *IVA*, 2:86–91, 1952.

[129] M. J. Martín-Alfonso, F. J. Martínez-Boza, F. J. Navarro, M. Fernández, and C. Gallegos. Pressure-Temperature-Viscosity Relationship for Heavy Petroleum Fractions. *Fuel*, 86 (1–2):227–233, Jan. 2007. doi: 10.1016/j.fuel.2006.05.006.

[130] J. C. Maxwell. On the Dynamical Theory of Gases. *Philos. Trans. Roy. Soc. London*, 157 (0):49–88, Jan. 1867. doi: 10.1098/rstl.1867.0004.

[131] A. B. Metzner and R. E. Otto. Agitation of non-Newtonian Fluids. *AIChE J.*, 3(1):3–10, Mar. 1957. doi: 10.1002/aic.690030103.

[132] A. B. Metzner and J. C. Reed. Flow of non-Newtonian Fluids-Correlation of the Laminar Transition and Turbulent-Flow Regions. *AIChE J.*, 1(4):434–440, 1955. doi: 10.1002/aic.690010409.

[133] A. B. Metzner and J. S. Taylor. Flow Patterns in Agitated Vessels. *AIChE J.*, 6(1):109–114, Mar. 1960. doi: 10.1002/aic.690060121.

[134] A. B. Metzner, R. H. Feehs, H. L. Ramos, R. E. Otto, and J. D. Tuthill. Agitation of Viscous Newtonian and non-Newtonian Fluids. *AIChE J.*, 7(1):3–9, Mar. 1961. doi: 10.1002/aic.690070103.

[135] T. G. Mezger. *Das Rheologie Handbuch*. Vincentz Network, Hannover, 2nd edition, 2006.

[136] MHI Vestas. MHI Vestas Signs Firm Order for Largest MW Project in Company History. http://www.mhivestasoffshore.com/wp-content/uploads/2018/08/MVOW3.jpg. Accessed: 2018-09-14.

[137] M. Mooney. Explicit Formulas for Slip and Fluidity. *J. Rheol.*, 2:210–222, Apr. 1931. doi: 10.1122/1.2116364.

[138] M. Munk. Wind Driven Propeller. NACA. *Technical Memorandums*, 201:1–12, 1920.

[139] S. Nagata. *Mixing – Principles and Applications*. Kodansha LTD., Tokyo, 1975.

[140] C. L. M. H. Navier. Sur les Lois des Mouvements des Fluides, en ayrant Égard à l'Adhésion des Molécules. *Annales de chimie et de physique*, 19:244–255, 1822.

[141] I. Newton. *Philosophiae Naturalis Principia Mathematica*. Sumptibus Societatis, Amsterdam, 1714.

[142] NEWWAY air bearings, 2019. URL `https://www.newwayairbearings.com/catalog/product/13mm-air-bushings/`. Accessed: 2019-12-26.

[143] NEWWAY air bearings, 2019. URL `https://www.newwayairbearings.com/catalog/product/12mm-x-24mm-flat-rectangle-air-bearings/`. Accessed: 2019-12-26.

[144] Nortek AS. Vector Cable Probe GA – Technical specification, May 2016. URL `https://www.nortekgroup.com/products/vector-300-m/pdf-init`. Rev. A, Accessed: 2016.

[145] Nortek AS. Vector Cable Probe GA – Technical drawings, 2016. URL `https://www.nortekgroup.com/assets/documents/NGA008-002....Rev.A...Vector-Cable-Probe-GA.pdf`. Accessed: 2016.

[146] H. Oebius. Sohlerosion durch Schiffspropeller. Technical Report 987/84, Versuchsanstalt für Wasserbau und Schiffsbau, 1980.

[147] H. Oebius. Charakterisierung der Einflussgrößen Schiffumströmung und Propellerstrahl auf die Wasserstraßen. In *Mitteilungsblatt der Bundesanstalt für Wasserbau Nr. 82*, pages 7–22. Bundesanstalt für Wasserbau (BAW), Karlsruhe, 2000.

[148] V. L. Okulov and G. A. M. van Kuik. The Betz-Joukowsky Limit: On the Contribution to Rotor Aerodynamics by the British, German and Russian Scientific Schools. *J. Wind Energy*, 15(2):335–344, Apr. 2011. doi: 10.1002/we.464.

[149] J. G. Oldroyd. On the Formulation of Rheological Equations of State. *Proceedings of the Royal Society of London. Series A. Mathematical and Physical Sciences*, 200(1063): 523–541, Feb. 1950. doi: 10.1098/rspa.1950.0035.

[150] W. Ostwald. Ueber die Geschwindigkeitsfunktion der Viskosität disperser Systeme. I. *Kolloid-Zeitschrift*, 36(2):99–117, Feb. 1925. doi: 10.1007/bf01431449.

[151] W. Ostwald. Ueber die rechnerische Darstellung des Strukturgebietes der Viskosität. *Kolloid-Zeitschrift*, 47(2):176–187, Feb. 1929. doi: 10.1007/bf01496959.

[152] A. Palaniraj and V. Jayaraman. Production, Recovery and Applications of Xanthan Gum by Xanthomonas Campestris. *J. Food Eng.*, 106(1):1–12, Sept. 2011. doi: 10.1016/j.jfoodeng.2011.03.035.

[153] S. P. Patel, G. Ranjan, and V. S. Patel. Rheological Properties of Guar Gum and Hydroxyethyl Guar Gum in Aqueous Solution. *Int. J. Biol. Macromol.*, 9(6):314–320, Dec. 1987. doi: 10.1016/0141-8130(87)90001-8.

[154] E. L. Paul, V. A. Atiemo-Obeng, and S. M. Kresta, editors. *Handbook of Industrial Mixing: Science and Practice*. Willey, Hoboken, 2004. ISBN 978-0-471-45144-0.

[155] J. Pawlowski. *Die Ähnlichkeitstheorie in der physikalisch-technischen Forschung: Grundlagen und Anwendung*. Springer-Verlag, Berlin, 1971.

[156] J. Pawlowski. Prozessbeziehungen bei nichtnewtonschen Stoffen – Kritik des Metzner-Otto-Konzeptes. *Chem. Ing. Tech.*, 76(7):910–914, Feb. 2004. doi: 10.1002/cite.200403388.

[157] A. S. Pensado, M. J. P. Comuñas, and J. Fernández. The Pressure-Viscosity Coefficient of Several Ionic Liquids. *Tribol. Lett.*, 31(2):107–118, July 2008. doi: 10.1007/s11249-008-9343-0.

[158] C. Pfleiderer and H. Peterman. *Strömungsmaschinen*. Springer, Berlin, 2005.

[159] N. Phan-Thien. *Understanding Viscoelasticity: Basics of Rheology*. Springer, Berlin, 2002.

[160] H. F. Phillips. Blades for Deflecting Air, 1884.

[161] A. C. Pipkin. *Lectures on Viscoelasticity*. Springer, Heidelberg, 1972.

[162] A. C. Pipkin and R. I. Tanner. A Survey of Theory and Experiment in Viscometric Flows of Viscoelastic Liquids. In *Mechanics Today 1*, pages 262–321. Pergamon Press Inc., 1972.

[163] J. L. Poiseuille. *Recherches Expérimentales sur le Mouvement des Liquides dans les Tubes de Très-Petits Diamètres*. Imprimerie Royale, Paris, 1844.

[164] L. Prandtl. Tragflügeltheorie. I. Mitteilung. *Nachrichten von der Gesellschaft der Wissenschaften zu Göttingen, Mathematisch-Physikalische Klasse*, 1918:451–477, 1918.

[165] L. Prandtl. Tragflügeltheorie. II. Mitteilung. *Nachrichten von der Gesellschaft der Wissenschaften zu Göttingen, Mathematisch-Physikalische Klasse*, pages 107–137, 1919.

[166] L. Prandtl. 7. Bericht über Untersuchungen zur ausgebildeten Turbulenz. *ZAMM - Journal of Applied Mathematics and Mechanics / Zeitschrift für Angewandte Mathematik und Mechanik*, 5(2):136–139, 1925. doi: 10.1002/zamm.19250050212.

[167] M. J. Prosser. The Hydraulic Design of Pump Sumps and Intakes. Technical report, British Hydrodynamics Research Association, 1977.

[168] B. Rabinowitsch. Über die Viskosität und Elastizität von Solen. *Z. Phys. Chem. A*, 145(1):1–26, Nov. 1929.

[169] N. Rajaratnam. *Turbulent Jets (Developments in Water Science, Volume 5)*. Elsevier Science Ltd., Amsterdam, 1976. ISBN 0-444-41372-3.

[170] W. J. M. Rankine. On the Mechanical Principles of the Action of Propellers. *Trans. Inst. Naval Architects*, 6:13–39, 1865.

[171] W. J. M. Rankine. On the Theoretical Limit of the Efficiency of Propellers. *The Engineer*, 23:25, Jan. 1867.

[172] W. J. M. Rankine, W. J. Millar, and P. Guthrie. *Miscellaneous Scientific Papers: by W. J. Macquorn Rankine*. C. Griffin and company, London, 1881.

[173] T. Ree and H. Eyring. Theory of non-Newtonian Flow: I. Solid Plastic System. *J. Appl. Phys.*, 26(7):793–800, July 1955. doi: 10.1063/1.1722098.

[174] H. Reichardt. *VDI-Forschungsheft 414, Gesetzmäßigkeiten der freien Turbulenz*. VDI-Verlag GmbH, Berlin, 1985.

[175] M. Reiner. A Mathematical Theory of Dilatancy. *Am. J. Math.*, 67(3):350, July 1945. doi: 10.2307/2371950.

[176] M. Reiner. *Selected Papers on Rheology*. Elsevier Science & Technology, Amsterdam, 1975.

[177] M. Reiner and R. Schoenfeld-Reiner. Viskosimetrische Untersuchungen an Lösungen hochmolekularer Naturstoffe. I. Mitteilung. Kautschuk in Toluol. *Kolloid-Zeitschrift*, 65(1): 44–62, Oct. 1933. doi: 10.1007/bf01428857.

[178] T. Reviol. *Experimentelle und numerische Untersuchungen eines modifizierten Propeller-Viskosimeters zur Bestimmung der Fließeigenschaften nichtnewtonscher Medien mit inhomogenem Charakter*. Dissertation thesis, TU Kaiserslautern, Kaiserslautern, 2010.

[179] T. Reviol, S. Kluck, and M. Böhle. Erweiterung der Auslegungsverfahren von Rührern und Anwendung an einem Propellerviskosimeter. *Chem. Ing. Tech.*, 86(8):1230–1240, Aug. 2014. doi: 10.1002/cite.201300100.

[180] T. Reviol, S. Kluck, F. Genuit, V. Reim, and M. Böhle. Investigation of the Influence of Viscoelastic Behaviour on the Agitation of non-Newtonian Fluid Flow. *Chem. Eng. Sci.*, 152:55–64, Oct. 2016. doi: 10.1016/j.ces.2016.05.035.

[181] T. Reviol, S. Kluck, and M. Böhle. A new Design Method for Propeller Mixers Agitating non-Newtonian Fluid Flow. *Chem. Eng. Sci.*, 190:320–332, Nov. 2018. doi: 10.1016/j.ces.2018.06.033.

[182] T. Reviol, S. Kluck, G. Ettringer, and M. Böhle. Investigation of Propeller Mixer for Agitation of non-Newtonian Fluid Flow to Predict the Characteristics within the Design Process. *Chem. Eng. Sci.*, 191:420–435, Dec. 2018. doi: 10.1016/j.ces.2018.05.028.

[183] O. Reynolds. An Experimental Investigation of the Circumstances Which Determine Whether the Motion of Water Shall Be Direct or Sinuous, and of the Law of Resistance in Parallel Channels. *Philos. Trans. Roy. Soc. London*, 174(0):935–982, Jan. 1883. doi: 10.1098/rstl.1883.0029.

[184] O. Reynolds. An Experimental Investigation of the Circumstances Which Determine Whether the Motion of Water Shall Be Direct or Sinuous, and of the Law of Resistance in Parallel Channels. *Proc. Roy. Soc. London*, 35(224–226):84–99, Jan. 1883. doi: 10.1098/rspl.1883.0018.

[185] D. Riabouchinsky. Methode des Variables de Dimension Zero, et son Application en Aerodynamique. *L'aérophile*, 1:407–408, 1911.

[186] L. F. Richardson. The Supply of Energy from and to Atmospheric Eddies. *Proceedings of the Royal Society A: Mathematical, Physical and Engineering Sciences*, 97(686):354–373, July 1920. doi: 10.1098/rspa.1920.0039.

[187] F. Rieger and V. Novak. Scale-Up Method for Power Consumption of Agitators in the Creeping Flow Regime. *Chem. Eng. Sci.*, 27(1):39–44, 1972. doi: 10.1016/0009-2509(72)80139-8.

[188] F. Rieger and V. Novak. Power Consumption of Agitators in Highly Viscous non-Newtonian Liquids. *Trans. Inst. Chem. Eng.*, 51:105–111, 1973.

[189] F. Rieger and V. Novak. Power Consumption Scale-Up in Agitating non-Newtonian Fluids. *Chem. Eng. Sci.*, 29(11):2229–2234, 1974. doi: 10.1016/0009-2509(74)80031-X.

[190] C. D. Rielly. Mixing in food processing. In P. J. Fryer, D. L. Pyle, and C. D. Rielly, editors, *Chemical Engineering for the Food Industry*, pages 383–433. Springer, 1997. ISBN 978-1-4613-6724-6. doi: 10.1007/978-1-4615-3864-6_10.

[191] R. S. Rivlin. Hydrodynamics of non-Newtonian Fluids. *Nature*, 160(4070):611–611, Nov. 1947. doi: 10.1038/160611a0.

[192] N. Rott. Note on the History of the Reynolds Number. *Annu. Rev. Fluid Mech.*, 22(1): 1–12, Jan. 1990. doi: 10.1146/annurev.fl.22.010190.000245.

[193] R. C. Rowe, P. J. Sheskey, and M. E. Quinn, editors. *Handbook of Pharmaceutical Excipients*. Pharmaceutical Press and American Pharmaceutical Association, London, 6th edition, 2009.

[194] M. Rudman, H. M. Blackburn, L. J. W. Graham, and L. Pullum. Turbulent Pipe Flow of Shear-Thinning Fluids. *J. Non-Newtonian Fluid Mech.*, 118:33–48, 2004. doi: 10.1016/j.jnnfm.2004.02.006.

[195] L. Rudolph, M. Schäfer, V. Atiemo-Obeng, and M. Kraume. Experimental and Numerical Analysis of Power Consumption for Mixing of High Viscosity Fluids with a Co-Axial Mixer. *IChemE*, 85:568–575, 2007. doi: 10.1205/cherd06178.

[196] J. H. Rushton, E. W. Costich, and H. J. Everett. Power Characteristics of Mixing Impellers – Part I. *Chem. Eng. Prog.*, 46(8):395–404, Aug. 1950.

[197] J. H. Rushton, E. W. Costich, and H. J. Everett. Power Characteristics of Mixing Impellers – Part II. *Chem. Eng. Prog.*, 46(9):467–476, Sept. 1950.

[198] G. R. Sanderson. Applications of Xanthan Gum. *Polym. Int.*, 13(2), June 1981. doi: 10.1002/pi.4980130207.

[199] D. T. Sandwell. Biharmonic Spline Interpolation of GEOS-3 and SEASAT Altimeter Data. *Geophys. Res. Lett.*, 14(2):139–142, 1987. doi: 10.1029/GL014i002p00139.

[200] H. Schlichting. Laminare Strahlausbreitung. *ZAMM - Zeitschrift für Angewandte Mathematik und Mechanik*, 13(4):260–263, 1933. doi: 10.1002/zamm.19330130403.

[201] H. Schlichting and H. Gersten. *Grenzschichttheorie*. Springer, Berlin, 2006.

[202] H. Schlichting and E. Truckenbrodt. *Aerodynamik des Flugzeugs – Grundlagen aus der Strömungsmechanik, Aerodynamik des Tragflügels (Teil 1)*. Springer, Berlin, 2nd edition, 1967.

[203] H. Schlichting and E. Truckenbrodt. *Aerodynamik des Flugzeugs – Aerodynamik des Tragflügels (Teil 2), des Rumpfes der Flügel-Rumpf-Anordnung und der Leitwerke*. Springer, Berlin, 2nd edition, 1967.

[204] G. Schmitz. Theorie und Entwurf von Windrädern optimaler Leistung. *Zeitschrift der Universität Rostock*, 5:379–391, 1955.

[205] P. Schümmer. Untersuchungen über das Rühren viskoelastischer Flüssigkeiten im laminaren Bereich. *Chem. Ing. Tech.*, 41:1156–1163, 1969. doi: 10.1002/cite.330412103.

[206] A. Schneider. *A Consistent Large Eddy Approach for Lattice Boltzmann Methods and its Application to Complex Flows*. Dissertation thesis, Technische Universität Kaiserslautern, 2015.

[207] A. Schneider and M. Böhle. Lattice Boltzmann Simulation of the Flow Field in Pump Intakes – A new Approach. In *Proceedings of the ASME 2013 Fluids Engineering Division Summer Meeting*, July 2013.

[208] A. Schneider, D. Conrad, and M. Böhle. Lattice Boltzmann Simulation of the Flow Field in Pump Intakes – A new Approach. *ASME J. Fluids Eng.*, 137(3):031105-1–031105-10, Mar. 2015. doi: 10.1115/1.4028777.

[209] P. J. Schubel and R. J. Crossley. Wind Turbine Blade Design. *Energies*, 5:3425–3449, 2012. ISSN 1996-1073. doi: 10.3390/en5093425.

[210] W. Send. Otto Lilienthal und der Mechanismus des Schwingenflugs – Zum Gedächtnis an Otto Lilienthals Tod 1896 vor 100 Jahren. In *DGLR Jahrestagung*, number DGLR-JT96-030, Dresden, Sept. 1996.

[211] S. M. Shekar and S. Jayanti. Mixing of Power-Law Fluids Using Anchors: Metzner-Otto Concept Revisited. *AIChE J.*, 49(1):30–40, 2003. doi: 10.1002/aic.690490105.

[212] H. Snel. Review of the Present Status of Rotor Aerodynamics. *Wind Energy*, 1(S1):46–69, Jan. 1998. doi: 10.1002/(SICI)1099-1824(199804)1:1+<46::AID-WE3>3.0.CO;2-9.

[213] H. Snel. Review of Aerodynamics for Wind Turbines. *Wind Energy*, 6(3):203–211, 2003. doi: 10.1002/we.97.

[214] Y.-S. Son, S.-W. Park, D.-W. Park, and J.-W. Lee. Effect of the Rheological Properties of Aqueous Xanthan Gum Solution on Chemical Absorption of Carbon Dioxide with Diisopropanolamine. *Korea-Aust. Rheol. J.*, 21(2):109–117, June 2009.

[215] B. Sørensen. History of, and Recent Progress in, Wind-Energy Utilization. *Annu. Rev. Energy Env.*, 20(1):387–424, 1995.

[216] J. H. Spurk. *Dimensionsanalyse in der Strömungslehre*. Springer, Berlin, 1992.

[217] J. H. Spurk and N. Aksel. *Strömungslehre – Einführung in die Theorie der Strömungen*. Springer, Heidelberg, 2010.

[218] M. Stieß. *Mechanische VerfahrVerfahren – Partikeltechnologie 1*. Springer, Berlin, 2009.

[219] G. G. Stokes. On the Theories of the Internal Friction of Fluids in Motion, and of the Equilibrium and Motion of Elastic Solids. *Trans. Cambridge Phil. Soc.*, 8:287–305, 1845.

[220] P. A. Tanguy, F. Thibault, and E. B. de la Fuente. A New Investigation of the Metzner-Otto Concept for Anchor Mixing Impellers. *Can. J. Chem. Eng.*, 74(2):222–228, Apr. 1996. doi: 10.1002/cjce.5450740207.

[221] J. Thomson. Report Made to the President and Council of the Royal Society, of Experiments on the Friction of Disc Revolving in Water. In *Proceedings of the Royal Society of London*, pages 509–511, 1855.

[222] P. Todtenhaupt and G. Zeiler. *Handbuch der Rührtechnik*. EKATO Rühr- und Mischtechnik, Schopfheim, 1990.

[223] W. Tollmien. Berechnung turbulenter Arbeitsvorgänge. *Zeitschrift für angewandte Mathematik und Mechanik*, 6(6):468–478, Dec. 1926.

[224] L. G. Torres, F. Flores, and E. Galindo. Apparent Yield Stress of Xanthan Solutions and Broths. *Bioprocess. Eng.*, 12(1–2):41–46, Jan. 1995.

[225] M. D. Torres, B. Hallmark, and D. I. Wilson. Effect of Concentration on Shear and Extensional Rheology of Guar Gum Solutions. *Food Hydrocoll.*, 40:85–95, Oct. 2014. doi: 10.1016/j.foodhyd.2014.02.011.

[226] J. Ulbrecht and K. Wichterle. Schnell laufende Rührwerke bei laminarer Strömung. *Chem. Ing. Tech.*, 39(11):656–658, 1967. doi: 10.1002/cite.330391104.

[227] W. C. Unwin. On the Friction of Water against Solid Surfaces of Different Degrees of Roughness. In *Proceedings of the Royal Society of London*, pages 54–58, 1880.

[228] L. Urban. *Methode zur Auswahl von Rührwerken für klärtechnische Mischbecken*. Dissertation thesis, Technische Universität Kaiserslautern, 2008.

[229] G. A. M. van Kuik. The Lanchester-Betz-Joukowsky limit. *J. Wind Energy*, 10(3):289–291, 2007. doi: 10.1002/we.218.

[230] A. Vaschy. Sur les Lois de Similitude en Physique. In *Annales télégraphiques*, volume 19, pages 25–28, 1892.

[231] H. Vollmers and J. C. Rotta. Similar Solutions of the Mean Velocity, Turbulent Energy and Length Scale Equation. *AIAA Journal*, 15(5):714–720, May 1977. doi: 10.2514/3.60681.

[232] P. Wang. *Investigation of the Characteristics a Novel Design Propeller for Mixing of non-Newtonian Fluids*. Dissertation thesis, Technische Universität Kaiserslautern, 2019.

[233] P. Wang, T. Reviol, S. Kluck, P. Würtz, and M. Böhle. Mixing of non-Newtonian Fluids in a Cylindrical Stirred Vessel Equipped with a Novel Side-Entry Propeller. *Chem. Eng. Sci.*, 190:384–395, Nov. 2018. doi: 10.1016/j.ces.2018.06.034.

[234] P. Wang, T. Reviol, H. Ren, and M. Böhle. Effects of Turbulence Modeling on the Prediction of Flow Characteristics of Mixing non-Newtonian Fluids in a Stirred Vessel. *Chem. Eng. Res. Des.*, 147:259–277, July 2019. doi: 10.1016/j.cherd.2019.05.001.

[235] P. Wang, T. Reviol, H. Ren, and M. Böhle. Experimental Investigation of the Mixing Characteristics of non-Newtonian Fluids through an Ultrasonic Doppler Anemometer (UDA). *Exp. Therm Fluid Sci.*, 109:109866, Dec. 2019. doi: 10.1016/j.expthermflusci.2019.109866.

[236] K. H. Wassmer and K. D. Hungenberg. A Unified Model for the Mixing of Non-Newtonian Fluids in the Laminar, Transition and Turbulent Region. *Macromol. Mater. Eng.*, 290(4): 294–301, Apr. 2005. doi: 10.1002/mame.200400328.

[237] A. White and E. Brenner. Studies in Agitation, IV. Power Measurements. *Trans. Amer. Inst. Chem. Eng.*, 30:585–597, 1934.

[238] K. Wichterle, J. Proscaronkova, and J. Ulbrecht. Schnell laufende Rührwerke bei laminarer Strömung. Teil II: Simulation des mechanischen Rührens durch einen rotierenden niedrigen Zylinder. *Chem. Ing. Tech.*, 43(15):867–870, 1971. doi: 10.1002/cite.330431506.

[239] K. Wieghardt. *Strömungslehre*. Teubner, Stuttgart, 1974.

[240] R. E. Wilson and P. Lissaman. *Applied Aerodynamics of Wind Power Machines*. Corvallis, Or., Oregon State Elsevier, s.l., 1974.

[241] J. C. Wood, E. R. Whittemore, and W. L. Badger. The Measurement of Stirrer Performance. *Chemical and Metallurgical Engineering*, 27(24):1176–1179, 1922.

[242] R. M. Wood, F. B. Bradfield, and M. Barker. Multiplane Interferrence Applied to Airscrew Theory. Technical Report 639, Aeronautical Research Committee, Sept. 1919. Reports and Memoranda.

[243] H. E. Wulff. *The Traditional Crafts of Persia*. MIT Press, Cambridge, 1966.

[244] K. Yasuda. *Investigation of the Analogies between Viscometric and Linear Viscoelastic Properties of Polystyrene Fluids*. PhD thesis, Massachusetts Institute of Technology, 1979.

[245] W. Zimm. *Über die Strömungsvorgänge im freien Luftstrahl*. Verlag des Vereines deutscher Ingenieure, Berlin, 1921.

[246] M. Zlokarnik. *Rührtechnik – Theorie und Praxis*. Springer, Berlin, 1999.

[247] M. Zlokarnik. *Scale-up: Modellübertragung in der Verfahrenstechnik*. Wiley-VCH, Berlin, 2000. ISBN 978-3527298648.

Appendix

A. Measurement devices

A.1. Viscometer

R/S Rheometer main instrument (minimum configuration)

1	R/S Rheometer
2	Measuring bob coupling
3	Mounting flange
4	Pt100-clamp fixture (accessory)
5	Pt100 (accessory)
6	Standard measuring bob (accessory)
7	Standard measuring cup (accessory)
8	Measuring cup bottom, or thread protection (accessory)
9	Measuring cup screw fitting
10	Stand
11	AC-adaptor
12	Direct current coupling
13	Mains connection cable
14	Data transmission cable (accessory

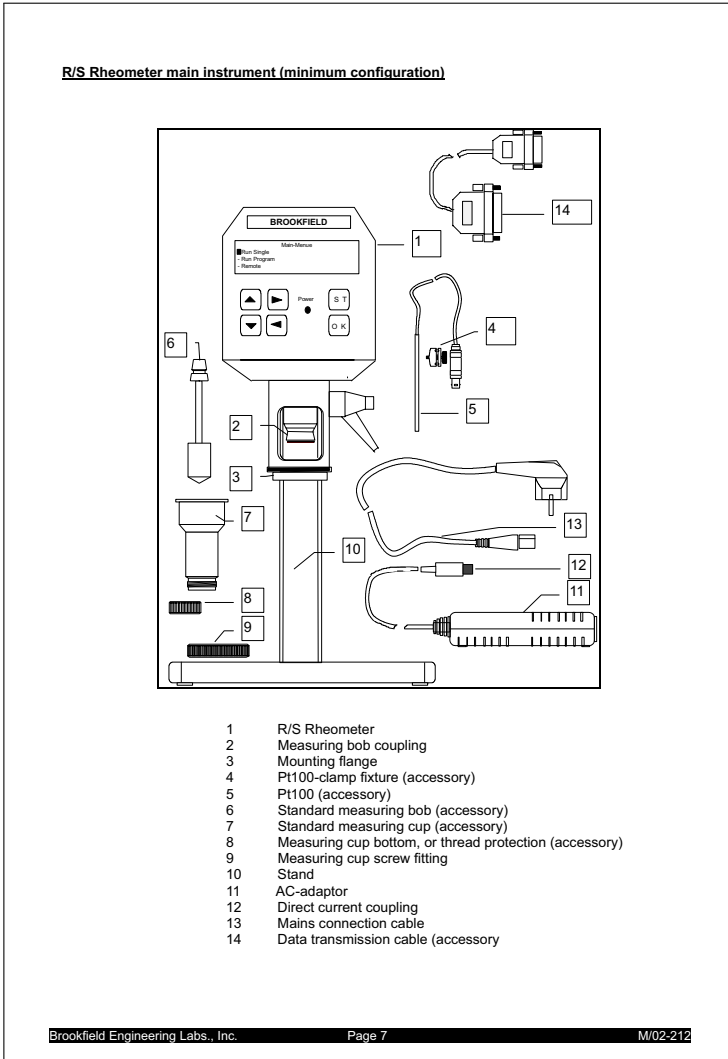Brookfield Engineering Labs., Inc.   Page 7   M/02-212

Figure A.1. *Technical specifications of viscometer type R/S from BROOKFIELD ENGINEER-ING LABORATORIES, INC. [28], excerpt from the data sheet, page 7, overview of the measurement device*

VIII. Technical data

R/S Rheometer	
Dimensions	480 mm x 300 mm x 290 mm
Weight	8 kg
Nominal operating voltage **Power consumption (average)** **Power consumption (maximum)**	+/- 15 V, 5 V 12 W 22 W

Ambience conditions
Temperature
    in operation
    out of operation
Relative humidity (not condensable)
    in operation
    out of operation
	
	10° to 40°C
	10° to 45°C
	
	20% to 80%
	10% to 90%

Accuracy	± 1.0 % of maximum range value ± 1 digit
Torque range **Mains operation**	 0.05 to 50 mNm
Torque resolution	0.01 mNm
Speed range	0.7 min^{-1} to 800 min^{-1}
Angle resolution	0.8 mrad
Temperature range	Depending on temperature control device used -20°C to +180°C
Shear rate range	Depending on measuring system used 0.9 s^{-1} to $4 \times 10^3 \text{ s}^{-1}$
Shear stress range	Depending on measuring system used 0.7 Pa to 3.4×10^4 Pa
Viscosity range The given range is a standard value (not maximum value)	Depending on measuring system used 1×10^{-3} Pas to 3×10^3 Pas

AC-Adaptor	
Dimensions	160 mm x 85 mm x 35 mm
Weight	0.5 kg

Power supply
   Mains voltage
   secondary voltages (Output)
   output-current
   output power
	
	from 100 up to 240 V AC
	5 V, +/- 15 V DC
	2 A, 0.9 / -0.2 A
	20 W

Frequency range of mains voltage	50 bis 60 Hz

Environment conditions
Temperature
    in operation
    out of operation
Relative humidity (not condensable)
    in operation
    out of operation
	
	+10°C to +40°C
	+10°C to +45°C
	
	20% to 80%
	10% to 90%

Figure A.2.   *Technical specifications of viscometer type R/S from BROOKFIELD ENGINEERING LABORATORIES, INC. [28], excerpt from the data sheet, page 52, technical data*

FTK-CC	
Dimensions (Width x Height x Depth)	94 mm x 55 mm x 170 mm
Weight	600 g
Temperature range	
standard range	-10°C to +90°C
with cooling device	-20°C to +180°C

Measured or evaluated values
The preset values and measured values are listed below as well as all evaluated values:

Value	Symbol	Physical Unit
Speed	n	[min^{-1}]
Torque (relative) (1000 ‰ $\triangleq$ 50 mNm)	M	[1]
Temperature	T	[°C]
Time	t	[s]
Shear rate	$\dot{\gamma}$	[s^{-1}]
Shear stress	τ	[Pa]
Dynamic viscosity	η	[Pas]

Figure A.3.   *Technical specifications of viscometer type R/S from BROOKFIELD ENGINEER-ING LABORATORIES, INC. [28], excerpt from the data sheet, page 53, technical data*

APPENDIX

A1 Data sheets of standard measuring systems

Table Standard cylinder measuring systems according to DIN 53019 / ISO 3219
(consists of measuring bob and measuring cup)
For R/S Rheometer three types of measuring bobs are available:

- MB-CC48 ... CC8 DIN/RC
- MB-CC48 ... CC8 DIN/FTK
- MBA-CC48...CC8 DIN/FTK with EMB-CC48...CC8

Measuring system	CC48	CC45	CC25	CC14	CC8
Shear rate range [s^{-1}]	0 ... 4,114	0 ... 1,032	0 ... 1,032	0 ... 1,032	0 ... 1,032
Shear stress range [Pa]	0 ... 206	0 ... 195	0 ... 1141	0 ... 6501	0 ... 34,844
Viscosity range [Pas]	0.005 ... 32	0.020 ... 15	0.118 ... 100	0.672 ... 500	3.60 ... 3,000
Filling volume [ml]	70	100	17	3	0.5
Shear rate factor $K_{\dot{\gamma}}$ [min/s]	5.142	1.291	1.291	1.291	1.291
Shear stress factor $\tau_{‰}$ [Pa]	0.1900	0.1958	1.1418	6.501	34.844
Radius of measuring bob R_i [mm]	23.9	22.5	12.5	7	4
Radius of measuring cup R_a [mm]	24.4	24.4	13.56	7.59	4.34
Radius of shaft R_s [mm]	3.5	3.5	3.5	2.1	1.2
Angle of measuring bob cone α [°]	120	120	120	120	120
Distance between lower edge of meas. bob and meas. cup bottom L' [mm]	35	35	15.5	13	12
Immersion of measuring shaft L" [mm]	22.5	22.5	12.5	7	4
Length of meas. bob L [mm]	67.5	67.5	37.5	21	12
Ratio of Radii δ = **Error!**	1.0209	1.0844	1.0848	1.0843	1.0850
Resistance coefficient c_L	1.1	1.1	1.1	1.1	1.1
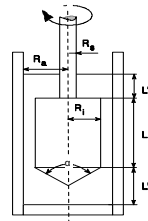
Measuring geometrie DIN 53019

The given ranges are standard values (not maximum values).

Figure A.4. *Technical specifications of viscometer type R/S from BROOKFIELD ENGINEER-ING LABORATORIES, INC. [28], excerpt from the data sheet, page 55, data of measuring systems, system CC48, CC45 and CC25 were applied*

A.2. Torque sensors

Technical Specifications DRWPL

Supply voltage:	12 V DC ± 10 %
Power consumption:	approx. 200 mA
Rise time 10-90 %:	2 ms
Limit frequency −3 dB:	200 Hz (optional 1 kHz)
Voltage output:	0 to ± 10 V
Internal resistance:	100 Ω
Ripple:	< 100 mVss
Nonlinearity/max. measurement error (of full scale):	0,1 %
Hysteresis:	0,1 %
Deviation at zero point:	≤ ± 100 mV
Max. measurement error:	0,1 % (FS / of full scale)
Operating temperature:	0 - 60 °C
Compensated temperature range:	5 - 45 °C

Temperature error
  Zero point:
  Sensitivity:
	0,02 % / K
	0,01 % / K

Mechanical overload:	100 %
Internal protection:	IP 67 DIN 40050
Cable length:	2,5 m (standard)
Connection:	flying leads

Factory calibration right-/ left load in 25% steps. Special calibration on request.

EMV Immunity for interference   (DIN EN 50082-2) *1

Enclosure	Severity
HF line interference	
150 kHz - 80 MHz (AM)	10 V
ESD (Electrostatic discharge)	Air 8 kV / Contakt 4 kV
Enclosure	
Electromagnetic field	
80 Mhz - 1000 MHz (AM)	10 V/m
150 kHz - 80 MHz (AM)	20 V/m
Leads - Connection Cable	
Burst (fast transients)	2 kV

*1 Severity / criterion: industrial environment; Cable lenght ≤ 30 m. Application not outside buildings.

Interference Emission (EN 55011)
Disturbance Voltage (electromagnetic disturbances)   Class B (150 kHz -   30 MHz)
Radiated Emission (electromagnetic disruption axis)   Class B (30 MHz - 1000 MHz)

Speed Option (n)	
max. rev.:	up to 10 000 min^{-1} *2
Output:	open-collector
Internal pull up:	10 kΩ (5 V level)
External pull up:	24 V max . / 20 mA
Pulses / rev.:	60

*2 with suitable external wiring 20.000 min^{-1}
  (or speed max.)

Angle Option (w)	
max. rev.:	up to 3 000 min^{-1} *3
Output:	open-collector
Internal pull up:	10 kΩ (5 V level)
External pull up:	24 V max
Pulses / rev.:	360
Resolution:	1°
Phase shift	Channel A 90° at right spin of propulsion side.

*3 with suitable external wiring 15.000 min^{-1}
  (or speed max.)

E︵H messtechnik gmbh   hagstrasse 10   D-74417 gschwend   germany   tel. +49 (0)7972-9310-0   sales@eth-messtechnik.de   www.eth-messtechnik.de
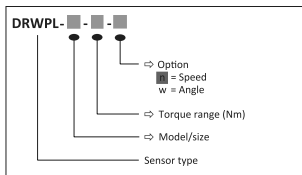
Figure A.5. *Technical specifications of torque sensor type DRWPL-I resp. II from ETH Messtechnik [62], excerpt from the data sheet, available torque sensors are DRWPL type I-0.1 Nm, type I-0.5 Nm and type II-10 Nm*

Technical Specifications DRWPL

Sizes	Torque range (Nm)	Spring constant C (Nm/rad)	Mass moment of inertia J (g•cm²)			Rated axial load (N) *	Rated radial load (N) *
			Total	Drive side	Measuring side		
I	0,1	33	7,7	6,8	0,9	140	1,5
	0,2	33	7,7	6,8	0,9	140	1,5
	0,5	86	7,9	6,9	0,8	160	2
	1	86	7,9	6,9	0,8	210	3,5
	2	173	7,9	7,0	1,0	210	6,5
II	5	936	111	77	34	930	10
	10	2017	111	78	33	930	20
	20	3626	112	78	34	930	50
	50	5808	116	80	36	930	110
III	50	15.471	984	560	424	1820	60
	100	25.696	993	564	429	1820	130
	200	41.762	1020	578	442	1820	250
	300	48.872	1047	591	456	1820	380
IV	500	205.695	11.778	6455	5323	4160	522
	1000	290.236	12.011	6572	5439	4160	1019
	1500	327.886	12.277	6705	5572	4160	1502

*The values for axial and radial load apply to the non-fixed housing

Ordering code system

DRWPL- ▪ - ▪ - ▪

⇨ Option
▪ = Speed
w = Angle

⇨ Torque range (Nm)

⇨ Model/size

Sensor type

Available Accessories

Supply and display unit: ValueMasterBase
Couplings

Figure A.6. *Technical specifications of torque sensor type DRWPL-I resp. II from ETH Messtechnik [62], excerpt from the data sheet, available torque sensors are DRWPL type I-0.1 Nm, type I-0.5 Nm and type II-10 Nm*

A.3. Ultrasonic Doppler anemometry

A.3.1. Technical specifications

VELOCIMETER

Vector - 300 m

NORTEK

Sample 3D velocity at up to 64 Hz for small-scale research in coastal areas

The Vector is a high-accuracy single-point current meter that is capable of acquiring 3D velocity in a very small volume at rates up to 64 Hz. It is widely used for sediment transport applications, small-scale turbulence measurements and coastal engineering studies. It has an excellent track record of delivering outstanding data quality in a variety of applications. This version is suitable for use down to a depth of 300 m. The Vector's titanium version is suitable for investigating deep- water currents.

Figure A.7. *Technical specifications of Ultrasonic Doppler Anemometer, Vector from Nortek AS [144], page 1, excerpt from catalogue*

VELOCIMETER

Vector - 300 m

NORTEK

Highlights

✓ Small-scale turbulence

✓ Sampling up to 64 Hz

✓ Small sampling volume for measurements
   close to boundaries

Applications

✓ Wave orbital studies

✓ Studies of bottom boundary layers

✓ Ocean engineering projects

✓ Coastal studies

✓ River turbulence

✓ Low flow measurements

✓ Flux measurements

Figure A.8. *Technical specifications of Ultrasonic Doppler Anemometer, Vector from Nortek AS [144], page 2, excerpt from catalogue*

VELOCIMETER

Vector - 300 m

NORTEK

Technical specifications

→| Water velocity measurements	
Maximum profiling range	N/A
Distance from probe	0.15 m
Sampling volume diameter	15 mm
Sampling volume height (user-selectable)	5-20 mm
Cell size	N/A
Velocity range	±0.01, 0.1, 0.3, 1, 2, 4, 7 m/s (software-selectable)
Adaptive ping interval	N/A
Accuracy	±0.5% of measured value ±1 mm/s
Velocity precision	typ. 1% of velocity range (at 16 Hz)
Sampling rate (output)	1-64 Hz
Internal sampling rate	100-250 Hz
→ Distance measurements	
Minimum range	N/A
Maximum range	N/A
Cell size	N/A
Accuracy	N/A
Sampling rate	N/A
→ Echo intensity	
Acoustic frequency	6 MHz
Resolution	0.45 dB
Dynamic range	90 dB
→ Sensors	
Temperature:	Thermistor embedded in end bell
Temp. range	-4 to +40 °C

Figure A.9. *Technical specifications of Ultrasonic Doppler Anemometer, Vector from Nortek AS [144], page 3, excerpt from catalogue*

```
VELOCIMETER
```

Vector - 300 m

NORTEK

→ Sensors	
Temp. accuracy/resolution	0.1 °C/0.01 °C
Temp. time response	10 min
Compass:	Magnetometer
Accuracy/resolution	2º/0.1º for tilt < 20°
Tilt:	Liquid level
Accuracy/resolution	0.2°/0.1°
Maximum tilt	30°
Up or Down	Automatic detect
Pressure:	Piezoresistive
Standard range	0-20 m (inquire for options)
Accuracy/precision	0.5% FS / Better than 0.005% of full scale
→ Analog inputs	
No. of channels	2
Supply voltage to analog output devices	Three options selectable through firmware commands:1) Battery voltage/500 mA, 2) +5 V/250 mA, 3) +12 V/100 mA
→ Data recording	
Capacity (standard):	9 MB, can add 4/16 GB
Data record (Standard)	24 bytes at sampling rate + 28 bytes/second
Data record (IMU)	72 bytes at sampling rate
→ Real-time clock	
Accuracy	±1 min/year
Backup in absence of power	4 weeks
→ Data communications	
I/O	RS-232 or RS-422
Communication baud rate	300-115 200 Bd
Recorder download baud rate	600/1200 kBd for both RS-232 and RS-422

Figure A.10.   *Technical specifications of Ultrasonic Doppler Anemometer, Vector from Nortek AS [144], page 4, excerpt from catalogue*

VELOCIMETER

# Vector - 300 m

NORTEK

→ Data communications	
User control	Handled via "Vector" software, ActiveX® function calls, or direct commands.
Analog outputs	3 channels standard, one for each velocity component or two velocities and pressure.
Output range	0–5 V, scaling is user-selectable.
Synchronization	TTL (5V tolerant) sync in/sync out, start on sync, sample on sync
→ Connectors	
Bulkhead (Impulse)	MCBH-8-FS
Cable	PMCIL-8-MP on 10 m polyurethane cable
→ Software	
Functions	Deployment planning, instrument configuration, data retrieval and conversion (for Windows®).
→ Multi unit operation	
Software	N/A
I/O	N/A
→ Power	
DC input	9–15V DC
Maximum peak current	3 A
Max. consumption	1.5 W at 64 Hz
Typical consumption, 4 Hz	0.6 – 1 W
Sleep consumption	< 100 µA
Transmit power	2 adjustable levels
→ Batteries	
Battery capacity	50 Wh (alkaline or Li-ion),165 Wh (lithium), single or dual
New battery voltage	13.5 V DC (alkaline)
Data collection capacity	Refer to planning section in software

Figure A.11. *Technical specifications of Ultrasonic Doppler Anemometer, Vector from Nortek AS [144], page 5, excerpt from catalogue*

VELOCIMETER

Vector - 300 m

NORTEK

⟶ Environmental

Operating temperature	–4 to +40 °C

Figure A.12. *Technical specifications of Ultrasonic Doppler Anemometer, Vector from Nortek AS [144], page 6, excerpt from catalogue*

VELOCIMETER

Vector - 300 m

NORTEK

$\longrightarrow$ Environmental	
Storage temperature	-20 to +60 °C
Shock and vibration	IEC 721-3-2
Depth rating	300m
$\longrightarrow$ Materials	
Standard model	POM housing, titanium probe and fasteners
$\longrightarrow$ Dimensions	
Maximum diameter	75 mm
Maximum length	468 mm (housing only), 246 mm (fixed stem) add 100 mm for double battery
$\longrightarrow$ Weight	
No batteries	Weight in air: 2.32 kg, in water: buoyant
2 batteries	Weight in air: 3.20 kg, in water: 0.54 kg
$\longrightarrow$ Options	
Probe mounted on fixed stem or on 2 m cable	
Vertical or horizontal probes	
Alkaline, lithium or Li-ion external batteries	
IMU - Inertial Measurement Unit	

Figure A.13. *Technical specifications of Ultrasonic Doppler Anemometer, Vector from Nortek AS [144], page 7, excerpt from catalogue*

A.3.2. Technical drawings
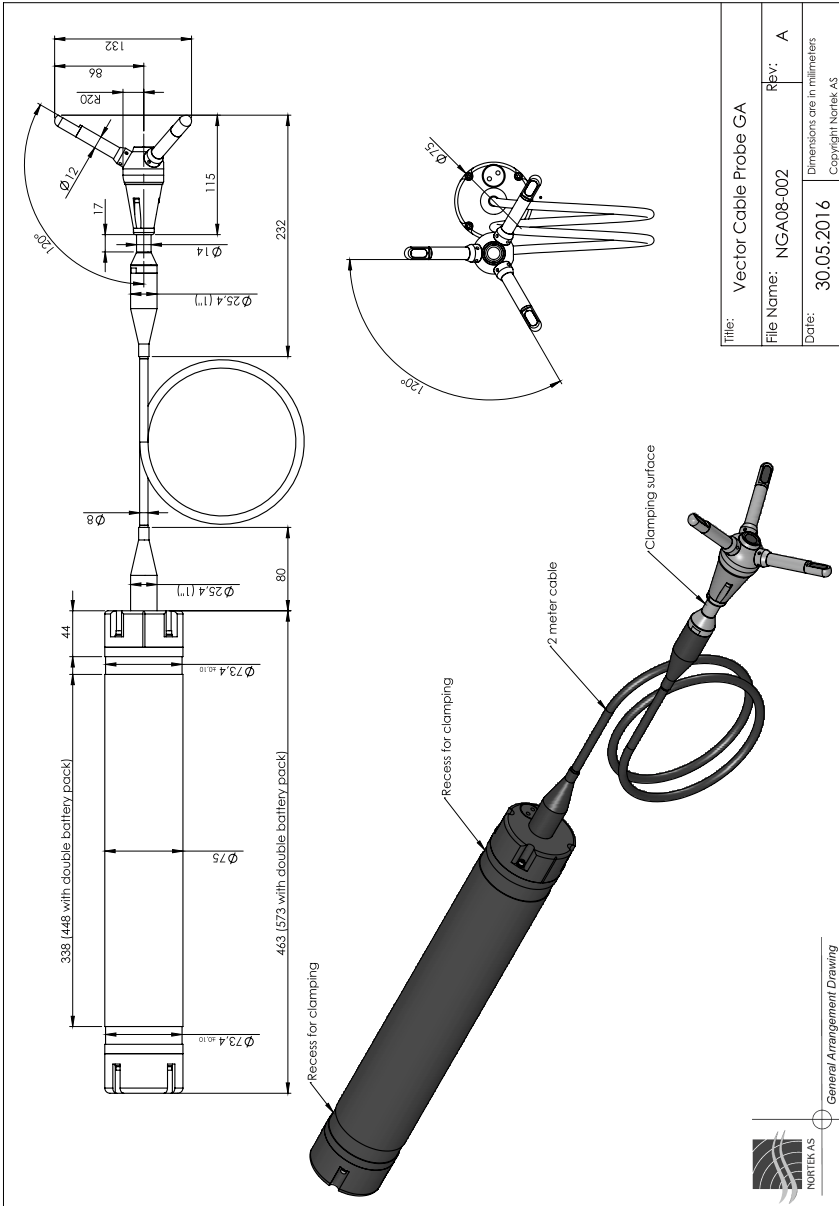
Figure A.14. *Technical drawings of Ultrasonic Doppler Anemometer, Vector from Nortek AS [145]*

B. Drive devices

B.1. DC-motors

Planetary Small Geared Motor PE with DC Motor, Size 1

Housing: Steel, zinc-plated, sealed against lubricant leaks and protected against dust, can be mounted in any position.
Gearbox: 1st gearbox stage: plastic gears, other gears made from steel.
Bearing: Motor roller bearing. Gearbox: sintered bronze plain bearing.
Lubrication: Maintenance free grease lubrication.
Motor: DC motor 24 V. Nominal motor speed 6,000 min^{-1}, Pinion milled into motor shaft. Free lead ends.
Sense of rotation can be changed by swapping leads over.
Protection class according to VDE 0530: IP 21.
Insulation class according to VDE 0530: E.
Operating mode as per VDE 0530: S1.

Ordering Details: e.g.: Type, Size 1, Voltage, Output Speed, Product No.

Size 1

Product No. 24 V	Nominal Output Speed min^{-1}	Ratio i	max. continous Torque Nm	max. Starting Torque Nm	Nominal Motor Power W	Output Power W	Gearbox Efficiency %	a mm	b mm	Weight kg
430 440 24	200	30:1	0,46	0,6	12	9,6	80	141	27	0,55
430 441 24	67	90:1	1,20	1,8	12	8,4	70	148	34	0,6
430 442 24	50	120:1	1,60	2,2	12	8,4	70	148	34	0,6
430 443 24	29	210:1	2,80	3,3	12	8,4	70	148	34	0,6
430 444 24	22	270:1	2,90	3,3	10	6,7	65	155	41	0,65

Permissible radial shaft load F$_R$: 30 N (middle shaft).
Permissible axial shaft load F$_A$: 0 N.
Tolerances +/- 10%.

Note

The efficiency stated in the table is valid for properly run-in gearboxes at operating temperature. To prevent the gearbox from being overloaded, the stated limit loads must not be exceeded. At reversed operation the limit loads must be multiplied with the factor 0.75.

Also available as an option with 12 V motors and larger gear ratio up to 54880:1.

MÄDLER®

709

Figure B.1. *Technical specifications of DC-motor, Size 1 from Maedler Gmbh, excerpt from catalogue [127]*

Planetary Small Geared Motor PE with DC Motor, Size 2

Housing: Steel, zinc-plated, sealed against lubricant leaks and protected against dust, can be mounted in any position.
Gearbox: 1st gearbox stage: plastic gears, other gears made from steel.
Bearing: Motor roller bearing. Gearbox roller bearing / plain bearing.
Lubrication: Maintenance free grease lubrication.
Motor: DC motor 24 V. Nominal motor speed 3,000 min-1, Pinion milled into motor shaft. Free lead ends. Sense of rotation can be changed by swapping leads over.
Protection class according to VDE 0530: IP 41.
Insulation class according to VDE 0530: F.
Operating mode as per VDE 0530: S1.

Ordering Details: e.g.: Type, Size 2, Voltage, Output Speed, Product No.
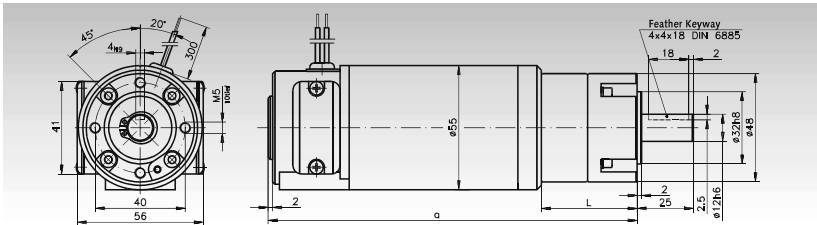
Size 2

Product No. 24 V	Nominal Output Speed min^{-1}	Ratio i	max. continous Torque Nm	max. Starting Torque Nm	Nominal Motor Power W	Output Power W	Gearbox Efficiency %	a mm	b mm	Weight kg
430 450 24	600	5:1	1,00	3,0	54	49	90	164,5	43,0	1,5
430 451 24	500	6:1	1,30	3,5	54	49	90	164,5	43,0	1,5
430 452 24	392	7,66:1	1,00	3,0	46	41	90	164,5	43,0	1,5
430 453 24	143	21:1	3,20	12,0	55	47	85	181,0	59,5	1,6
430 454 24	120	25:1	4,00	14,5	55	47	85	181,0	59,5	1,6
430 455 24	100	30:1	4,80	14,5	55	47	85	181,0	59,5	1,6
430 456 24	83	36:1	5,50	16,0	55	47	85	181,0	59,5	1,6
430 457 24	65	46:1	5,60	16,0	45	38	85	181,0	59,5	1,6
430 458 24	51	59:1	6,00	16,0	48	32	85	181,0	59,5	1,6

Permissible radial shaft load F_R: from i=5:1 to i=7,66:1: 112 N;   from i=21:1 to i=59:1: 150 N (always middle shaft).
Permissible axial shaft load F_A: from i=5:1 to i=7,66:1: 100 N;   from i=21:1 to i=59:1: 110 N.
Tolerances +/- 10%.

Note

The efficiency stated in the table is valid for properly run-in gearboxes at operating temperature. To prevent the gearbox from being overloaded, the stated limit loads must not be exceeded. At reversed operation the limit loads must be multiplied with the factor 0.75.

Optionally also available with DC speed sensor, incremental encoder and brake.

Also available as an option with larger gear ratio up to 450:1.

*Speed controllers
Page 696*

MÄDLER ®

Figure B.2.   *Technical specifications of DC-motor, Size 2 from Maedler Gmbh, excerpt from catalogue [127]*

B.2. Hydraulic motor

Technical Information   OML and OMM Orbital Motors

Technical data

Technical data for OMM with 16 mm and 5/8 in cylindrical shaft

Type			OMM	OMM	OMM	OMM	OMM	OMM
Motor size			**8**	**12.5**	**20**	**32**	**40**	**50**
Geometric displacement	cm³ [in³]		8.2 [0.50]	12.5 [0.77]	19.9 [1.22]	31.6 [1.93]	39.8 [2.43]	50 [3.08]
Max. speed	min⁻¹ [rpm]	cont.	1950	1550	1000	630	500	400
		int.[1]	2450	1940	1250	800	630	500
Max. torque	Nm [lbf•in]	cont.	11 [95]	16 [140]	25 [220]	40 [350]	45 [400]	46 [410]
		int.[1]	15 [135]	23 [200]	35 [310]	57 [500]	70 [620]	88 [780]
Max. output	kW [hp]	cont.	1.8 [2.4]	2.4 [3.2]	2.4 [3.2]	2.4 [3.2]	2.2 [3.0]	1.8 [2.4]
		int.[1]	2.6 [3.5]	3.2 [4.3]	3.2 [4.3]	3.2 [4.3]	3.2 [4.3]	3.2 [4.3]
Max. pressure drop	bar [psi]	cont.	100 [1450]	100 [1450]	100 [1450]	100 [1450]	90 [1310]	70 [1020]
		int.[1]	140 [2030]	140 [2030]	140 [2030]	140 [2030]	140 [2030]	140 [2030]
		peak[2]	200 [2900]	200 [2900]	200 [2900]	160 [2320]	160 [2320]	160 [2320]
Max. oil flow	l/min [US gal/min]	cont.	16 [4.2]	20 [5.3]	20 [5.3]	20 [5.3]	20 [5.3]	20 [5.3]
		int.[1]	20 [5.3]	25 [6.6]	25 [6.6]	25 [6.6]	25 [6.6]	25 [6.6]
Max. starting pressure with unloaded shaft	bar [psi]		4 [60]	4 [60]	4 [60]	4 [60]	4 [60]	4 [60]
Min. starting torque	at max. press. drop cont. Nm [lbf•in]		7 [60]	12 [105]	21 [185]	34 [300]	38 [335]	41 [365]
	at max. press. drop int. Nm [lbf•in]		10 [90]	17 [150]	29 [255]	48 [425]	62 [550]	79 [700]
Min. speed[3]	min⁻¹ [rpm]		50	40	30	30	30	30

Type			Max. inlet pressure
OMM 8 - 50	bar [psi]	cont.	140 [2030]
		int.[1]	175 [2538]
		peak[2]	225 [3260]

[1] Intermittent operation: the permissible values may occur for max. 10% of every minute.
[2] Peak load: the permissible values may occur for max. 1% of every minute.
[3] Operation by lower speeds may be slightly less smooth.

Figure B.3.   *Technical specifications of hydraulic motor, type OMM8 from Danfoss [47], excerpt from technical data sheet, page 25*

Danfoss

Technical Information   **OML and OMM Orbital Motors**

Function diagrams

Function diagrams

Explanation of function diagram use, basis and conditions can be found under *Speed, torque and output*.

- LIght grey: Continuous range
- Light red: Intermittent range (max. 10% operation every minute)

Max. permissible continuous/intermittent pressure drop for the actual shaft version can be found under *Technical data*.

Intermittent pressure drop and oil flow must not occur simultaneously.

OMM 8 function diagram

OMM 8

151-1117.11
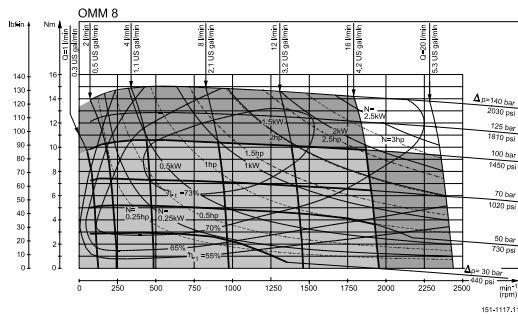
OMM 12.5 function diagram

OMM 12.5

151-994.10
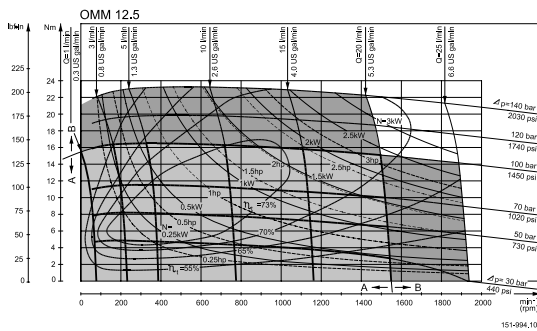
Figure B.4. *Technical specifications of hydraulic motor, type OMM8 from Danfoss [47], excerpt from technical data sheet, page 29*

B.3. Bearings

B.3.1. Radial bearing

SPECIFICATIONS: 12mm x 24mm	#S121201
Input Pressure	.41 MPa (60psi)
Ideal Load N (lbs)	36 (8)
Stiffness N/micron (lbs/u in) [1]	5 (0.03)
Flow NLPM (SCFH [1]	0.1 (0.03)
Fly Height[1]	5 microns
Bearing Size	12mm x 24mm
Bearing Height mm (in)	10 (0.39)
Bearing Weight grams (oz.)	6 (0.2)
Housing Material/Finish	Aluminum/Anodized
Porous Media Material	Carbon
Bearing Face Surface Size - Carbon mm (in)	24.00 x 11.99 (0.95 x 0.47)
Flatness mm (in)	0.0005 (0.00002)
Ball Socket Size	6mm
Pressure Port Thread	M3 x 0.5
Viable Pressure Range	.414-.552MPa (60psi - 80psi)
Maximum Allowable Pressure Supply	.689 MPa (100psi)
Resolution[3]	Infinite
Maximum Speed[4]	50m/sec
Common Guide Surfaces	Granite, hard-coated aluminum, ceramics, glass, stainless steel, plated steel
Suggested Guide Surface Finish[5]	16 RMS

Figure B.5. *Technical specifications of radial air bearing, type S121201 from NEWWAY air bearings [142], dimensions*
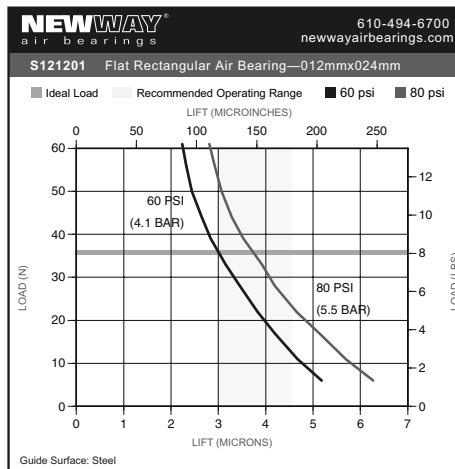
Figure B.6. *Technical specifications of radial air bearing, type S121201 from NEWWAY air bearings [142], performance data*
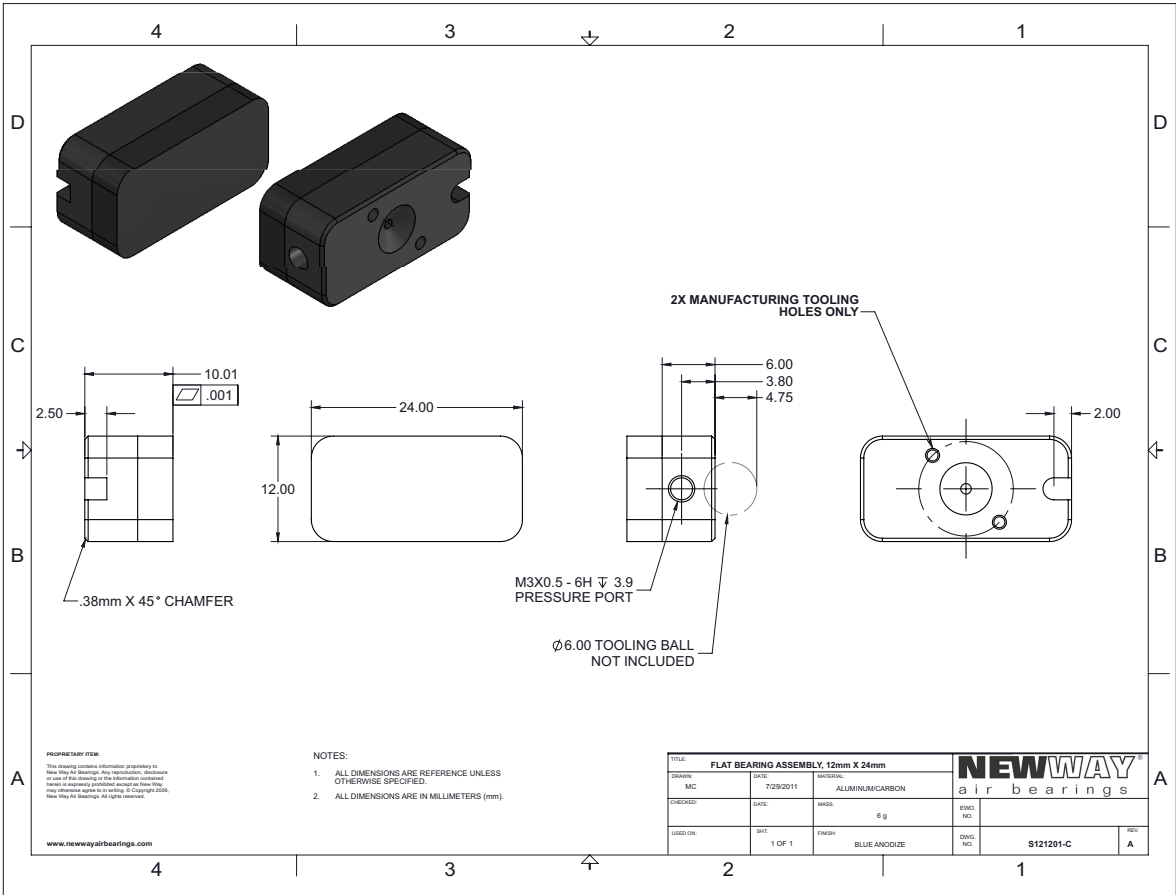
Figure B.7. *Technical drawings of radial air bearing, type S121201 from NEWWAY air bearings* [142]

B.3.2. Axial bearing

SPECIFICATIONS: 13mm #S301301	
Input Pressure	.41 MPa (60psi)
Radial Load Max N (lbs)	44 (10)
Radial Stiffness N/μm (lbs/μ in)	11 (0.06)
Pitch Moment Max N-m (lbs-in)	0.8 (7.5)
Pitch Stiffness N-m/mil rad (lbs-in/mil rad)	2.1 (19.0)
Flowrate on Shaft NLPM (SCFH)	2.24 - 3.11 (4.75 - 6.60)
Air Gap (at maximum recommended load) microns	4
Bushing Inside Diameter - ID mm +0.0051 , -0.0000	13
Bushing Outside Diameter - OD mm (in)	23.7 (0.932)
Bushing Length mm (in)	51 (2.000)
Bushing Weight grams (oz.)	32.6 (1.15)
Housing Material/Finish	Aluminum/Anodized
Porous Media Material	Carbon
Recommended Shaft Outside Diameter - OD mm	13.0000
Recommended Shaft Tolerance (g6) μm	-5 , -17
Pressure Port Threads	M3 x 0.5
Viable Pressure Range MPa (psi)	0.414 - 0.552 (60 - 80)
Maximum Allowable Pressure Supply MPa (psi)	0.689 (100)
Resolution	Infinite
Maximum Speed m/sec (ft/sec)	50 (164.04)
Common Shaft Materials	Anodized aluminum, stainless steel, nickel plated steel, ceramics, glass

Figure B.8.   *Technical specifications of axial air bearing, type S301301 from NEWWAY air bearings [143], dimensions*
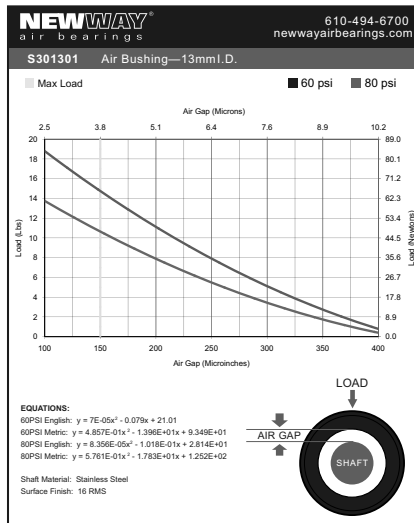
Figure B.9.   *Technical specifications of axial air bearing, type S301301 from NEWWAY air bearings [143], performance data*
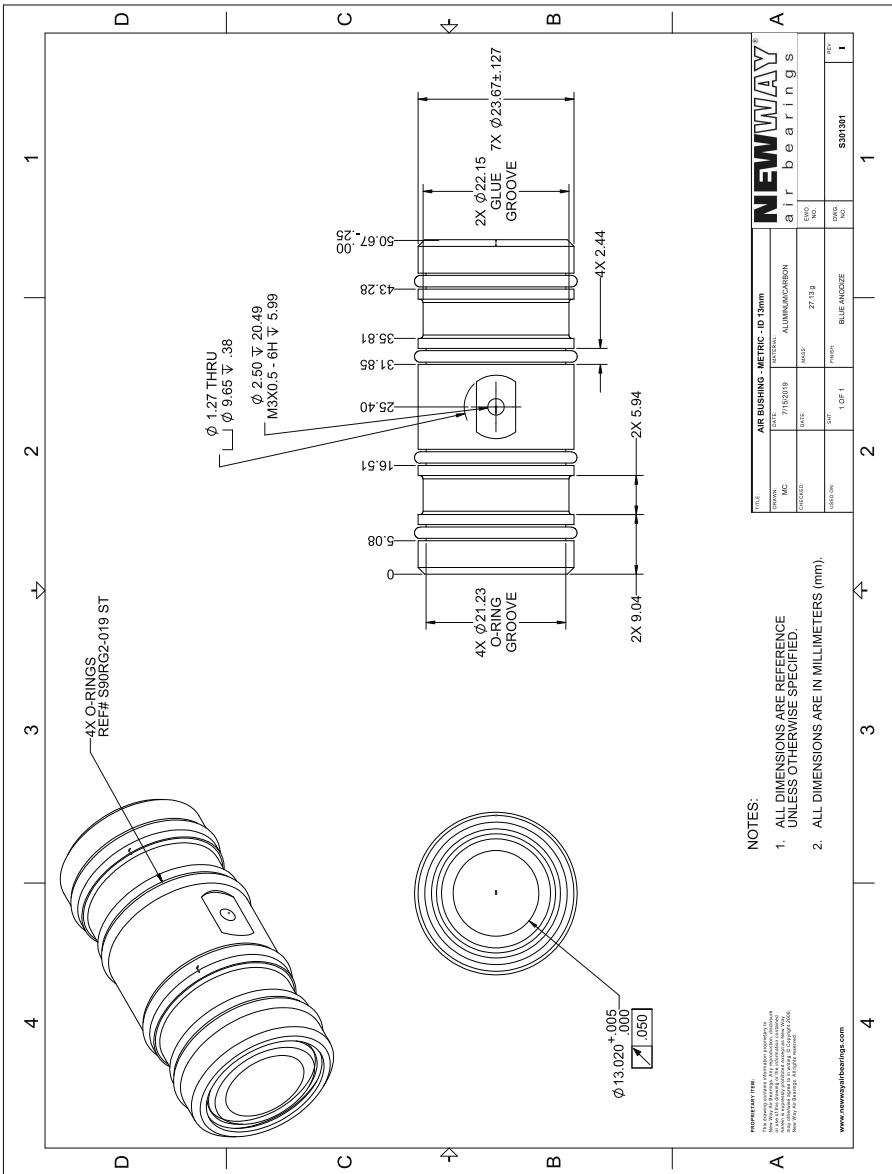
Figure B.10. *Technical drawings of axial air bearing, type S301301 from NEWWAY air bearings* *[143]*

C. Model fluid

C.1. Xanthan gum

IX. Industrial Applications

CP Kelco manufactures industrial xanthan gum products to meet formulation criteria such as long-term suspension and emulsion stability in alkaline, acid and salt solutions; temperature resistance and pseudoplasticity. See **Table 12**, which lists the typical physical properties of **KELZAN**® xanthan gum. In addition, a range of differentiated xanthan gum products designed to meet specific applications requirements has been developed.

These include a transparent grade to improve clarity of solutions, and a dispersible grade for low shear mixing conditions. **Table 13** is a partial list of the differentiated products currently available.

Enhanced Acid Stability

To compensate for an expected decrease in viscosity during storage of acid-based cleaners, manufacturers traditionally use higher concentrations of xanthan gum. **KELZAN ASX** was developed specifically for use in acid-based cleaners.

Unlike conventional xanthan gum products that lose effectiveness at low pH levels when used at lower concentrations, **KELZAN ASX** maintains viscosity on storage. With **KELZAN ASX** in the formulation, product shelf life is extended and use level is up to 30% lower than that of traditional xanthan gum.

Table 12
Typical Physical Properties of KELZAN® Xanthan Gum

Physical state	Cream-colored powder
Mesh Size	40 mesh (381 µm)
Moisture content	12%
Ash	10%
Color	70
Specific gravity	1.6
Bulk density[b]	52.4 lb./cu. ft. (842 kg/m^3)
Browning temperature	320°F (160°C)
Charring temperature	520°F (270°C)
Ignition temperature	†
Viscosity[a] 1% solution in 1% KCl	1400 cP
As a 1% solution (distilled water)	950 cP
pH	7.0
Surface tension	75 (dynes/cm^2)
Freezing point	32°F (0.0°C)

† Spontaneous combustion did not occur in air.
[a] 60 rpm, 25°C (77°F) Brookfield LVF viscometer, spindle 3.
[b] 42 mesh product.

Table 13
Selected Xanthan Gum Products for Industrial and Animal Feed Applications

Product	Description
KELZAN®	Standard viscosity grade. (Use **KELZAN T** if transparent solutions are required.)
KELZAN AR	Less pseudoplastic (smoother flowing) solutions than other **KELZAN** products. Better compatibility with alkali than other **KELZAN** products.
KELZAN ASX	Better acid stability than other **KELZAN** products. (Use **KELZAN ASX T** if transparent solutions are required.)
KELZAN CC	Low cellulase activity. Recommended for products, which contain a cellulose ether.
KELZAN HP	Higher suspending power than other **KELZAN** products.
KELZAN RD	Virtually dust-free; excellent powder flow properties. Concentrated stock solutions (up to 5%) prepared by adding quickly to well stirred water.
KELZAN S	Disperses in water without lumping, even when the stirring is slow. (Use **KELZAN ST** if transparent solutions are required.)
KELFLO®	Food-grade for animal feed applications.

21

Figure C.1. *Technical specifications of Xanthan gum, type KELZAN from CPKelco [45], excerpt from technical data sheet*

C.2. Carboxymethyl cellulose

Technical Data Sheet

DOW

WALOCEL™ CRT 40000 PV
Purified Sodium Carboxymethyl Cellulose

Introduction

WALOCEL™ CRT 40000 PV purified sodium carboxymethyl cellulose is a polyanionic cellulosic thickener. Due to its anionic character, it imparts a distinct rheology to waterborne caulks and sealants. This high viscosity additive imparts excellent thickening efficiency with a strong pseudoplastic rheology, whereby sagging and in-can layering can be optimized.

Typical Physical Properties

These properties are typical but should not be considered specifications.

Appearance	White to slightly yellowish powder
Solubility	Water soluble; delayed solubility in pH-neutral cold water
Viscosity[1], mPa•s	35,000-50,000
pH (2% solution)	Neutral
Volatiles, water, %, max.	10

[1]2% solution in water, Haake Rotovisko RV 100, shear rate 2.55s[-1], 20°C

Viscosity curve of 1% and 2% aqueous solution of WALOCEL™ CRT 40000 PV (Solution in water, Haake Rotovisko RV 100, 20°C)
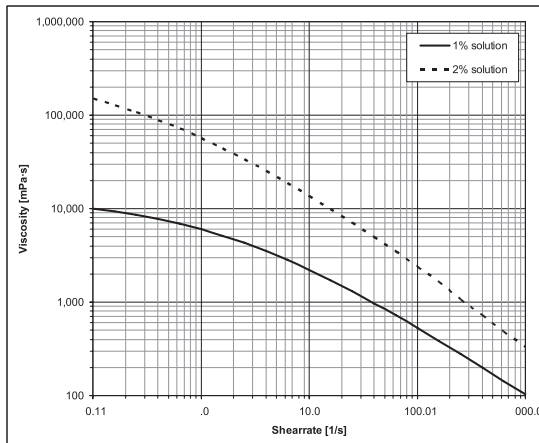
Figure C.2. *Technical specifications of carboxymethyl cellulose, type WALOCEL CRT 40000 PV from DowDuPont [55], excerpt from technical data sheet*

D. Historic figures
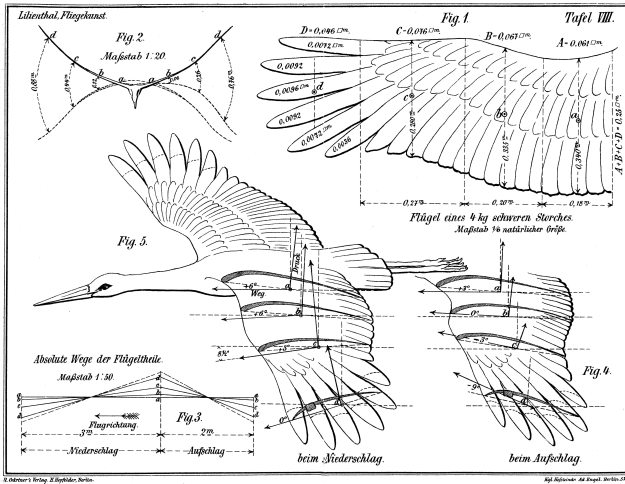
Figure D.1. *Historic illustration of sections of a stork's wing by Lilienthal [125], first recognition of effects between flow at an unsymmetrical airfoil and caused forces*
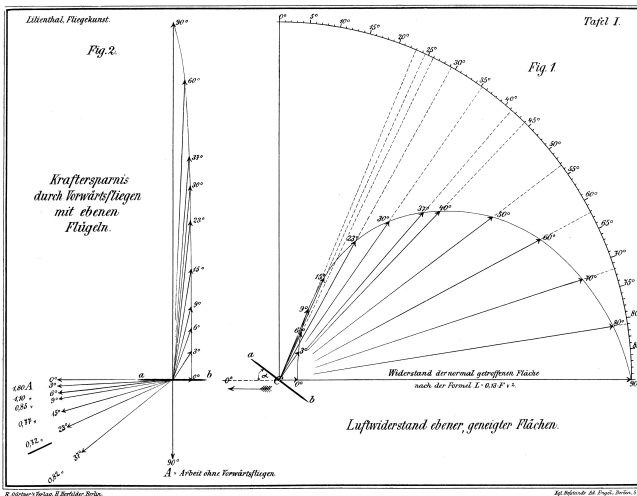
Figure D.2. *Historic illustration of a polar curve of a flat plate, by Lilienthal [125], first recognition of effects between flow at an unsymmetrical airfoil and caused forces*
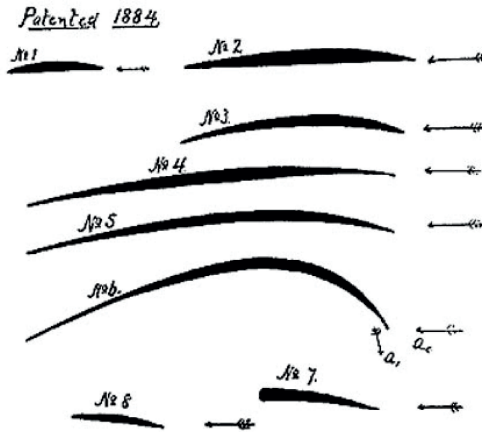
Figure D.3. *Historic patent from Phillips, investigated profile forms, excerpt from patent No. 13678 [160]*

E. Results

E.1. Polar plot database
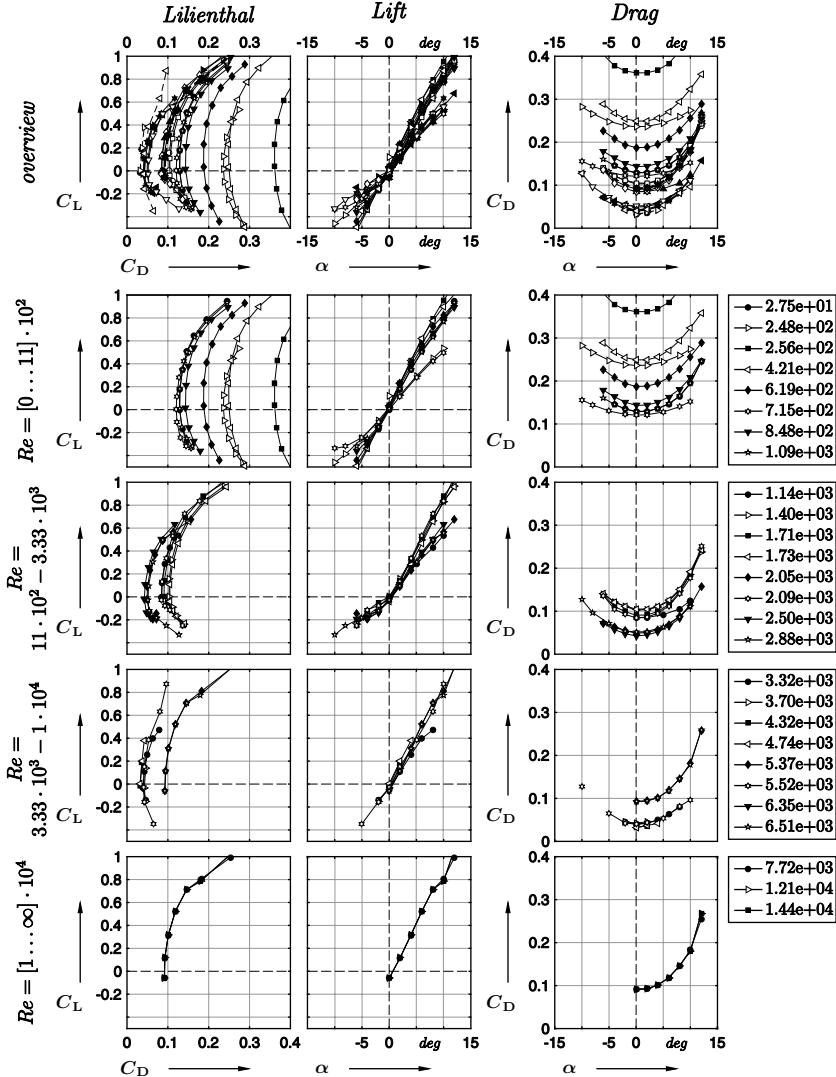
Figure E.1. *Resulting profile polar plots accordingly to Lilienthal, lift- and drag polar curve as array curves with the Reynolds number according to Chhabra and Richardson [38] as array parameter, all investigated* **parameter variations for profile E817**
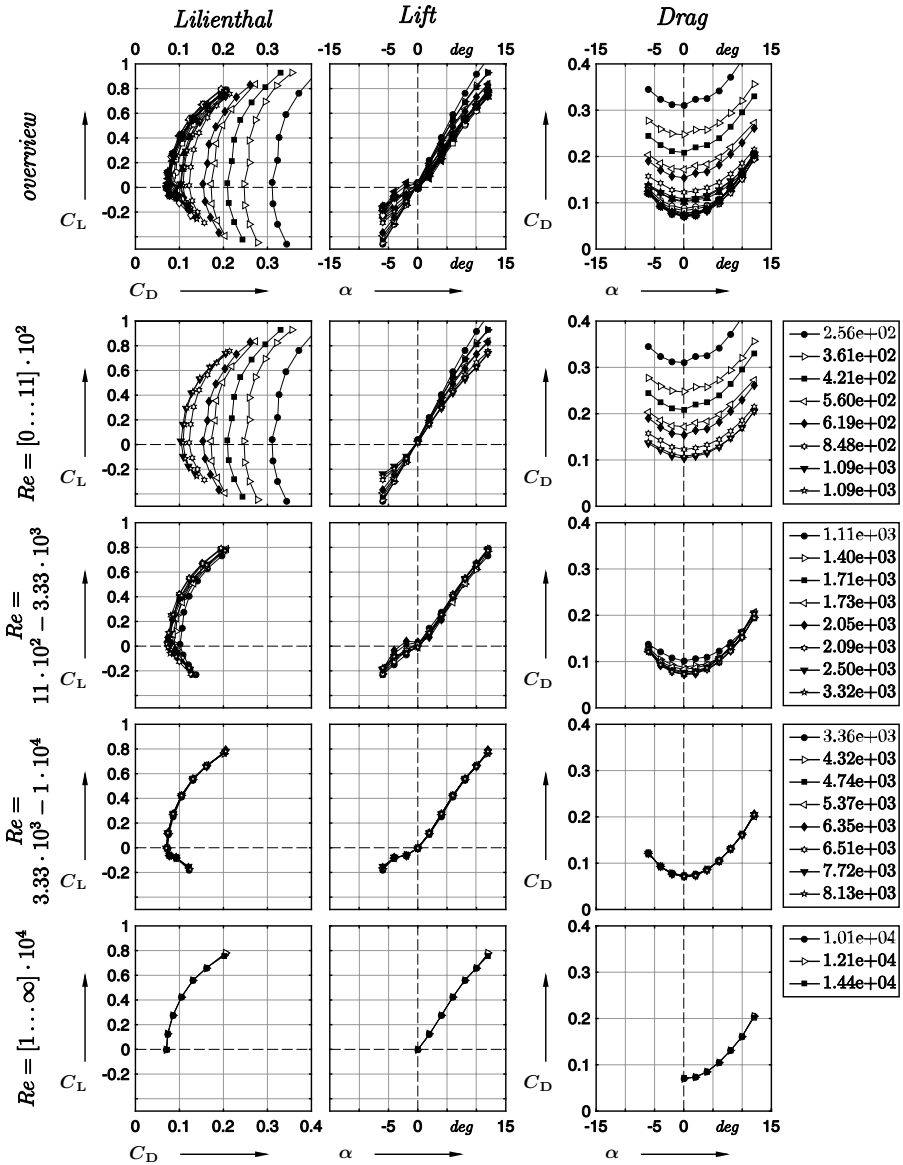
Figure E.2. *Resulting profile polar plots accordingly to Lilienthal, lift- and drag polar curve as array curves with the Reynolds number according to Chhabra and Richardson [38] as array parameter, all investigated **parameter variations for profile NLF1015***
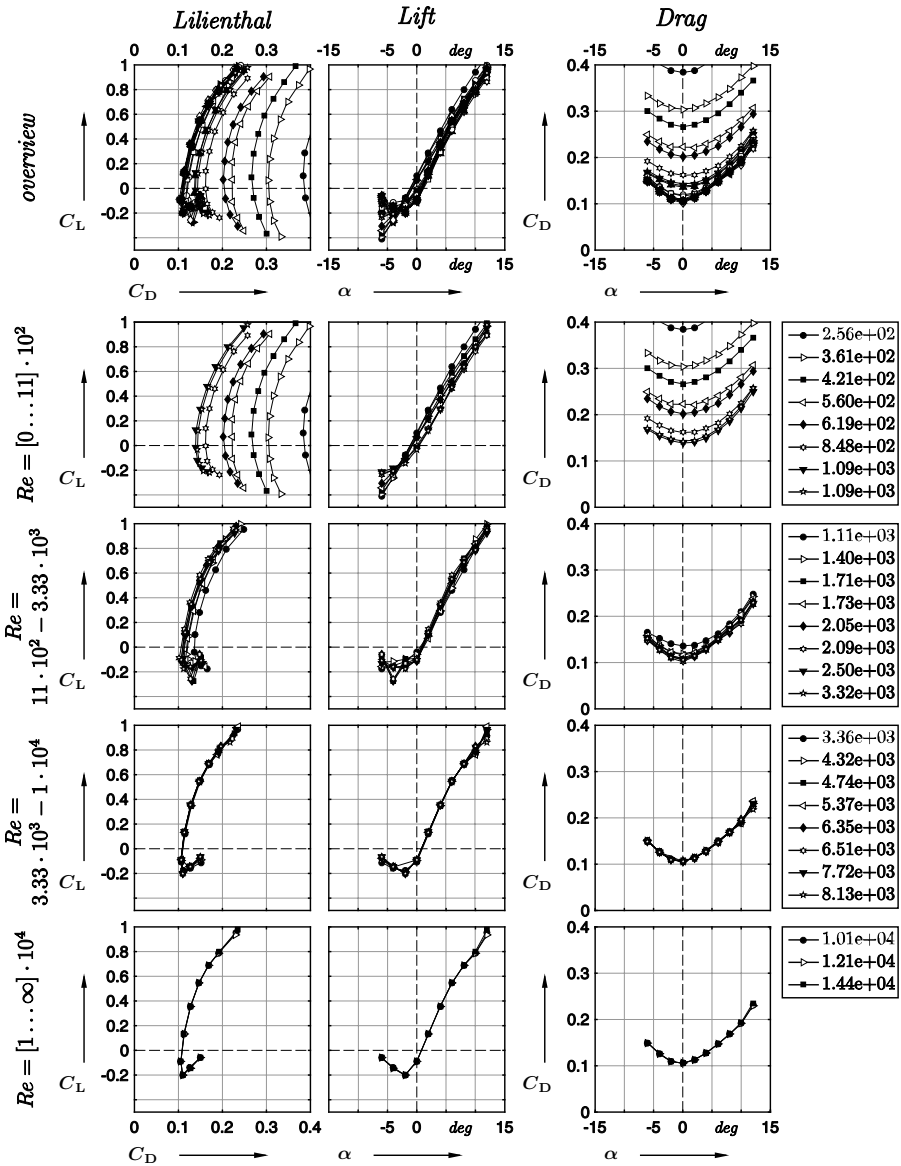
Figure E.3. *Resulting profile polar plots accordingly to Lilienthal, lift- and drag polar curve as array curves with the Reynolds number according to Chhabra and Richardson [38] as array parameter, all investigated **parameter variations for profile FX60-126***

E.2. Jet distribution

E.2.1. True-to-scale velocity
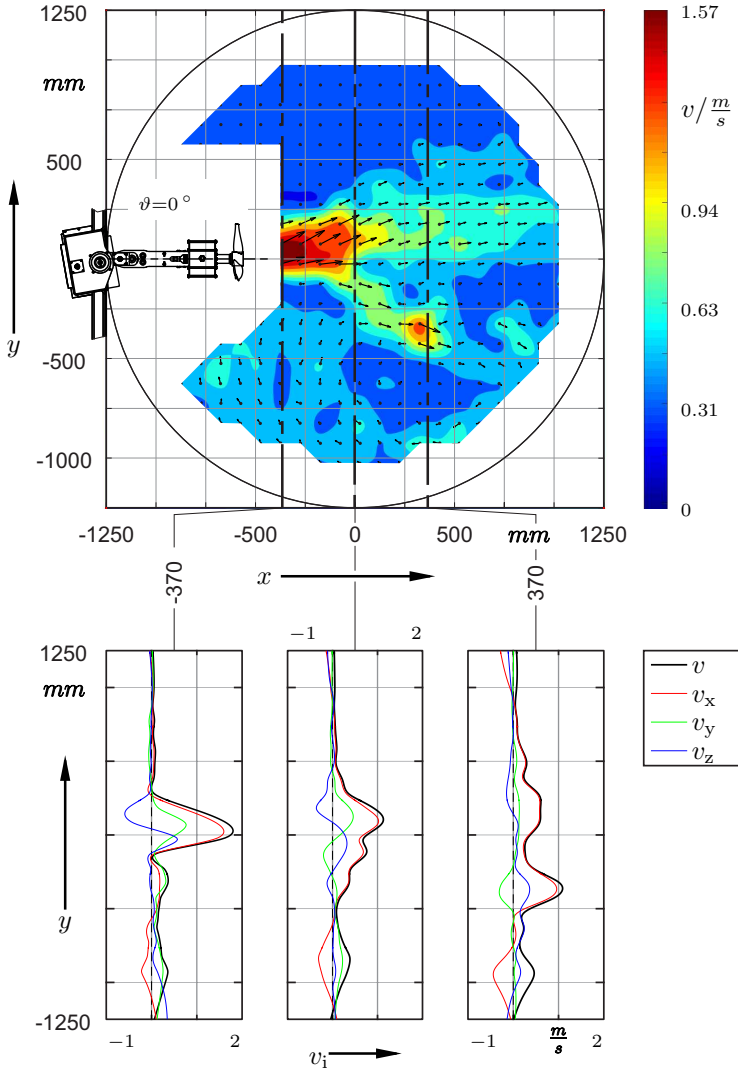
Figure E.4. **Measurement result C1-N085**, velocity contour plot true-to-scale with vector plot and evaluation of the velocity vector for cross-section planes at $x = -370$, $x = 0$ and $x = 370\,mm$, drawn for machine-level $z = 0.9\,m$, accuracy of the applied UDA sensor: $\pm 0.5\,\%$
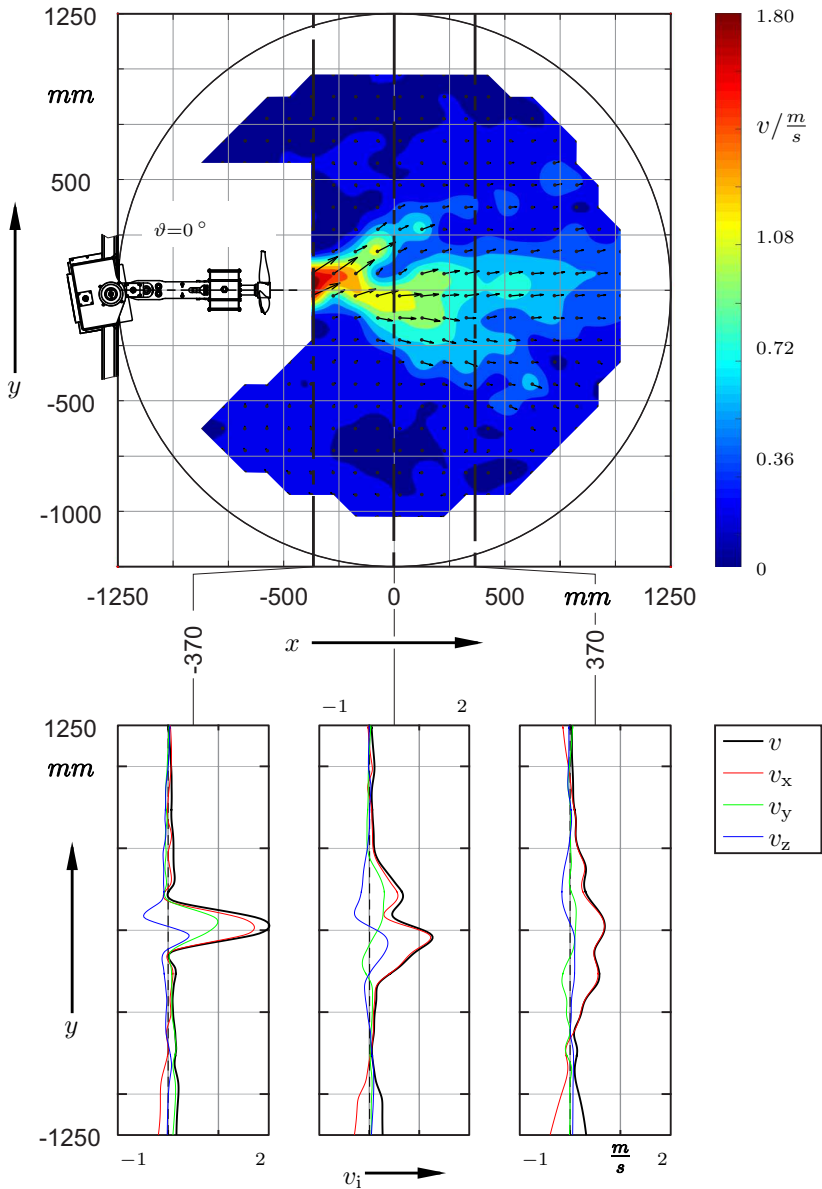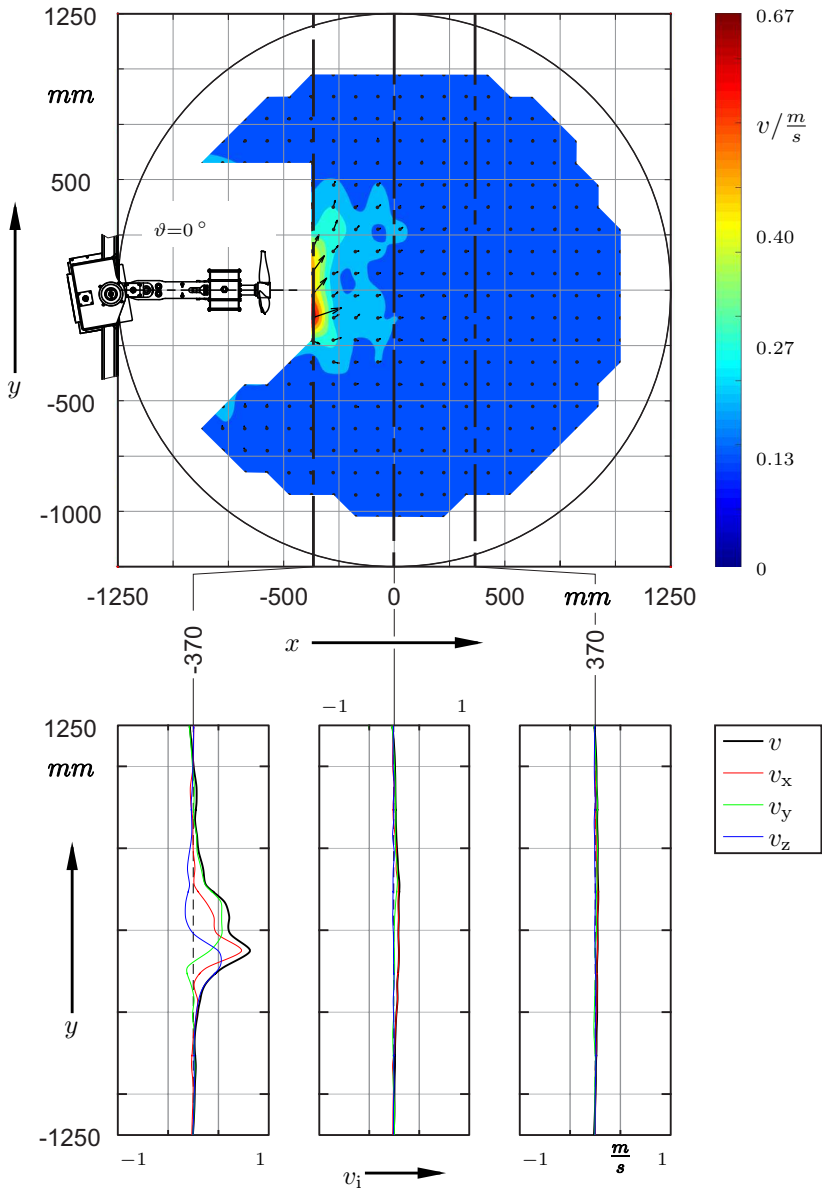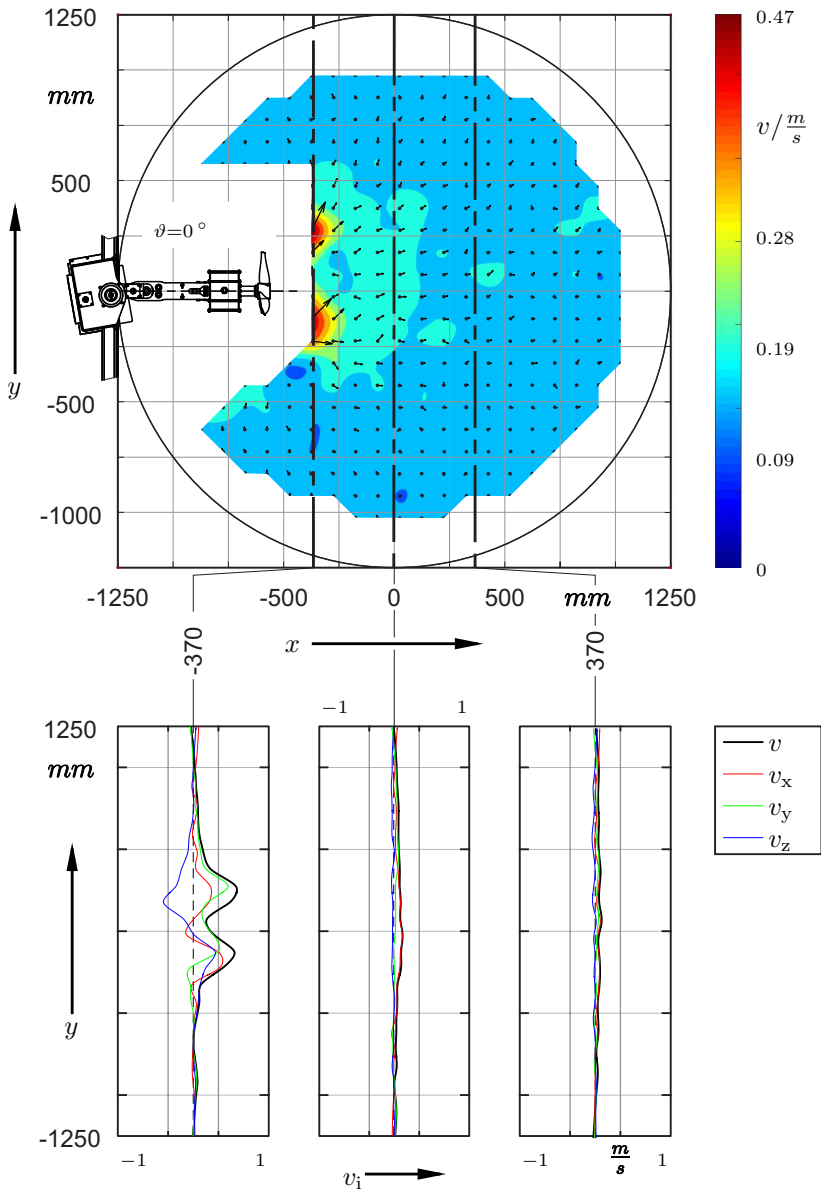
Figure E.5. *Measurement result C1-N100, velocity contour plot true-to-scale with vector plot and evaluation of the velocity vector for cross-section planes at $x = -370$, $x = 0$ and $x = 370\,mm$, drawn for machine-level $z = 0.9\,m$, accuracy of the applied UDA sensor: $\pm 0.5\,\%$*
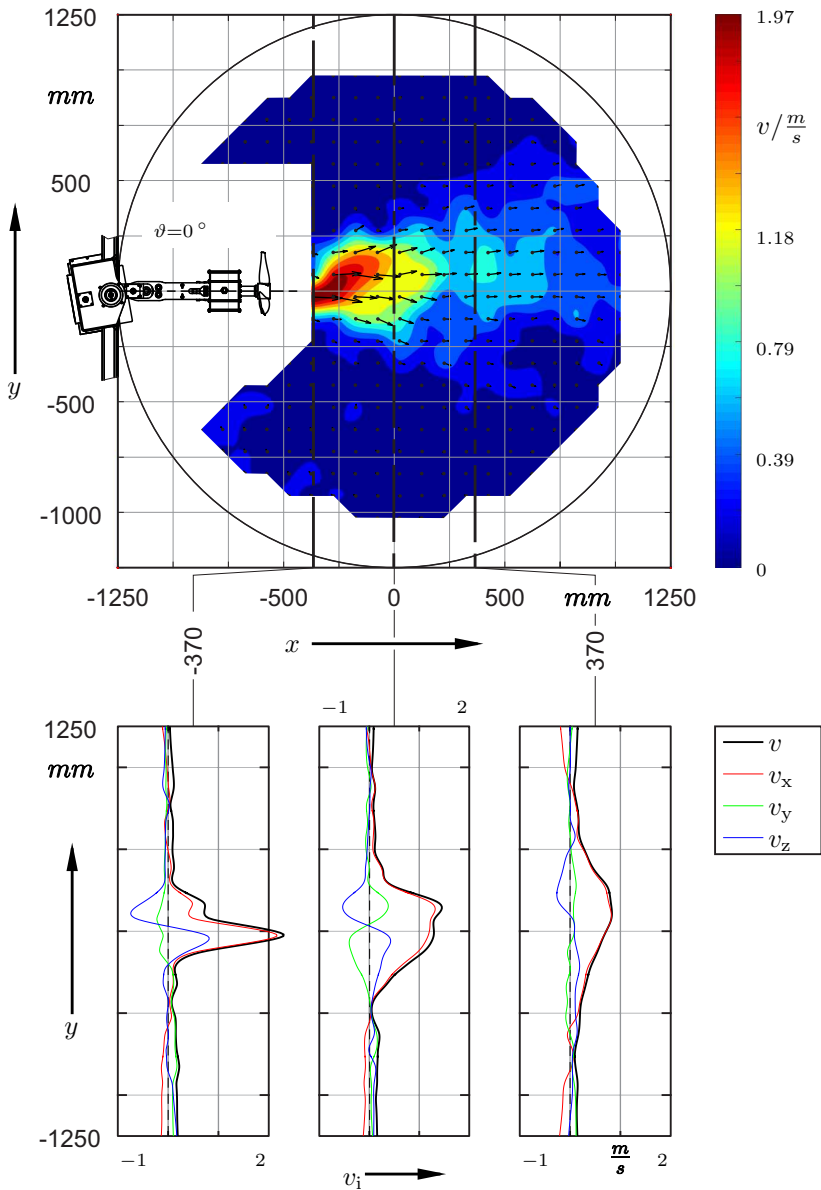
Figure E.6. *Measurement result C1-N115, velocity contour plot true-to-scale with vector plot and evaluation of the velocity vector for cross-section planes at $x = -370$, $x = 0$ and $x = 370\,mm$, drawn for machine-level $z = 0.9\,m$, accuracy of the applied UDA sensor: $\pm 0.5\,\%$*
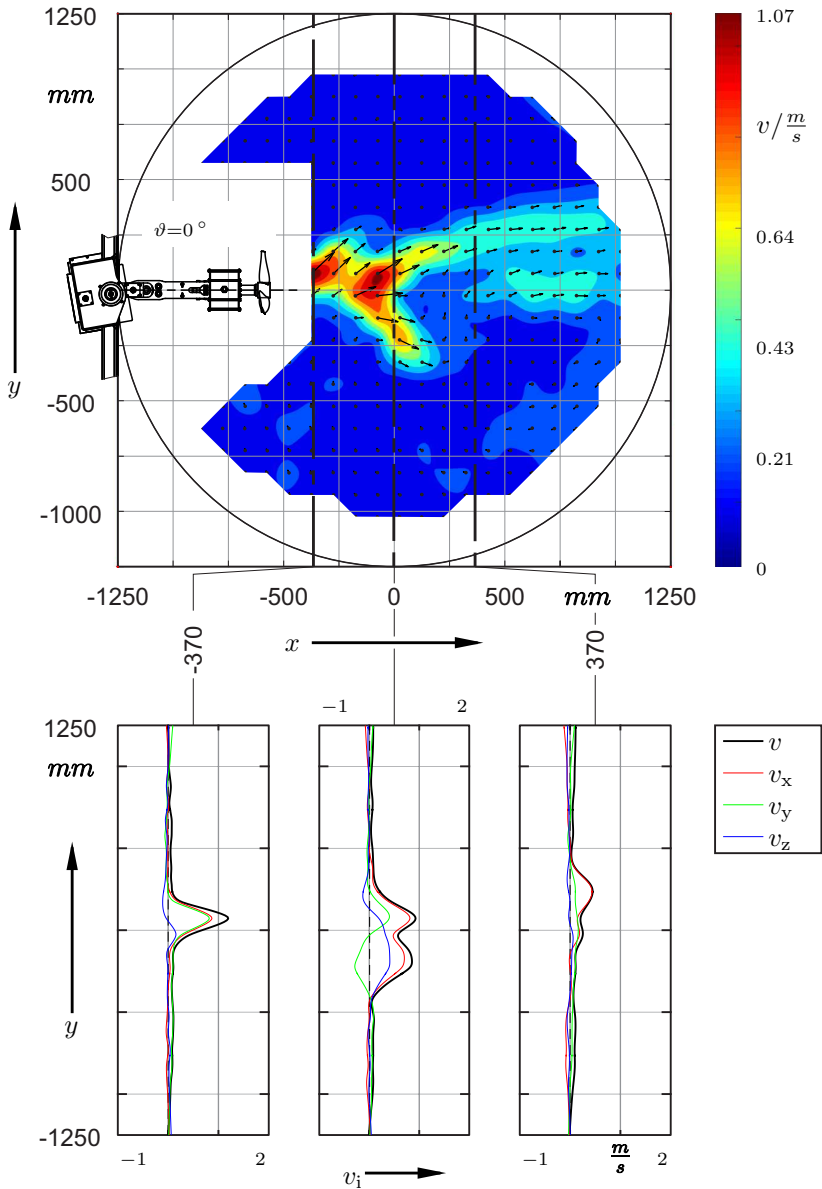
Figure E.7. *Measurement result C2-N085, velocity contour plot true-to-scale with vector plot and evaluation of the velocity vector for cross-section planes at $x = -370$, $x = 0$ and $x = 370\,mm$, drawn for machine-level $z = 0.9\,m$, accuracy of the applied UDA sensor: $\pm 0.5\,\%$*
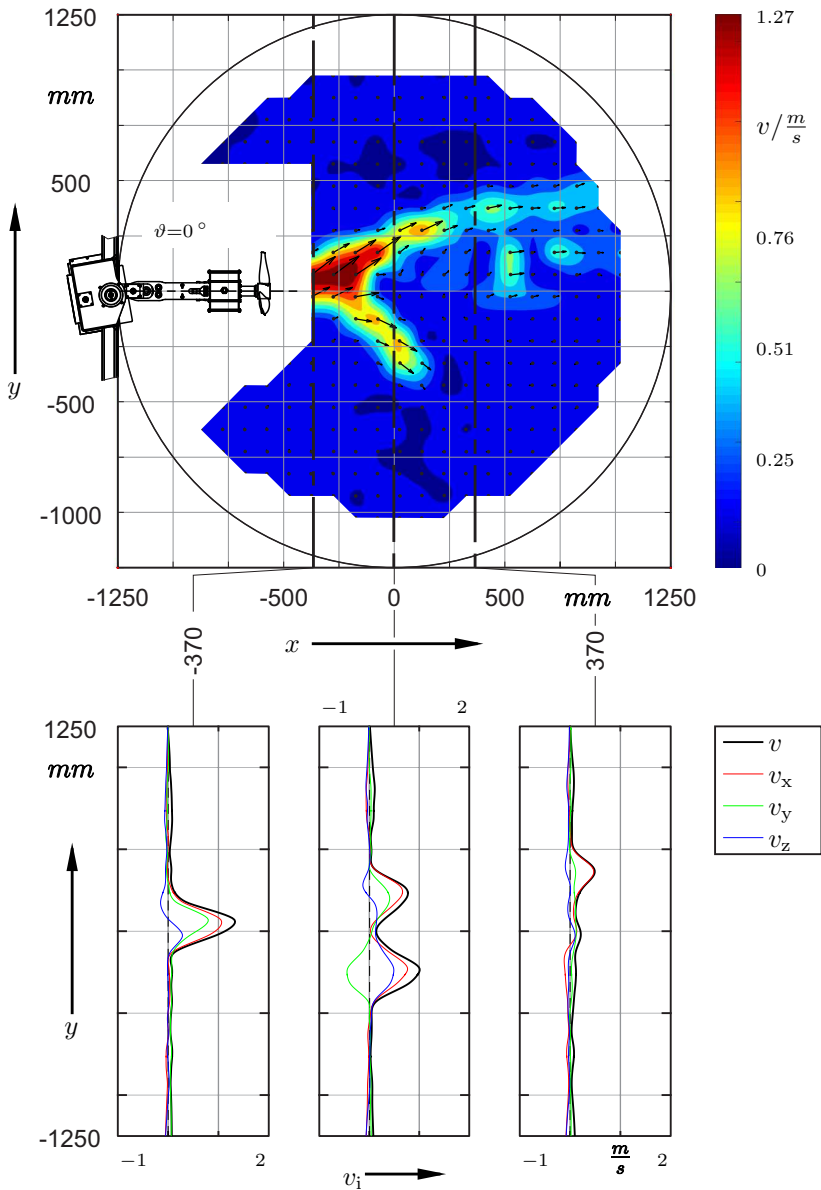
Figure E.8. **Measurement result C2-N100**, *velocity contour plot true-to-scale with vector plot and evaluation of the velocity vector for cross-section planes at $x = -370$, $x = 0$ and $x = 370\,mm$, drawn for machine-level $z = 0.9\,m$, accuracy of the applied UDA sensor: $\pm 0.5\,\%$*
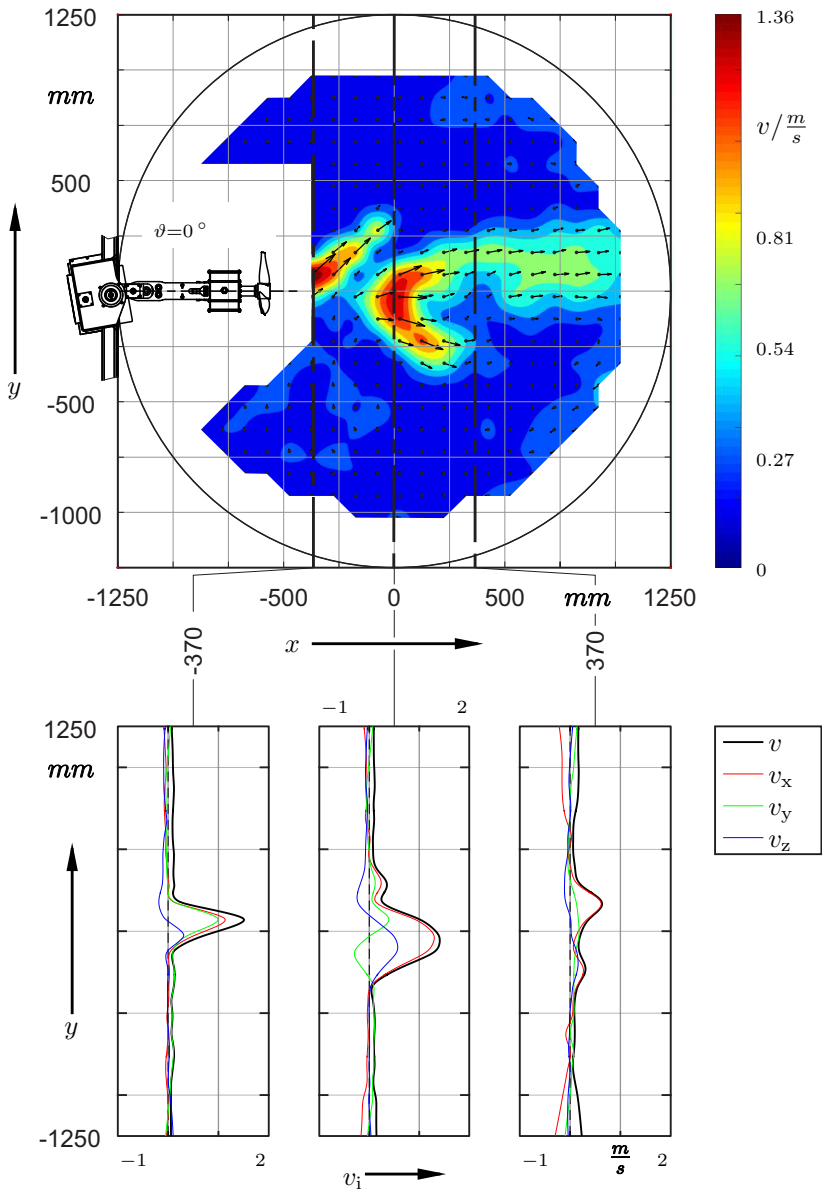
Figure E.9.   Measurement result C2-N115, *velocity contour plot true-to-scale with vector plot and evaluation of the velocity vector for cross-section planes at $x = -370$, $x = 0$ and $x = 370\,mm$, drawn for machine-level $z = 0.9\,m$, accuracy of the applied UDA sensor:* $\pm 0.5\,\%$
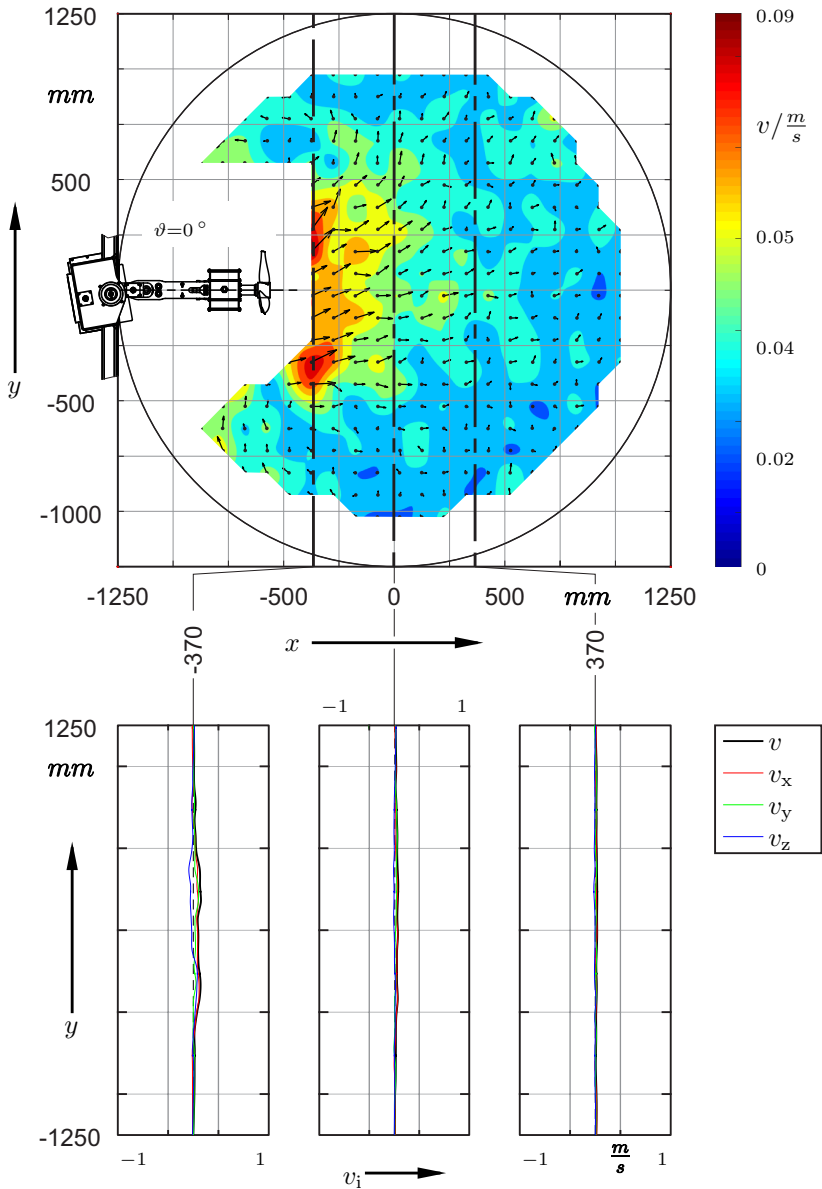
Figure E.10. *Measurement result C3-N085, velocity contour plot true-to-scale with vector plot and evaluation of the velocity vector for cross-section planes at $x = -370$, $x = 0$ and $x = 370\,mm$, drawn for machine-level $z = 0.9\,m$, accuracy of the applied UDA sensor: $\pm 0.5\,\%$*

Figure E.11. *Measurement result C3-N100, velocity contour plot true-to-scale with vector plot and evaluation of the velocity vector for cross-section planes at $x = -370$, $x = 0$ and $x = 370\,mm$, drawn for machine-level $z = 0.9\,m$, accuracy of the applied UDA sensor: $\pm 0.5\,\%$*

Figure E.12. *Measurement result C3-N105, velocity contour plot true-to-scale with vector plot and evaluation of the velocity vector for cross-section planes at $x = -370$, $x = 0$ and $x = 370\,mm$, drawn for machine-level $z = 0.9\,m$, accuracy of the applied UDA sensor: $\pm 0.5\,\%$*
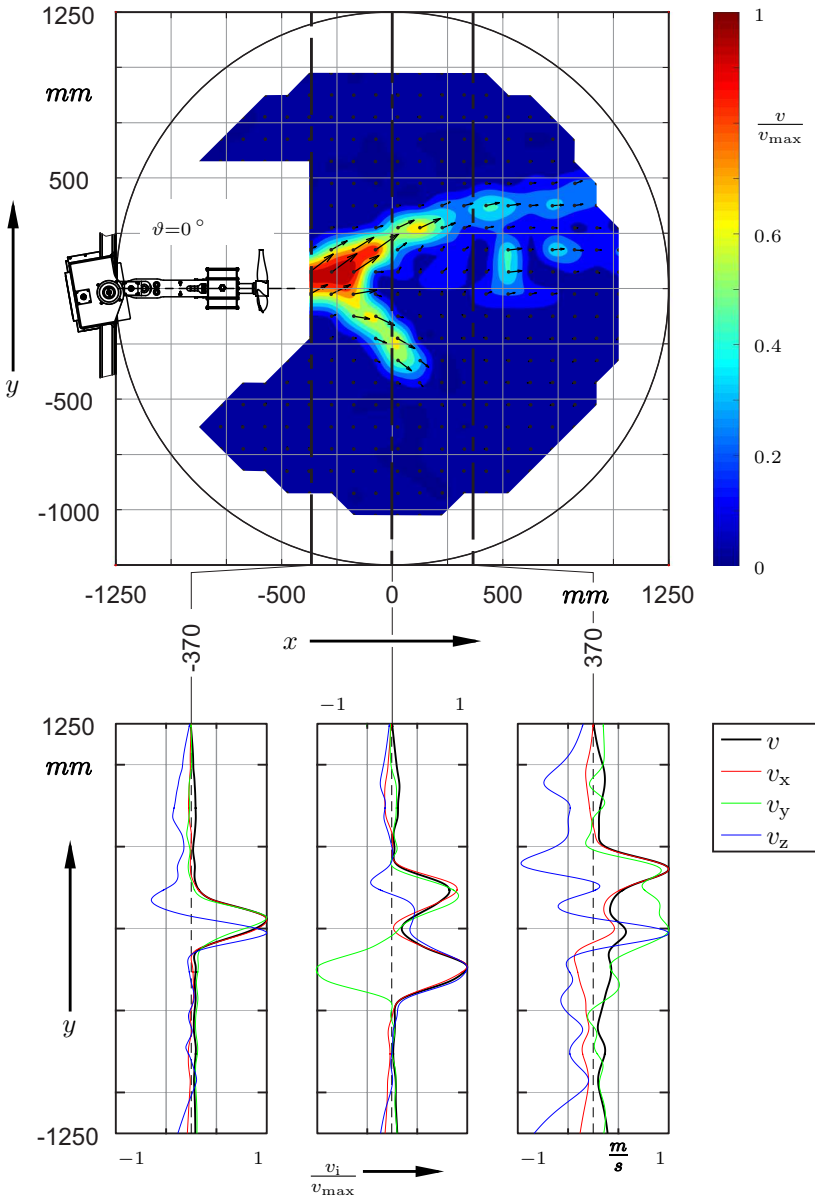
E.2.2. Normalised velocity
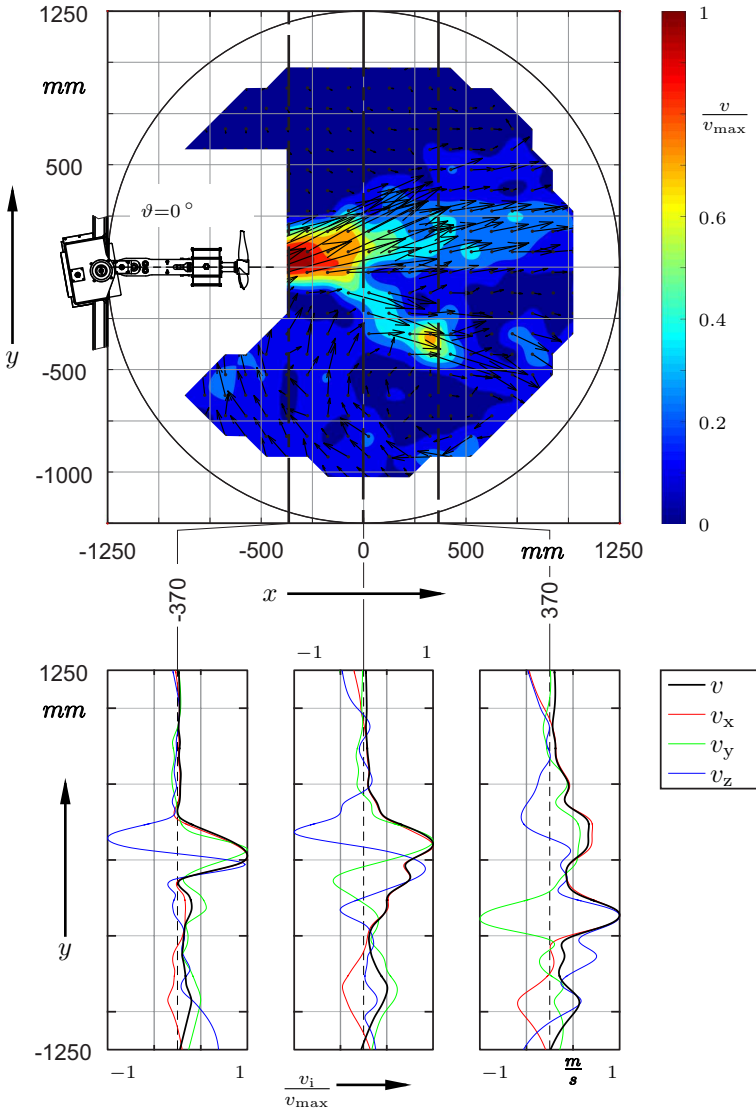
Figure E.13. *Measurement result C1-N085, normalised velocity contour plot v/v_{max} with vector plot and evaluation of the normalised velocity vector v_i/v_{max} for cross-section planes at $x = -370$, $x = 0$ and $x = 370\,mm$, drawn for machine-level $z = 0.9\,m$, maximum velocity magnitude of contour: $v_{max} = 1.5667\,m/s$, accuracy of the applied UDA sensor: $\pm 0.5\,\%$*
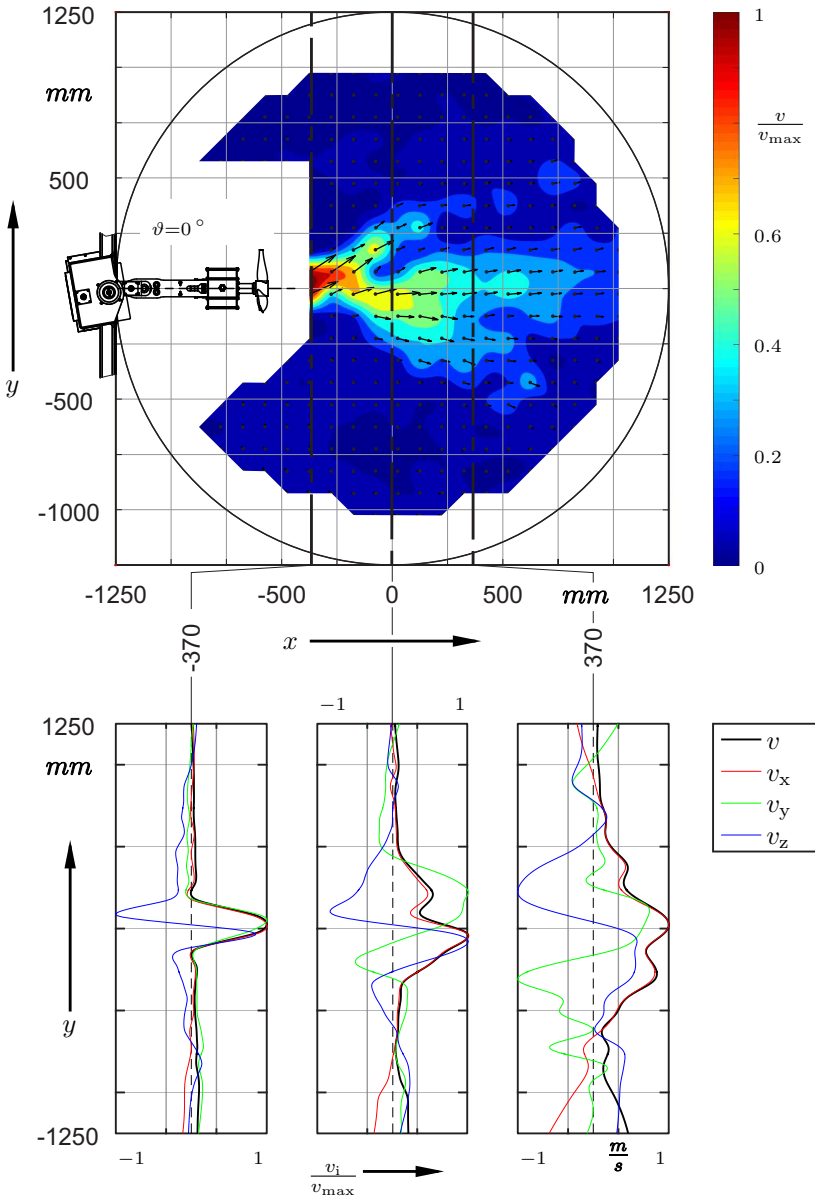
Figure E.14. *Measurement result C1-N100, normalised velocity contour plot $v/v_{\max}$ with vector plot and evaluation of the normalised velocity vector $v_i/v_{\max}$ for cross-section planes at $x = -370$, $x = 0$ and $x = 370\,mm$, drawn for machine-level $z = 0.9\,m$, maximum velocity magnitude of contour: $v_{\max} = 1.7997\,m/s$, accuracy of the applied UDA sensor: $\pm 0.5\,\%$*
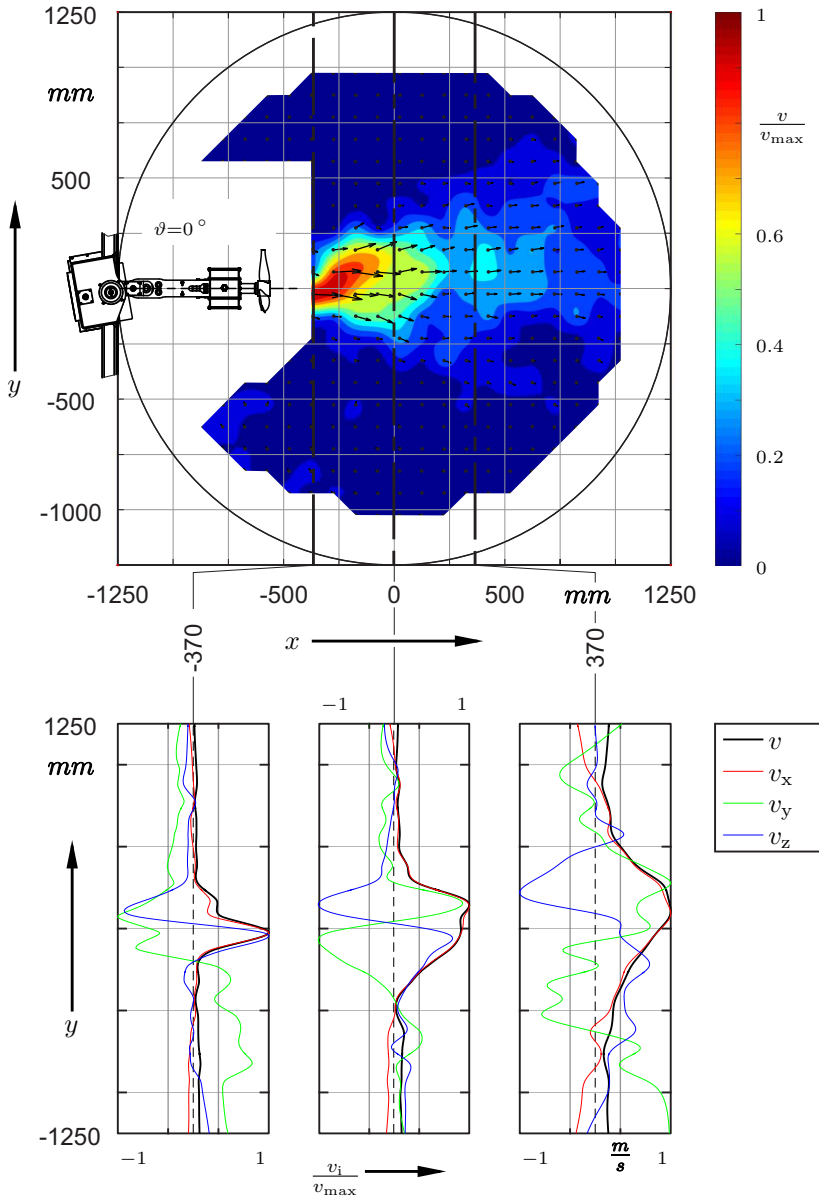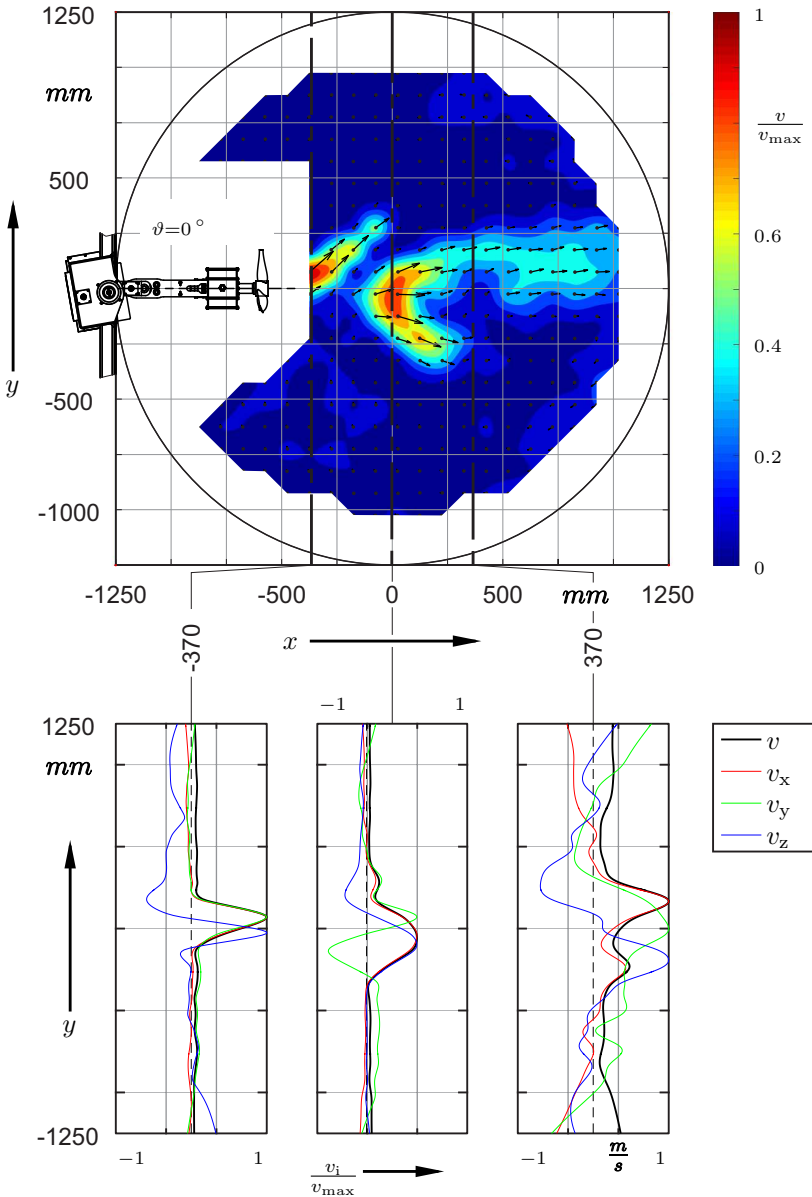
Figure E.15. *Measurement result C1-N115*, normalised velocity contour plot $v/v_{\max}$ with vector plot and evaluation of the normalised velocity vector $v_{\mathrm{i}}/v_{\max}$ for cross-section planes at $x = -370$, $x = 0$ and $x = 370\,mm$, drawn for machine-level $z = 0.9\,m$, maximum velocity magnitude of contour: $v_{\max} = 1.9671\,m/s$, accuracy of the applied UDA sensor: $\pm 0.5\,\%$
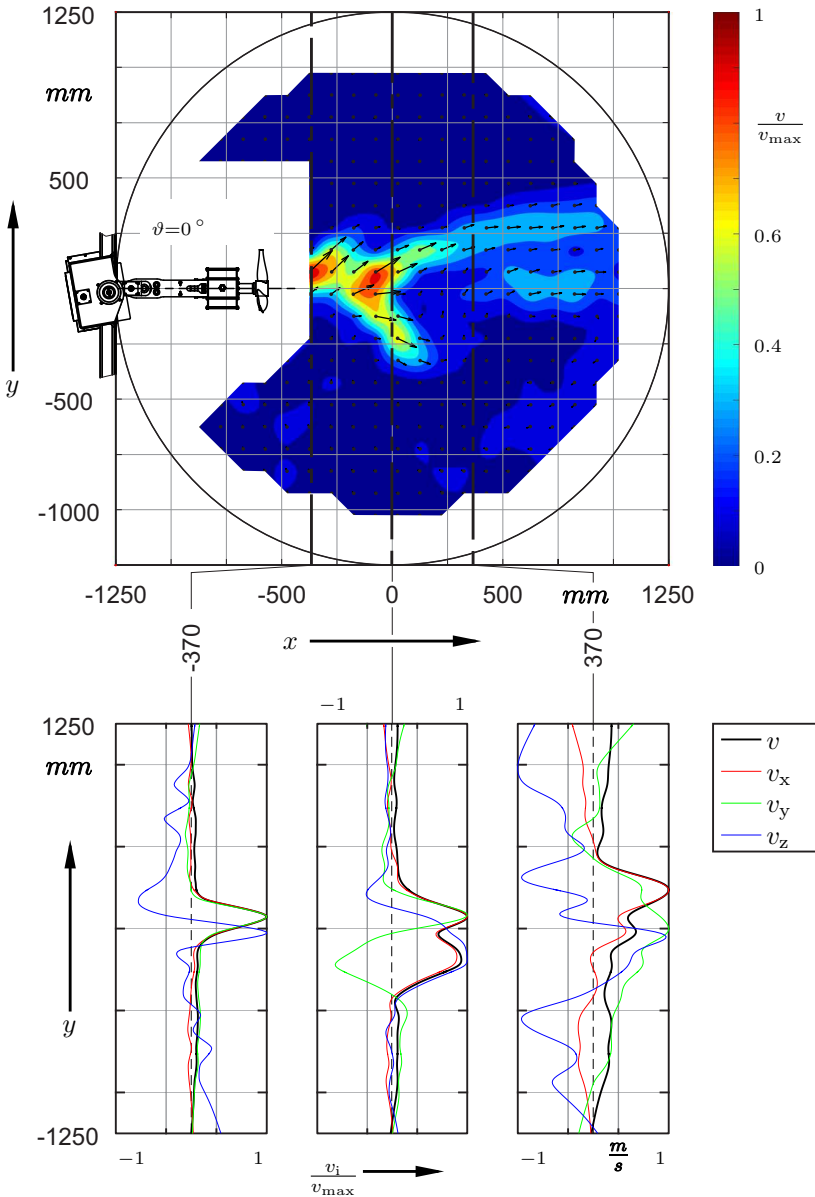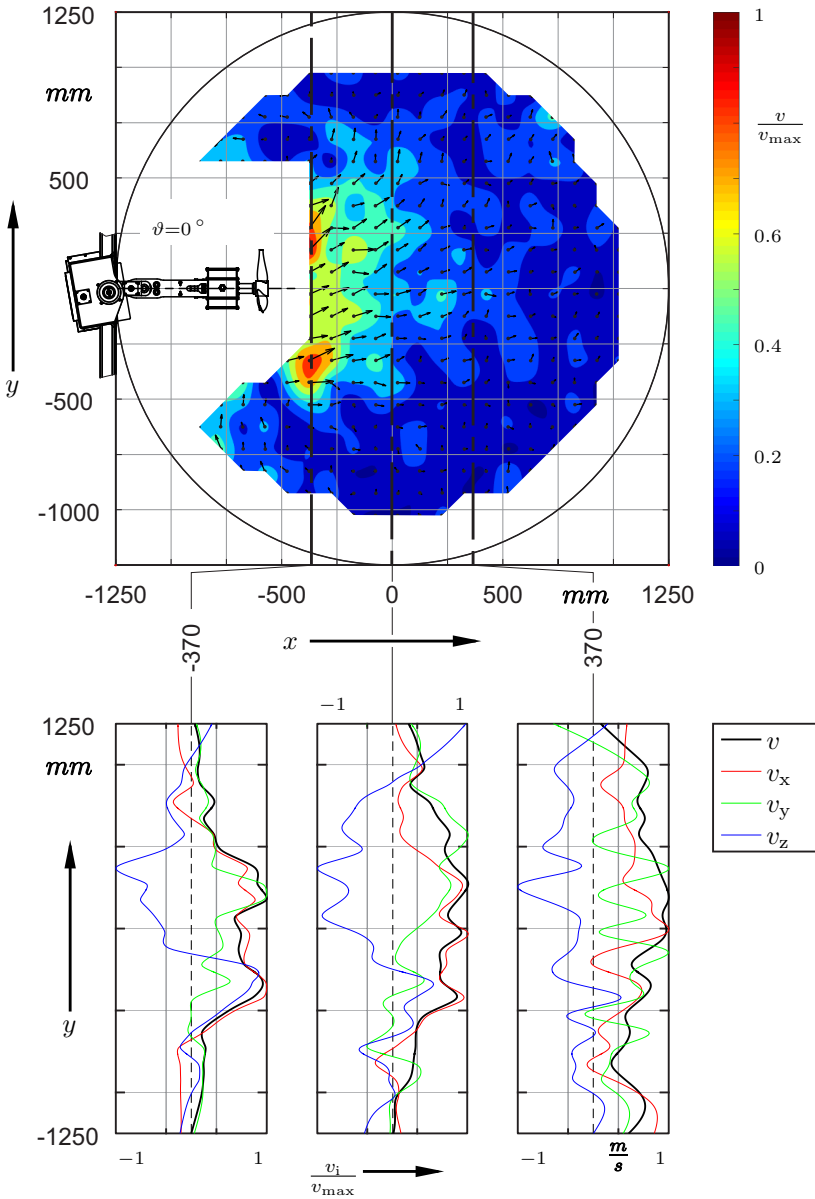
Figure E.16. *Measurement result C2-N085, normalised velocity contour plot v/v_{max} with vector plot and evaluation of the normalised velocity vector $v_{\mathrm{i}}/v_{\mathrm{max}}$ for cross-section planes at $x = -370$, $x = 0$ and $x = 370\,mm$, drawn for machine-level $z = 0.9\,m$, maximum velocity magnitude of contour: $v_{\mathrm{max}} = 1.0717\,m/s$, accuracy of the applied UDA sensor: $\pm 0.5\,\%$*

Figure E.17. **Measurement result C2-N100**, *normalised velocity contour plot $v/v_{\max}$ with vector plot and evaluation of the normalised velocity vector $v_i/v_{\max}$ for cross-section planes at $x = -370$, $x = 0$ and $x = 370\,mm$, drawn for machine-level $z = 0.9\,m$, maximum velocity magnitude of contour: $v_{\max} = 1.2681\,m/s$, accuracy of the applied UDA sensor: $\pm 0.5\,\%$*
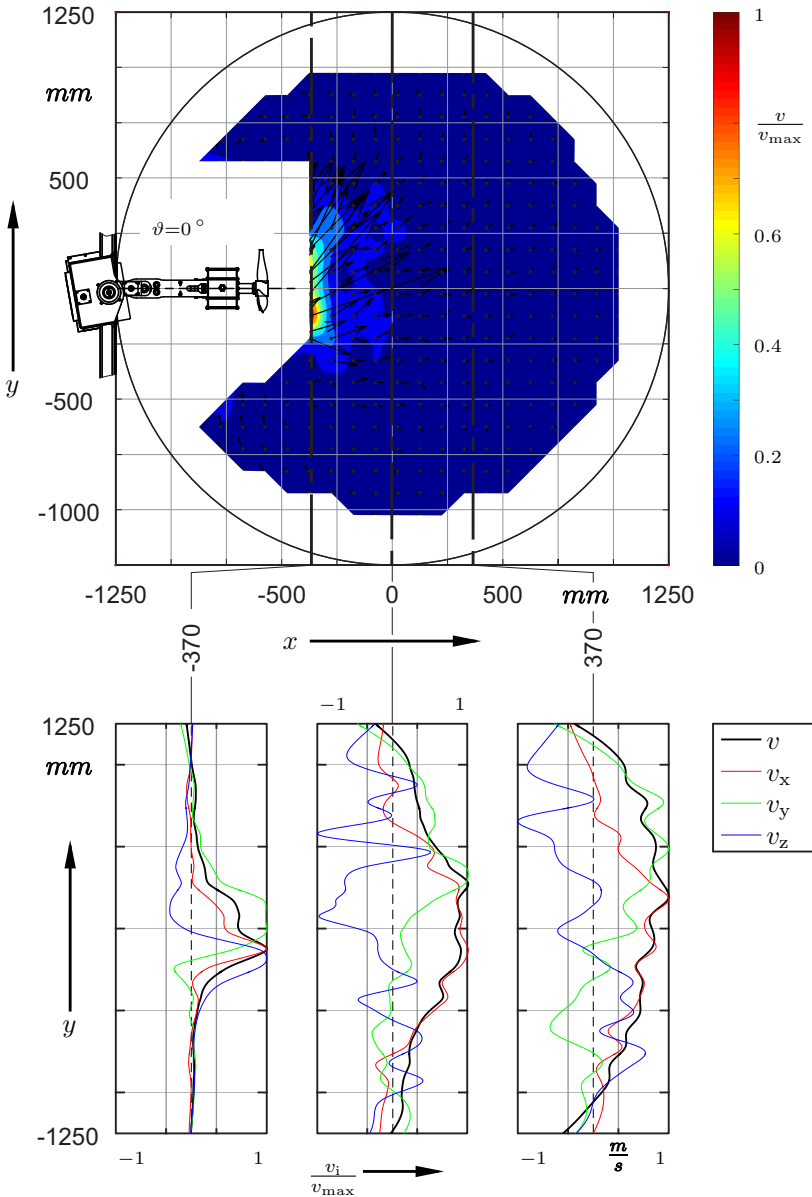
Figure E.18. *Measurement result C2-N115, normalised velocity contour plot $v/v_{\max}$ with vector plot and evaluation of the normalised velocity vector $v_i/v_{\max}$ for cross-section planes at $x = -370$, $x = 0$ and $x = 370\,mm$, drawn for machine-level $z = 0.9\,m$, maximum velocity magnitude of contour: $v_{\max} = 1.3557\,m/s$, accuracy of the applied UDA sensor: $\pm 0.5\,\%$*
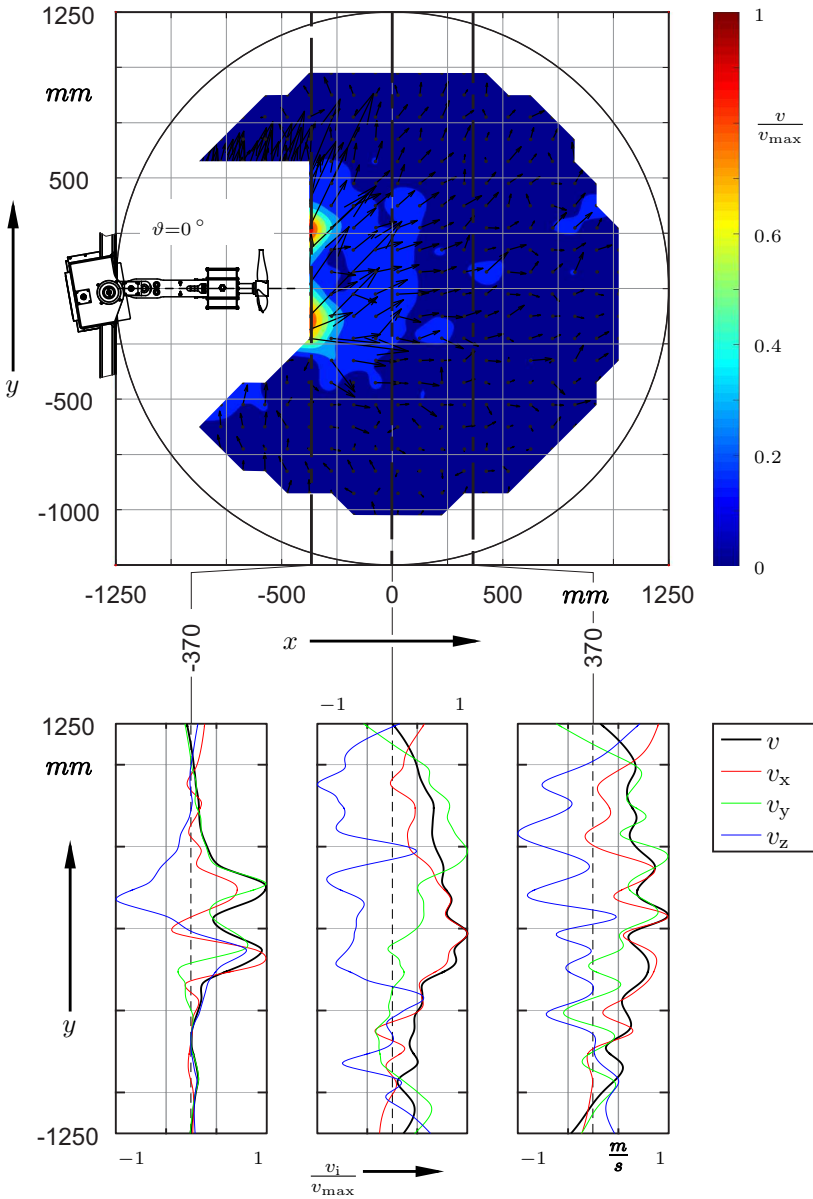
Figure E.19. *Measurement result C3-N085, normalised velocity contour plot v/v_{max} with vector plot and evaluation of the normalised velocity vector v_i/v_{max} for cross-section planes at $x = -370$, $x = 0$ and $x = 370\,mm$, drawn for machine-level $z = 0.9\,m$, maximum velocity magnitude of contour: $v_{max} = 0.0894\,m/s$, accuracy of the applied UDA sensor: $\pm 0.5\,\%$*

Figure E.20. *Measurement result C3-N100, normalised velocity contour plot $v/v_{\max}$ with vector plot and evaluation of the normalised velocity vector $v_i/v_{\max}$ for cross-section planes at $x = -370$, $x = 0$ and $x = 370\,mm$, drawn for machine-level $z = 0.9\,m$, maximum velocity magnitude of contour: $v_{\max} = 0.6706\,m/s$, accuracy of the applied UDA sensor: $\pm 0.5\,\%$*

Figure E.21. *Measurement result C3-N105, normalised velocity contour plot $v/v_{\max}$ with vector plot and evaluation of the normalised velocity vector $v_i/v_{\max}$ for cross-section planes at $x = -370$, $x = 0$ and $x = 370\,mm$, drawn for machine-level $z = 0.9\,m$, maximum velocity magnitude of contour: $v_{\max} = 0.4726\,m/s$, accuracy of the applied UDA sensor: $\pm 0.5\,\%$*
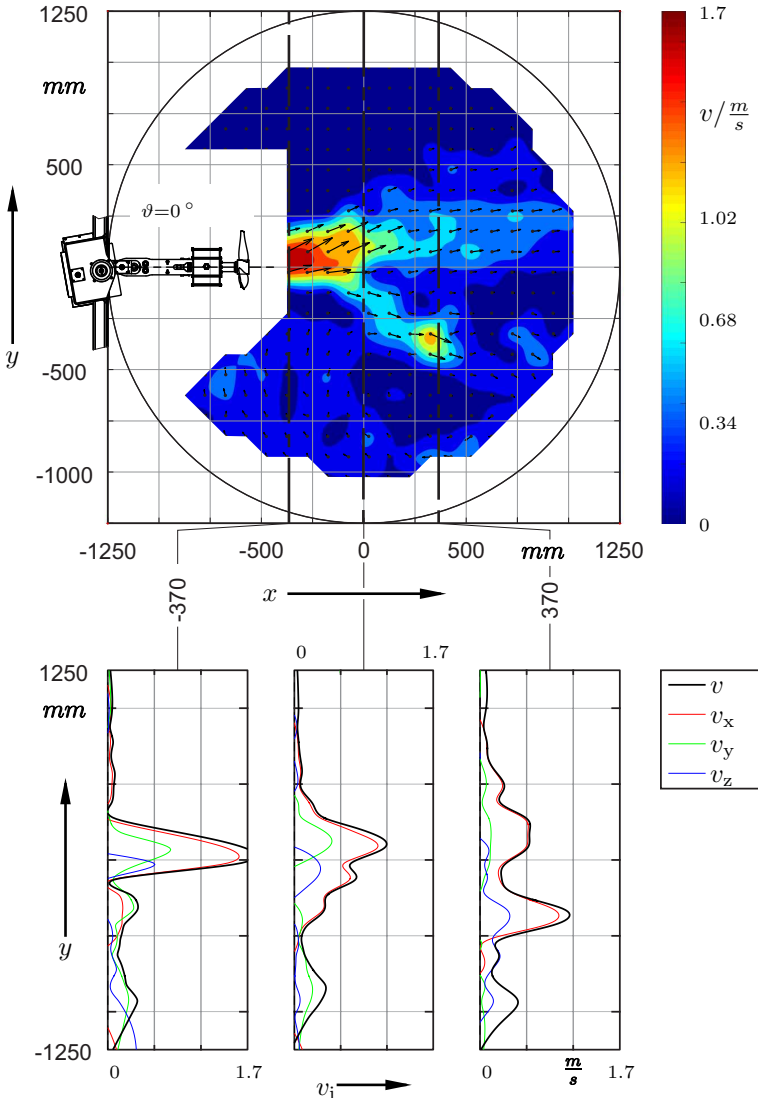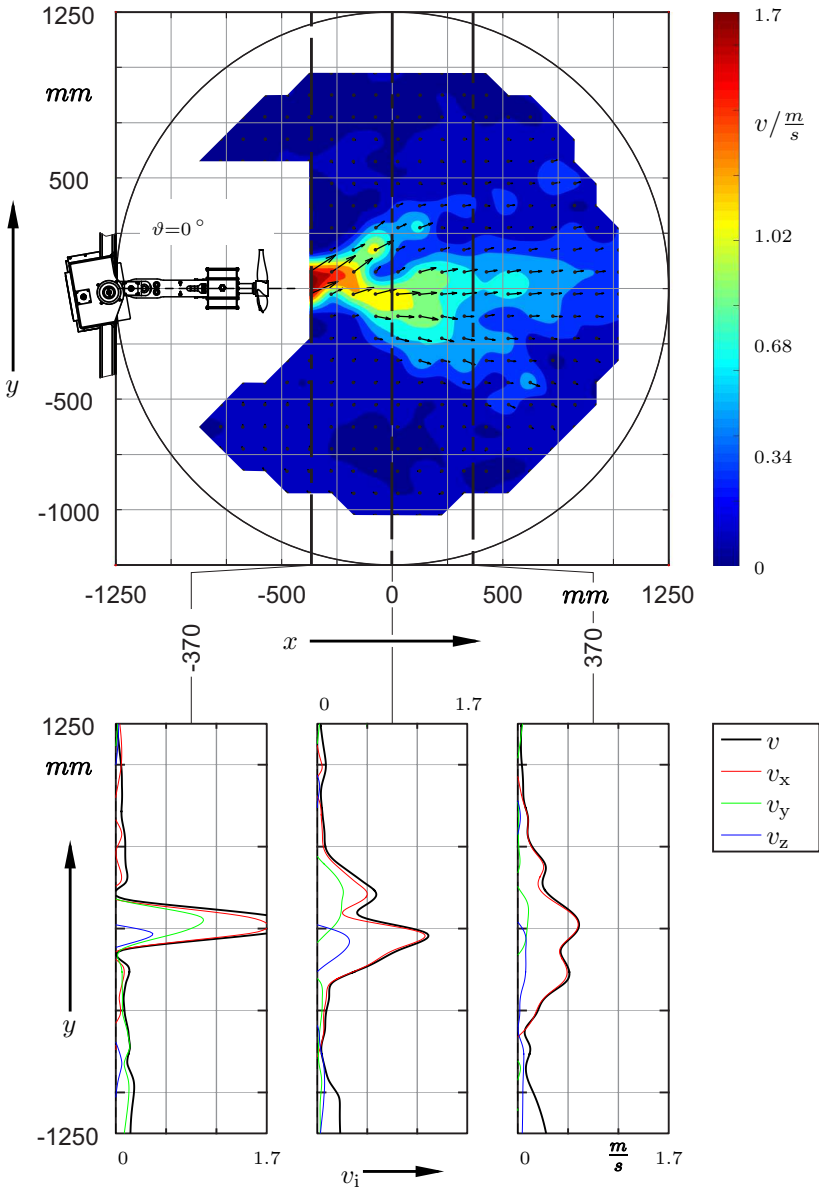
E.2.3. Similarly scaled velocity

Figure E.22. *Similarly scaled **measurement result C1-N085**, velocity contour plot scaled to $v_{\max} = 1.7\,m/s$ with vector plot and evaluation of the normalised velocity vector for cross-section planes at $x = -370$, $x = 0$ and $x = 370\,mm$, drawn for machine-level $z = 0.9\,m$, accuracy of the applied UDA sensor: $\pm 0.5\,\%$*
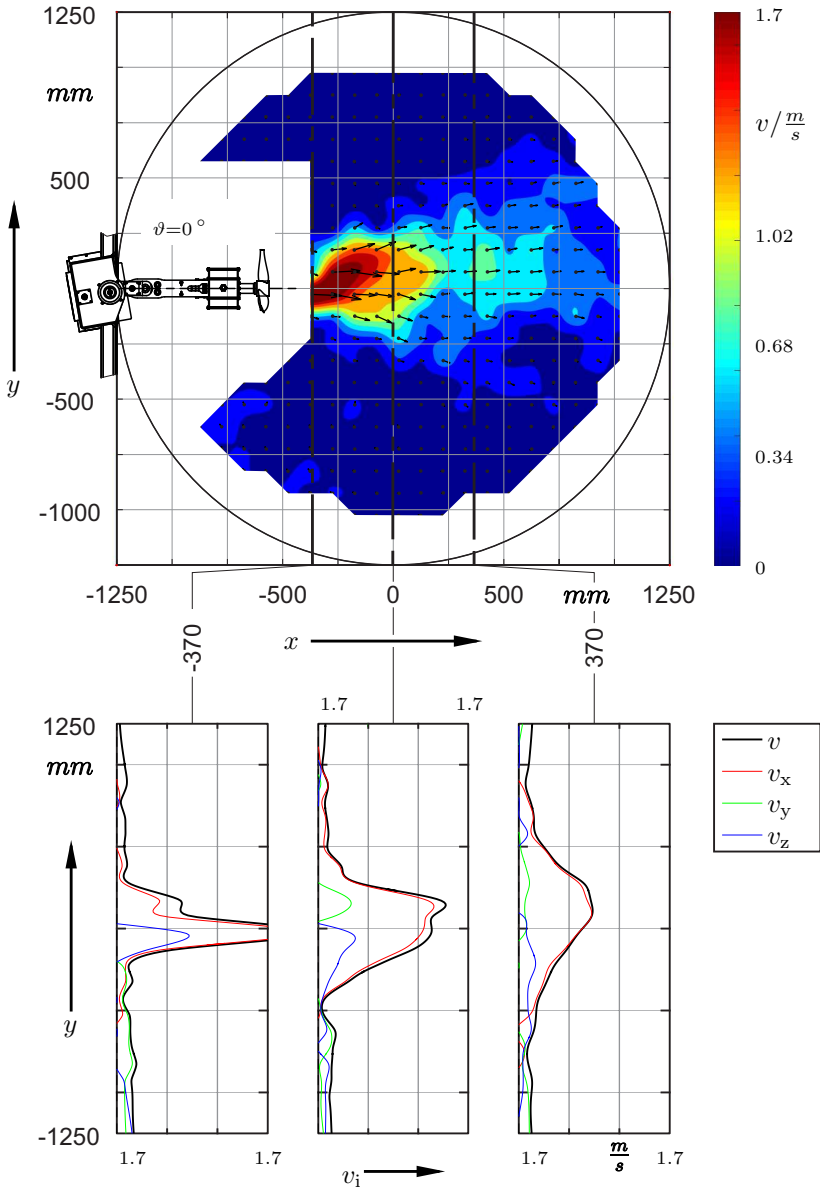
Figure E.23. *Similarly scaled **measurement result C1-N100**, velocity contour plot scaled to $v_{\text{max}} = 1.7\,m/s$ with vector plot and evaluation of the normalised velocity vector for cross-section planes at $x = -370$, $x = 0$ and $x = 370\,mm$, drawn for machine-level $z = 0.9\,m$, accuracy of the applied UDA sensor: $\pm 0.5\,\%$*

Figure E.24. *Similarly scaled **measurement result C1-N115**, velocity contour plot scaled to $v_{\mathrm{max}} = 1.7\,m/s$ with vector plot and evaluation of the normalised velocity vector for cross-section planes at $x = -370$, $x = 0$ and $x = 370\,mm$, drawn for machine-level $z = 0.9\,m$, accuracy of the applied UDA sensor: $\pm 0.5\,\%$*
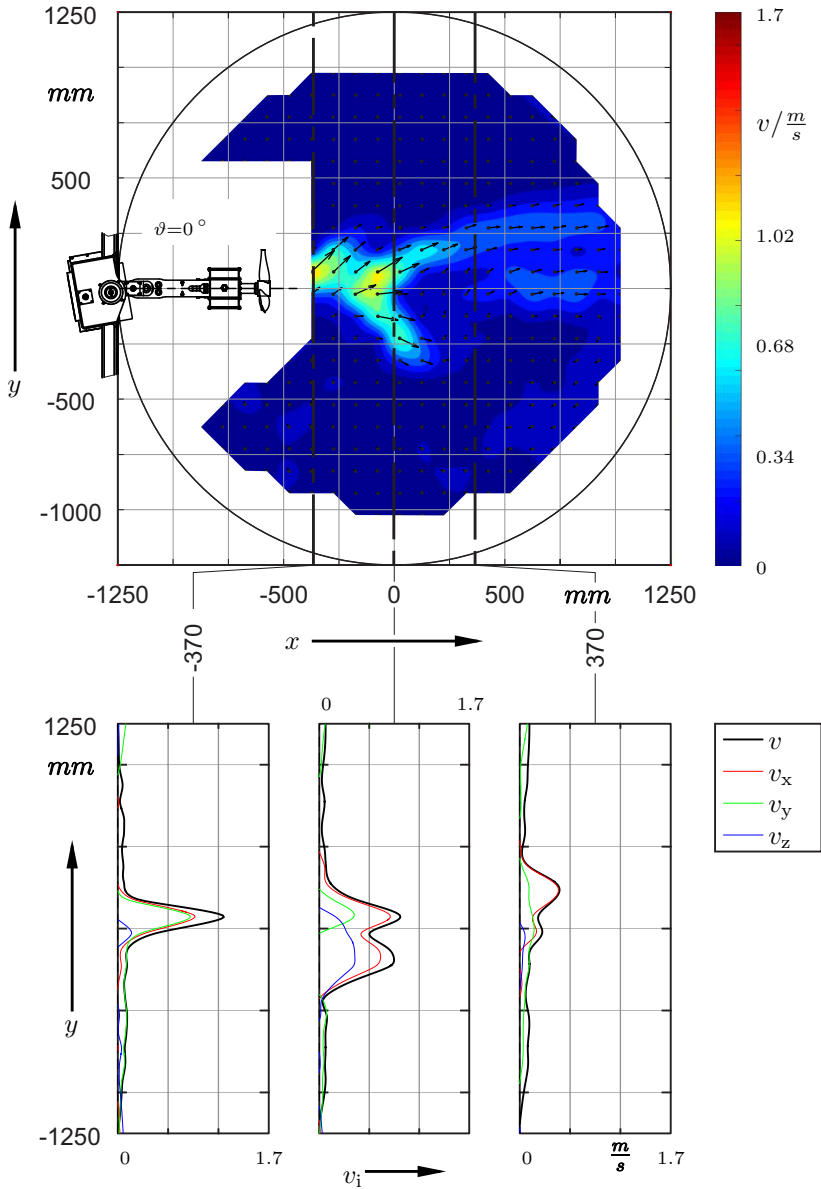
Figure E.25. *Similarly scaled **measurement result C2-N085**, velocity contour plot scaled to $v_{max} = 1.7\,m/s$ with vector plot and evaluation of the normalised velocity vector for cross-section planes at $x = -370$, $x = 0$ and $x = 370\,mm$, drawn for machine-level $z = 0.9\,m$, accuracy of the applied UDA sensor: $\pm 0.5\,\%$*
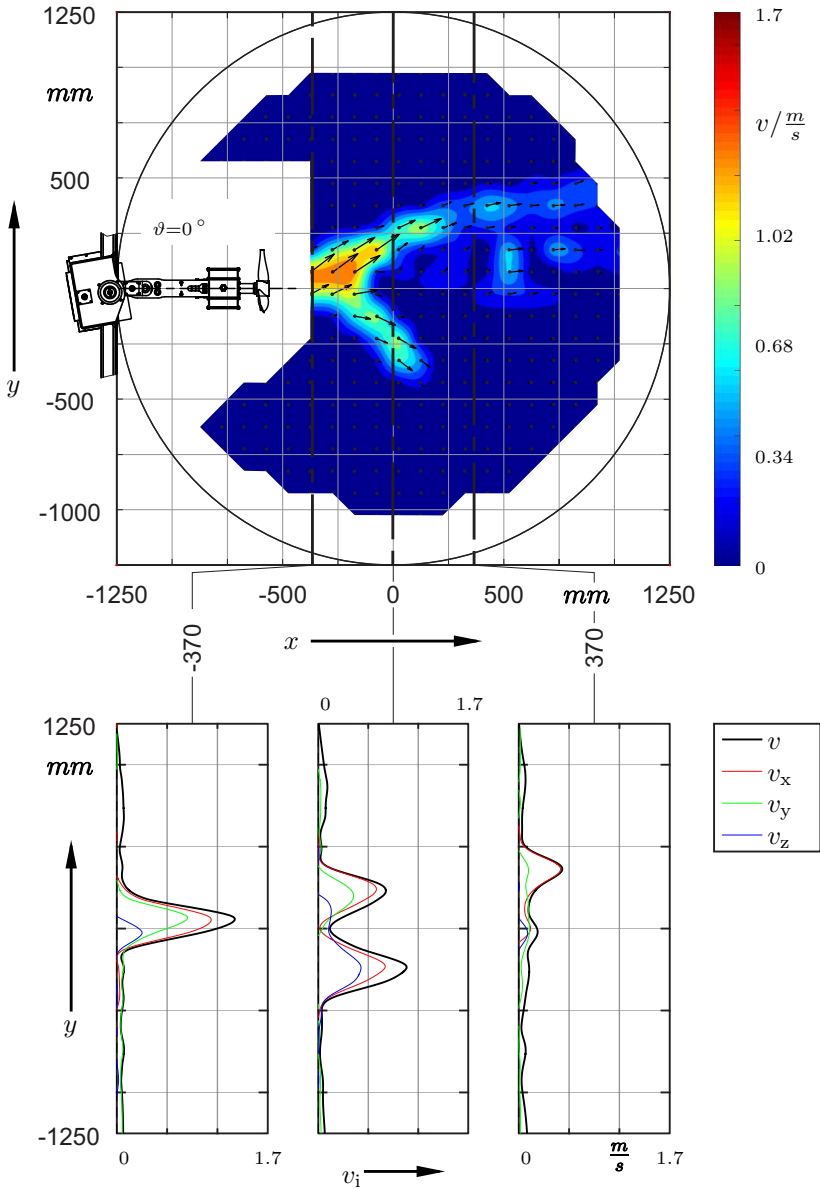
Figure E.26. *Similarly scaled* **measurement result C2-N100**, *velocity contour plot scaled to* $v_{\max} = 1.7\,m/s$ *with vector plot and evaluation of the normalised velocity vector for cross-section planes at* $x = -370$, $x = 0$ *and* $x = 370\,mm$, *drawn for machine-level* $z = 0.9\,m$, *accuracy of the applied UDA sensor:* $\pm 0.5\,\%$
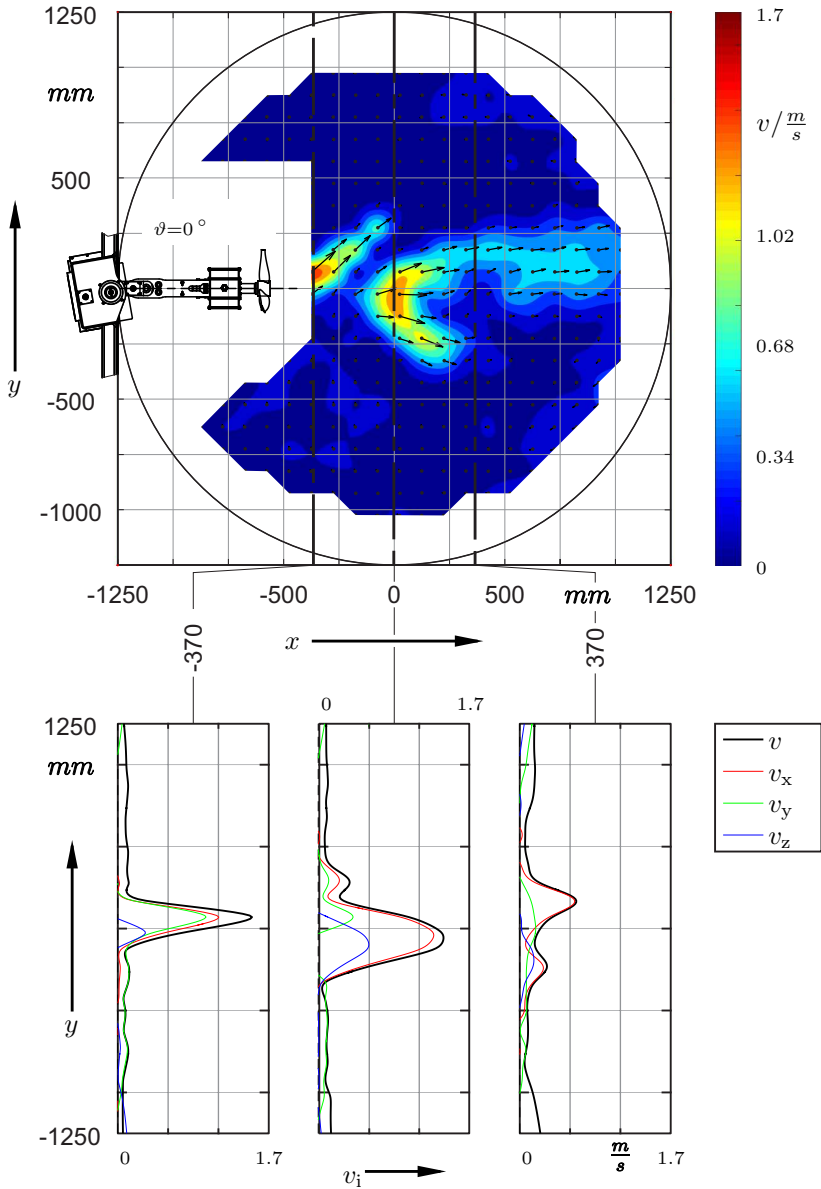
Figure E.27. *Similarly scaled **measurement result C2-N115**, velocity contour plot scaled to* $v_{\mathrm{max}} = 1.7\,m/s$ *with vector plot and evaluation of the normalised velocity vector for cross-section planes at* $x = -370$, $x = 0$ *and* $x = 370\,mm$, *drawn for machine-level* $z = 0.9\,m$, *accuracy of the applied UDA sensor:* $\pm 0.5\,\%$
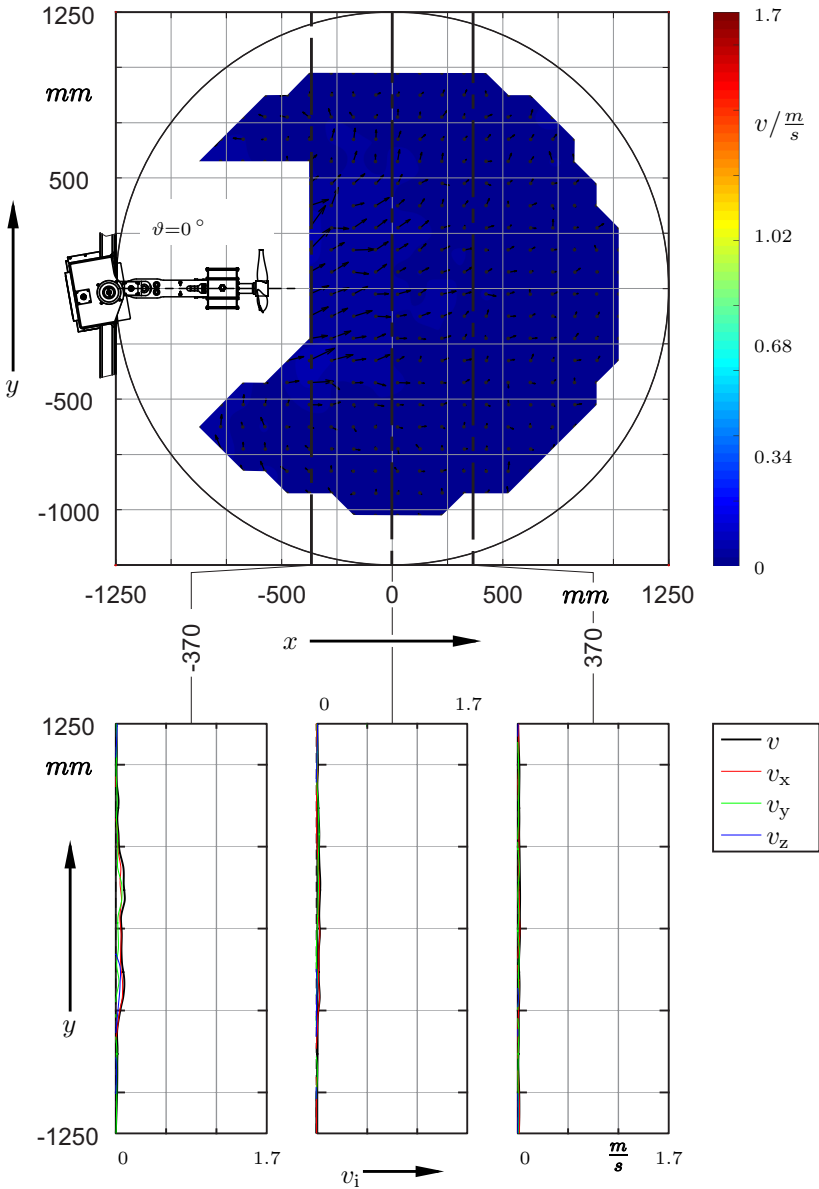
Figure E.28. *Similarly scaled **measurement result C3-N085**, velocity contour plot scaled to $v_{\max} = 1.7\,m/s$ with vector plot and evaluation of the normalised velocity vector for cross-section planes at $x = -370$, $x = 0$ and $x = 370\,mm$, drawn for machine-level $z = 0.9\,m$, accuracy of the applied UDA sensor: $\pm 0.5\,\%$*

Figure E.29. *Similarly scaled **measurement result C3-N100**, velocity contour plot scaled to $v_{\mathrm{max}} = 1.7\,m/s$ with vector plot and evaluation of the normalised velocity vector for cross-section planes at $x = -370$, $x = 0$ and $x = 370\,mm$, drawn for machine-level $z = 0.9\,m$, accuracy of the applied UDA sensor: $\pm 0.5\,\%$*
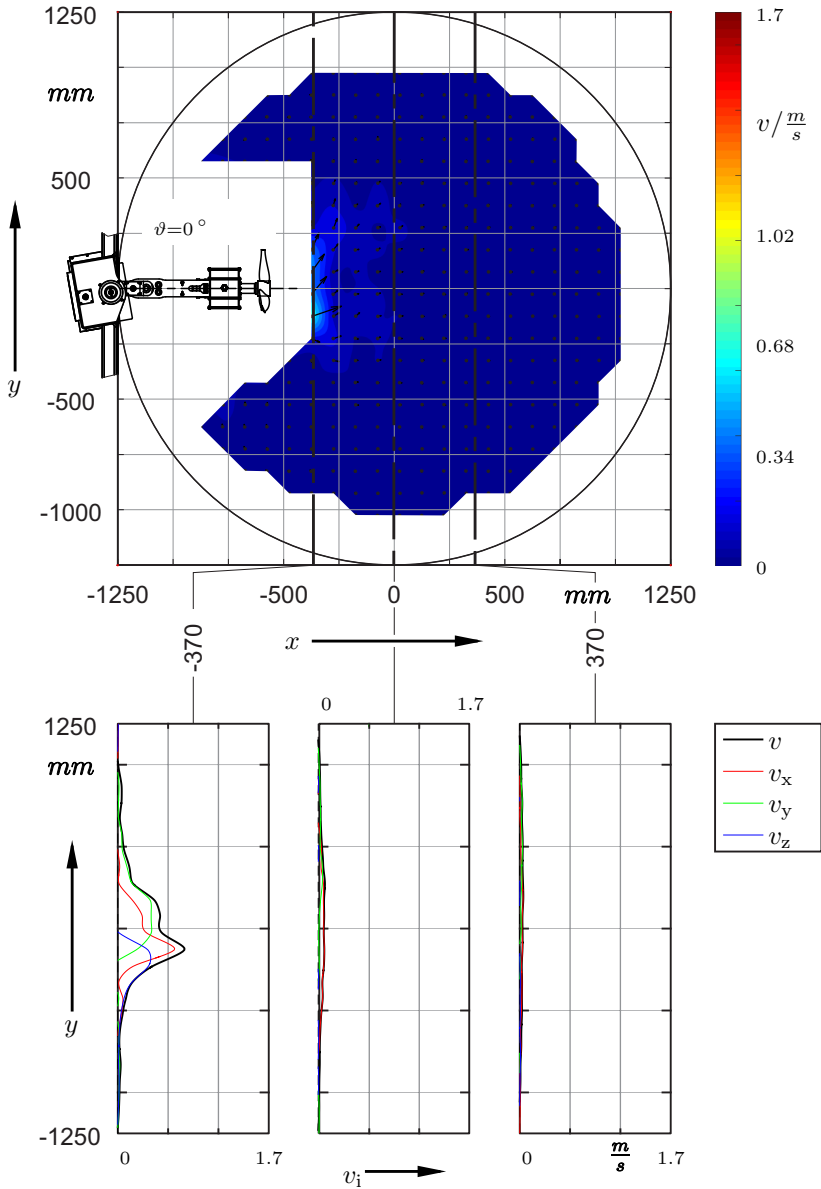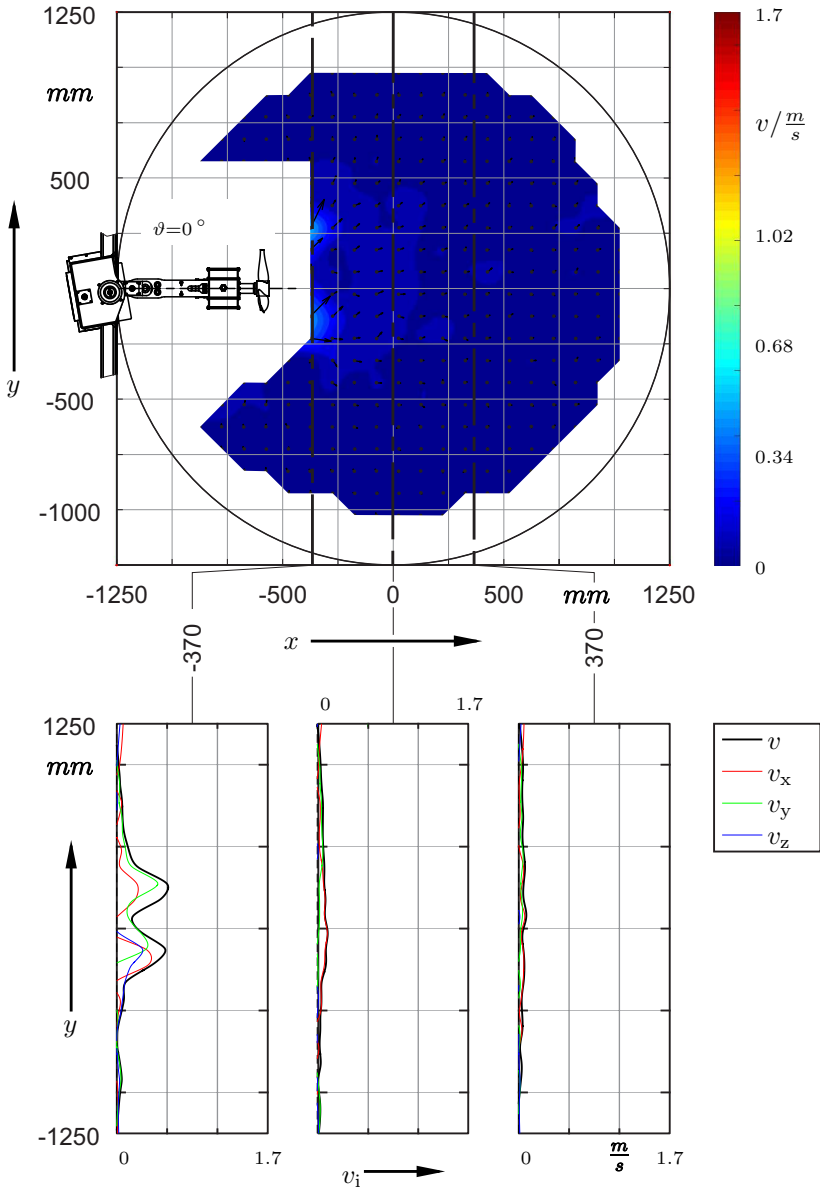
Figure E.30. *Similarly scaled **measurement result C3-N105**, velocity contour plot scaled to $v_{\max} = 1.7 \, m/s$ with vector plot and evaluation of the normalised velocity vector for cross-section planes at $x = -370$, $x = 0$ and $x = 370 \, mm$, drawn for machine-level $z = 0.9 \, m$, accuracy of the applied UDA sensor: $\pm 0.5 \, \%$*

Supervised student work

Student research thesis

Zenner, Sebastian	Energieeffizienzanalyse der Gruppenkläranlage Winnweiler	2011
Schulz, Sebastian	Entwurf der hydraulischen Komponente einer Kreiselpumpe mit anschließender Validierung der Leistungscharakteristik in Versuch und Simulation	2011
Besand, Christian	Konzeptentwicklung und Auslegung eines hydrostatischen Fahrantriebs für selbstfahrende Erntemaschinen	2011
Trimborn, Florian	Numerische Untersuchung des Durchflusses eines viskoelastischen Mediums durch eine konische Düse	2011
Nerjes, Onno	Numerische Untersuchung einer Radialpumpe mit OpenFOAM	2012
Genuit, Fabian	Untersuchung von medizintechnischen Drainagen	2012
Arnold, Christian	Konzepterstellung Luttenventilator	2012
Mirmilstein, Alexander	Entwicklung einer Software zur Vorauslegung der Wasserwege von Pumpspeicherkraftwerken	2012
Neumann, Matthias	Untersuchung des Energieverbrauchs des "Japanischen Gartens" Kaiserslautern mit Ziel des emissionsfreien Betriebes	2012
Forster, Jérôme	Vermessung des Nachlaufdralls einer schnellläufigen Windkraftanlage	2013
Sorg, Sebastian	Ermittlung des Leistungskennfeldes einer schnellläufigen Windkraftanlage	2013

Genuit, Fabian	Untersuchung des Einflusses viskoelastischer Medien auf die Leistungscharakteristik eines Propellerviskosimeters	2013
Arnold, Christian	Auslegungsmethoden von Rührern für den Einsatz in nicht-Newtonschen Medien	2014
Nieswiodek, Viola Kim	Verfahren zur Leistungsauslegung von Rührern zum Einsatz in nicht-Newtonschen Medien am Beispiel von Biogasanlagen	2014
Kaiser, Simon	Softwareseitige Auslegung einer Prüfstandssteuerung eines Propellerviskosimeters auf Grundlage des Arduino Uno Mikrocontrollers	2015
Zoller, Adrian	Hardwareseitige Auslegung einer Prüfstandssteuerung eines Propellerviskosimeters auf Grundlage des Arduino Uno Mikrocontrollers	2015
Berger, Constantin	Ermittlung von Profilpolaren von low-Re-Profilen beim Einsatz in nicht-newtonschen Medien	2015
Reim, Viktor	Bestimmung der elastischen und viskosen Eigenschaften von Modellmedien in der Rührerauslegung	2015
Schießer, Jan	Untersuchung und Analyse der aktuellen Technik der Profilaerodynamik von schnellläufigen Windkraftanlagen	2015
Schmidt, Michael	Untersuchung und Analyse der aktuellen Technik von schnellläufigen Windkraftanlagen zum dezentralen Einsatz	2015
Enderlein, Marie	Untersuchung und Optimierung eines Wasserkanals mit numerischen Methoden	2016
Priemer, Christine	Numerische Untersuchung eines Propeller-Rührers mit OpenFOAM	2016
Boudgoust, Fabian	Bestimmung der Profilbeiwerte eines low-Re-Profils beim Einsatz verschiedener nichtnewtonscher Medien mit OpenFOAM	2018

Brenneisen, Jan	Auslegung einer schnellläufigen Windkraftanlage mit der Blattelementmethode und anschließende numerische Untersuchung	2020
Blechner, Max	Untersuchung des Einflusses von Quernuten im Unterbrecherbereich auf die Performance von Seitenkanalpumpen	2020
Neelam, Pooni	Untersuchung des Entwicklungsstandes von offshore Windkraftanlagen	2020
Paton, Inès	Auslegung einer schnellläufigen Windkraftanlage mit der Blattelementmethode und anschließende numerische Untersuchung	2020
Simon, Yann	Auslegung einer schnellläufigen Windkraftanlage mit der Blattelementmethode und anschließende numerische Untersuchung	2020

Final thesis

Stolz, Yannick	Untersuchungen an Geber- und Nehmerzylindern mit bewegten Dichtungen	2012
Nerjes, Onno	Ermittlung der Leistungskurve einer Versuchswindenergieanlage für verschiedene Anströmbedingungen	2012
Kucharczyk, Piotr	Auslegung und Konstruktion einer schnellläufigen Windkraftmodellanlage	2012
Besand, Christian	Aufbau eines virtuellen Fahrantriebs zur Ermittlung der Effizienz und des relativen Kraftstoffverbrauchs einer selbstfahrenden Erntemaschine	2012
Weirich, Dominik	Numerische Optimierung einer neuartigen Wasserstrahlpumpe	2013
Klag, Lisa	Auslegung einer schnellläufigen Windkraftanlage mit der Blattelementmethode und Untersuchung mit numerischen Methoden	2013
Eckhardt, Lisa	Untersuchung des Freistrahls beim Austritt aus dem Injektor einer Pelton-Turbine	2013
Adams, Benjamin	Machbarkeitsstudie zur Entwicklung eines Energiespeicherkonzeptes zur Absicherung der Strom- und Wärmeversorgung einer kommunalen Gebietskörperschaft	2013
Rüttgers, Michael	Untersuchung des Einflusses der Rauigkeit auf die Profilpolare eines Verdichters von Flugzeugtriebwerken mit CFD	2014
Kulawik, Florian	Programmierung eines Solvers zur Simulation eines linearviskosen, elastischen Fluides in OpenFoam mit Berücksichtigung rotierender Wände	2014
Baader, Frank	Validierung von OpenFOAM für eine turbulente Propellerströmung mit strukturviskosen Fluiden	2014

Genuit, Fabian	Beitrag zur Auslegung eines Propellerrührers zum Rühren nicht-Newtonscher Medien unter Verwendung einer Blattelementmethode	2014
Bambach, Sven	Programmierung eines Algorithmus zur automatischen Generierung eines CDF-Rechengitters für Schiffspropeller mit anschließender Validierung	2017
Müller, Hendrik	Auslegung einer schnellläufigen Windkraftanlage mit der Blattelementmethode	2017
Meurer, Catrin	Analyse geeigneter Netztopologien zur Untersuchung von Zylinderumströmungen unter Verwendung einer Grobstruktur-Turbulenzmodellierung	2019
Knapp, Sander	Untersuchung von Blattelementheizungen zum Einsatz in Windkraftanlagen mit der Finite-Elementen-Methode	2020

Curriculum Vitae

	Personal Information
Name	Thomas Reviol
Year of birth	1981
Place of birth	Saarbrücken
Nationality	German

	Work
01/2011–today	**Postdoc** as Akademischer Rat/Oberrat, Institute of Fluid Mechanics and Turbomachinery, University of Kaiserslautern
01/2008–12/2010	**Scientific assistant**, Institute of Fluid Mechanics and Turbomachinery, University of Kaiserslautern

	Academic education
October 11, 2010	**Doctoral examination** at Institute of Fluid Mechanics and Turbomachinery, University of Kaiserslautern, subject of dissertation thesis: *„Experimentelle und numerische Untersuchungen eines modifizierten Propeller-Viskosimeters zur Bestimmung der Fließeigenschaften nicht-Newtonscher Medien mit inhomogenem Charakter".*
10/2001 – 12/2007	**Study of mechanical and process engineering** at University of Kaiserslautern, subject of diploma thesis *„Optimierung der Zuströmverhältnisse in einem Kühlwasser-Einlaufkammerbauwerk mittels CFD".*

Community service	
2000–2001	Arbeiter Samariter Bund (ASB)

School education	
06/2000	Abitur
08/1991–06/2000	Secondary school
09/1987–07/1991	Primary school